Photocrystallographic studies of linkage isomerism

Warren, Mark

Award date:
2011

Awarding institution:
University of Bath

Photocrystallographic Studies
into
Linkage Isomerism

Mark R. Warren

A thesis submitted for the degree of Doctor of Philosophy

University of Bath

Department of Chemistry

April 2011

Abstract

The work described in this thesis utilises a new and rapidly developing branch of diffraction experiment called 'photocrystallography'. Photocrystallography is the study of photo-induced processes in a crystal using X-ray crystallographic techniques. Within this report photocrystallography is used to investigate the structures of photoactivated metastable linkage isomers of *trans*ition metal nitro complexes.

Chapter 1 contains a brief review of current state-of-the-art photocrystallography, as applied to molecular complexes. Complementary techniques are described and a detailed description of linkage isomerism is also presented.

Chapter 2 contains the fundamentals of crystallography giving a background and understanding of the experiments reported within this thesis.

The design and implementation of the LED ring, enabling photocrystallographic experiments to be carried out routinely is described in Chapter 3. The LED ring is an array capable of holding six LEDs in close proximity to the crystal without affecting the diffraction experiment and has been used successfully to photoactivate the crystal.

Chapters 4 and 5 describe the research into the binding modes of the nitrite ligand to a metal centre for a series of complexes supported by a range of nitrogen, phosphorus and arsenic based auxiliary ligands. These chapters explore the different nitrite coordination modes adopted from synthesis, the photocrystallographic investigations of the linkage isomers *trans*formation and the temperature dependant equilibrium between the binding modes. Novel *in-situ* crystallographic experiments of both thermally and photochemically activated *trans*formations have been carried out on the $Ni(Et_4en_2)(\eta^2\text{-}ONO)(\eta^1\text{-}NO_2)$ complex and have been shown to give rise to the formation of metastable linkage isomers within the single crystal. The first 100% fully reversible linkage isomerism is also reported for $Ni(dppe)(NO_2)Cl$, with a series of related compounds also exhibiting this high single-crystal to single-crystal *trans*formation. In Chapter 6, the kinetics of the linkage isomerism *trans*formation is explored by monitoring the peak intensity change upon irradiation, using both powder diffraction and single crystal diffraction techniques.

Acknowledgements

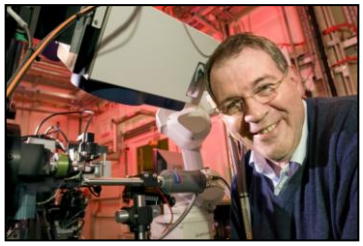

I would like to thank Prof. Paul Raithby for all his guidance, giving me a number of great opportunities throughout my Ph.D, and making my project thoroughly enjoyable and interesting. I am also grateful for his friendship and continuous care.

I especially thank Dr. Simon Brayshaw for being a super postdoc within the group, for his wealth of knowledge and continuous help. The rest of the Raithby group has greatly contributed to my work in both synchrotron time and within the lab. I thank Dr. Steffi Schiffers for all her input into the project and especially for efficient scheduling of many dedicated nights at synchrotron experiments, Chris Woodall for all his interesting and in-depth lab discussions, Sara Fuertes Lorda for always being courteous and holding doors open, and Lauren Hatcher for her work as a project student and her input into this thesis.

I am grateful for inputs and ideas especially at the beginning of the project from Dr Andrew Johnson and to Dr. Mary Mahon for her support in the crystallography lab.

I am thankful for all the encouragement and continuous support Anna Stevenson has provided throughout my PhD and for making the time spent at Bath during these years a happy and treasured time.

I am particularly appreciative of the help from my parents Robert and Rosie Warren, for their continuous willingness to help in anyway possible with my research, from reading and correcting vast amounts, to understanding and computational expertise.

The work carried out in this thesis would not be possible without the beamline scientists providing an excellent service and a willingness to adapt the instruments. My thanks go to Dr. John Warren (Daresbury), Dr. Simon Teat, Dr. Christine Beavers (ALS), Dr. Dave Allen and co workers at Diamond Light Source.

I would like to thank Dr. Tim Easun and Dr. Mike George in Nottingham for their low-temperature Raman spectroscopy on the nickel complexes.

I would also like to thank the EPSRC for financial support.

Abbreviations

Ω	Solid angle	LIESST	light-induced spin-state trapping
sr	Steradian	LED	light emitting diodes
Δ_{oct}	delta octahedral	LMCT	Ligand to metal charge *trans*fer
ΔG	Gibbs free energy	LUMO	Lowest unoccupied molecular orbital
τ	Lifetime	LS	Low-spin
Å	Angstrom (10^{-10} m)	η	Coordination bond order
a,*b*,*c*	Unit cell axis	mcd	Milli Candle Intensity
α, *β*, *γ*	Unit cell angles	min	Minute
CSD	Crystallographic structural database	mm	Millimetre
d	d-orbitals	M-L	Metal ligand
DAC	Diamond Anvil Cell	MS	Metastable
DFT	Density Functional Theory	nm	Nanometer
dppe	1,2-*Bis*(diphenylphosphino)ethane	NO_2	Nitro ligand
dcpe	1,2-*Bis*(dicyclohexylphosphino)ethane	*ONO*	Nitrito ligand
DCM	Dichloromethane	P	Energy required to pair an electron
DSC	Differential scanning calorimetry	ρ	Electron density
e_g	Bonding octaheral d obitals	GPa	Giga Pascal
EGC	Environmental gas cell	T	Temperature
en	Ethylenediamine	TGA	ThermoGravimetric Analyzer
$F_{(hkl)}$	Structure Factor	t_{2g}	Non-bonding octaheral d obitals
$F_{(calc)}$	Calculated Structure Factor	*R*	Right
$F_{(obs)}$	Observed Structure Factor	R	Gas constant
F.T.	Fourier *trans*formation	R_1	R-factor
IR	Infrared	RMS	Root mean squared deviation
J	spin-orbit coupling	s	Second
GS	Ground state	*S*	Left
h	hour	S	Spin-spin coupling
HOMO	Highest occupied molecular orbital	THF	Tetrahydrofuran
HS	High-spin	UV	Ultra Violet
		v	Wavelength of the Photon
h	Planck's constant	V	Volts
Hz	Hertz	YAG	yttrium aluminium garnet
K	Kelvin	XFEL	X-ray Free Electron Lasers
k_b	Boltzmann Constant	W	Watt
K_{eq}	Equilibrium constant	wR_2	Weighted R-factor
L	Orbit-orbit coupling		

Contents Page

Chapter 1 – Introduction

Chapter 1 - Introduction

X-ray crystallography is the definitive analytical tool for obtaining full three-dimensional molecular structures of a crystalline material. At present, it is most commonly used for the characterisation of reactants or products in a reaction. Crystals are generally viewed as rigid solid-state materials, but there is a surprising amount of flexibly within the structure, thus allowing a wide variety of molecular rearrangement within the crystal without major crystal decomposition.

Advances in X-ray beam intensity, detectors systems, cryogenics, computer power and software have opened up a range of new crystallographic experiments in addition to traditional ground-state structure determination. By applying non-ambient techniques it is now possible to perform other experiments, in conjunction with the diffraction experiment, and by doing so it is possible to obtain three-dimensional structures at discrete steps during a reaction process, to investigate transient species or to obtain crystal structures not achievable through normal methods.

Due to the nature of the crystallographic experiments there are physical limitations in the number of ways in which to induce a single-crystal to single-crystal transformation. A single-crystal to single-crystal transformation can be achieved by either changing the crystal's physical environment or applying an external stimulus e.g. by altering the temperature (cryogens), pressure (diamond anvil cell), atmosphere (environmental gas cell), irradiation (photon irradiation) or using an applied electrical field.

There are a wide variety of chemical processes that can be investigated using the application of non-ambient conditions coupled with single crystal X-ray experiments. The chemical and physical process may be reversible or irreversible, and in the case of a reversible process the equilibrium position can be controlled by the tuning of the non-ambient conditions. It is thus possible to characterise transient species with only nanosecond lifetimes.

1.1. Non-Ambient Techniques

1.1.1. Temperature Variation

Temperature-induced structural phase transitions are by far the most common type of single-crystal to single-crystal transformations investigated using crystallography and have been extensively studied ever since the introduction of cryogenics.

Over the last couple of decades, the development of reliable cryogenics has made it possible to obtain crystal structures routinely with temperature ranges from 80 K to 500 K. Oxford Cryosystems has developed the Cryosteam Plus ($N_{2(l)}$ 80-500 K) and N-HeliX ($He_{(l)}$ 28-300 K).[1] Likewise, Oxford Diffraction has developed the Cryojet HT ($N_{2(l)}$ 90-490 K) and the Helijet ($He_{(l)}$ 10 to 90 K).[2] Extreme low temperatures down to 3 K are possible, developed by Durham University.[3] At central facilities there are closed cryostats capable of reaching temperature below 10 K.[4]

In addition to studying low-temperature structural phase transitions, there are many additional benefits to running low temperature diffraction experiments and it has become routine to collect data at temperatures of 80 to 150 K. Firstly, the use of perfluoroether oil which freezes at lower temperatures holds the crystal in place and makes the crystal mounting easier. Cooling the crystal to a low temperature reduces the thermal motions of atoms and results in better refined atom positions which not only gives more reliable and accurate bond lengths and angles, but also mosaicity is decreased resulting in superior quality data sets to higher resolutions.[5]

Having access to these temperature ranges not only improves the quality of diffraction experiments, but opens up a vast number of variable low temperature parametric studies which can give essential information about the physical and chemical properties of the material. Obtaining structural information around the transition point can give an insight into the mechanism. The next part of the chapter contains a selection of case studies that illustrate the diversity of thermally-induced phase transitions in crystallography.

1.1.1.1. Thermally-Induced Spin-Crossover

Octahedral metal centres with a d^4 to d^7 electronic configuration, particularly those of the first row transition metals, adopt either a high-spin (HS) or low-spin (LS) configuration depending on metal size, oxidation state, type of ligands and physical environment. If the splitting between the t_{2g} and e_g (Δ_{oct}) energy levels is smaller than the energy required to pair an electron (P), then the complex adopts an HS configuration (Figure 1a) and *vice versa* for LS complexes (Figure 1b).[6]

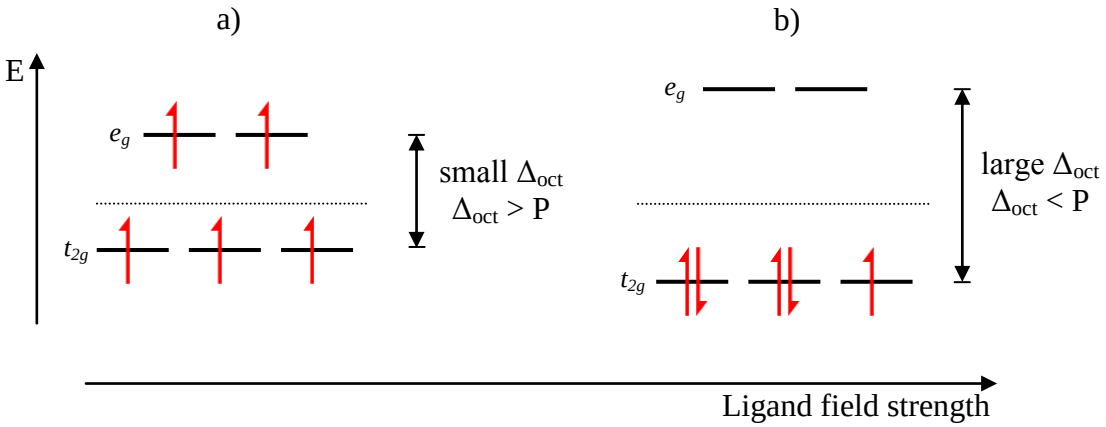

Figure 1: High-spin $(t_{2g})^3(e_g)^2$ (a) and low-spin $(t_{2g})^5$ (b) electronic configurations of d^5metal complex

By altering the ligands attached to the metal centre, the Δ_{oct} splitting can be adjusted in such a way that the difference in energy between the high-spin and low-spin configuration is relatively small. Altering the physical environment either through temperature, pressure, magnetic fields or illumination can induce a change in the electronic spin-state of the complex.

For a thermally-induced transition to occur, the difference in energy between the two states has to be approximately equal to k_bT (k_b is the Boltzmann constant and T is the temperature (K)). As the complex undergoes thermally-induced transition from HS to LS with a reduction in temperature, electrons in the e_g orbitals (*anti*bonding with respect to M-L) move into t_{2g} orbitals (bonding or non-bonding with respect to M-L) resulting in a contraction in metal-ligand bond length. For this reason crystallography is an ideal analytical tool for investigating these changes by monitoring the M-L bond lengths.[6]

Thermally-Induced Spin-Crossover Case-Study

The greatest number of spin-crossover systems reported to date is for complexes containing an iron(II) metal centre (d^6). A typical example of a thermally-induced spin-crossover is *cis-bis*(thiocyanato)*bis*(1,10-phenanthroline)iron(II), $[Fe(phen)_2(NCS)_2]$ first identified in 1966.[7] The thermally-induced phase determined by X-ray diffraction identifies a spin-crossover with a sharp transition at the critical temperature of 176.5 K. The X-ray structure of the HS (293 K) and LS (130 K) species reveals a difference of the Fe-N(Phen) and Fe-N(NCS) bond lengths of 0.2 and 0.1 Å respectively, accompanied by a 0.5 % reduction in unit cell volume. Figure 2 displays the overlaid structures of the HS (293 K) and LS (130 K) X-ray structures (KEKVIC and KEKVIC01 from the Cambridge Structural Database) which has a RMS (root mean squared deviation) of 0.185 Å.[8] Once spin-crossover complexes are converted to LS systems, they are able to be photo-induced *in-situ* to form HS* at low temperature, this process is know as light-induced spin-state trapping (LIESST) and is discussed in more detail later in this chapter.

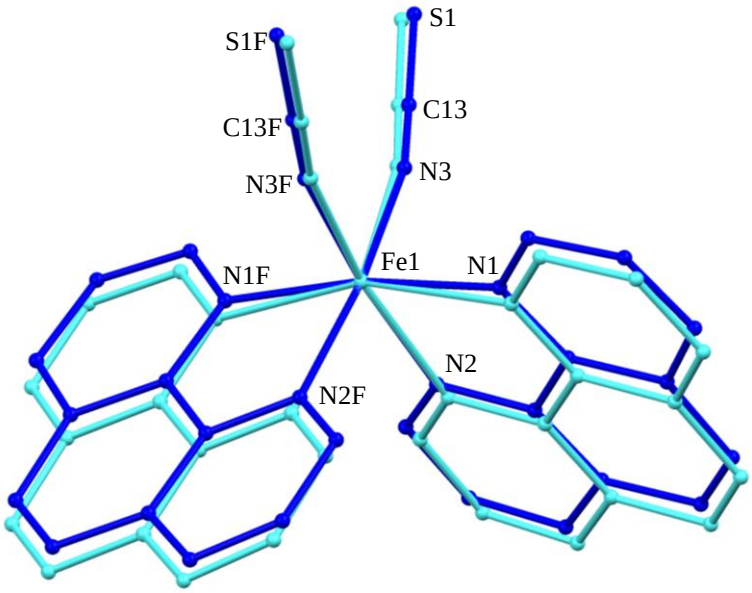

Figure 2: Structural overlay of the molecular structure $[Fe(phen)_2(NCS)_2]$ of HS at 293 K (turquoise) and LS at 130 K (blue).[8]

1.1.1.2. Low Temperature Polymorph Phase Transition

Carrying out polymorph studies on pharmaceutical products is an essential element in the development and marketing of a drug. Different polymorphs of a material can have different physical properties which may be related to the bioavailability, safety and efficacy of the drug. The identification of a different polymorph of the same material may create a loophole in the patents, allowing another company to market the different polymorphs, and therefore vast amounts of money are invested into obtaining all possible forms. Knowledge of the phase transition and the thermodynamic state is important for the manufacturing, storage and transportation of the drug.

Low-Temperature Phase Transition in Pharmaceuticals Case Study

Efavirenz is an anti-HIV drug which has a number of known polymorphs. Crystals of Form (1) Efavirenz can be prepared from an acetonitrile/water layered recrystallization. At 250 K, the material crystallizes in the orthorhombic space group $P2_12_12$ with Z' equal to 3. Reducing the temperature below 180 K, the crystal existing as form (1) undergoes a single-crystal to single-crystal transformation with a structural rearrangement of the cyclopropyl groups resulting in the loss of symmetry and change to the monoclinic space group $P2_1$ with $Z' = 6$.[9]

1.1.1.3. High Temperature Phase Transition

Instead of reducing the temperature to induce a transformation, the energy required to overcome the barrier between two different states can be provided by heating the crystal to elevated temperatures. Specialised equipment to obtain extreme high temperatures is available. For example, the heating stage on the STOE IPDS II can routinely collect data at temperatures ranging from 350 to 1100 K.[10-11]

The $_{D,L}$-Norleucine (2-aminohexanoic acid), $C_6H_{13}NO_2$, is a naturally occurring α-amino acid regularly found in proteins and possesses a number of extensively studied phase transitions.[12] As the transition temperatures are well-known, the compound may be used as a reference system for thermal behaviour. Figure 3 shows the high temperature single-crystal to single-crystal phase transition when the compound is elevated to temperatures of 390 K using a hot stage microscope, it

converts from the α-form (Figure 3a) to the γ-form (Figure 3b) accompanied by a colour change. Retention of crystallinity is observed through the phase transition with minor crystal shearing, and a well-defined reversion to the α-form (Figure 3c) occurs with a decrease in temperature to 385 K.[13]

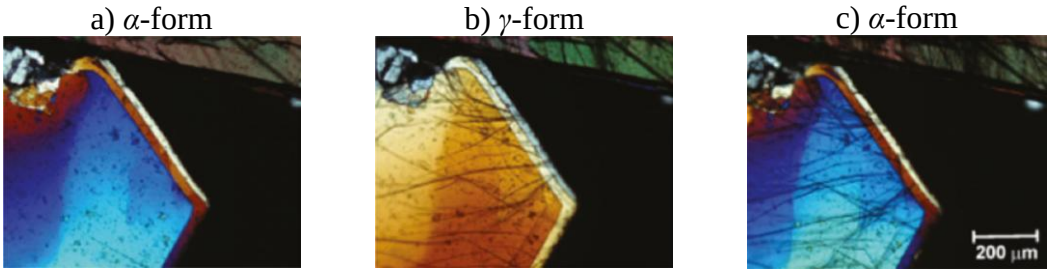

Figure 3: Single-crystal to single-crystal transformation in $_{D,L}$-Norleucine using a hot stage microscope. a) α-form at 385 K, b) γ-form at 390 K and c)) α-form at 385 K. [13]

The *in-situ* crystallographic experiment started with a collection at 385 K confirming the existence of the α-form (Figure 4a). From this starting point, the temperature was slowly increased whilst the unit cell was continuously collected. A change in the unit cell dimensions was observed at 390 K. At 395 K, the temperature was halted and a second crystal structure was obtained and confirmed as the γ-form. The phase transition induces a conformational change of a 108º rotation of the aliphatic chain. An additional symmetry element is introduced due to the rearrangement of the aliphatic chain, resulting in a space group change from $P2_1/c$ to $C2/c$.[13]

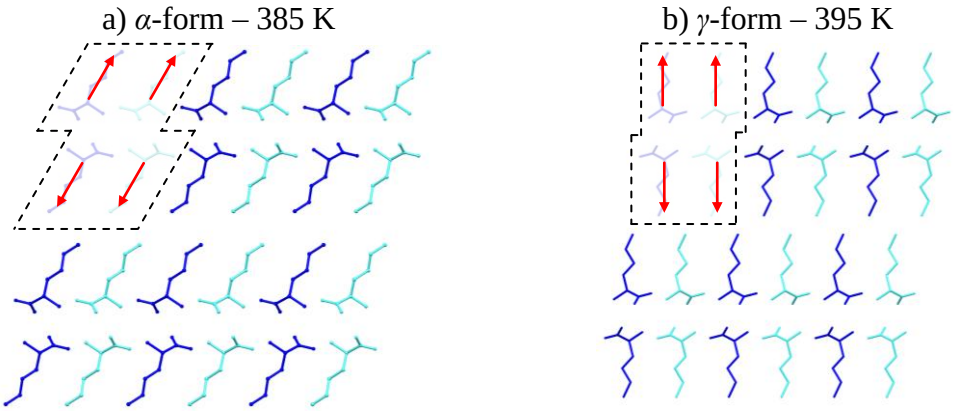

Figure 4: Packing plots of the 2-aminohexanoic acid structure down the b-axis with blue molecules being R and turquoise being S conformation a) α-form at 385 K and b) γ-form at 395 K.

1.1.2. High Pressure

High pressure studies can be used to investigate a wide variety of research applications and single-crystal X-ray diffraction has recently become a viable analytical method. The Diamond Anvil Cell (DAC) has been developed so that crystal can be investigated to extreme pressure, of over a hundred thousand times atmospheric pressure.

The Moggach DAC,[14] based on the Merrill Bassett[15] design, consists of two brilliant or modified brilliant diamonds precisely parallel. Placed in the middle of these two diamonds is a beryllium or tungsten gasket with a small hole into which the crystal, ruby and hydrostatic fluid can be added. The diamonds are fastened in place by tungsten backing seats which in turn are contained in a steel vice. The two halves can be pulled together by three screws in the steel vice (Figure 5). In doing so, the diamonds come together deforming the tungsten gasket and creating a seal around the sample chamber. The small chip of ruby is added as the behaviour under pressure is well-documented and the florescence can be measured using Raman spectroscopy to determine the pressure.[14]

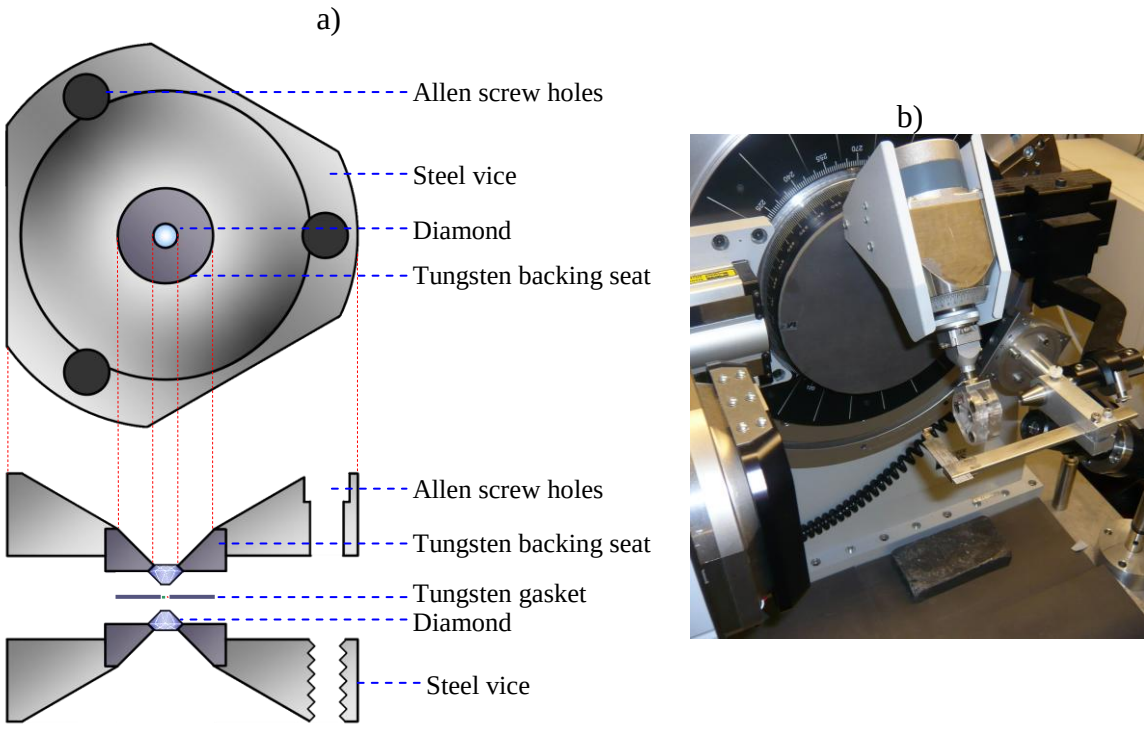

Figure 5: a) Schematic of the DAC and b) Photograph of mounted DAC at station 9.8, Daresbury.

Although there have been many years of development and numerous designs of high pressure cells, they have all involve a similar problem of data incompleteness due to the angle restriction, caused by the backing seats shadowing the diffracted X-rays (Figure 6a). In addition, the frames collected commonly have powder rings caused by diffraction of the tungsten gasket. A third problem is that diamond also diffracts giving large intense peaks. Figure 6b clearly shows an overloading diamond reflection. Improvements in data-processing software have come some way toward alleviating these problems.

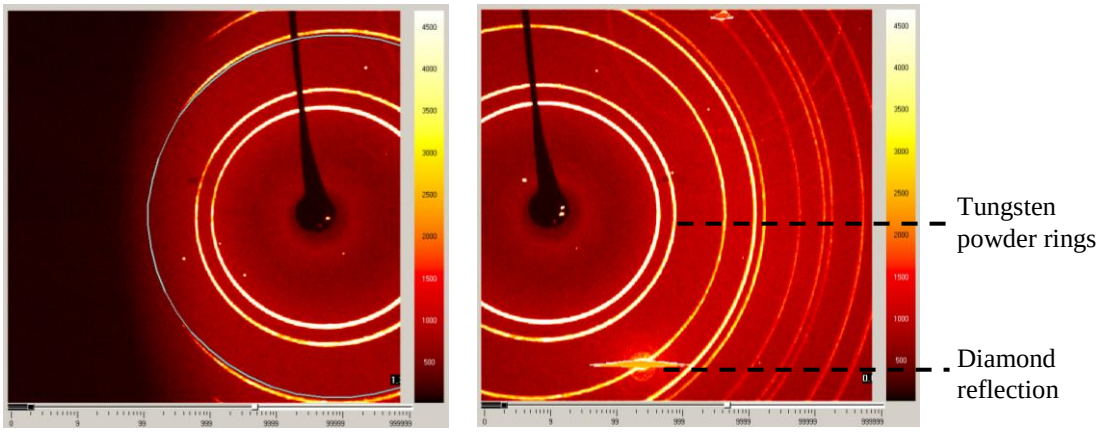

Figure 6: High pressure data collection showing a) shadowing effect from backing seats. b) beryllium powder ring and diamond overloaded reflection.

High Pressure Case Study

There are many interesting studies carried out using high pressure X-ray crystallography; one particular study investigates the control of magnetic anisotropy with the aim to develop single-molecule magnets.[16-20] Using the diamond anvil cell X-ray structures of $[Mn_{12}O_{12}(OAc)_{16}(H_2O)_4]$ are obtained from ambient to 2.5 GPa pressures. The increase in pressures induces a structural reorganization with alignment of the Jahn-Teller axes of eight manganese centres. Magnetic measurements reveal that the structural reorganization, caused by high pressure results in complete switching from 100% fast-relaxing to 100 % slow-relaxing species. In Figure 7, the structural differences from ambient pressure to 2.5 GPa show many of the bent Jahn-Teller axial bonds of the manganese realigning to form a slow-relaxing isomer.[21]

a) Ambient pressure b) 2.5 GPa pressure

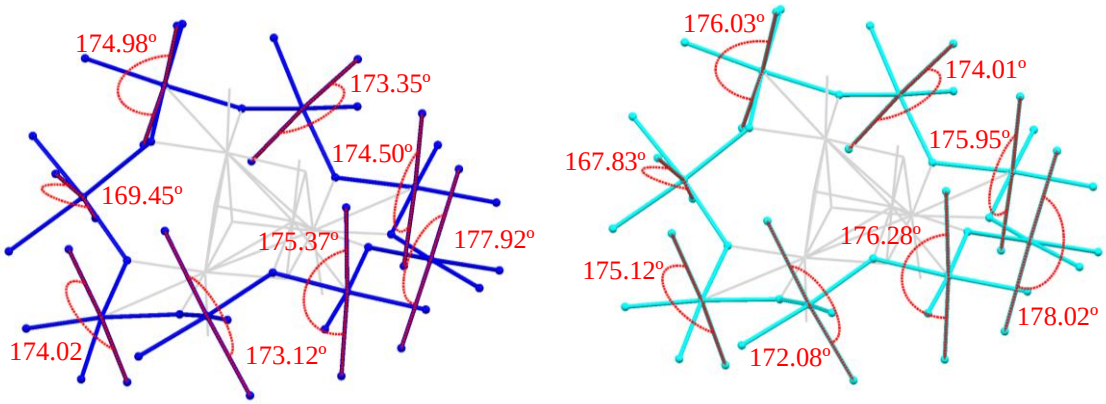

Figure 7: Structures of $[Mn_{12}O_{12}(OAc)_{16}(H_2O)_4]$ at a) ambient (blue) and b) 2.5 GPa (turquoise) pressures. All carbon and hydrogen atoms as well as solvent molecules have been removed for clarity. The main body of the Mn cluster has been faded out. Angles are measured using Mercury from the structure provided in the supplementary information.[21]

1.1.3. Study of Crystals under Evacuation and Absorption of Gases

Porous materials have been of great interest in recent years due to their potential uses in many applications such as gas separation, catalysis, sensing and gas storage.[22-24] Porous materials sometimes have tuneable pores which can be functionalised for their specific use. It is fundamental to understand the interactions that are going on within the pores to be able to construct new and improved materials.

Gas Removal Case Study

The framework of $[AgL_2]NO_3.2MeOH$ where L = N-phenylisonicotinamide crystallises in the triclinic space group *P*-1. The methanol guest molecules assemble in the channels along the *a*-axis (Figure 8a). If a single-crystal of this material is placed under vacuum for a period of two hours the solvent guest molecules are removed. The removal of the methanol causes the channels collapse and the crystal undergoes a single-crystal to single-crystal transformation to a new phase (Figure 8b). Figure 8a shows the crystal structure before and after the period of evacuation with major reorganisation of the crystal structure and ligand conformation. Upon rearrangement there is an increase in symmetry, resulting in a space group change from *P*-1 to $P2_1/c$.[25]

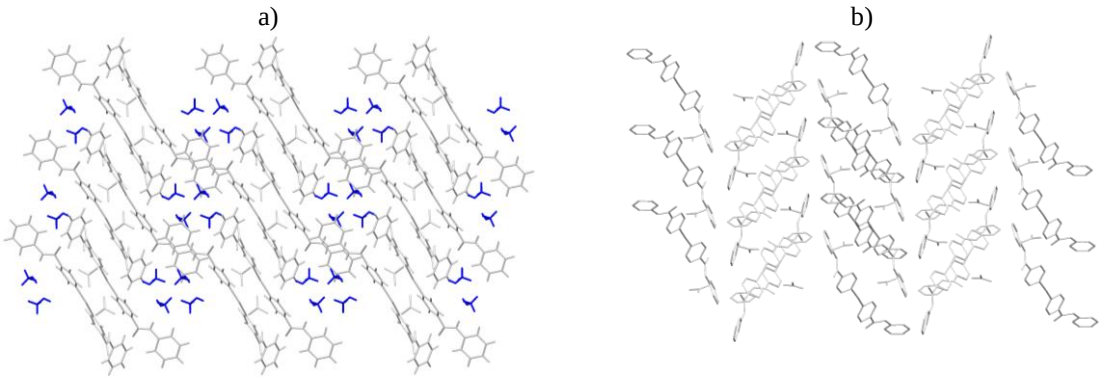

Figure 8: Molecular structures of a) $[AgL_2]NO_3.2MeOH$ and b) $[AgL_2]NO_3$ after two hours vacuum. Guest solvent molecules and nitrate counters-ions are removed and replaced with void space (turquoise).[25]

The previous example clearly illustrates the phase transition involved in the removal of solvent molecules. Using the environmental gas cell (EGC) it is now possible to carry out *in-situ* experiments (Figure 9). Three-dimensional snapshots of the removal or addition of guest molecules as the process occurs can be achieved. The EGC can be attached to a standard goniometer head, and because of the relatively small foot-print, standard X-ray data collections can be undertaken without concerns about some of the reflections being obscured by the cell. The EGC consists of a borosilicate or quartz 2.0 or 3.5 mm diameter capillary with a 0.01 mm wall thickness which is glued into a small recess in the main body of the cell. A single-crystal can be glued onto a glass fibre which sits in the centre of the capillary. The main body is attached to a flexible tube connected to an external vacuum and gas controller unit. The entire EGC can be connected to either a vacuum, a pure gas or mixture of gases.[26] Alternative designs have an entrance and exit tubing which allow flow of a specified gas over the crystal.

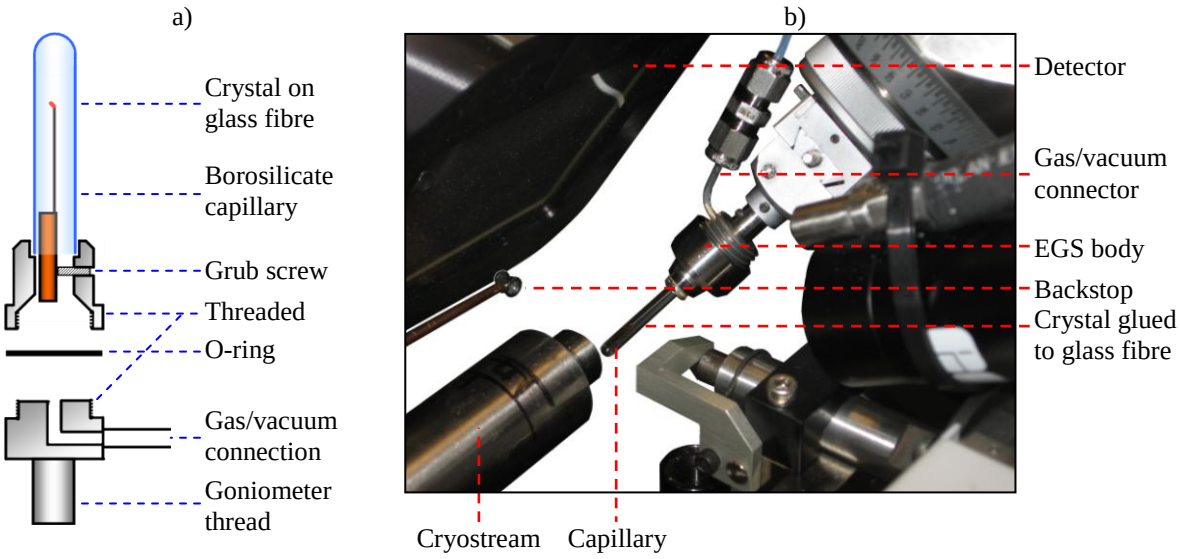

Figure 9: a) Schematic image of EGC [26] b) Photograph of EGS at the ALS San Francisco

Gas Removal Using the EGC Case Study

The EGS was used to investigate the dehydration and NO gas addition in the flexible organic framework Cu-SIP-3. The crystal was glued to glass fibre and placed into the EGS, then it was subjected to a vacuum at elevated temperatures of 435 K causing a phase transition and the removal of the water molecules (Figure 10). The diffraction resolution dramatically dropped with the initial removal of the water molecules, but the material regained crystallinity when the complete phase transition occurred. The crystal was then subjected to nitric oxide at 1 bar which resulted in the loss of crystallinity.[27]

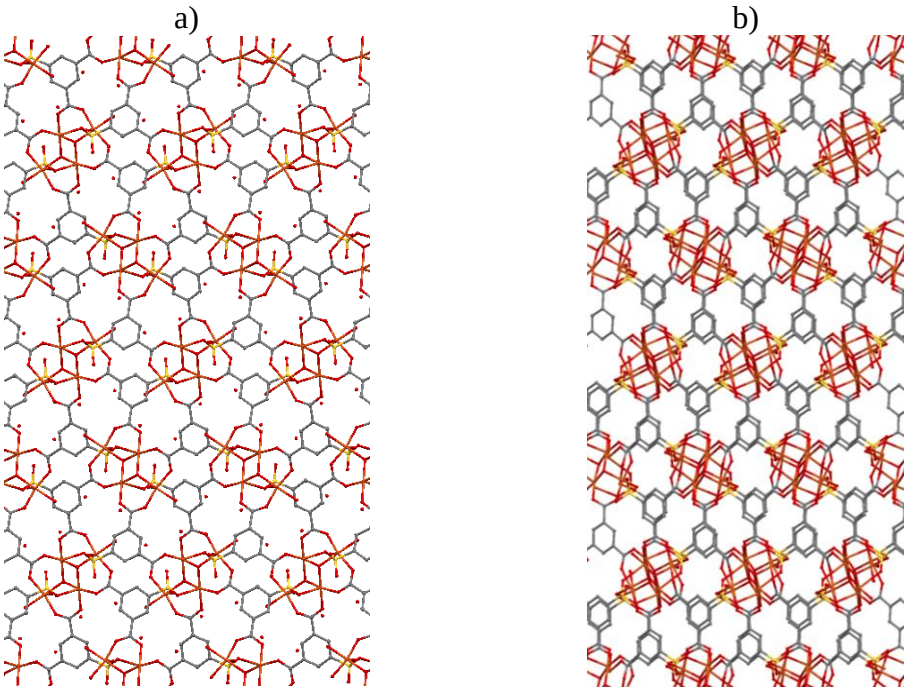

Figure 10: Packing diagram of Cu-SIP-3 at a) before 355 K and b) after the phase transition 435 K.

1.1.4. Applied Electric Field

Impurity migration, piezoelectric and dielectric properties of crystals can be investigated crystallographically using an applied electric field *in-situ*. The experimental set-up consists of placing the crystal between two electrodes capable of exerting electric fields in the order of 10-40 kV cm^{-1} (Figure 11). Lattice expansion/contraction, atoms displacement, bond polarisation and charge transfer among atoms or ions can be induced by an electric field and measured crystallographically.[28]

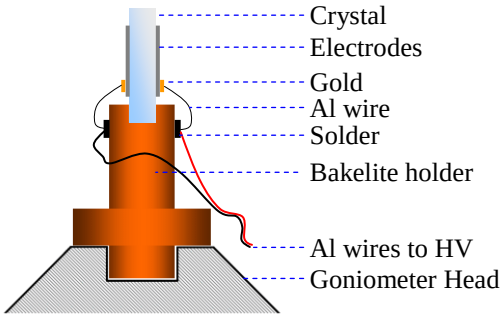

Figure 11: Standard set-up of goniometer head to apply the electric field.

Applied Electric Field Case Study

A crystallographic experiment in which an electric field was applied *in-situ* was used to investigate KDP (KH_2PO_4). The 10 x 10 x 0.3 mm^3 crystal is mounted as displayed in Figure 11 with electrodes (2 mm smaller than the crystal face) evaporated to the optically polished *hkl*(00±1) crystal faces. The amplitude of voltage was kept constant at 400 V and is applied in the form of a square wave with a frequency of 30 Hz and synchronised with the scintillation detector. Under these conditions, ordering in the hydrogen atoms perpendicular to the electric field, displacement of the phosphorus along the electric field line and shortening of the *b*-axis occurred. Due to that slight structural rearrangement there is a space group change from *I*-42*d* to *Fdd*2.[28]

1.1.5. Photon Irradiation

1.1.5.1. Photochemistry

In general, chemical reactions proceed *via* a transition state, which is an intermediate state between the reactants and products. Conventionally, thermal energy is used to excite the reactants to the transition state by bond breaking and reorientation from thermally excited vibrational modes (stretching and bending).[29-30] In photochemistry, the energy is supplied as light in the form of quantised photons, and the absorption of at least one photon creates an electronically excited state. The electronic excitation normally occurs from a redistribution of electrons by excitation from the HOMO to the LUMO using light with a wavelength of comparable energy. As a result of excitation of the electrons, the excited state has a different distribution of electrons in its molecular orbitals, so its equilibrium geometry can be quite different from that of the starting material. The electronically excited state is not thermodynamically stable and can decay either by luminescence (emission of light), transforming the electronic energy into the vibrational energy, or in certain cases, through a photochemical transformation due to change in the electron distribution at the molecular level.[29-31]

There are several possible electronic configurations for the newly-formed excited state depending on the alignment of electron spins. The stability of the new species formed is affected by the electronic configuration and each energy state has a term symbol describing the configuration.[29-30]

Equation 1:	Term Symbol = $^{2S+1}L_J$

The stability of an excited state is described by the term symbol. The term symbol comprises three elements; spin-spin coupling (S), orbit-orbit coupling (L) and spin-orbit coupling (J). The first can be described in terms of spin quantum number and is the net spin alignment for a system. For example, in a $2e^-$ system, the electrons can align parallel (↑↑) where the spin quantum number equals S = 1, the multiplicity of 2S+1 = 3, giving a triplet state. If the electrons align anti-parallel (↑↓), then S = 0 and therefore multiplicity of 1, giving a singlet state. For a given system, the relative energy will decrease with an increase in multiplicity. The next energy term to

consider is the orbit-orbit coupling (L), which is determined from the combination of the orbital angular momentum of the electrons. Finally, the spin-orbit coupling (J) comes from the angular quantum number and is worked out from a combination of the spin-spin and orbit-orbit coupling (J = |L+S|, |L+S-1|…|L-S|). A spectroscopic spin selection rule determines if the transition is allowed or forbidden. An allowed transition is a transition with a non-zero dipole moment and therefore a non-zero intensity. The spin selection rule states that the spin cannot change the relative orientation, $\Delta S = 0$, so transitions are only allowed from the same multiplicity and not from the 'flipping' of spins. The orbital selection rule states that transitions involving the redistribution of electrons in a single quantum shell are forbidden, e.g. d→d is forbidden. Finally, the parity rule is for centrosymmetric molecules and states that only transitions that are accompanied by a change in parity are possible. The selection rules can play a vital role in the determination of excited lifetimes.[29-30]

The Jablonski scheme (Figure 12) shows the other routes of decay, either through emission (fluorescence or phosphorescence), internal conversion or intersystem crossing. Internal conversion is the transition of an electron from a higher to a lower electronic state within the same state (e.g. S_1 to S_0). This normally occurs from a vibrationally low energy level to a vibrationally high energy level in the lower electronic state, which then relaxes rapidly to Boltzmann distribution; the energy is lost as heat. Intersystem Crossing converts the total electronic and vibrational energy into another state (e.g. S to T).[29-30]

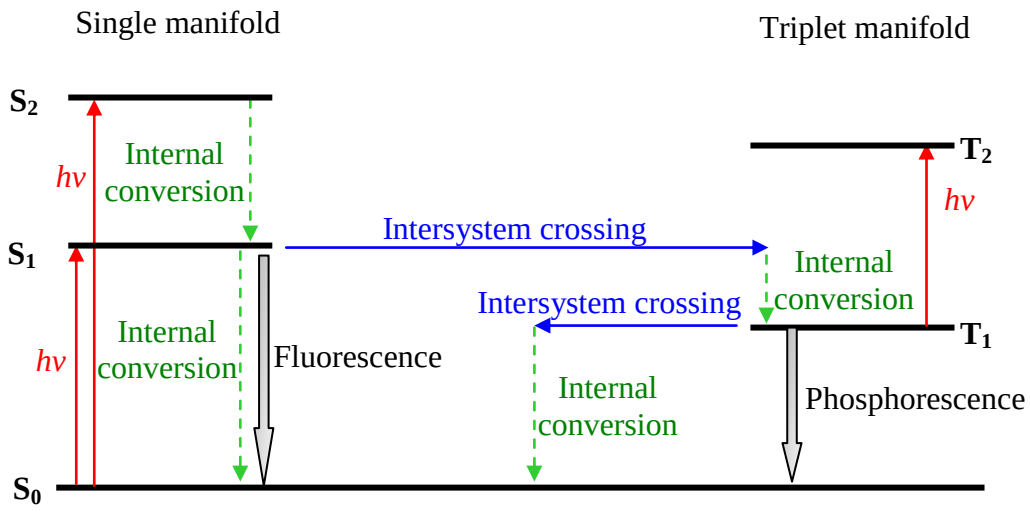

Figure 12. Jablonski scheme. [29 30]

1.1.5.2. Photocrystallography

Many previous investigations into photo-excitation have been undertaken using solution-based spectroscopy. Some of these techniques include UV absorption and emission, as well as infrared spectroscopy (IR). But, as most of the applications of optical and electro-optical materials are in the solid-state, these solution results do not necessarily give the complete picture. For solution-based spectroscopy, the nature of the solvent can effect the environment of the light-induced excited state. Solid state crystallography can offer an alternative, precise and accurate analytical tool.

Even though the X-ray scattering process occurs on the time scale of ~10^{-18} seconds, the complete data collection often takes several hours and therefore gives a time-averaged structure of the crystalline material.

Consequently, photochemical processes which may generate transient species that have lifetimes in the picosecond range mean that crystallography studies of the structures are extremely challenging. However, with advances in beam intensity, pulsed lasers, computing power and cryogenics, diffraction patterns can be measured for shorter and shorter periods of time. It is now possible to determine structures that are metastable at low temperatures, or species that have picosecond lifetimes. The study of photo-induced processes in crystals using X-ray crystallographic techniques is now generally referred to as 'photocrystallography'.[32-34]

Time-Scale Procedures of Photocrystallographic Experiments

Crystallographic time-resolved studies have different experimental procedures depending of the lifetimes (τ) of the excited species.[34] The structures of irreversible (τ = ∞) and Metastable species (τ > minutes) can be obtained using steady-state procedures. These experiments involve the collecting of a ground state structure, irradiation of the crystal and collection of a second data set with the irradiation removed. To achieve high conversion, the crystal can be further irradiated after which another data collection is obtained (Figure 13).[35]

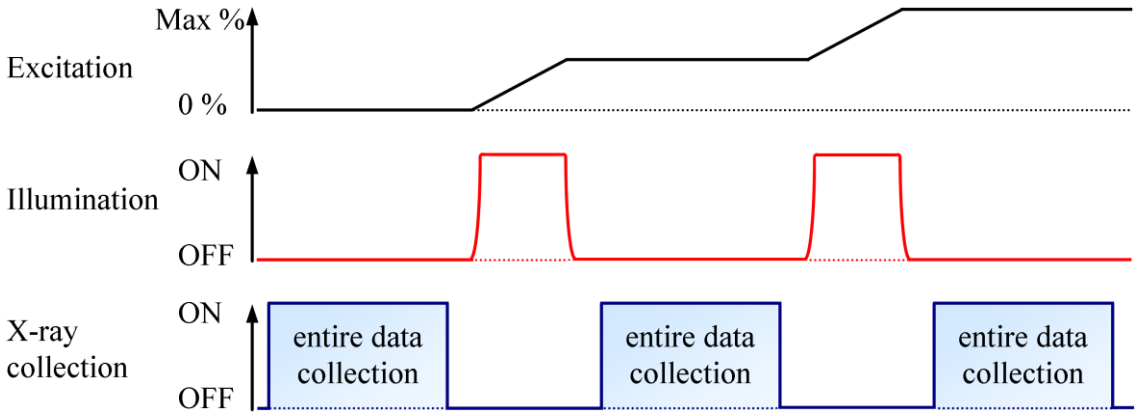

Figure 13: Schematic diagram of steady-state photocrystallographic procedures.

For lifetimes between minutes and milliseconds, *pseudo*-steady-state methods are implemented, in which X-ray datasets are obtained while the crystal is continuously irradiated (Figure 14).[35]

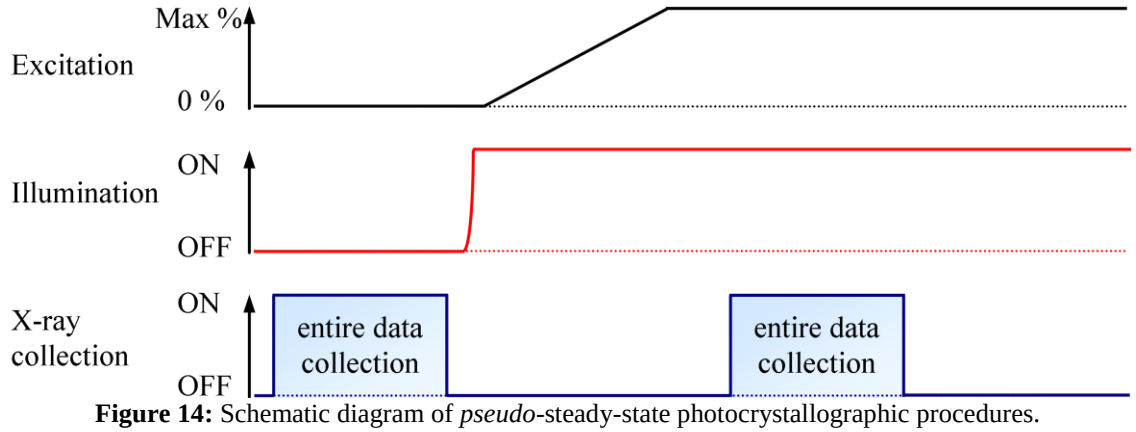

Figure 14: Schematic diagram of *pseudo*-steady-state photocrystallographic procedures.

For lifetimes less than milliseconds, a pump-probe approach is necessary, in which the crystal is irradiated (pump) immediately prior to the collection of a diffraction image (probe). This process occurs numerous times to build up an entire data set. For this to be done efficiently the X-rays and light source have to be pulsed in some

way. For lifetimes from milliseconds-microseconds, the optically pulsed laser is synchronised with a mechanical chopped X-ray beam (Figure 15). For lifetimes less than microseconds, it is necessary to use a synchrotron, taking advantage of the pulsed nature of the X-ray source. [31,33-34,36]

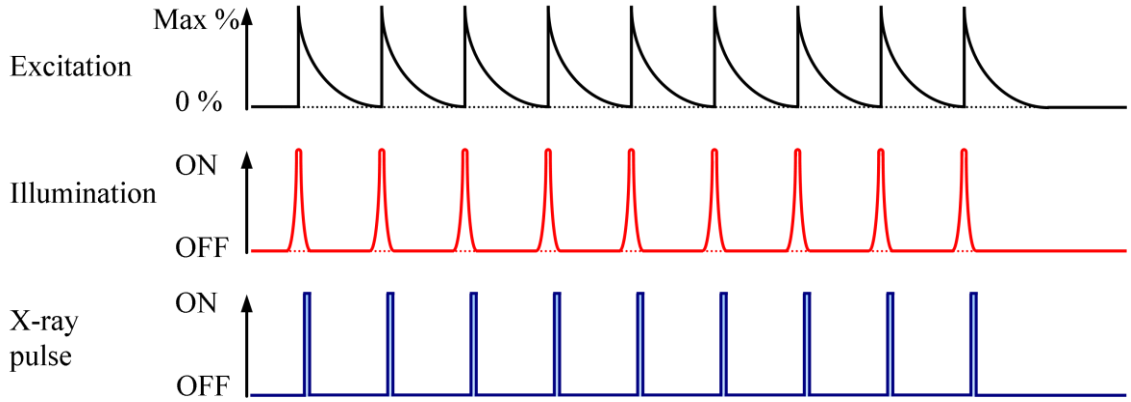

Figure 15: Schematic diagram for pump-probe photocrystallographic procedures.

1.1.5.3. Steady-state Methods

Irreversible Reactions

In an irreversible photo-induced reaction, the products are stable and thus can be investigated using steady-state methods as described above. Unlike reactions in the solution, in the solid state the molecules are essentially in fixed position. Thus, for reactions to take place in the solid-state there has to be enough flexibility within the lattice or enough space surrounding the groups which are altering. For bimolecular processes, the neighbouring molecules must also be aligned in the correct orientation. As these reactions are topological, crystal engineering is often involved in the design of the systems that undergo irreversible single-crystal to single-crystal reactions. The next section describes the techniques and possibilities of these steady-state methods.

[2+2] Cycloaddition

Woodward–Hoffmann rules of frontier orbital theory state that for a pericyclic reaction to occur the highest molecular orbital (HOMO) and lowest unoccupied molecular orbital (LUMO) have to be in the correct symmetry. The pericyclic reaction for a [4+2]-cycloaddition has this correct orbital orientation, and therefore thermal energy drives the reaction. The orbitals in a [2+2]-cycloaddition and [4+4]-cycloaddition reaction do not have the correct symmetry and thus the reaction can only occur after being photo-activated. Figure 16 shows the orbital rearrangement necessary for a [2+2]-cycloaddition reaction to proceed.[37]

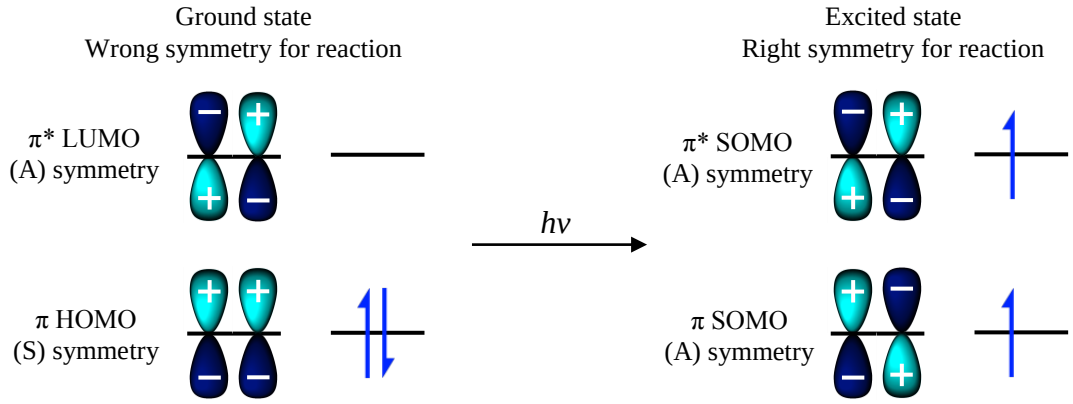

Figure 16: Frontier orbital diagrams of the symmetry requirements of [2+2]-cycloadditions.

Bimolecular [2+2]-cycloaddition or [4+4]-cycloaddition solid-state reactions have to meet certain structural requirements as well as the correct orbital symmetry. In

crystals, the molecules only have a small amount of flexibility about a specific position, so the molecules have to be aligned in the correct orientation and within a fixed distance for a reaction to occur. Ideally, the ligands have to be aligned parallel with a separation of less than 4.2 Å to the neighbouring ligand.[38-40] However, there are many examples which do not undergo photochemical reaction or only achieve very low conversion even though they meet the structural requirements and the examples outlined in this section are the exceptions.[41]

[2+2]-Cycloaddition of coumarin-3-carboxylic acid Case Study

The aligned double bonds of coumarin-3-carboxylic have an intermolecular distance of 3.632 Å, well within the maximum separation postulated. After a high quality ground-state crystal structure is obtained (Figure 17a), the crystal is irradiated for prolonged periods using a 150 W mercury lamp. A crystal structure of the complete [2+2]-cycloaddition is obtained from the data even though there is major crystal degradation accompanying the transformation (Figure 17b). It was noted in this study that other candidates for [2+2]-cycloaddition reactions such as 5-bromouracil and maleic acid which meet the structural requirement, show no evidence of [2+2]-cycloaddition even after three days of irradiation. This lack of reactivity was attributed to the presence of strong hydrogen-bonding between the monomer units that would have been disrupted if the solid state reaction had occurred.[41]

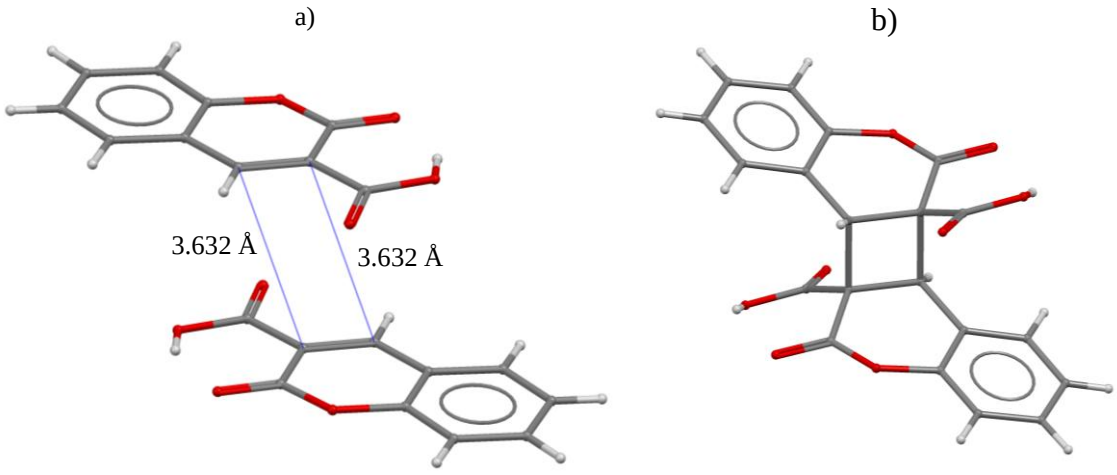

Figure 17: Molecular structures of coumarin-3-carboxylic acid a) ground-state and b) after [2+2]-cycloaddition photoreaction.[41]

[2+2]-Cycloaddition in a Framework Case Study

Crystal engineering to design pairs of parallel double bonds within the distance of 4.2 Å is no trivial task. One way to ensure the ligands crystallize in the

desired formations is to make framework structures in which ligands capable of photoreaction are held in place. Even with the ligands aligned in the correct orientation, transformations in 1D, 2D or even 3D coordination polymers are rare, perhaps due to a lack of flexibility. A recent investigation has been carried out into the photoreaction capabilities of [Zn(bpe)-(muco)]·DMF·H_2O where bpe is *trans*-1,2-*bis*(4-pyridyl)ethene and muco is *trans,trans*-hexa-2,4-diene-dioic acid. In this structure, the bpe ligands are positioned in the correct orientation and the intermolecular distance between the double bonds is 3.789 Å. When the crystal is photoactivated at room temperature major decomposition is observed, however when the crystal is photoactivated at 223 K using a Xenon light source *in-situ*, a 100% single-crystal to single-crystal [2+2]-cycloaddition is seen. The formation of the cyclobutane ring is accompanied by major structural rearrangement and unit cell deformation. [42]

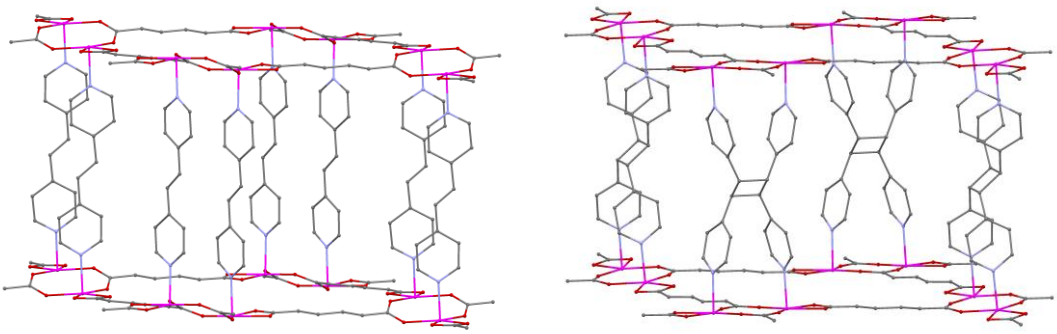

Figure 18: Crystal structure of [Zn(bpe)-(muco)]·DMF·H_2O (a) before and (b) after irradiation.[42]

[4+4]-cycloaddition of bi(anthracene-9,10-dimethylene)

The phenomenon of light induced [4+4]-cycloaddition in the single-crystal is rare in comparison to the [2+2]-cycloaddition. In one report, the single-crystal transformation of bi(anthracene-9,10-dimethylene) is investigated (Figure 19). Like the previous [2+2]-cycloaddition reaction, the monomer units within the structure are held in place ready for a photochemical reaction.[43] In the bi(anthracene-9,10-dimethylene) compound, the anthracene components are secured as a dimer by ethylene connections. Due to the high light sensitivity all preparation is carried out in the absence of light. The resulting single-crystal is irradiated while rotating, using a 100 W mercury lamp with the addition of glass and water filters to remove wavelengths less than 410 nm. The removal of high energy wavelengths ensures good radiation penetration of the crystal and homogeneity of the photoreaction.

Prolonged irradiation resulted in crystal decomposition, and a 40 % maximum conversion of the photoreacted product was achieved.[43]

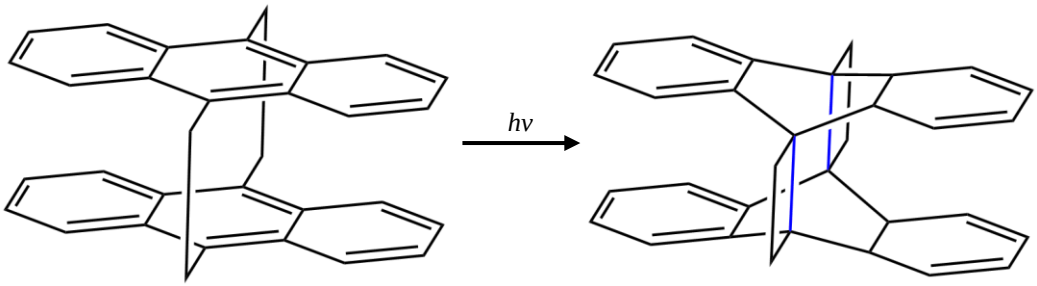

Figure 19: 2D structures of the [4+4]-cycloaddition photoreaction with the new bond highlighted in blue.

Diarylethenes

Diarylethenes are a class of compounds which can undergo pericyclic reactions. Unlike the previous examples, diarylethenes can react either thermally or photochemically, each method providing a different stereoisomerism. Figure 20 shows the thermal mechanism in which the reaction goes through a disrotatory mechanism resulting in a *cis* product.

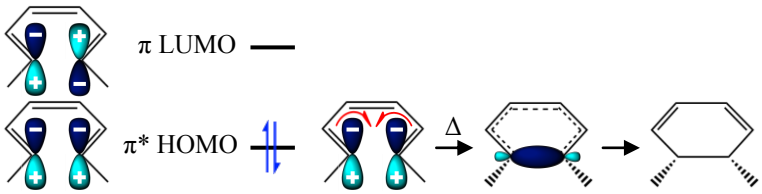

Figure 20: Stereochemistry in thermally-induced reaction of diartlethylenes.

Figure 21 shows the photoactivated pathway in which an electron is promoted from the HOMO to the LUMO, resulting in an orbital symmetry change. Consequently, the reaction proceeds through a conrotatory mechanism resulting in a *trans* product. Diarylethenes have received great interest in recent years for potential molecular switches because of their high thermal irreversibility, because the photochromism process only occurs under specific wavelengths, because of their sensitivity and their ability of undergo reversible transformations using different wavelengths.

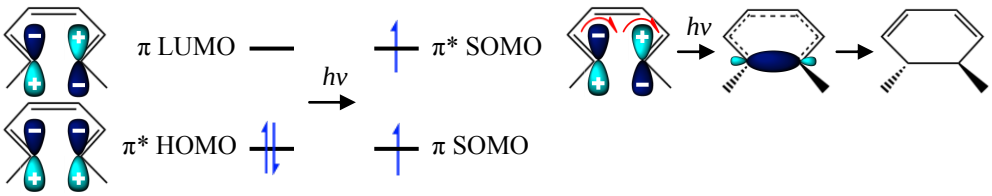

Figure 21: Stereochemistry in photo-induced reaction of diartlethylenes.

Work within our research group on the ring closure reactions of platinum containing dithienylethene systems has produced remarkable high conversion within the single-

crystal. Irradiation of a single-crystal of the complex with 400 nm light resulted in 80% conversion to the closed form.[44] The result shows significant improvement on previous single-crystal studies of dithienylethene ring closure (< 20%). The high conversion is suggested to occur because of the additional metal centres which allow the reaction to proceed *via* a triplet sensitized pathway.[44]

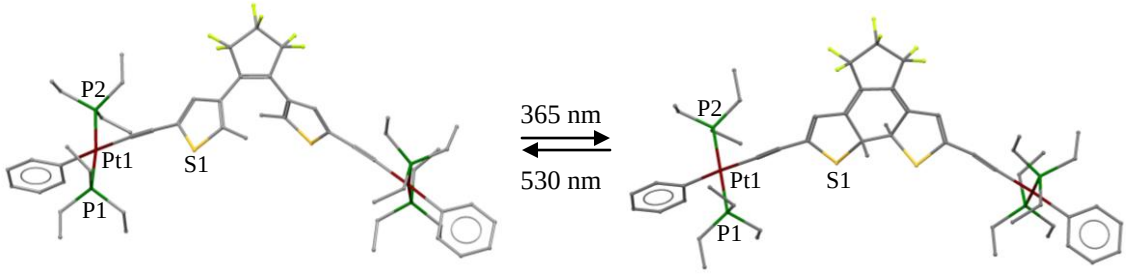

Figure 22: Crystal structures of platinium-dithienylethene ring closure of 80 % conversion.

Cis/Trans Isomerisation

Crystal decomposition due to transformation within the lattice is a major problem in the area of photocrystallography. One example of isomerisation in the single-crystal shows how this problem can be overcome by introducing a host framework around the species of interest. Tiglic acid ((Z/E)-2-methylbut-2-enoic acid) was incorporated within a host of CECR (C-ethylcalix[4]resorinarene). The crystal was irradiated at 325 nm using a 48 mW He/Cd laser for accumulated periods of 1, 3, 6 and 12 hours, resulting in a *cis/trans* (*Z to E*) isomerisation. Data sets were collected 1 hour after the light source was removed and a maximum photostationary conversion of 30 % was obtained (Figure 23).[45]

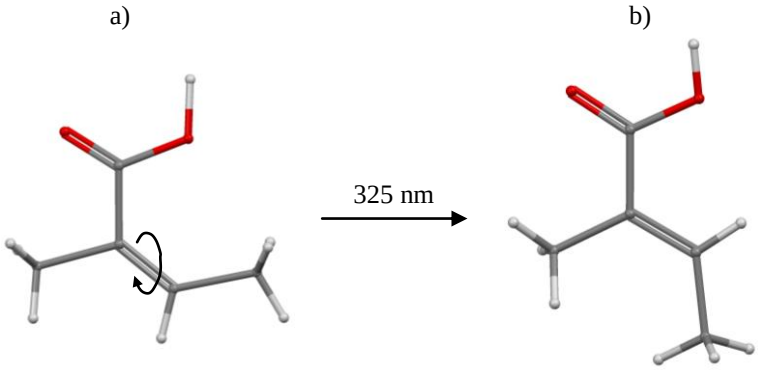

Figure 23: Crystal structures of tiglic acid a) *E*-conformation before exposure and b) 30 % occupancy of *Z*-conformation.

1.1.5.4. Thermal Trapping of Species

Light-Induced Spin-State Trapping

As discussed previously, octahedral metal centres with d^4 to d^7, particularly those of the first row transition metals, can adopt either a high-spin (HS) or low-spin (LS) electronic configuration. The conversion from HS to LS can be induced by a reduction in temperature. If the sample is irradiated at extremely low temperatures using a specific wavelength the complex is photoactivated from a LS species, back up to a thermally trapped HS electronic transition, previously seen at higher temperature. This process is know as light-induced spin-state trapping (LIESST)

Light-Induced Spin-State Trapping Case Study

One recent example of the LIESST phenomena investigated the iron (II) spin-crossover complex of $[(Fe(3\text{-bpp})(NCS)_2)_2(4,4'\text{bypiridine})].2CH_3OH$. In this complex there are two iron centres separated by a 4,4'-bipyridine ligand. At an ambient temperature, both metal centres exist in the HS configuration and the compound crystallises in the monoclinic space group $P2_1/c$ (phase I). The temperature was slowly reduced whilst the unit cell dimensions were continuously monitored to determine the phase transition temperature. The first transition occurs at 161 K and does not affect the electronic configuration, but involves a space group change from $P2_1/c$ to Cc with a slight rearrangement of the 4,4'-bipyridine (phase II). The second phase transition occurs when cooling to 113 K. The transition corresponds to spin-crossover from HS-HS to HS-LS and is accompanied by structural rearrangements causing another space group change from Cc to P-1. If the crystal is then cooled to 30 K and irradiated using 670 nm laser of 5 mW power, the complex undergoes LIESST and the HS-LS metal centres are converted back to the HS-HS state. Using these techniques, a low temperature structure can be collected of the HS-HS species which is not achievable through normal methods. This can then be used as a direct comparison tool to the HS-LS structure without having to account for the differences in temperature.[46]

Linkage isomerism

Two metal complexes are linkage isomers if they contain an ambidentate ligand bound through a different atom in each isomer. Switching between the

different coordination modes can be achieved either thermally or photochemically. When the complex is photo-activated, it may be possible to thermally trap the new species in what is known as a metastable state. In general, metastable-states have a longer lifetime than transient excited states and may exist for infinite time periods at low temperature, but are energetically less stable than the ground-state. This state can be thought of as a local minimum (metastable), where energy is necessary to get over an energy barrier to reach the global minimum which is lower in energy. The metastable-state can be completely stable under certain conditions as indicated above, therefore lifetimes are much greater than the time required for a complete X-ray analysis and so can be investigated easily.[31,34]

Linkage Isomerism in Nitrite (NO_2^-)

The nitrite ion (NO_2^-) is an ambidentate ligand and can bind to the metal centre through more than one donor atom, either the nitrogen or one or both of the oxygen atoms. DFT calculations suggest the nitrate group may bind to a metal centre with a large number of possible coordination modes. Figure 24 shows coordination modes of the nitrate ligand, all have been determined crystallographically apart from (e) and (f).[34] The different coordination modes are accessible through the use of differing synthetic conditions such as temperature or irradiation.

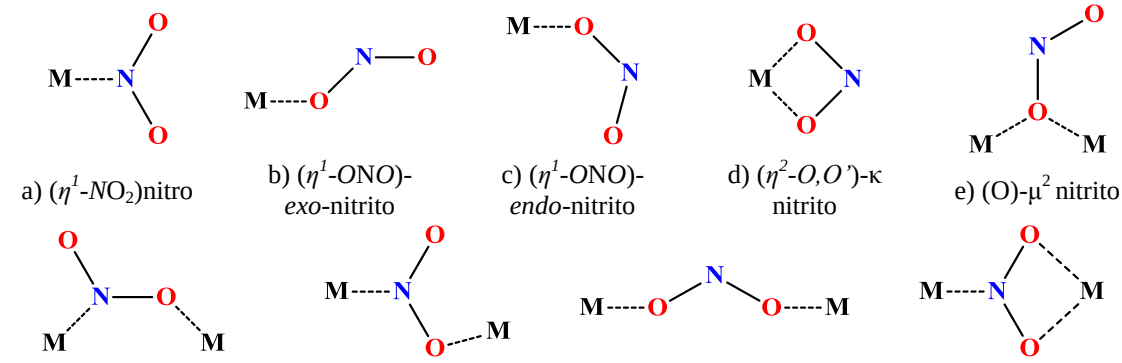

Figure 24: Coordination modes of NO_2^- ligand[34]

A study of the literature shows that the most common coordination modes are nitro 'a' and nitrito 'b' which are found in complexes with relatively inert metal centres including cobalt(III), rhodium(III), iridium(III) and platinum(IV).

Balzani et al. in 1968 carried out a range of photochemical experiments on $[Co(NH_3)_5(NO_2)](NO_3)_2$ in the solid and solution states. Broadband irradiation in the solid-state under standard conditions converted the nitro (η^1-NO_2) to the nitrito (η^1-

*O*NO) form. From the IR spectra of Nujol mulls, the initial bands from the nitro complex are still present at 1430, 1315 and 825 cm^{-1} but are reduced in intensity, and new bands from the converted nitrito also appear at 1460 and 1065 cm^{-1}, showing that there is not a complete transformation. A 100% conversion is possible by irradiating the solid suspension in Nujol mull. Further experiments show that when the 100% conversion sample is placed in a dark room, a back-reaction to the initial nitro species occurs, showing that the species is thermally unstable at room temperature.[47]

Experiments carried out by Grenthe highlighted the differences between nitrito formed by direct synthesis and by the reversible photochemical reaction from the nitro complex $[Co(NH_3)_5NO_2]Cl_2$. In the solid-state, synthesis of both nitro and nitrito structures crystallize in the same space group. From time-resolved powder diffraction patterns of the reaction path, new peak positions arise and intensities vary (Figure 25). This indicates that the thermal isomerisation reaction occurs through two distinctive steps. From analysing the powder patterns using the peak positions to work out the unit cell parameters and the peak intensities for the electron density, the first step is considered to be an intramolecular change of coordination around the Co metal centre from six to seven in the transition state. The change of coordination is due to the change in bond-modes in nitro (η^1-NO_2) to (η^2-N,O)-κ bonding mode. The second step is a slow *pseudo* rotation rearrangement. The nitrite species is also formed through photoisomerisation from the more thermodynamically stable nitro complex. Interestingly, this structure is different from the one originally *exo*-nitrito*(η^1-O*NO*)* synthesised.[48]

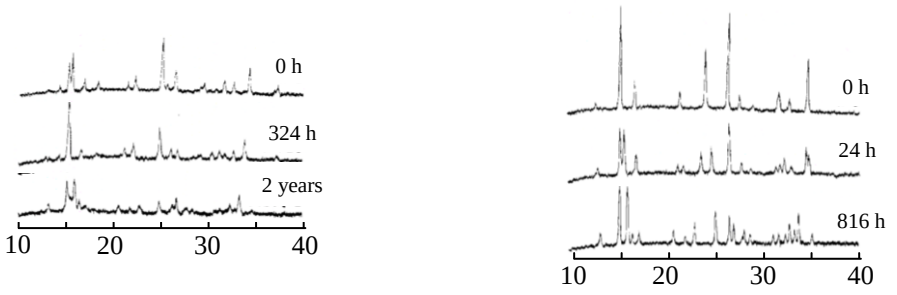

Figure 25: Powder diffraction patterns of time-resolved linkage isomers of $[Co(NH_3)_5ONO]Cl_2$.[48]

The first photocrystallographic experiments on $[Co(NH_3)_5(NO_2)]2Cl$ were carried out by Ohba in 1992. A ground state structure was obtained at 116 K in the absence of light to confirm the nitro (η^1-*N*O_2) species (Figure 26a). Irradiating the single-

crystal for a period of two hours using a 150 W Xe lamp produced a transformation to the *exo*-nitrito (η^1-*O*NO) species with a 8.9 % occupancy split over two sites (91.1 % of the nitro (η^1-*N*O_2) ground-state species remains) (Figure 26b). Subsequent irradiation for an additional two hours increases the population of the *exo*-nitrito to 14.5 % again split over two sites.[49]

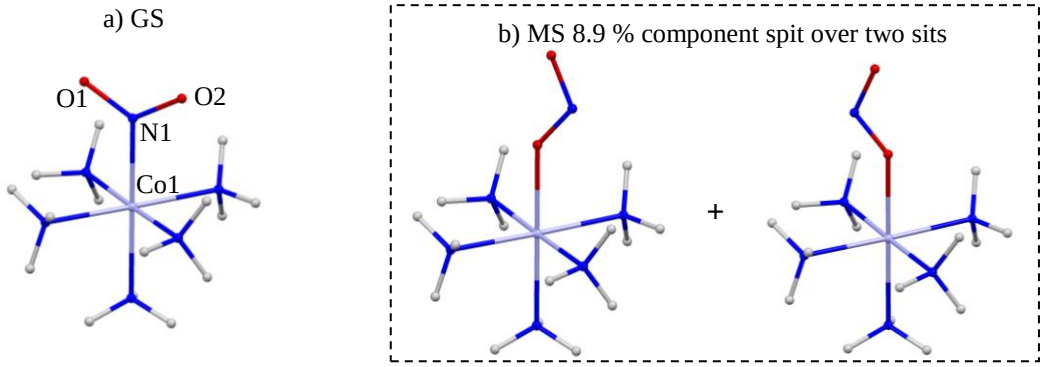

Figure 26: Single-crystal molecular structure of [Co(NH3)5(NO2)]2Cl ground-state (a), light-induced metastable-state (b).

For nickel metal centres, database mining of the ambidentate nitrite ligand reveals that there are two main bonding modes synthetically available. The nitro-(η^1-*N*O_2) is the electronically favoured conformation in the absence of steric effects.[50] The *exo*-nitrito (η^1-*O*NO) species becomes the favoured product for bulky axillary ligands.[51-53]

Complexes of *trans-bis*(aminoethyl-morpholine)dinitro(η^1-*N*)nickel(II), *trans-bis*(aminoethyl-piperidine)dinitro(η^1-*N*)nickel(II), and *trans-bis*(aminoethyl-pyrrolidine)dinitro(η^1-*N*)nickel(II) produce a perfect balance between steric and electronic factors, resulting in a equilibrium between the nitro (η^1-*N*O_2) and *exo*-nitrito (η^1-*O*NO) in solution (Figure 27). In general, crystals of the *exo*-nitrito (η^1-*O*NO) species form a couple of minutes after the reaction process. From the filtered solution, after a few days of slow evaporation, crystals of the nitro (η^1-*N*O_2) species are produced (thermodynamic product).[50,54-55]

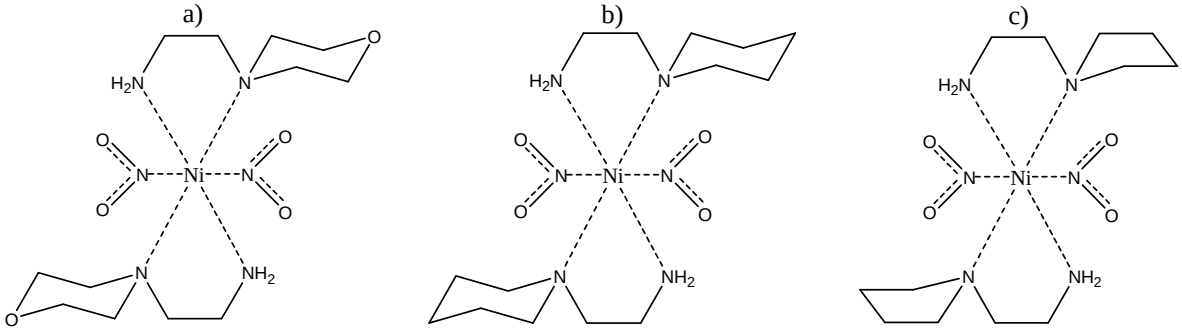

Figure 27: 2D structure of $Ni(L)_2(NO_2)_2$ where L is morpholine (a), piperidine (b) and pyrrolidine (c).

The presence of both isomers in solution suggests that the two bonding modes have similar energies and thus provide a good starting platform for the search of bonding modes of nitro linkage isomers using photo-crystallography. Within the Raithby group, these systems have been photocrystallographically studied. The dinitro(η^1-*N*)-*bis*(aminoethyl-morpholine)nickel complex undergoes linkage isomerisation when irradiated at 100 K using 470 nm for 3 hours. The resulting crystal structure consists of three components; 78 % nitro (η^1-NO_2) ground-state remains and the remaining 22 % is converted to a new metastable *endo*-nitrito (η^1-*O*NO) split over two sites (Figure 28). Interestingly, this is not the same nitrite-binding mode formed from crystallisation.[56] Likewise, when the dinitro(η^1-*N*)-*bis*(aminoethyl-piperidine)nickel is photocrystallographically investigated, the irradiation produces a new metastable species with an occupancy of 18 % of the *endo*-nitrito (η^1-*O*NO) binding mode (Figure 29).[56]

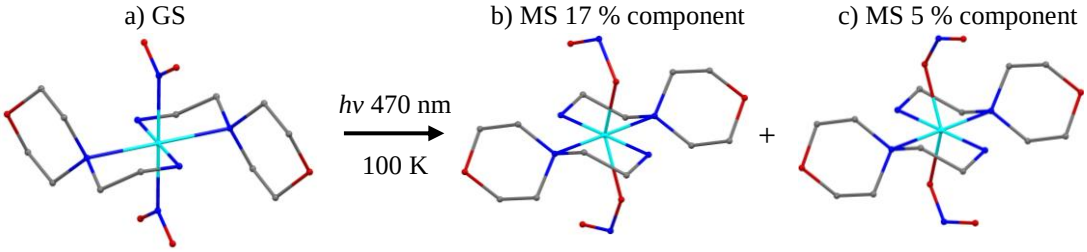

Figure 28: Ground-state (a) and metastable state compounds (b-c) of *bis*(aminoethyl-morpholine)dinitro(η^1-*N*)nickel.[56]

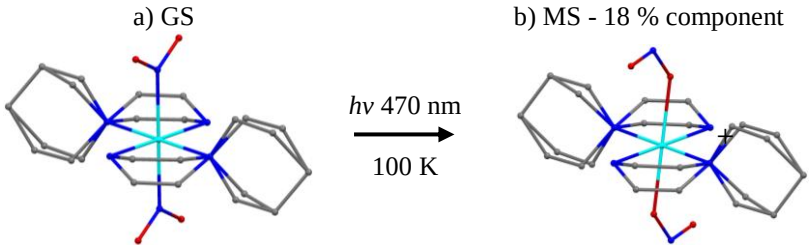

Figure 29: Ground-state (a) and metastable-state compounds (b-c) of *bis*(aminoethyl-pyrrolidine)dinitro(η^1-*N*)nickel(II).[56]

Irradation of *bis*(aminoethyl-pyrrolidine)dinitro(η^1-*N*)nickel(II) systems produce a metastable crystal structure consisting of three components: ground state nitro-(η^1-NO_2), an *endo*-nitrito (η^1-*O*NO) binding mode with a occupancy of 20 %, and also a 10 % component of the *exo*-nitrito (η^1-*O*NO) formation. The 10 % *exo*-nitrito (η^1-*O*NO) conformation is similar to what is achieved from the kinetic synthetic product (Figure 30).[56] Parametric variable-temperature studies revealed that in all three systems, the metastable *exo*-nitrito (η^1-*O*NO) state exists to a temperature of 120 K.

At temperatures above 120 K the metastable *exo*-nitrito converts back to the ground state.

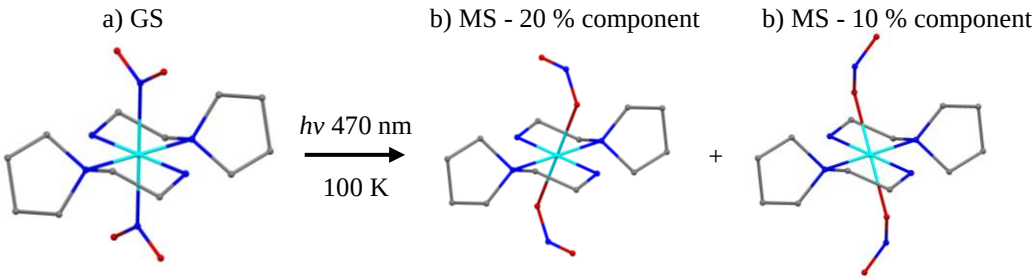

Figure 30: Ground-state (a) and metastable-state compounds (b-c) of *bis*(aminoethyl-pyrrolidine)dinitro(η^1-*N*)nickel.[56]

In 2005, Coppens and co-worker investigated the first double *iso*nitrosy and nitrito linkage isomerism for the compound $[Ru(bpy)_2(NO)(NO_2)]2(PF_6)$. In this species, the ground state coordination modes of nitro (η^1-*N*O_2) and nitrosyl (η^1-*N*O) are converted to the metastable-states of nitrosyl (η^1-*N*O) and *endo*-nitrito (η^1-*O*NO) at 200 K with 11.6 % conversion *via* an intramolecular redox reaction involving oxygen transfer. At 90 K, different experimental results are observed and produced coordination modes of *iso*-nitrosyl (η^1-*O*N) and *exo*-nitrito (η^1-*O*NO) with a 9.1 % occupancy (Figure 31).[57]

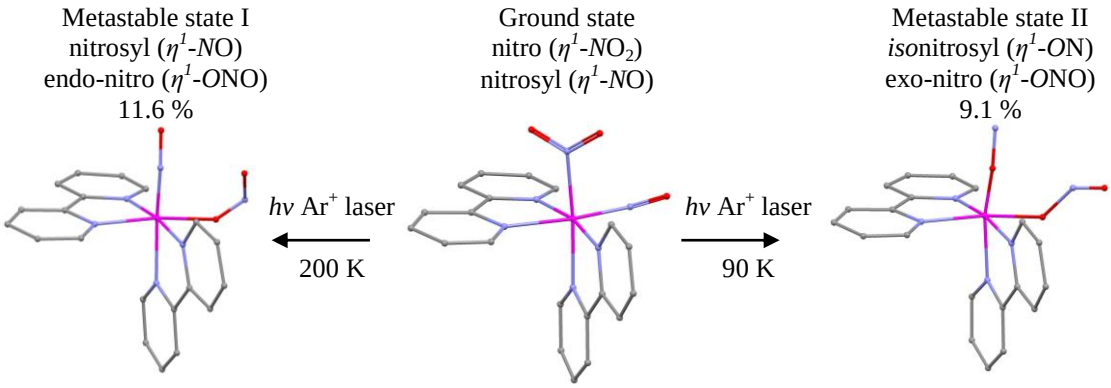

Figure 31: Single-crystal molecular structure of [Ru(bpy)2(NO)(NO2)]2(PF6) ground-state (middle), light-induced metastable-state MS_1 (left) and MS_2 (right).[57]

DFT calculations and IR spectroscopy of Fe(TPP)(NO)(NO_2) (TPP is tetraphenylporphyrinato dianion) have been used to help in the analysis of the biological activity of NO and NO_2 coordination in heme proteins. The investigations reveal a number of double-linkage isomers metastable-states of combinations of nitro and nitrosyl bonding modes. The results indicate that the isonitrosyl (-ON) linkage isomer is electronically less stable than the nitrito (-ONO) linkage isomer.[58-59]

The linkage isomerism of nitrite ligands can also be obtained through conventional methods of heating the material over a certain threshold. For the complexes *trans-bis*(N-alkyl-diaminoethane)di(nitro)nickel(II), where alkyl = propyl or isoproyl, the bulkier N-isopropyl side group produces both nitro and nitrito, whereas the more flexible N-propyl ligands produce only the nitro bonding mode. DSC and TGA high temperature studies reveal an irreversible phase transition at 408-423 K occurring in *trans-bis*(N-propyl-1,2-diaminoethane)dinitronickel(II), but not in *trans-bis*(N-isopropyl-1,2-diaminoethane)dinitronickel(II).[60]

The *trans-bis*(1,2-benzenediamine)dinitronickel(II) undergoes a reversible high temperature phase transition involving linkage isomerism at 383-393 K in the solid-state, with a distinctive colour change from red to blue. Diffraction experiments of the single-crystal are not possible due to crystal decomposition at the elevated temperatures, suspected to be caused by the linkage isomerism process.[61] There have been a number of other high temperature studies on the solid-state material, but there has been no crystallographic evidence of the single-crystal to single-crystal phase transition.

Linkage Isomerism in Nitrosyl (NO^-)

The possible coordination modes of the nitrosyl ligand are shown in Figure 32 and the modes have been established crystallographically.[62] The metastable complexes are accessible thermally or photochemically.

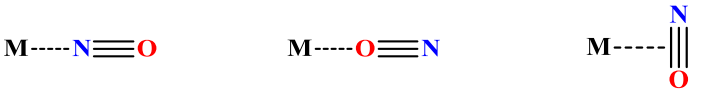

Nitrosyl (η^1-*N*O) Isonitrosyl (η^1-*O*N) Side-on (η^2-*NO*)

Figure 32: Linkage isomers of nitrosyl ligand.[62]

The first observation of nitrosyl linkage isomerism was reported by Rest in 1977 using frozen gas matrix photolysis. These infrared experiments showed a new very low stretching frequency of the nitrosyl ligand in [Ni(NO)(η^5-Cp*)] which was thought be a photoionisation product.[63] The true nature of this species was not understood until 1998 when it was revealed in a photocrystallographic investigation.[64]

At a similar time, the compound $Na_2[Fe(CN)_5(NO)].2H_2O$ sodium nitroprusside (SNP) was spectroscopically investigated by Hauser and Oestreich who observed a new low temperature isomer of nitrosyl, detected using Mössbauer spectroscopy in solution. The species had a quadrapole splitting and an isomer shift different to that at high temperature.[65-66] The low temperature species was confirmed separately by Woike and Guida who studied the decay of the new isomer in the solid-state using either DSC, Raman or IR spectroscopy.[67-71]

In 1990, Wokie investigated the first ruthenium based nitrosyl linkage isomerism using the $K_2[RuCl_5(NO)]$ complex *via* Raman spectroscopy.[72] The work sparked a number of studies on *tran*-$K_2[Ru(NO_2)_4(NO)(OH)]$, as well as osmium analogue and other similar derivatives.[73-76]

Extensive research into linkage isomerism for a diverse number of systems using frozen gas matrix photolysis, Mössbauer spectroscopy, DSC, Raman and IR spectroscopy, reveal that these systems underwent a dramatic structural change of the nitrosyl ligand, but it was not until photochemical X-ray and neutron crystallographic studies were undertaken that the true nature of the new species was identified.[77]

Photocrystallographic Investigations of Nitrosyl Linkage Isomerism

In 1994, Coppens *et al.* established the first photocrystallographic investigations of the bonding mode of the nitrosyl ligand in the $Na_2[Fe(CN)_5(NO)].2H_2O$ system previously investigated spectroscopically by Hauser, Oestreich, Woike and Guida. The single-crystal to single-crystal transformation of the nitrosyl ligand was clearly indicated by changes in the electron density map induced by irradiation.[78] The full structure of both ground state and excited state was photocrystallographically established in 1997 at reduced temperatures using a 543 nm Ar^+ laser. The results established two photoinduced metastable-states dependent on the irradiation wavelength and duration of excitation. Figure 33 shows the single-crystal X-ray diffraction structure, 'a', being the ground-state nitrosyl (η^1-*N*O) structure chemically formed and from which X-ray data is collected before any irradiation. When the compound is irradiated using 230-600 nm light an excited state structure forms which immediately decays with luminescence to MS^{II} 'c' which is now a side-on nitrosyl (η^2-*ON*) bound isomer, with 10% conversion. This metastable compound is stable below temperatures of 150 K. With prolonged irradiation, MS^{II} metastable-state converts to MS^{I} 'b' with η^1-*O* bound with 37% conversion, which is similarly trapped at temperatures below 195 K.[79]

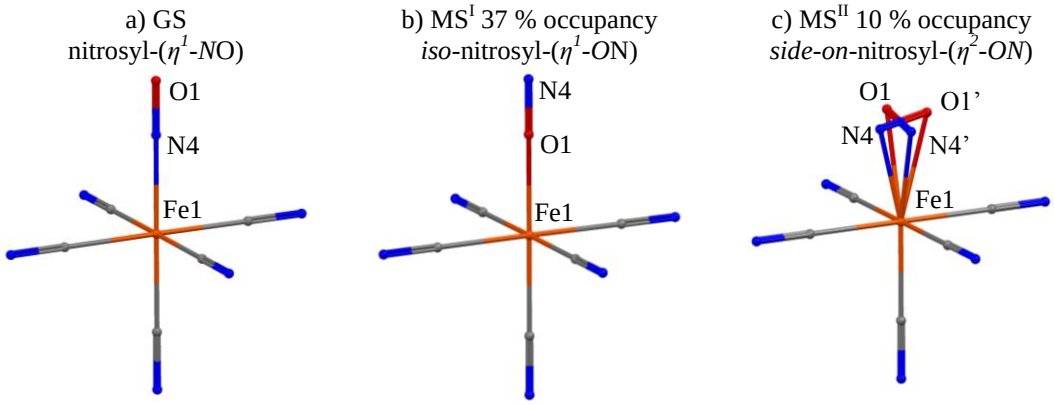

Figure 33: $Na_2[Fe(CN)_5(NO)].2H_2O$ of the (a) ground-state (b) metastable-state (I) and (c) metastable-state (II)

In 1996, Coppens utilised the photocrystallographic technique to investigate linkage isomerism in $K_2[M(NO_2)_4(NO)(OH)]$, which had been identified previously using IR spectroscopy and DSC.[73-76] In the photocrystallographic experiments, the η^1-*N* bound ground-state was identified before any irradiation for comparison purposes, after which the crystals were irradiated using lasers to achieve 16 % conversion to the η^1-*O* bound isomer (Figure 34).[80-81]

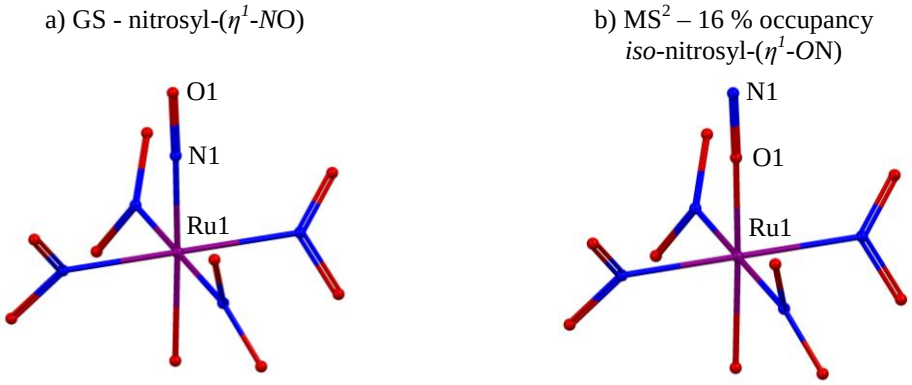

Figure 34: Crystallographic structures of *trans*-$K_2[M(NO_2)_4(NO)(OH)]$ metastable-states [80-81]

As previously discussed, the true nature of the photolysis product of [Ni(NO)(η^5-Cp*)] was not fully understood using conventional spectroscopic techniques. The photocrystallographic investigations indicate a rearrangement from the nitrosyl-(η^1-*N*O) bound isomer to a side-on (η^2-*NO*) species (Figure 35), with a Ni-N-O angle of 92º (MS2). This isomerisation occurred with 47 % conversion, using a 458nm Ar^+ 150 mW/cm^2 laser.[64]

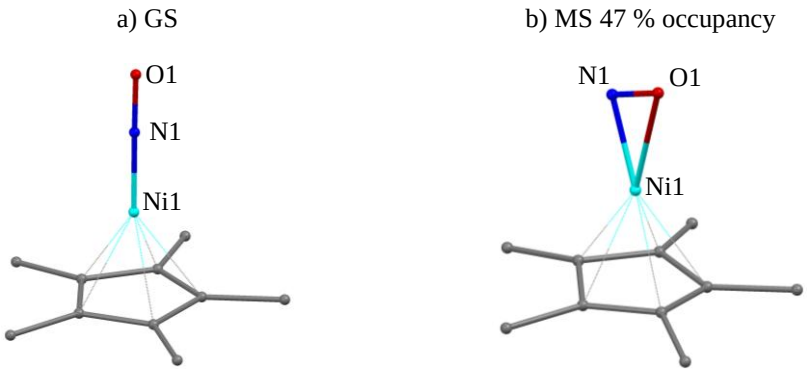

Figure 35: Single-crystal molecular structure of the a) ground-state structure and b) metastable-state (II) of CpNi(NO).[64]

The crystal structure of the ground-state contains two independent molecules. The nitrosyl groups in these two molecules have a slightly different structural environment in terms of intermolecular distances to the nearest atoms. This minor change in the cavity around the nitrosyl results in the metastable side-bound conformation to be fully ordered in one molecule and partially ordered in the other. There are also distortions in the Cp ligand with the methyl groups attached to the C_5 ring staying in the same position while the central ring and Ni move an equal distance towards the nitrosyl ligand, resulting in the methyl groups being bent out of the five-membered ring plane.[64]

One recent crystallographic study of linkage isomerism in nitrosyl complexes, obtained very high conversions and the occurrence of different coordination modes depending on the excitation wavelengths. A crystal with two independent molecules of $[Ru(py)_4Cl(\eta^1\text{-}NO)](PF_6)_2.½H_2O$ in the asymmetric unit was irradiated at 80 K for a period of 1 hour using a 473 nm laser with a light intensity of 400 mW cm^{-2}, resulting in a *iso*-nitrosyl (η^1-*O*N) metastable-state (I) with occupancies of 91.5 % and 92.8 %. Further excitation using a 980 nm laser with a light intensity of 60 mW cm^{-2} for 30 minutes caused a transformation from the disordered structure of 8 % nitrosyl (η^1-*N*O) and 92% *iso*-nitrosyl (η^1-*O*N) into 35.0 % and 60.2 % conversion to the *side-on*-nitrosyl (η^2-*ON*) MS^{II} with some reversion to the ground-state structure. The linkage isomerism is accompanied by a shortening of the *trans*-Ru-Cl bonds, equatorial Ru-N bonds and a colour change from orange in the GS to green in MS^{I} and to black in MS^{II}. The extremely high conversion to *iso*-nitrosyl is suggested to be due to the absorption cross sections of the ground-state and metastable-state (I) being far enough apart to prevent the reversion from the MS to the GS, unlike in other solid-state linkage isomerisation reactions.[82]

Linkage Isomerism in Sulphur Dioxide (SO_2^-)

Another ligand which has potential for linkage isomerisation is SO_2 which is isoelectronic with NO_2^-. As with NO_2^-, when SO_2 complexes are irradiated the ligand may coordinate to the metal centre in several different ways (Figure 36). Crystal structures containing the bonding motifs (a)-(d) have been determined crystallographically, whereas (e)-(h) have only been hypothesised.[83]

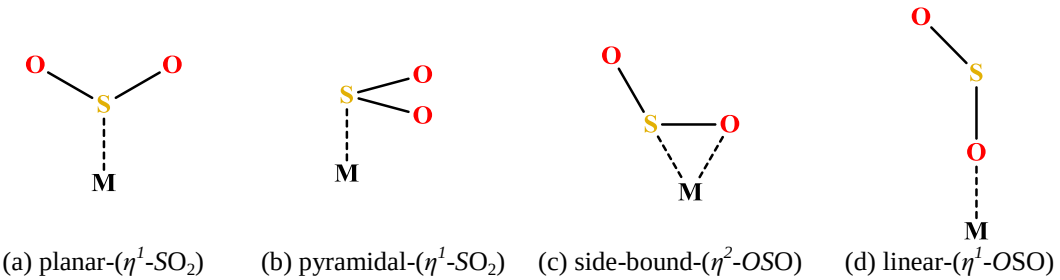

(a) planar-(η^1-SO_2) (b) pyramidal-(η^1-SO_2) (c) side-bound-(η^2-*OS*O) (d) linear-(η^1-*O*SO)

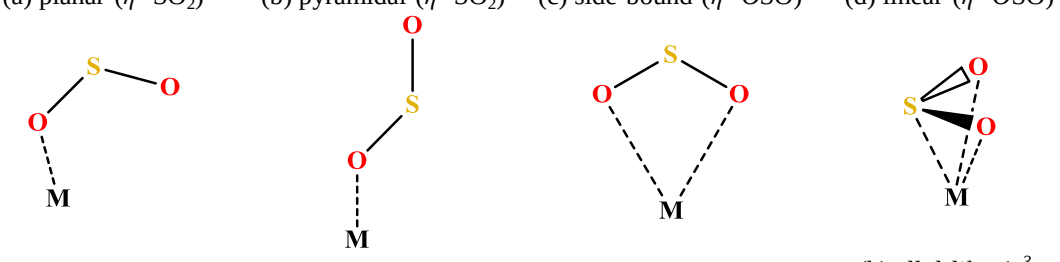

(e) *endo*-(η^1-*O*SO) (f) *exo*-(η^1-*O*SO) (g) chelate-(η^2-*OO*S) (h) allyl-like-(η^3-*SOO*)

Figure 36: Linkage isomers of SO_2 ligand [83]

Case Study: $[Ru(SO_2)(NH_3)_4X]Y$ where X is Cl^-, CF_3COO^- or H_2O and Y is Cl^-, BPh_4^-, $C_6H_5SO_3^-$ or $CH_3C_6H_4SO_3^-$

In 1979, Johnson and Dew recognised the isomeric properties of SO_2 from low temperature IR spectra of *trans*-$[Ru(NH_3)_4(SO_2)Cl]Cl$.[84] Irradiation of KBr pellets or Nujol mulls with 365 nm light at 195 K produced new bands in the IR spectra of 1165 and 940 cm^{-1} believed to arise from the side-bound-(η^2-*OS*O) state. Johnson and Dew noticed that by using different excitation periods and temperatures, different metastable-states could be obtained. Irradiation at the lower temperature of 25 K for a period of 30 seconds gave a 2nd metastable-state with a new band at 1180 cm^{-1}. Under the same conditions, irradiating for a prolonged period of time, or cooling the 1st metastable-state, a 3rd metastable-state is achieved with bands at 1285, 1130 and 560 cm^{-1}.

In 2002, Coppens et al. investigated the *trans*-$[Ru(NH_3)_4Cl(SO_2)]Cl$ complex and established the existence of metastable-states of sulphur dioxide using photocrystallography. The crystal was mounted on the diffractometer, cooled to 90 K and irradiated *in-situ* using a 488 nm Ar-CW-laser for two hours, causing a change in colour from bright orange-brown to deep brown. After the laser was turned off, the temperature was maintained at 90 K and data collection was delayed for ten minutes in order to dissipate any heat accumulated from irradiation. The resulting crystal structure shows a 10 % conversion from the (η^1-*S*O_2)-bound to the (η^2-*OS*O)-side-bound isomer.[85]

$[Ru(NH_3)_4(H_2O)(SO_2)]^{2+}$ with counter ions of $C_6H_5SO_3^-$, $MeC_6H4SO_3^-$ and BPh_4^-

In 2003, Coppens investigated the linkage isomerisation in a related system with water *trans* to the sulphur dioxide, $[Ru(NH_3)_4(H_2O)(SO_2)]^{2+}$. The study investigated the metal complex partnered with a number of different counter-ions including $C_6H_5SO_3^-$, $MeC_6H_4SO_3^-$ and BPh_4^-. The complex with $C_6H_5SO_3^-$ counter-ions was irradiated for only ten minutes, producing a conversion of 11% to the side-bound-(η^2-*OS*O) isomer (Figure 37). With prolonged irradiation periods, major crystal decomposition occured.[85-86] Irradiation a crystal of $[Ru(NH_3)_4(H_2O)(SO_2)]^{2+}$ with a $CH_3C_6H_4SO_3^-$ counter-ions using a 488 nm light from a Ar-CW-laser for 10 minutes producing a 20 % conversion from the ground-state (η^1-*S*O_2) isomer to a

similar side-bound-(η^2-*OSO*) isomer. The isomerisation is accompanied by a colour change from pale yellow to deep red (Figure 38).

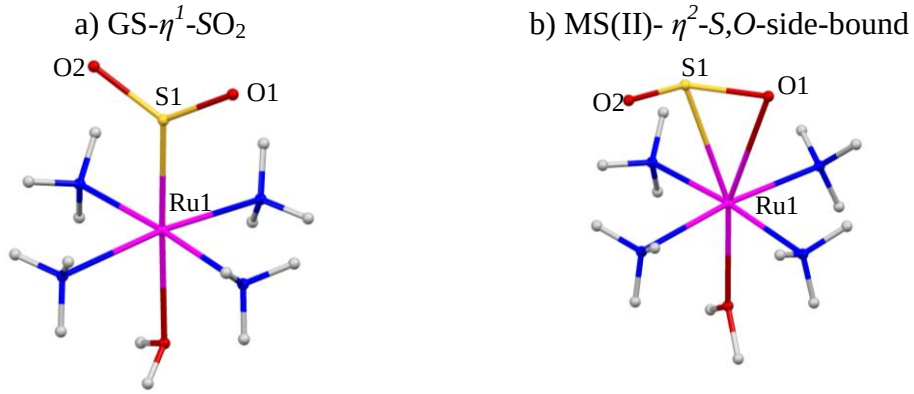

Figure 37: Single-crystal molecular structure of $[Ru(NH_3)_4(H_2O)(SO_2)]2C_6H_5SO_3$ ground-state (left), light-induced metastable-state MS_2 (right).

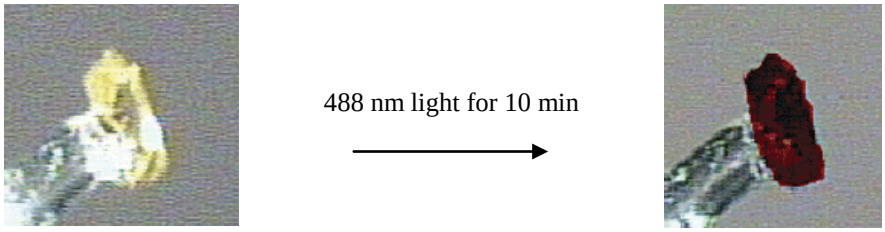

Figure 38: Colour of crystal of *trans*-$[Ru(NH_3)_4(H_2O)(SO_2)]2(Tos)$ before (left) and after (right) irradiation.

In 2006, Raithby *et al* determined a new metastable bonding mode of sulphur dioxide for the same system, using different experimental conditions. The mounted crystal was flash cooled to 13 K in the dark where a ground-state structure was determined. The crystal was irradiated for 75 minutes using a tungsten lamp. Photocrystallographic experiments show a 56 % contribution of the ground-state (η^1-SO_2) component, a 8 % second metastable-state (η^2-*OSO*) component previously found in Coppens investigations, and a new novel bonding mode of sulphur dioxide with 36 % of first metastable-state (MS1) (η^1-*OSO*) component (Figure 39).[86]

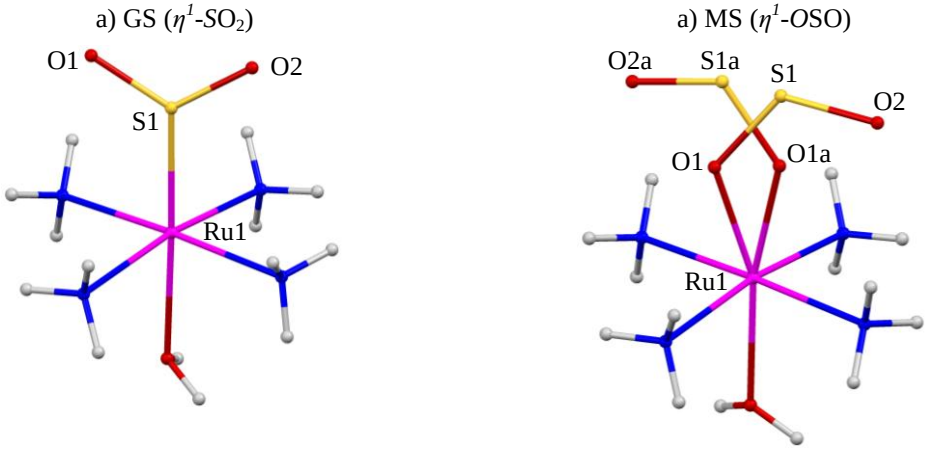

Figure 39: Single-crystal molecular structure of *trans*-[$Ru(NH_3)_4(H_2O)(SO_2)$]2(Tos) ground-state (left), light-induced metastable-state MS_1 (right).[86]

$[Ru(NH_3)_4(CF_3CO_2)(SO_2)](CF_3CO_2)_2$

Coppens also reported that $[Ru(NH_3)_4(CF_3CO_2)(\eta^1\text{-}SO_2)](CF_3CO_2)_2$, under the same irradiation condition as for the $C_6H_5SO_3^-$ analogue, gives a 37.5 % conversion to the second metastable-state (MS2) side-bound(η^2-*OSO*). All the literature accounts of photocrystallographic studies of linkage isomerism is summarised in Table 1. With exception of the Woike's study on the $[Ru(py)_4Cl(\eta^1\text{-}NO)](PF_6)_2.½H_2O$ system, the maximum level of excitation is generally under 50%, this may be because of low levels of light penetration, disruption of the crystal structure leading to crystal degradation or as Woike suggests, an equilibrium between the ground state and excited states.[82]

Table 1: Conversion of all linkage isomerism complexes in investigated using crystallography.

Crystal System	Ambidentite ligand and Coordination Mode		Conversion (%)	Irradiation Source	Temp (K)	ref
	GS	MS				
$[Co(NH_3)_5(NO_2)]$ 2Cl	nitro (η^1-NO_2)	*exo*-nitrito (η^1-*O*NO)	14.5 %	150 W Xe lamp	116 K	49
$Ni(aem)_2(NO_2)_2$		*endo*-nitrito (η^1-*O*NO)	23 %	470 nm LEDs	100 K	56
$Ni(aepi)_2(NO_2)_2$		*endo*-nitrito (η^1-*O*NO)	18 %	470 nm LEDs	100 K	56
$Ni(aepy)_2(NO_2)_2$		*endo*-nitrito (η^1-*O*NO) *exo*-nitrito (η^1-*O*NO)	20 % 10 % (30 %)	470 nm LEDs	100 K	56
$[Ru(bpy)_2(NO)(NO_2)]$ 2(PF_6)	nitro (η^1-NO_2) nitrosyl (η^1-*N*O)	nitrosyl (η^1-*N*O) *endo*-nitrito (η^1-*O*NO)	11.6 %	458nm Ar^+ laser	200 K	57
$[Ru(bpy)_2(NO)(NO_2)]$ 2(PF_6)	nitro (η^1-NO_2) nitrosyl (η^1-*N*O)	*iso*-nitrosyl (η^1-*O*N) *endo*-nitrito (η^1-*O*NO)	9.1 %	458nm Ar^+ laser	90 K	57
$2Na[Fe(CN)_5(NO)]$ $2H_2O$	nitrosyl (η^1-*N*O)	*iso*-nitrosyl (η^1-*O*N) *side-on*-nitrosyl (η^2-*ON*)	10 % 37 %	543 nm Ar^+ laser 543 nm Ar^+ laser	50 K	79
$[M(NO_2)_4(NO)(OH)]$ 2K		*iso*-nitrosyl (η^1-*O*N)	16 %	lasers	50 K	80-81
$[Ni(NO)(\eta^5$-Cp*)]		*side-on*-nitrosyl (η^2-*ON*)	47 %	458nm Ar^+ laser	25 K	64
$[Ru(py)_4Cl(NO)]$ $2(PF_6)_2$ ½H_2O		*iso*-nitrosyl (η^1-*O*N) *side-on*-nitrosyl (η^2-*ON*)	92 % 46 %	473 nm laser 980 nm laser	80 K	82
$[Ru(NH_3)_4Cl(SO_2)]$ Cl	sulphur dioxide η^1-SO_2	*side-on*-(η^2-*OSO*)	10 %	488nm Ar^+ laser	90 K	85
$[Ru(NH_3)_4(H_2O)(SO_2)]$ $(C_6H_5SO_3)$		*side-on*-(η^2-*OSO*)	11 %	488nm Ar^+ laser	90 K	85
$[Ru(NH_3)_4(H_2O)(SO_2)]$ $(CH_3C_6H_4SO_3)$		*side-on*-(η^2-*OSO*)	20%	488nm Ar^+ laser	90 K	85
$[Ru(NH_3)_4(H_2O)(SO_2)]$ $(CH_3C_6H_4SO_3)$		*side-on*-(η^2-*OSO*) *endo*-(η^1-*OSO*)	8 % 36 % (44 %)	365 nm W lamp	13 K	86
$[Ru(NH_3)_4(C_2O_2F_3)$ $(SO_2)]$ 2($C_2O_2F_3$)		*side-on*-(η^2-*OSO*)	38 %	488nm Ar^+ laser	90 K	85

1.1.5.5. Pump-Probe Experiments

The first truly time-resolved photocrystallographic experiments on molecular systems were undertaken on the $[Pt(pop)_4](NEt_4)_4$ system, where 'pop' is $(H_2P_2O_5)^{2-}$, due to the relatively long lifetime of the triplet excited state of ~50 microseconds. The crystal was irradiated at 355 nm using a pulsed Nd:YAG laser (5100 Hz, 80-130 J) synchronised with the mechanically chopped X-ray beam. Excitation of the system promotes electrons from antibonding ($d\sigma^*$) to bonding (p) Pt-Pt orbitals, which induces a shortening of the Pt-Pt bonding length by 0.28(9) Å and a rotation of Pt square coordination plane. The photoexcited component in the crystal structure has occupancy ranging from 2-6 %.

Copper (I) complexes are known throughout literature for undergoing metal-ligand and ligand-metal change transfer upon excitation. These excited states have a prolonged triplet lifetime accompanied by structural distortions. The distortions are comparable to that seen in the geometry changes from Cu^I to Cu^{II} which prefer tetrahedral and square planar geometry, respectively. The photoexcited crystals of the $[Cu(dmp)(dppe)](PF_6)$ (where dmp is 2,9'-dimethylphenanthroline and dppe is 1,2-*bis*(diphenylphosphino)ethane) show a slight structural rearrangement, with the coordination geometry around the metal centre flattening typical for a transition from a Cu^I to a *pseudo* Cu^{II} state. The triplet excited state has bi-exponential decay *via* phosphorescence emission with lifetimes of 88 and 552 microseconds at 16 K.[87]

The largest structural change observed using pump-probe crystallography techniques is for dirhodium complexes which inherently have very soft metal-metal bond interactions, and as a result Rh-Rh bond length vary significantly. In the $[Rh_2(dimen)_4]^{2+}$ (where dimen is 1,8-diisocyanomethane) system, the metal-metal bond length varies with different counter-ions and for this reason the $[Rh_2(dimen)_4](PF_6)_2$ system was investigated photocrystallographically. When crystals of $[Rh_2(dimen)_4](PF_6)_2$ are irradiated using 355 nm Nd/vanadate laser at 23 K and synchronised with a mechanically chopped X-ray beam (9.5 microseconds), electrons are promoted from the antibonding 4dσ* to bonding 5pσ orbitals causing a dramatic shortening of the Rh-Rh bond length of 0.86 Å and rotation of the molecule

of 18º. The lifetime of these species at 23 K is 11.7 microseconds and the excited state had a population of 2.5 %.[87]

The first nanosecond time-resolved experiments were carried out on the N,N-dimethylaminobenzonitrile (DMABN) ligand using time-resolved powder diffraction. The picoscecond structural changes are investigated using a pulsed laser synchronised with the polychromatic X-ray pulses from a synchrotron. By varying the delay between the pump (laser) and probe (X-rays), a snapshot of the transient species can be obtained, providing a crystallographic movie. Intensity changes in the range of 1-10 % are observed, corresponding to a 26-30 % structural changes with rotation around the N by 12º and an increased torsion from 0º(1) to 10º(1).[88]

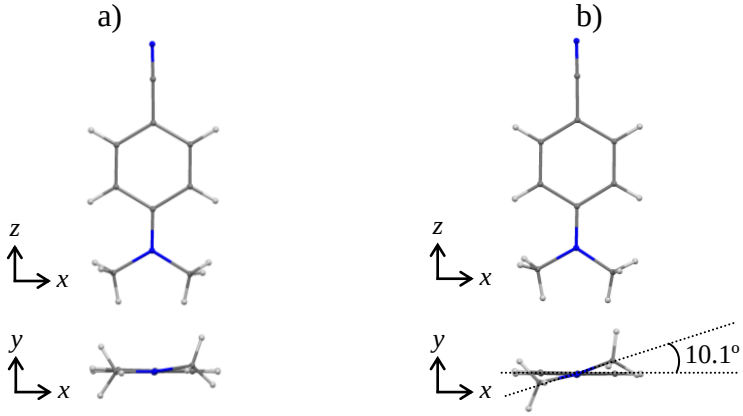

Figure 40: Molecular structures of DMABN a) before and b) after irradiation.

1.1.5.6. X-ray Free Electron Lasers (XFEL)

X-ray Free Electron Lasers (XFEL) may provide a possible method to obtain information in the femtosecond time domain. The XFEL produces 100 fs pulses with extreme intensities (10^{12} photons per pulse). The extreme intensities have so much energy that any molecule or micro crystal decomposes rapidly and give one-shot experiments. As the pulses from the XFEL are shorter than that of the lifetime (~2-10 fs) of the sample, it can be probed before any electronic modifications occur. These studies are in the very early stages of development and it is intriguing to imagine the future potential unfold.[89]

1.1.5.7. Industrial Applications

It is evident that time-resolved crystallography allows investigation of many types of processes and over the past decades has been at the forefront of research opening up many new possibilities. With further development, it should be possible to analyse more, process more on a shorter and shorter time scale, and achieve a better understanding.

More specifically, photocrystallographic experiments have been used to investigate the bonding modes of small ambidentate ligands and through this work a number of potential industrial applications have been assessed. For example, the use of nitrosyl in medical biological systems and linkage isomers being used in complexes as small scale digital storage etc. In today's world, digital storage is of great importance as a result of the increasing use of computational devices in our daily lives. Although the size of storage elements has continued to drop over the years, this may not continue due to physical limitations.[90] One possible alternative is the exploitation of linkage isomerism, but there are many engineering problems to overcome e.g. the ability to "address a single molecule".[91-92] The different coordination modes can be seen as 'on' or 'off' and a large number of these can be built-up to produce digital storage in the binary form.

The nitrosyl isomer plays a part in many biological systems and has been recognized in the process of physiological and pathological responses. The nitrosyl molecule acts as a signalling molecule to regulate blood pressure, neurotransmission, inhibition of platelet aggregation, cell-mediated immune response, antimicrobial activity, cell death and tumor regression. The recent discovery that nitrosyl plays a vital role in physiological and pathological responses has raised interest in the mechanics of the processes, including the effect of stimuli such asfrom *pH*, heat and light. Literature has suggested that the using photocrystallography to investigate the bonding modes and interactions can help establish the nature of the processes.[93]

1.2. Conclusions

This chapter reports the diversity of transformations that can occur in the crystal induced by a range of physical environment in conjunction with the diffraction experiment, these include altering the temperature (cryogens), pressure (diamond anvil cell) or atmosphere (environmental gas cell) electrical field or photon irradiation. From these experiments it is possible to achieve three-dimensional structures at discrete steps during a reaction process, investigate transient species or to obtain crystal structures not achievable through normal methods.

The photocrystallographic experiment changes depend on the lifetime of the material. Steady state method can be used to determine irreversible reaction and thermally trapped species. New advances in both hardware and software have made it possible to use pump-probe techniques to determine species down to picosecond lifetimes.

From the experiments discussed in this chapter there are number of ideas and procedures which can be introduced into future studies to increase the chances of success, these include:

- An interesting observation is that data quality can be affected during the transformation, but on completion of the transformation the system can regain crystallinity. This was the case with removal of solvent molecules from a framework, during the transition the data quality dramatically reduced, and only regained crystallinity when the transformation reached completion.[25]
- Irradiation at low temperature can dramatically reduce crystal degradation as observed in the [2+2]-cycloaddition system.[42]
- For highly light sensitive compounds, preparation in the absence of light is key to obtain a clean starting ground state crystal structure without the presence of any photoinduced product.[43]
- In many non-ambient investigations, the transformation causes the unit cell dimensions to change. Continuously monitoring the unit cell while the

crystal environment is altered can give an real time measurement of the reaction progress.[46]

- For the linkage isomerism process carrying out the photochemical reaction at different temperature can affect the coordination modes observed.[57]

Overall, the crystal has a surprising amount of flexibility and can undergo dramatic structural rearrangement. The transformation within a single crystal does not always reach completeness, in general this may be because of low levels of light penetration, disruption of the crystal structure leading to crystal degradation or as it reaches a photostationary point at equilibrium between the ground state and excited states.[82]

1.3. Aims and objectives

There are many complexes containing ambidentate ligands capable of undergoing linkage isomerism, many of which have been extensively studied in solution. However, many of potential industrial applications for these materials are in solid state, and therefore to truly understand the mechanism and improve the material, the analysis must be performed in the same state. More recently, photoinduced linkage isomerism has been studied using crystallography which gives an accurate model of the species in the solid state photoreaction.

The aim of the research outlined in this thesis has been to investigate the nitrate ambidentate ligand in complexes to find systems which:

- Are capable of high percentage conversion to the metastable state without loss of crystallinity.
- To find systems which are metastable to higher temperatures.
- To modify crystal packing and so reduce crystal degradation by introducing systems with:
  - Bulky ligands
  - Counter-ions
  - Networks
- To investigate the reaction rates and the factors which affect them.
- To apply knowledge gained to design new systems.

1.4. References

1	Cryosystems, O. *Oxford Cryosystems Ltd, 3 Blenheim Office Park, Lower Road, Long Hanborough, Oxford, OX29 8LN, United Kingdom*, http://www.oxfordcryosystems.co.uk/.
2	Oxford_Instruments *Oxford Diffraction Ltd, 10 Mead Road, Oxford Industrial Park, Yarnton, Oxfordshire, OX5 1QU*, http://www.oxford-diffraction.com/products/sample-environment-devices/.
3	Probert, M. R.; Robertson, C. M.; Coome, J. A.; Howard, J. A. K.; Michell, B. C.; Goeta, A. E. *J. Appl. Crystallogr.* **2010**, *43*, 1415.
4	Wilkins, S. B.; Spencer, P. D.; Hatton, P. D.; Tanner, B. K.; Lafford, T. A.; Spence, J.; Loxley, N. *Rev. Sci. Instrum.* **2002**, *73*, 2666.
5	Goeta, A. E.; Howard, J. A. K. *Chem. Soc. Rev.* **2004**, *33*, 490.
6	Gutlich, P.; Garcia, Y.; Goodwin, H. A. *Chem. Soc. Rev.* **2000**, *29*, 419.
7	Konig, E.; Madeja, K. *Chem. Commun.* **1966**, 61.
8	Gallois, B.; Real, J. A.; Hauw, C.; Zarembowitch, J. *Inorg. Chem.* **1990**, *29*, 1152.
9	Mahapatra, S.; Thakur, T. S.; Joseph, S.; Varughese, S.; Desiraju, G. R. *Cryst. Growth Des.* **2010**, *10*, 3191.
10	STOE_IPDS_II *Hilpertstr. 10, 64295 Darmstadt, Germany*, http://www.stoe.com/pages/products/accessories_single.html.
11	Kruger, H.; Breil, L. *J. Appl. Crystallogr.* **2009**, *42*, 140.
12	Grunenberg, A.; Bougeard, D.; Schrader, B. *Thermochim. Acta* **1984**, *77*, 59.
13	Coles, S. J.; Gelbrich, T.; Griesser, U. J.; Hursthouse, M. B.; Pitak, M.; Threlfall, T. *Cryst. Growth Des.* **2009**, *9*, 4610.
14	Moggach, S. A.; Allan, D. R.; Parsons, S.; Warren, J. E. *J. Appl. Crystallogr.* **2008**, *41*, 249.
15	Merrill, L.; Bassett, W. A. *Rev. Sci. Instrum.* **1974**, *45*, 290.
16	Gatteschi, D.; Sorace, L. *J. Solid State Chem.* **2001**, *159*, 253.
17	Oshio, H.; Nakano, M. *Chem. Eur. J.* **2005**, *11*, 5178.
18	Ribas-Arino, J.; Baruah, T.; Pederson, M. R. *J. Am. Chem. Soc.* **2006**, *128*, 9497.
19	Inglis, R.; Jones, L. F.; Karotsis, G.; Collins, A.; Parsons, S.; Perlepes, S. P.; Wernsdorfer, W.; Brechin, E. K. *Chem. Commun.* **2008**, 5924.
20	Cirera, J.; Ruiz, E.; Alvarez, S.; Neese, F.; Kortus, J. *Chem. Eur. J.* **2009**, *15*, 4078.
21	Parois, P.; Moggach, S. A.; Sanchez-Benitez, J.; Kamenev, K. V.; Lennie, A. R.; Warren, J. E.; Brechin, E. K.; Parsons, S.; Murrie, M. *Chem. Commun.* **2010**, *46*, 1881.
22	Eddaoudi, M.; Kim, J.; Rosi, N.; Vodak, D.; Wachter, J.; O'Keeffe, M.; Yaghi, O. M. *Science* **2002**, *295*, 469.
23	Morris, R. E.; Wheatley, P. S. *Angew. Chem. Int. Ed.* **2008**, *47*, 4966.
24	Rosi, N. L.; Eckert, J.; Eddaoudi, M.; Vodak, D. T.; Kim, J.; O'Keeffe, M.; Yaghi, O. M. *Science* **2003**, *300*, 1127.
25	Mukherjee, P. S.; Lopez, N.; Arif, A. M.; Cervantes-Lee, F.; Noveron, J. C.

Chem. Commun. **2007**, 1433.
26 Warren, J. E.; Pritchard, R. G.; Abram, D.; Davies, H. M.; Savarese, T. L.; Cash, R. J.; Raithby, P. R.; Morris, R.; Jones, R. H.; Teat, S. J. *J. Appl. Crystallogr.* **2009**, *42*, 457.
27 Allan, P. K.; Xiao, B.; Teat, S. J.; Knight, J. W.; Morris, R. E. *J. Am. Chem. Soc.* **2010**, *132*, 3605.
28 van Reeuwijk, S. J.; Puig-Molina, A.; Graafsma, H. *Phys. Rev. B: Condens. Matter* **2000**, *62*, 6192.
29 Wayne, C. E.; Wayne, R. P. *Oxford Chemistry Primers* **1996**, *1*, 1.
30 Turro, N. J.; Ramamurthy, V.; Scaiano, J. C. *University Science Books* **2008**, *1*, 1.
31 Cole, J. M. *Acta Crystallogr. Sect. A* **2008**, *64*, 259.
32 Coppens, P.; Zheng, S. L.; Gembicky, M.; Messerschmidt, M.; Dominiak, P. M. *CrystEngComm* **2006**, *8*, 735.
33 Raithby, P. R. *Crystallogr. Rev.* **2007**, *13*, 121
34 Cole, J. M. *Chem. Soc. Rev.* **2004**, *33*, 501.
35 Brayshaw, S. K.; Knight, J. W.; Raithby, P. R.; Savarese, T. L.; Schiffers, S.; Teat, S. J.; Warren, J. E.; Warren, M. R. *J. Appl. Crystallogr.* **2010**, *43*, 337.
36 Coppens, P.; Vorontsov, II; Graber, T.; Gembicky, M.; Kovalevsky, A. Y. *Acta Crystallogr. Sect. A* **2005**, *61*, 162.
37 Woodward, R. B.; Hoffmann, R. *Angew. Chem. Int. Ed.* **1969**, *8*, 781.
38 Schmidt, G. M. J. *J. Chem. Soc.* **1964**, 2014.
39 Cohen, M. D.; Schmidt, G. M. J. *J. Chem. Soc.* **1964**, 1996.
40 Cohen, M. D.; Schmidt, G. M. J.; Sonntag, F. I. *J. Chem. Soc.* **1964**, 2000.
41 Mahon, M. F.; Raithby, P. R.; Sparkes, H. A. *CrystEngComm* **2008**, *10*, 573.
42 Mir, M. H.; Koh, L. L.; Tan, G. K.; Vittal, J. J. *Angew. Chem. Int. Ed.* **2010**, *49*, 390.
43 Trzop, E.; Turowska-Tyrk, I. *Acta Crystallogr. Sect. B: Struct. Sci.* **2008**, *64*, 375.
44 Brayshaw, S. K.; Schiffers, S.; Stevenson, A. J.; Teat, S. J.; Warren, M. R.; Bennett, R. D.; Sazanovich, I. V.; Buckley, A. R.; Weinstein, J. A.; Raithby, P. R. *J. Am. Chem. Soc.* **2010**, (submitted).
45 Zheng, S.-L.; Messerschmidt, M.; Coppens, P. *Acta Crystallogr. Sect. B: Struct. Sci.* **2007**, *63*, 644.
46 Kaiba, A.; Shepherd, H. J.; Fedaoui, D.; Rosa, P.; Goeta, A. E.; Rebbani, N.; Letard, J. F.; Guionneau, P. *Dalton Trans.* **2010**, *39*, 2910.
47 Balzani, V.; Ballardi.R; Sabbatin.N; Moggi, L. *Inorg. Chem.* **1968**, *7*, 1398.
48 Grenthe, I. N., Ellika. *Inorg. Chem.* **1979**, *18*, 1869.
49 Kubota, M.; Ohba, S. *Acta Crystallogr. Sect. B: Struct. Sci.* **1992**, *48*, 627.
50 Das, D.; Laskar, I. R.; Ghosh, A.; Mondal, A.; Okamoto, K.; Chaudhuri, N. R. *J. Chem. Soc., Dalton Trans.* **1998**, 3987.
51 Goodgame, D. M.; Hitchman, M. A. *Inorg. Chem.* **1964**, *3*, 1389.
52 Elsayed, L.; Ragsdale, R. O. *Inorg. Chem.* **1967**, *6*, 1640.
53 Goodgame, D. M.; Hitchman, M. A. *Inorg. Chem.* **1965**, *4*, 721.
54 Chattopadhyay, T.; Ghosh, M.; Majee, A.; Nethaji, M.; Das, D. *Polyhedron* **2005**, *24*, 1677.

55 Laskar, I. R.; Maji, T. K.; Das, D.; Lu, T. H.; Wong, W. T.; Okamoto, K.; Chaudhuri, N. R. *Polyhedron* **2001**, *20*, 2073.

56 Brayshaw, S. K.; Easun, T. L.; George, M. W.; Griffin, A. M. E.; Johnson, A. L.; Raithby, P. R.; Savarese, T. L.; Schiffers, S.; Warren, J. E.; Warren, M. R.; Teat, S. J. *Dalton Trans.* **2010** (accepted).

57 Kovalevsky, A. Y.; King, G.; Bagley, K. A.; Coppens, P. *Chem. Eur. J.* **2005**, *11*, 7254.

58 Novozhilova, I. V.; Coppens, P.; Lee, J.; Richter-Addo, G. B.; Bagley, K. A. *J. Am. Chem. Soc.* **2006**, *128*, 2093.

59 Lee, J.; Kovalevsky, A. Y.; Novozhilova, I. V.; Bagley, K. A.; Coppens, P.; Richter-Addo, G. B. *J. Am. Chem. Soc.* **2004**, *126*, 7180.

60 Chattopadhyay, T.; Ghosh, M.; Banerjee, A.; Banu, K. S.; Das, D.; Nethaji, M. *Transition Met. Chem.* **2007**, *32*, 531.

61 Supriya, S.; Das, S. K. *Inorg. Chem. Commun.* **2009**, *12*, 364.

62 Bitterwolf, T. E. *Coord. Chem. Rev.* **2006**, *250*, 1196.

63 Crichton, O.; Rest, A. J. *J. Chem. Soc., Dalton Trans.* **1977**, 987.

64 Fomitchev, D. V.; Furlani, T. R.; Coppens, P. *Inorg. Chem.* **1998**, *37*, 1519.

65 Hauser, U.; Oestreich, V.; Rohrweck, H. D. *Z. Phys. A: Hadrons Nucl.* **1977**, *280*, 125.

66 Hauser, U.; Oestreich, V.; Rohrweck, H. D. *Z. Phys. A: Hadrons Nucl.* **1977**, *280*, 17.

67 Zeitschrift fur KristallograhieZollner, H.; Woike, T.; Krasser, W.; Haussuhl, S. *Z. Kristallogr.* **1989**, *188*, 139.

68 Woike, T.; Krasser, W.; Bechthold, P. S.; Haussuhl, S. *Solid State Commun.* **1983**, *45*, 499.

69 Woike, T.; Krasser, W.; Bechthold, P. S.; Haussuhl, S. *Solid State Commun.* **1983**, *45*, 503.

70 Woike, T.; Krasser, W.; Bechthold, P. S.; Haussuhl, S. *Phys. Rev. Lett.* **1984**, *53*, 1767.

71 Guida, J. A.; Piro, O. E.; Aymonino, P. J. *Solid State Commun.* **1986**, *57*, 175.

72 Woike, T.; Zollner, H.; Krasser, W.; Haussuhl, S. *Solid State Commun.* **1990**, *73*, 149.

73 Woike, T.; Haussuhl, S. *Solid State Commun.* **1993**, *86*, 333.

74 Guida, J. A.; Piro, O. E.; Schaiquevich, P. S.; Aymonino, P. J. *Solid State Commun.* **1997**, *101*, 471.

75 Guida, J. A.; Piro, O. E.; Aymonino, P. J. *Inorg. Chem.* **1995**, *34*, 4113.

76 Fomitchev, D. V.; Coppens, P. *Comments Inorg. Chem.* **1999**, *21*, 131.

77 Ruedlinger, M. S., J.; Vogt, T.; Woike, T.; Haussuehl, S.; Zoellner, H *Physica B: Condensed Matter* **1992**, *180-181*, 293.

78 Pressprich, M. R.; White, M. A.; Vekhter, Y.; Coppens, P. *J. Am. Chem. Soc.* **1994**, *116*, 5233.

79 Carducci, M. D.; Pressprich, M. R.; Coppens, P. *J. Am. Chem. Soc.* **1997**, *119*, 2669.

80 Dmitry V. Fomitchev, P. C. *Inorg. Chem.* **1996**, *35*, 7021.

81 Dmitry V. Fomitchev, I. N. a. P. C. *Tetrahedron* **2000**, *56*, 6813.

82 Cormary, B.; Malfant, I.; Valade, L.; Cointe, M. B. L.; Toupet, L.; Todorova, T.; Delley, B.; Schaniel, D.; Mockus, N.; Woike, T.; Fejfarova,

	K.; Petricek, V.; Dusek, M. *Acta Crystallogr. Sect. B: Struct. Sci.* **2009**, *65*, 787.
83	Kovalevsky, A. Y.; Bagley, K. A.; Coppens, P. *J. Am. Chem. Soc.* **2002**, *124*, 9241.
84	Johnson, D. A. D., V. C *Inorg. Chem.* **1979**, *18*, 3273.
85	Kovalevsky, A. Y.; Bagley, K. A.; Cole, J. M.; Coppens, P. *Inorg. Chem.* **2003**, *42*, 140.
86	Bowes, K.; Cole, J.; Husheer, S.; Raithby, P.; Savarese, T.; Sparkes, H.; Teat, S.; Warren, J. *Chem. Commun.* **2006**, 2448.
87	Coppens, P.; Gerlits, O.; Vorontsov, II; Kovalevsky, A. Y.; Chen, Y. S.; Graber, T.; Gembicky, M.; Novozhilova, I. V. *Chem. Commun.* **2004**, 2144.
88	Techert, S.; Schotte, F.; Wulff, M. *Phys. Rev. Lett.* **2001**, *86*, 2030.
89	Chapman, H. N. *Nat. Mater.* **2009**, *8*, 299.
90	Ward, M. D. *J. Chem. Educ.* **2001**, *78*, 321.
91	R. Lloyd Carroll, C. B. G. *Angew. Chem.* **2002**, *41*, 4378.
92	Marcos Gomez-Lopez, J. A. P. a. J. F. S. *Nanotechnology* **1996**, *7*, 183.
93	Eroy-Reveles, A.; Leung, Y.; Beavers, C.; Olmstead, M.; Mascharak, P. *J. Am. Chem. Soc.* **2008**, 4447.

Chapter 2 – Crystallographic Background

Chapter 2 – Crystallographic Background

This chapter contains a description of the basic theory of X-ray crystallography and the diffraction methods that underpins the majority of the experiments presented in this thesis.

2.1. Crystallographic Background

2.1.1. Flow Chart of Crystallographic Procedure

The basic outline of the crystallographic procedure from crystallization to publication is shown in Figure 1. The following chapter briefly explains some of the important steps in the crystallographic flow chart.[1-2]

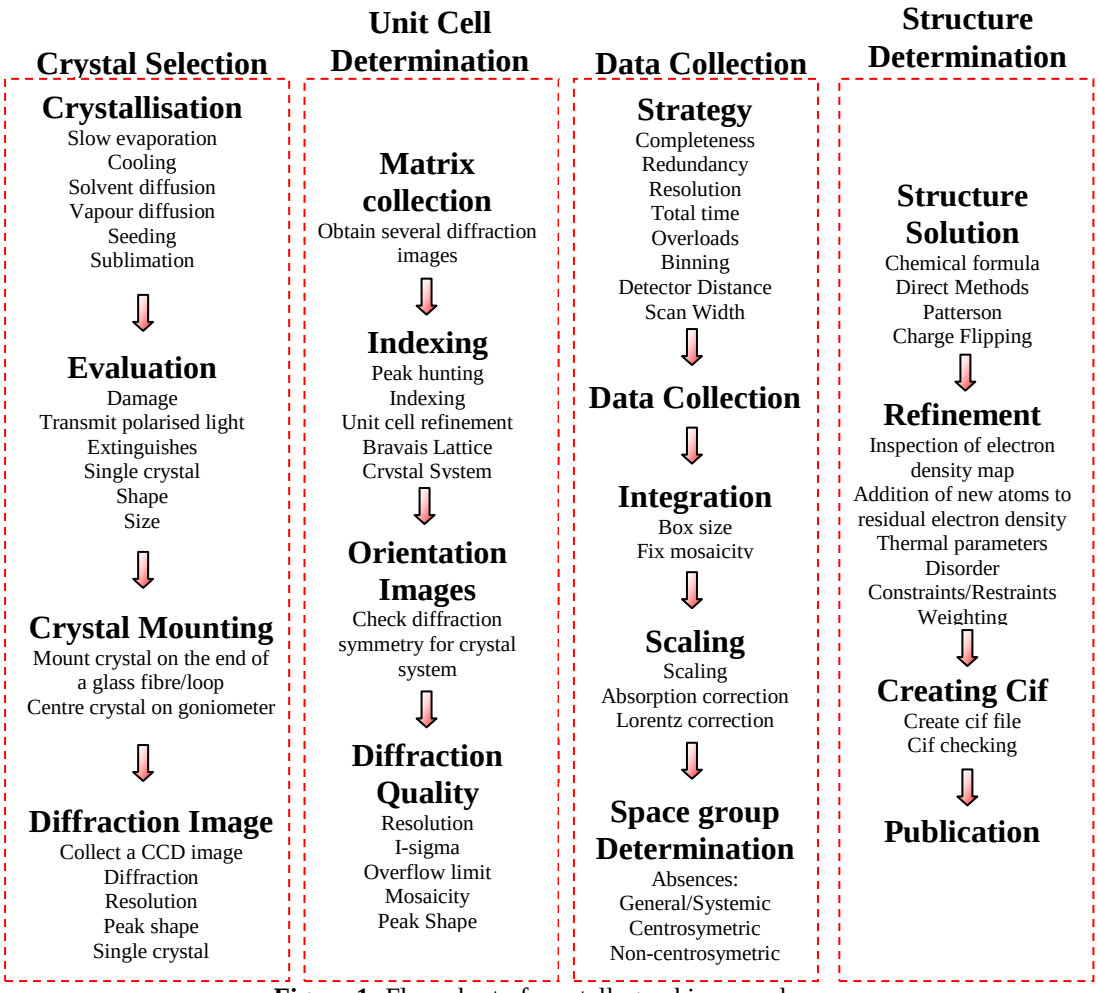

Figure 1: Flow chart of crystallographic procedure.

2.1.2. Crystalline Material

Single crystal X-ray crystallography is the diffraction technique used to determine the solid-state molecular structure (3D model) of crystalline materials providing information onatomic coordinates, displacement parameters, molecular arrangements, bond lengths, angles, torsions angles, non-bonding interactions and crystal packing. Crystalline materials contain a three-dimensional periodic arrangement of matter, with regular repeating patterns of atoms, molecules or ions in arrays of translationally equivalent positions. The successful determination of the structure is governed by the arrangement of molecules within the crystal being highly ordered. The X-ray wavelengths used are of a comparable length to distances between atoms in the structure.[1-2]

2.1.3. Unit Cell

Equivalent positions within a crystal are called lattice points. Lattice points can be joined up to form three-dimensional boxes called unit cells. The unit cell is the smallest repeating unit which shows the full symmetry when built up in a 3D manner forming the crystal lattice. The unit cell parameters can be used to describe the size and shape of the unit cell. These parameters include three cell dimensions-*a, b, c* and three angles-*α, β ,γ*.[1-3]

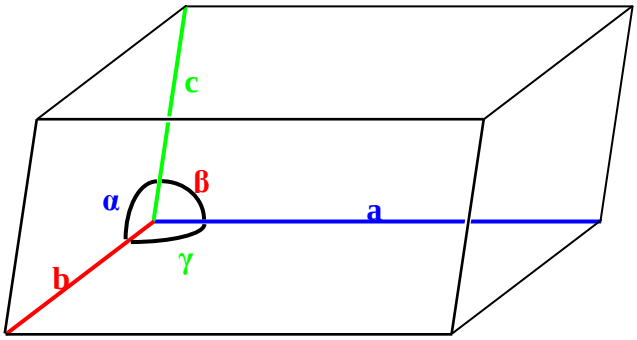

Figure 2: Unit cell diagram with dimensions (*a*,*b*,*c*) and angles (*α*,*β*,*γ*).[1-2]

2.1.4. Crystal Lattices

There are an infinite number of possible combinations of cell lengths and angles, but there are a finite number of ways that the parameters relate to each other, producing 7 crystal systems describing all the possible combinations (

Table **1**).[1-3]

Table 1: Crystal Systems[3]

Crystal System	Bravais Lattice	Unit Cell Dimensions	
Cubic	*P,I,F*	$a = b = c$	$\alpha = \beta = \gamma = 90^o$
Hexagonal	*P*	$a = b \neq c$	$\alpha = \beta = 90^o$, $\gamma = 120^o$
Trigonal	*P*	$a = b = c$	$\alpha = \beta = \gamma \neq 90^o$
Tetragonal	*P,I*	$a = b \neq c$	$\alpha = \beta = \gamma = 90^o$
Orthorhombic	*P,C,I,F*	$a \neq b \neq c$	$\alpha = \beta = \gamma = 90^o$
Monoclinic	*P,C*	$a \neq b \neq c$	$\alpha = \gamma = 90^o$, $\beta \neq 90^o$
Triclinic	*P*	$a \neq b \neq c$	$\alpha \neq \beta \neq \gamma \neq 90^o$

Within these crystal systems, the nature of repeating molecules or atoms can be described as a series of lattice points and there are four ways in which the lattice points can be arranged. The lattice types are primitive (P type), body-centred (I type), face-centred (F type) or (A, B, C type) as shown below (Figure 3). There are 14 possible permutations of the seven crystal systems combined with the four lattice types, these are called the 14 Bravais Lattices.[1-3]

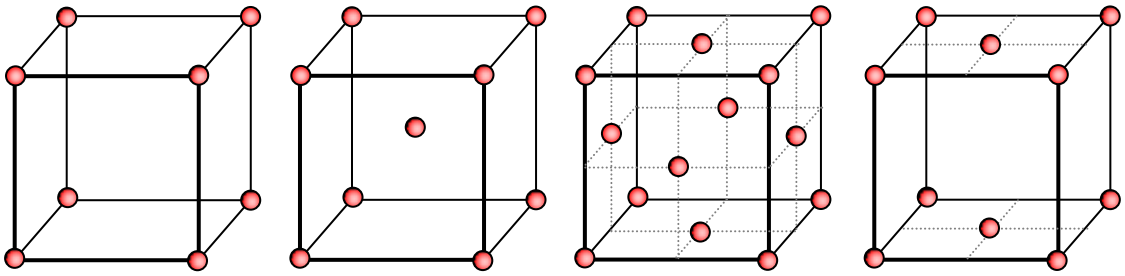

Figure 3: Lattice types[1-2]

2.1.5. Symmetry Elements within Crystals

The space group provides a description of all symmetry operations within the unit cells; this is how the molecules relate to each other in 3D space. There are two sets of categories; firstly, there are non-translational symmetry elements which include rotations, inversions, reflections and rotary inversions (Figure 4). The first symmetry element (a) is the symmetry about an axis of rotation (line), the rotation is always anticlockwise and can only be 1-, 2-, 3-, 4-, or 6-fold. The second (b) is simply the symmetry across a reflection plane (mirror plane). Inversion (c) is the symmetry about a point. Rotary inversion (d) is the combination of rotation and inversion.[1-3]

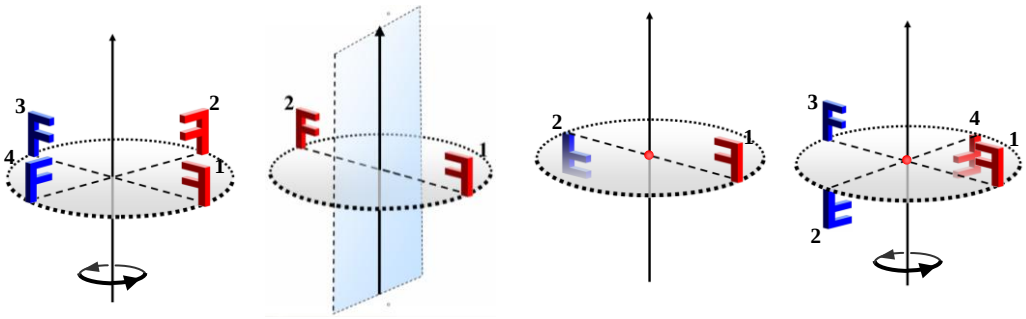

(a) Rotation (4 fold) (b) Reflection (c) Inversion (d) Rotary inversion (4 fold)

Figure 4: Illustration of non-translational symmetry elements, where F represents an asymmetric object.

The second category has translation symmetry elements which include screw axes and glide planes (Figure 5). A screw axis (e) is a rotation followed by a translation. For the example below, a 3_1 screw axis involves a rotation of 120º (360º/3) followed by a translation of a third of a unit cell (1/3) up the screw axis. When this is repeated three times, the atom, molecule or ion is a one unit cell above the original position with the same orientation. A glide plane (f) involves translation followed by a reflection. For example, a *c*-glide perpendicular to the a-axis involves a translation of half a unit cell in the c-axis, then a reflection in plane (mirror) perpendicular to the a-axis.

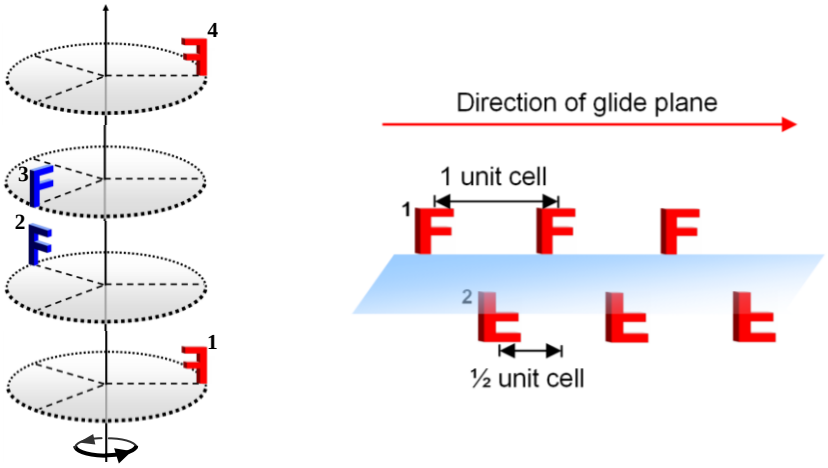

(e) Screw axis (3_1) (f) Glide Plane

Figure 5: Illustration of translational symmetry elements, where F represents an asymmetric object.

The combination of all the symmetry elements along with 14 Bravais lattices give a total of 230 possible space groups with different combinations of packing arrangements.[1-3]

2.1.6. X-ray Interaction with a Crystal

X-rays were discovered in 1895 by Röntgen and fully characterized in 1912 by von Laue.[3-4] X-rays are electromagnetic waves with wavelengths ranging from 0.01 to 10 nm. When a crystal is placed in an X-ray beam, the electrons within the molecules diffract the X-rays. In most directions, the diffracted X-rays are cancelled out (destructive interference), but in highly ordered material such as a crystal in a few specific directions, the X-rays are diffracted constructively. As the X-ray wavelength is comparable to interatomic distances between atoms in molecules, it is possible to use diffraction to obtain structural information about the molecule. The X-rays which were diffracted constructively can be determined by Bragg's Law.[1-2]

2.1.7. Bragg's Law

Miller indices are parallel sets of planes with the spacing between the lines corresponding to d-spacings, related to the equivalent positions in the unit cell. The distance between these planes within the crystal can be worked out using Bragg's Law (Figure 6). Bragg's Law is a construction that treats the diffraction process as if it is comparable to reflection of the X-ray beams from sets of parallel planes.[1-2,5]

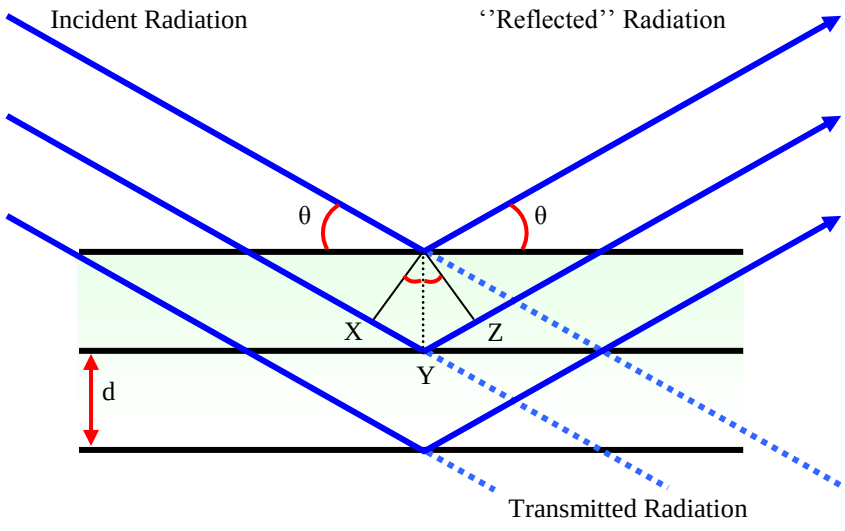

Figure 6: Bragg reflection from a set of planes with spacing d.[1-2,5]

The rays from the incident beam are always in phase and parallel until the point at which the top beam strikes the top layer in-line with 'Y'; the second beam continues to the next layer where it is scattered at point 'Y'. The second beam travels an extra distance equal to XY + YZ.[1-2,5]

Equation 1:	Difference in path length = XY + YZ

Diffraction spots occur when the reflected beams are coherent (in phase). This happens when the extra distance travelled by the second beam is equal to an integral (n) multiple of the wavelength (λ). As XY = YZ and XY is equal to d sinθ, this gives us Bragg's equation (Equation 2).[1-2,5]

Equation 2:	Difference in path length, $n\lambda = 2d\sin\theta$

2.1.8. Atomic Scattering Factors

Although Bragg's Law is a good way of predicting the peak positions, the X-rays are actually diffracted by the electron clouds surrounding the atomic nuclei and some energy is absorbed and emitted with a small amount of energy loss. How strongly the X-ray is diffracted is dependent on the number of electrons within the electron cloud and the angle of incidence (Figure 7). The measure of X-rays scattering amplitude of the atom is called the atomic scattering factor (f_j). With an increase in the number of electrons within the cloud the scattering increases but the scattering falls as the angle of incidence increases. At a zero scattering angle, the atomic scattering factor is equal to the number of electrons in the atom. As the scattering angle increases, the scattering function decreases due to X-rays hitting different parts of the electron cloud which will not give diffraction that is completely in phase. The scattering function will decrease more rapidly the more diffused the electron cloud is as a function of the scattering angle.[1-2,4-5]

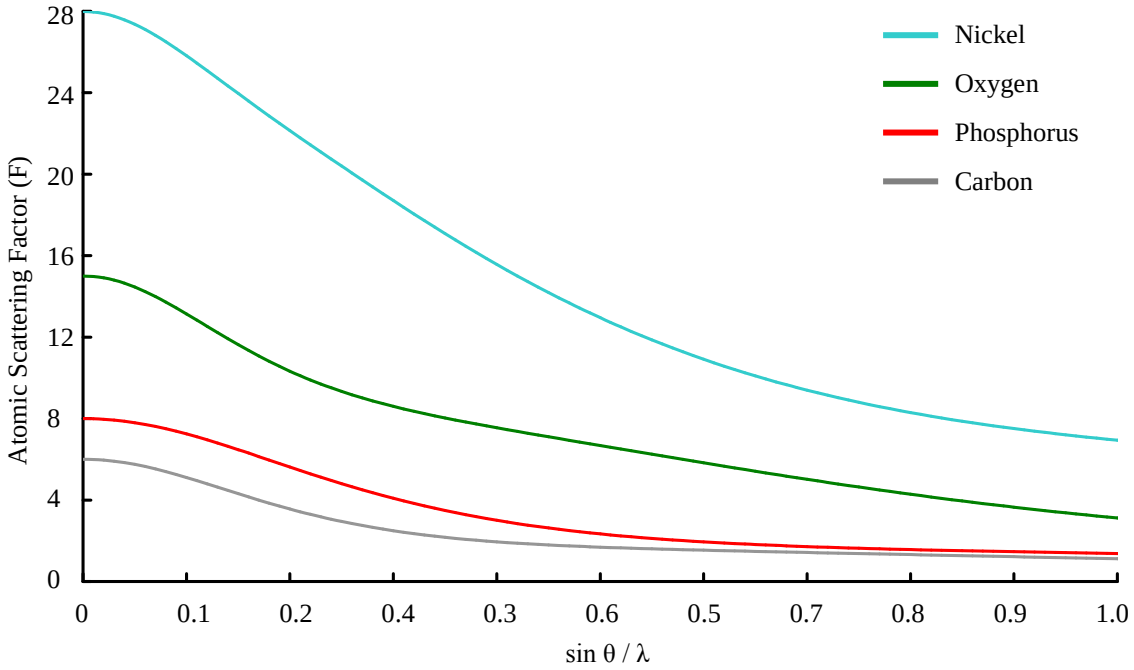

Figure 7: Atomic Scattering Factor.[4]

2.1.9. Absences and Intensity Distributions

The intensity of reflections within the diffraction pattern is due to the interference of waves scattered by atoms in a certain direction. The greater intensities come from atoms which scatter in-phase with each other, and absences come from atoms which scatter completely out of phase. For atoms that are related to each other by symmetry, the scattering effects are also related. Some symmetry operations can be readily identified by specific information in the intensities of the diffraction pattern.

General absences are a result of lattice centring and occur in non primitive lattices (F, A, B, C or I). The destructive interference of the X-ray will take place for certain reflections, according to the general absences that affect the entire diffraction pattern (Table 2).[3]

Table 2: Table of General Absences

Lattice type	Reflection	Reflection is absent for (with n integral)
P	hkl	none
I	hkl	h + k + l = 2n + 1 (sum of indices are odd)
F	hkl	either k + l = 2n + 1 or h + l = 2n + 1 or h + k = 2n + 1 (reflections must have all even or all odd indices to be observed)
A	hkl	k + l = 2n+1
B	hkl	h + l = 2n+1
C	hkl	h + k = 2n+1

Systematic Absences are a result of translational symmetry elements (screw axis and glide planes). The presence of these symmetry elements affects only subsets of reflections (Table 3).[3]

Table 3: Table of selected examples of systematic absence conditions

Symmetry Element	Reflection	Reflection is absent for (with n integral)
2_1-screw axis along a	h 0 0	h = 2n+1 (also applies for 4_2- and 6_3-screw axis)
2_1-screw axis along b	0 k 0	k = 2n+1 (also applies for 4_2- and 6_3-screw axis)
2_1-screw axis along c	0 0 l	l = 2n+1 (also applies for 4_2- and 6_3-screw axis)
3_1.screw axis along c	0 0 l	l = 3n+1, l = 3n+2 (also applies for 3_2-, 6_2- and 6_4-screw axis)
6_1-screw axis along c	0 0 l	l = 6n+1, l = 6n+2, l = 6n+3, l = 6n+4 and l = 6n+5,
c-glide prep. to *b*	h 0 l	l = 2n+1
a-glide prep. to *b*	h 0 l	h = 2n+1
a-glide prep. to *c*	h k 0	h = 2n+1
n-glide between a and *b* reflecting in the *c*-plane	h k 0	h + k = 2n+1
d-glide reflecting in the *c*-plane	h k 0	h + k = 4n

Although non-translational symmetry elements do not cause absences, they do affect the intensities of the reflections. Analysing the intensity distribution of normalized intensities can provide information as to whether the material crystallises in a centrosymmetric or non-centrosymmetric space group.[3]

2.1.10. Relationship between Crystal structure and Diffraction Pattern

In an X-ray data collection, the diffraction pattern is the build up of coherent waves scattered from the crystal (interference effects), and this is the Fourier transform of the crystal structure, and conversely the crystal structure is the Fourier transform of the diffraction pattern. The peak positions are relative to each other in the diffraction pattern and are inversely proportional to the dimensions and angles between the lattice points (unit cell dimensions). Thus, if the distance between peaks in a diffraction pattern has a large separation, then the unit cell dimension in that direction will be small and visa versa. The peak positions give information about the d-spacing, but do not give information about the unit cell contents. The unit cell contents are determined by the intensities and phases of the reflections. Thus, the crystal structure is in direct space (real space) and the diffraction pattern is in reciprocal space.[1-2]

2.1.11. Structure solution

As described previously, the diffraction pattern is the result of the scattered X-ray beam by the atom within the crystal. Each reflection has a specific amplitude and phase for a given wavelength. If all this information is present, the electron density distribution in a unit cell can easily be obtained by the Fourier transform of the diffraction pattern (equation 1).[1-2]

$$\rho(xyz) = \frac{1}{V}\sum_{hkl} F(hkl)\exp[-2\pi i(hx+ky+lz)]$$

Equation 3: Forward synthesis where: ρ is the electron density distribution with coordinates (x,y,z), V is the volume of the unit cell with dimensions (x,y,z), hkl corresponded to the planes within the crystal, F_{hkl} is the structure factor.[1-2]

From the X-ray diffraction experiment, hkl can be obtained from the spot locations, the volume of the unit cell can be obtained from the distances between the diffraction spots, and the amplitude ($F_{(hkl)}$) is the square root of the intensities. Unfortunately, the relative phase of the scattered diffracted beams cannot be directly obtained by the detector in a data collection. Therefore, the diffraction pattern cannot be used to determine the electron density distribution within the unit cell, directly, as the phases of the waves are missing. The puzzle of solving the crystal

structure without the information of the phases of the reflections is called "the phase problem". The phase problem can routinely be overcome as lost phase information is contained in the intensities and a number of properties of the crystal structure are known. Two computational methods generally used to solved the phase problem are the "Patterson method" and "Direct methods".[1-2]

Patterson Methods

The phases of reflections are lost during data collection and therefore the electron density distribution cannot be obtained directly; this problem can be overcome using the Patterson method in which the structure factors are squared and thus the phases are cancelled out. As a result, the electron density is not calculated but the vectors between atoms are obtained. The information about some of the atom coordinates can then be used to obtain the phases and the rest of the structure can be worked out during refinement.[1,6]

$$P(uvw) = \frac{1}{V}\sum_{hkl}\left|F(hkl)\right|^2 \cos[2\pi(hu + kv + lw)]$$

Equation 4: forward synthesis where: *P* is a closely related to the electron density distribution with coordinates (u,v,w), V is the volume of the unit cell and *hkl* corresponded to the planes within the crystal, F(*hkl*) is the structure factor.[1,6]

The unit cell coordinates (x,y,z) are designated by (u,v,w) in the Patterson map to distinguish between the difference of the electron density and closely related distribution obtained from the Patterson method (Equation 4). In the Patterson map, there is a peak corresponding to the vectors between pairs of atoms. This also applies to every atom corresponding to itself which has a zero distance between position; therefore the Patterson map will have the most intense peak at the origin (0,0,0) with contributions from all atoms. In a Patterson map the peaks are approximately twice as broad as in an electron density difference map because the peaks represent the full width of a vector between two atoms of finite size and, therefore, are not easily resolved. Structures which contain a few heavy atoms amongst lighter atoms produce a small number of intense peaks from the vectors between heavier atoms which can easily be distinguished in the map. These few peaks which have greatest contribution towards the electron density can then be used to locate the heavy atom positions in the structure and these positions can then be used to calculate approximate phases from the Fourier synthesis.[1-2,6]

Direct methods

Direct methods use logical steps to overcome the phase problem to obtain the crystal structure. As the structure factors obtained from the experiment and unknown phases are directly linked to the crystal structure, the phase can be extracted with the information known about the electron density distribution (Figure 8).[7-8]

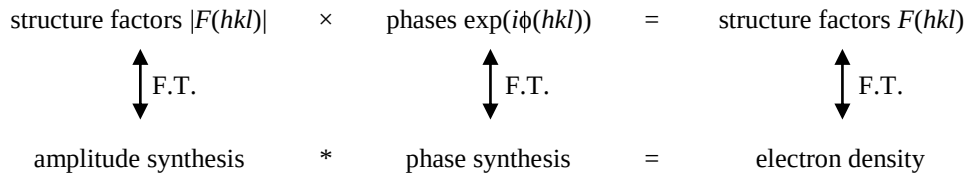

Figure 8: Relationship between amplitude, phases and electon density. Where 'F.T.' is the Fourier transformation and '*' is the convolution operator.[1-2]

The electron density distribution possesses a number of features which are used by the direct methods algorithm to correctly identify the electron density which corresponds to the crystal structure. The correct electron density must contain discrete atom positions, the electron density cannot be negative, atoms must have approximately equal scattering power, and atoms distributed randomly throughout the unit cell so there are not large areas of void space. When all these constraints are included in the direct methods calculations combinations of phases likely to produce a rational electron density distribution are obtained.

From the most intense reflections from the diffraction pattern (contributing the greatest to the electron density distribution), a few reflections are randomly assigned phase values (normally between 30 and 200 reflections). Using the probability relationship, these original assigned phases for specific reflections are propagated to generate other phase values. The phases obtained in this way are then used to calculate the electron density distribution. The resultant electron density map is then examined for recognizable molecular features. This process may be repeated many times before a solution is obtained.[1-2,7-8]

2.1.12. Refinement (least squares refinement)

The structural model obtained from the Patterson or direct methods approach is generally not complete, as in many cases part of the structure is missing and some of the phases are not correct. The aim of refinement is to improve both the phase and structure model so that $F_{(calc)}$ more closely resembles $F_{(obs)}$. As the structure model

becomes more complete through refinement, the phases can be calculated more accurately and produce a better map, which in turn can produce a better structural model so more atoms can be distinguished. This cycle can be repeated many times before the final model is complete. The difference between the diffraction pattern and the electron density map is used to assess the reliability of the crystal structure throughout the refinement process. R_1 and wR_2 are standard and conversional calculations are used in crystallography to assess the quality of the crystal structure (Equation 5 and Equation 6 respectively).[1-2] In Equation 6 weights are incorporate to improve the reliability of the *R*-factor. Each reflection is multiplied by a weight relative to the intensity ($1/\sigma^2 F$), so that the most accurate reflections (greatest intensity) contribute more in the comparison between observed and calculated structure factors (F_{obs} and F_{calc}).[9-10]

$$R_1 = \frac{\sum \left| |F_{obs}| - |F_{calc}| \right|}{\sum |F_{obs}|}$$

Equation 5: *R*-factor.[1-2]

$$wR_2 = \left(\frac{\sum w(|F_{obs}| - |F_{calc}|)^2}{\sum (w|F_{obs}|)^2} \right)^{\frac{1}{2}}$$

Equation 6: Weighted *R*-factor.[1-2]

2.1.13. Modelling of disorder

Crystallographic disorder is a problem in many crystal structure analyses and there are a number of ways of modelling the disorder to improve the overall quality of the structure. The method used to model disorder for the work presented in the thesis is described here using a nitro/nitrito disorder by way of example.

Many of the crystal structures reported in this thesis contain an ambidenite ligand which is disordered over two or more positions. The disorder often contains parts with low occupancies which need to be constrained or have restraints to produce the most accurate model. The next section will describe the basics of modelling a disordered nitrite ligand with low occupancies using strategies used in structure solution in this thesis.

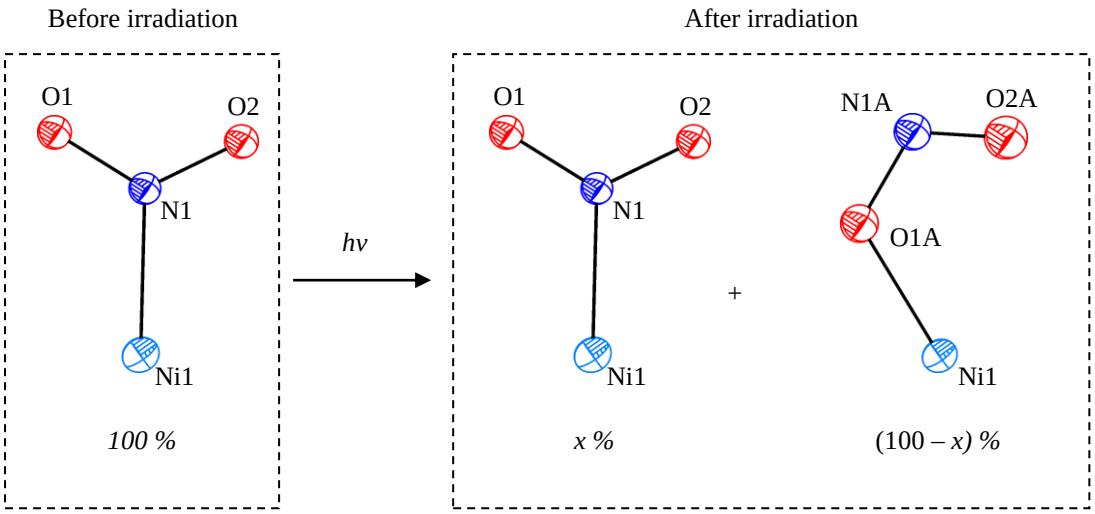

Figure 9: Disorder after irradiation to a nitro and nitrito coordination modes.

Many of the crystals reported in this thesis have mixtures of nitro and nitrito conformations. The structural model is a representation of the average distribution across the entire crystal. As a result, the crystal structure contains a percentage of both the nitro and nitrito (Figure 9). Realistically, these parts cannot be contained in the same molecule, but in the crystal structure it is modelled as disorder, as two or more partially occupied parts.[11-12]

SHELXL[11-12] is a command line language used in the refinement of crystal structures. SHELXL uses an .ins file to input all the crystallographic information (unit cell dimensions, symmetry, atom types, atom positions, thermal ellipsoids etc.) and commands (number of refinement cycles, number of residential peaks, type of map produced etc.) into the refinement program. The full explanation of the .ins file is beyond the scope of the thesis and further information can be found in literature.[11-12] Figure 10 shows the common crystallographic information and Shelx commands in an .ins file.[11-12]

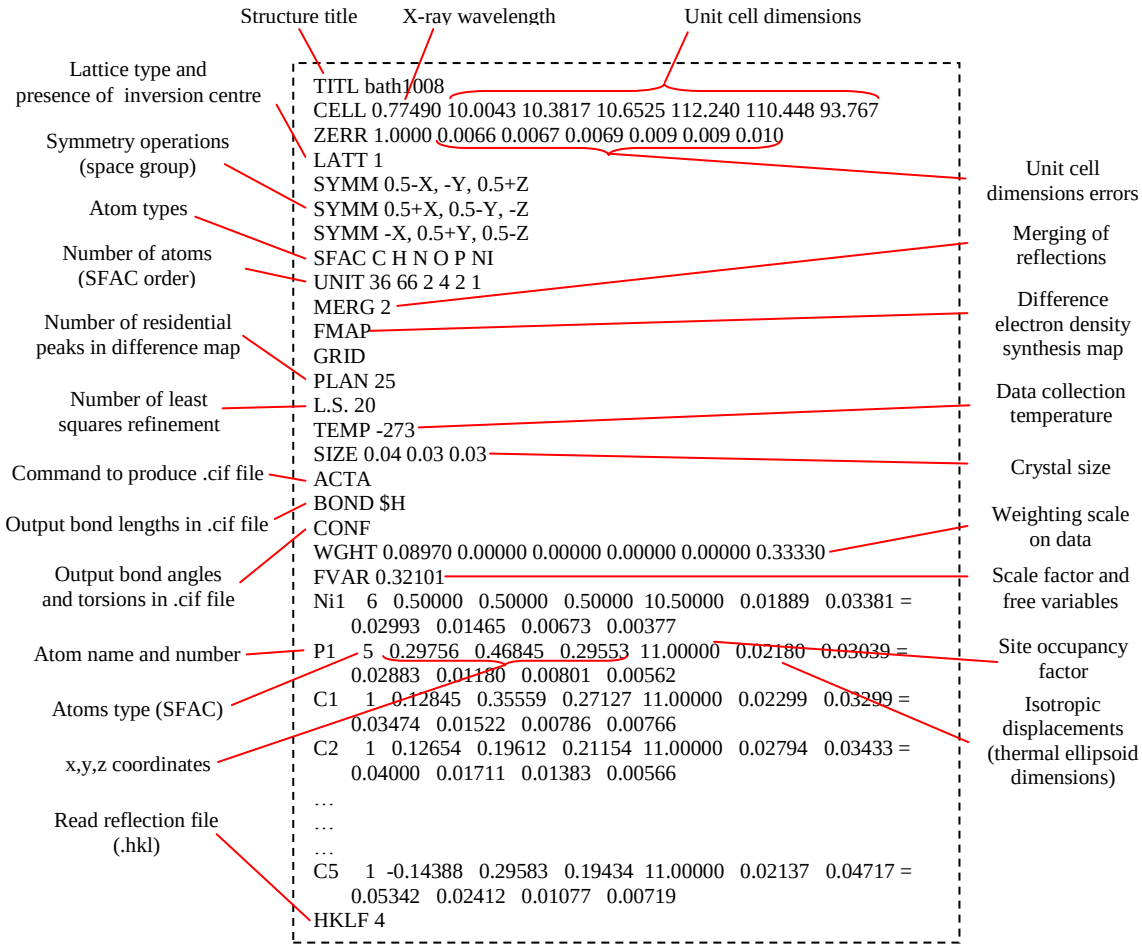

Figure 10: Ins file information.

To model disorder within a crystal structure the ins file needs to be edited. The first example will be of a two-part disorder of a nitrite ligand. After the disordered atoms positions have been found, the atoms involved need to be split into parts so the different atom configurations do not bond with one another in the crystal structure. This is simply achieved by adding PART 1 and PART 2 above the two sets of disordered atoms. At the end of the disordered atoms, PART 0 is used to indicate the end of the parts (Figure 12).[11-12]

Next, the step is to add the 'site occupancy factors' to each set of atoms. These are used to indicate whether the occupancy is fully or partially occupied. The number 11 indicates a fully-occupied atom, whereas 21, 31, 41 etc. indicate a partially-occupied site. In the nitrite disordered example PART 1 atoms are assigned a site occupancy of 21, and PART 2 atoms are assigned a site occupancy of -21 (Figure 13). The negative sign in front of the site occupancy factor means that the occupancy is equal to the remaining percentage, so that if the two occupancies are added together it

produces a fully occupied site (e.g. if O1, O2, N1 has a 54% occupancy (21), the O1A, O2A, N1A conformation will have a 46% occupancy (-21) to make up to a 100%). The starting occupancy is then added to the FVAR command (second number). The structure can then be refined. In the resulting res file, the second number after the FVAR indicates the refinement occupancy. From experience, this has an associated error of approximately ± 2% error.[11-12]

```
FVAR 0.11828
O1     4  -0.05620   0.36137  -0.09854  11.00000   0.03617   0.03445 =
       0.02535  -0.00868  -0.00322  -0.00378
O2     4  -0.11925   0.54197  -0.05944  11.00000   0.02302   0.04132 =
       0.03588   0.00020  -0.00711   0.00276
N1     3  -0.06770   0.46682  -0.05964  11.00000   0.01991   0.02592 =
       0.02087   0.00038  -0.00398  -0.00531
N1A    3  -0.10709   0.46623  -0.07828  11.00000   0.03666   0.05859 =
       0.03881   0.00723  -0.00768  -0.00985
O1A    4  -0.04897   0.40628  -0.07136  11.00000   0.03307   0.03876 =
       0.03329   0.00193  -0.00167  -0.01295
O2A    4  -0.12514   0.56863  -0.04437  11.00000   0.02613   0.06235 =
       0.05046   0.00927  -0.00356   0.01105
```

Figure 11: Starting coordinates.

```
FVAR 0.11828
PART 1
O1     4  -0.05620   0.36137  -0.09854  11.00000   0.03617   0.03445 =
       0.02535  -0.00868  -0.00322  -0.00378
O2     4  -0.11925   0.54197  -0.05944  11.00000   0.02302   0.04132 =
       0.03588   0.00020  -0.00711   0.00276
N1     3  -0.06770   0.46682  -0.05964  11.00000   0.01991   0.02592 =
       0.02087   0.00038  -0.00398  -0.00531
PART 2
N1A    3  -0.10709   0.46623  -0.07828  11.00000   0.03666   0.05859 =
       0.03881   0.00723  -0.00768  -0.00985
O1A    4  -0.04897   0.40628  -0.07136  11.00000   0.03307   0.03876 =
       0.03329   0.00193  -0.00167  -0.01295
O2A    4  -0.12514   0.56863  -0.04437  11.00000   0.02613   0.06235 =
       0.05046   0.00927  -0.00356   0.01105
PART 0
```

Figure 12: Addition of Parts (red).

```
FVAR 0.11828 0.54
PART 1
O1     4  -0.05620   0.36137  -0.09854  21.00000   0.03617   0.03445 =
       0.02535  -0.00868  -0.00322  -0.00378
O2     4  -0.11925   0.54197  -0.05944  21.00000   0.02302   0.04132 =
       0.03588   0.00020  -0.00711   0.00276
N1     3  -0.06770   0.46682  -0.05964  21.00000   0.01991   0.02592 =
       0.02087   0.00038  -0.00398  -0.00531
PART 2
N1A    3  -0.10709   0.46623  -0.07828 -21.00000   0.03666   0.05859 =
       0.03881   0.00723  -0.00768  -0.00985
O1A    4  -0.04897   0.40628  -0.07136 -21.00000   0.03307   0.03876 =
       0.03329   0.00193  -0.00167  -0.01295
O2A    4  -0.12514   0.56863  -0.04437 -21.00000   0.02613   0.06235 =
       0.05046   0.00927  -0.00356   0.01105
PART 0
```

Figure 13: Addition of site occupancy factors (red) and starting occupancy (blue).

In a number of structures reported in this thesis, the nitrite group is disordered over three or more parts. The 21 and -21 modelling of disorder can no longer be used and it is necessary to use the SUMP restraint. The different configurations can be 'split' into parts each with a given site occupancy factor (e.g. 21, 31, 41 etc.). In the SUMP command the first number indicates the sum of the occupancy of each part. The second number is the esd of the first number (total occupancy). The following pairs

of numbers indicate the starting occupancy (code 1 indicates for the occupancy to be freely refined) and site occupancy factor (e.g. 21, 31, 41 etc.) of the individual parts (Figure 14).[11-12]

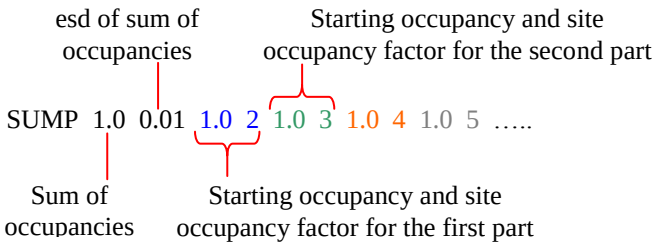

Figure 14: SUMP command.

The disordered parts in the crystal structure often have low occupancies, as a result these parts do not behave sensibly and restraints and constraints have to be introduced to improve the structural model. In a selection of structures from this thesis, the nitrite species bond lengths were restrained. The ideal bond lengths were obtained from either ground state models or from the mean bond lengths of previously studied structures from the CSD. The command to restrain bond lengths is DFIX. The first number in the DFIX command is the desired bond length, the second is the esd on the bond length, and finally the atoms associated with the bond (Figure 15). The DANG command can be used in a similar fashion as the DFIX command for 1-3 distances. Other useful commands to restrain bond lengths are the SADI and SAME.[11-12]

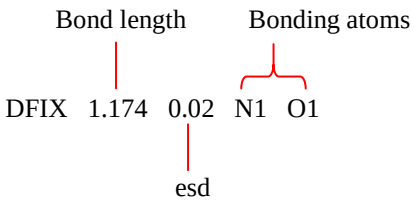

Figure 15: DFIX command.

Low occupancy atoms can have weakly defined displacement parameters. One possible way to improve the structural model is to introduce restraints on the displacement parameters. EADP, DELU and SIMU commands are used to restrain the displacement parameters. EADP set the same displacement parameters within the esd for the named atoms. DELU restrains the displacement parameters in the same direction of the named atoms. SIMU is a 'softer' restraint which makes the displacement parameters similar for the named atoms.[11-12]

2.1.14. Crystal Structure Validation

One of the most important and sometimes greatest challenges in crystallography is to validate the quality and reliability of the resulting crystal structure. There are a number of properties of the structure which needs to be thoroughly checked before publication. The *R*-factors produced in the least squares refinement can be a clear indication of the structure quality. For good quality data, a typical R_1 value should be in the range of 0.02 and 0.07. Once the best possible solution is achieved through refinement, the solution is checked to ensure:

- the refinement has converged.
- the structure is chemically sensible (e.g. ionic charge, chemical connectivity etc.)
- the displacement parameters do not have an unusual shape, are not visibly small or large compared to neighbouring atoms, and that adjacent displacements are in a sensible orientation relative to one another.
- there is no evidence of large peaks in the residual electron density structural model (Slant plane Fourier maps can clearly indicate wrongly assigned atoms or structural errors).

The Cambridge Structural Database (CSD), which is a database containing over 500,000 published crystal structures, can be used to check the parameters in the crystal structure. ConQuest is one particular program used to search the CSD. ConQuest can be used to check that the structural parameters lie within the normal distributions of previously published structures and quickly highlights dubious parameters.[13-14]

Each crystallographic parameter involved in the least squares refinement (unit cell dimensions, bond length, bond angle, torsion angle etc.) has an associated esds. (estimated standard deviations or standard uncertainties). Low value esds, which is an indication of high precision, are achieved by having a large number of reflections compared to parameters and a good correlation between observed and calculated data.[15]

A .cif file produced from the final crystal structure contains all the crystallographic information and can be computationally checked to see if there are any errors in the

data collection (resolution limit, I/sig etc.), data processing (resolution cut off, crystal system, laue group, space group, completeness etc.), and structural refinement (thermal ellipsoids, configuration, close contacts etc.). A free cif-checking application can be found on the IUCr website (http://scripts.iucr.org/cgi-bin/checkcif.pl).

2.2. References

1	Blake, S.; Bond, A.; Clegg, W.; Evans, J.; Goeta, A. E.; Howard, J. A. K.; Lehmann, C.; Main, P.; Parsons, S.; Sivia, D.; Sparkes, H. A.; Thompson, A.; Watkin, D. *X-ray Structure Analysis* **2009**.
2	Clegg, W. *Crystal Strcuture Determination*; Oxford University Press, **2004**; Vol. 60.
3	Hahn, T. *International Tables for Crystallography: Volume A Space Group Symmetry*; 5th ed.; Springer, **2005**.
4	Smart, L.; Moore, E. *Solid State Chemistry: An Introduction*; CRC Press Taylor & Francis Group, **2005**.
5	Bragg, W. *The Nobel Prize in Physics*, **1915**.
6	Patterson, A. L. *Physical Review* **1934**, *46*, 372.
7	Woolfson, M. M. *Rep. Progr. Phys.* **1971**, *34*, 369.
8	Hauptman, H.; Karle, J. *The Nobel Prize in Chemistry* **1985**.
9	Bruenger, A. T.; Kuriyan, J.; Karplus, M. *Science*, **1987**, *235*, 458.
10	Prince, E.; Boggs, T. *International Tables for Crystallography: Volume C Mathematical, Physical and Chemical Tables*; 3rd ed., **2004.**
11	Múller, P.; Herbst-Irmer, R.; Spek, A.; Schneider, T.; Sawaya, M. *Crystal Structure Refinement: A Crystallographer's Guide to SHELXL*; Oxford University Press, **2006.**
12	Sheldrick, G. M. *Acta Crystallogr., Sect. A: Found. Crystallogr.* **2008**, *A64*, 112.
13	Allen, F. H. Acta Crystallogr. Sect. B: Struct. Sci. **2002**, 58, 380.
14	Allen, F. H.; Taylor, R. *Chem. Soc. Rev.* **2004**, *33*, 463.
15	Schwarzenbach, D.; Abrahams, S. C.; Flack, H. D.; Prince, E.; Wilson, A. J. C. *Acta Crystallogr., Sect. A: Found. Crystallogr.* **1995**, *A51*, 565.

Chapter 3 – Photocrystallographic Set-Up

3.1. Background

Different light sources and wavelengths are utilised in photocrystallographic experiments depending on the system and type of investigation. The wavelength produced from the light source should be of an appropriate energy to cause electronic excitation which leads to the desired transformation. The most common types of illumination devices are broadband lamps and lasers (light amplification by the stimulated emission of radiation). This chapter discusses the advantages and disadvantages of these light sources and describes the use of LEDs (light emitting diodes) as an alternative light source for photocrystallography.

3.1.1. LASERs

Light amplification by stimulated emission of radiation (lasers) gives a low divergence and narrow monochromatic wavelength beam. Lasers consist of a gain medium which can be a gas, a liquid, a crystal, or another material e.g. a ruby crystal,[1] a yttrium aluminium garnet (YAG) crystal,[2] argon gas[3] etc. The gain medium is inside a cavity with a total reflective mirror (99.9 %) and partially reflective mirror (99 %) at either end. The atoms in the gain medium can be stimulated to an excited energy state by an electrical current or flash tube, and when electrons relax back to the ground state, light is emitted in the form of photons. When a population inversion is created with most of the atoms in the excited state, light amplification can be generated by stimulated emission, where all relaxations are triggered at the same time, giving photons with matching frequencies and phases producing a coherent beam.[4]

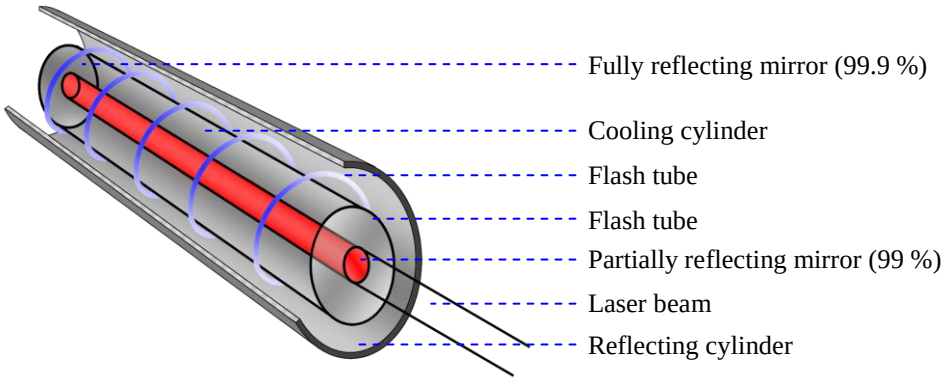

Figure 1: Simplified schematic of laser

The resulting laser wavelength is determined by the energy gap between HOMO and LUMO and by altering the gain medium, different wavelengths are achievable. There are two sorts of lasers: pulsed lasers which produce short intermittent bursts of photons with a precise time structure, and continuous wave lasers.

3.1.2. Broadband Lamps

Figure 2: 100 watt UV broadband lamp.

There are a number of different broadband lamps; the type of lamp used is governed by the nature of the experiment. In many photochemical experiments, 100 watt UV (peak max 365 nm) broadband lamps are commonly utilized. These lamps are normally mercury vapor lamps and when a voltage is supplied an arc is formed between the two electrodes through ionized mercury, emitting a range of radiation.

3.1.3. LEDs

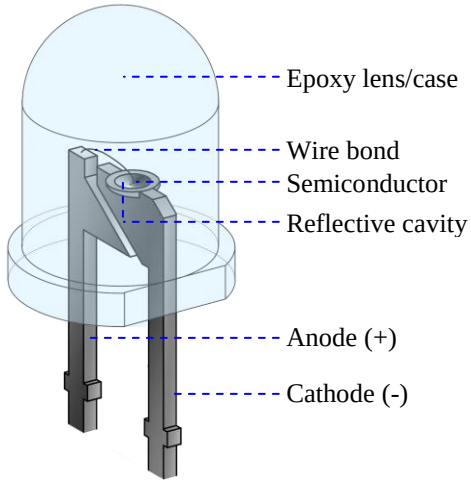

Figure 3: Simplified schematic of an LED.

Light emitting diodes (LEDs) consist of a small chip of semiconducting material doped with impurities to create a p-n junction. The small chip is connected to positive and negative terminals and when the critical voltage is applied, electrons relax from the conduction band down into the valence band emitting light in the form of photons. The colour of the LED is determined by the band gap. LEDs are commonly used in many everyday applications and are usually extremely cheap.[5-6]

3.1.4. Advantages and Disadvantages of Light Sources

One of the most significant differences between the three light sources used in photocrystallographic experiments is the intensity. LEDs and broadband lamps have a lower intensity compared to lasers; however a lower intensity source may allow greater control over the photoactivation and conversion rate. Lower intensity light sources often prevent rapid crystal decomposition, a problem which is common when using laser technology. The intensity of LEDs can easily be altered by changing the voltage or current, adapting to the system involved. However, an advantage of using a laser for problem systems which absorb photons predominantly at the surface, high intensity lasers with double the ideal wavelength can be used to excite the species using two-photon excitation, but these two photon of the same energy have to interact with the same molecule at the same time.[7]

Typically, the optimum wavelength of excitation is dependent on the compound being studied, and therefore having a light source with a wide range of wavelengths available is important. LEDs, in particular, have a diverse range of available wavelengths ranging from UV to IR, with narrow wavelength divergence. Likewise, certain lasers have tuneable wavelengths, but as they are very expensive, single wavelength lasers are more commonly used. With the use of filters, particular wavelength ranges can be selected from the spectrum of broadband lamps, but the wavelength diversity of broadband lamps tends to be greater than that of lasers and LEDs.

One major advantage of lasers is the narrow divergence beam, meaning that the laser can be situated away from the diffraction experiment and guided in to the crystal using mirrors. On the other hand, LEDs have a large incidence cone angle (~30º), and so the LEDs have to be situated in close proximity to the crystalline sample. It is also difficult to narrowly focus broadband lamps due to the physical size of the lamp and/or focusing the lenses and filters.

A major advantage of using LEDs over lasers and broadband lamps is that LEDs have almost no forward radiative heating effects which can alter the photoactivation process and/or reduce the quality of the crystallographic data.

It is important to state that, at present, lasers are the only light source capable of short lifetime excited state work due to their high intensity and the pulsed nature of the irradiation. In the future, LEDs may be implemented as they have the capabilities to be pulsed by alternating currents, but presently they lack the high intensities required to excite a detectable percentage in a short time period.

3.2. Single-Crystal Set-up

Overall, LEDs can provide an alternative light source for photocrystallographic experiments with the major benefits being: negligible forward radiative heat, low cost, diverse wavelengths and variable intensities. As discussed previously, LEDs have to be in close proximity to the crystal for the intensity to be effective. Ideally, this has to be done without affecting the diffraction experiment. In initial photocrystallographic studies, the LEDs were positioned close to the aligned crystal using a series of clamps and stands physically attached to the diffractometer base. Although successful results proved the concept of LEDs as an alternative light source, there were a number of experimental problems such as:

- Icing of the crystal was observed as the LEDs disrupted the flow of liquid nitrogen from the cryostat.
- Disruption of the data collection process with a vast number of restrictions on the machine drivers (*kappa, omega, theta and detector distance*).
- Incomplete datasets due to constrictions.
- Danger of crashing the detector or goniometer into the LED stand.

To overcome these problems, an ‘LED ring’ was designed and constructed. The LED ring allows six LEDs to surround a crystal without significantly affecting the diffraction experiment and can be positioned over the cryostats (Figure 4).

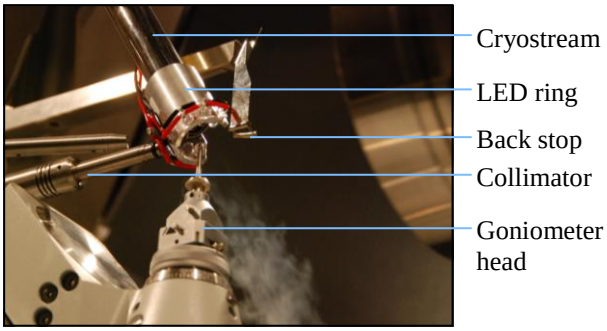

Figure 4: LED ring mounted on a diffractometer.

The LED ring consists of an aluminium cylinder with a small gap for an incoming X-ray beam (5 mm) and a large gap for diffracted X-rays (Figure 5). Around the top of the remaining section, six holes are drilled in which the LEDs can be placed. The LED ring is produced from aluminium as any localised heat produced by electrical discharge can quickly be dissipated into the aluminium metal ring and also it provides a reflective interior surface maximising the radiation from the LEDs. Additionally, aluminium as a material is cheap and its relatively soft nature allows the LED ring to be easily constructed. The LEDs are connected in parallel, so that in the case of one LED burning out, the others continue irradiating.

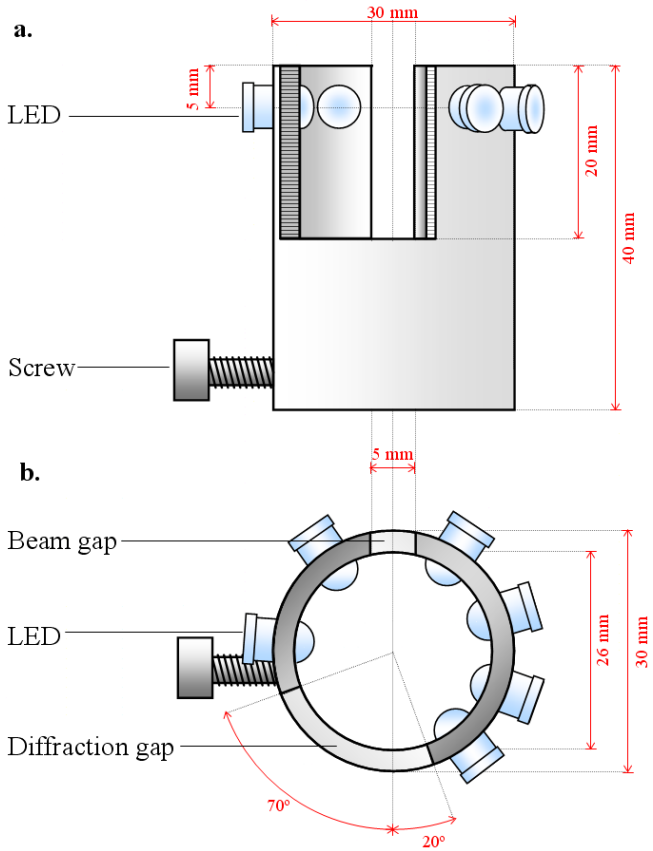

Figure 5: Schematic drawing of LED ring, a – side view and b – top view

In many of the photocrystallographic experiments reported in this thesis, the type of LED used is: 400 nm wavelength, 350 mcd intensity, 100 mW power and 30º viewing angle. The radiation that reaches the crystal is only a fraction of the intensity produced by the LED due to the distance from the source. To work out the intensity which reaches the crystal, the proportion of a crystal face is compared to the area of a 30º spherical cap 1 cm away (Figure 6).

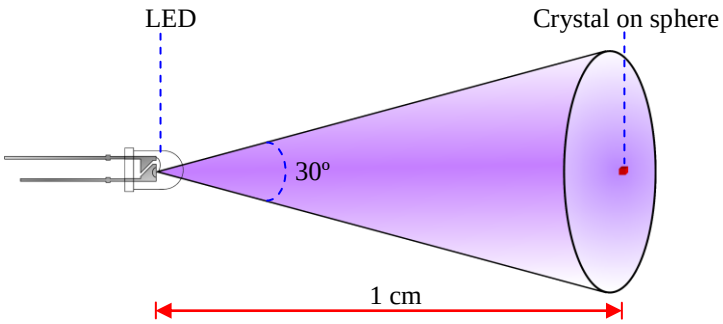

Figure 6: LED irradiation sphere with 30º viewing angle to a crystal 1 cm from the light source.

For a viewing angle of 30º (α) and a sphere radius (r) of 0.01 m, the surface area of the spherical cap is calculated using Equation 1 and Equation 2. Equation 1 gives the solid angle of $\Omega \approx 0.214$ sr, therefore the surface area which gets illuminated 1 cm from the LED is 2.141×10^{-5} m^2 (Equation 2). Assuming the crystal of interest has approximate dimensions of 0.05 × 0.05 × 0.05 mm, this gives a surface area of one of the faces as 2.5×10^{-9} m^2. Therefore the fraction of illumination produced by the LED which is reaching the crystal is 1.167×10^{-4}.

Equation 1: Solid angle (Ω) in steradian and α is the viewing angle.

$$\Omega = 2\pi\left(1-\cos\frac{\alpha}{2}\right)$$

Equation 2: Surface area of a spherical cap (m^2), Ω is the solid angle (1 sr = m^2·m^{-2}) and r is the radius.

$$S = \frac{\Omega}{r^2}$$

Equation 3: Energy of a photon (J), where h is Planck's constant (6.6261×10^{-34} Js), c is speed of light (299,792,458 m/s) and λ is wavelength (m).

$$E = \frac{hc}{\lambda}$$

For LEDs with a 100 mW output, the energy reaching the crystal using the fraction obtained above is 1.167×10^{-5} W. In one second this is 1.167×10^{-5} Ws = 1.167×10^{-5} J. As the energy reaching the crystal and the wavelength is known, it is possible to calculate the number of photons reaching the crystal per second. Using Equation 3, the energy of a photon with a 400 nm wavelength is 4.966×10^{-19} J. Therefore the

number of photons reaching the crystal per second is 2.350×10^{13} (Equation 4). The values produced are only approximations and in practice the intensity of the LED may vary throughout the 30º cone angle.

$$\text{Number of photons per second} = \frac{1.167\times10^{-6}\,J}{4.966\times10^{-19}\,J} \approx 2.350\times10^{13}\ \text{photon/sec}$$

Equation 4: Number of photons per second reaching the crystal.

Using a very basic model it is also possible to calculate the approximate efficiency of the photoreaction for the types of crystals discussed in this report. A typical compound has a unit cell volume of 2500 $Å^3$ (2.5×10^{-27} m^3), containing four complexes each with two ambidentate ligands capable of linkage isomerism. A crystal with the approximate dimensions of 0.05 × 0.05 × 0.05 mm has a total of 5×10^{13} unit cells and therefore 4×10^{14} ambidentate ligands. Using the LED ring with six 400 nm LEDs, it takes three seconds to activate every nitrite group in the crystal and if the process is a one-photon one excitation reaction, the timescale is two orders of magnitude less than the experimental results, i.e. an efficiency of less than 0.01%. There is probably a number of other factors which control the rate and efficiency of the photoreaction. A likely aspect to reduce the efficiency is the absorption of photons by surface molecules in the crystal which reduces the penetration depth. Another possibility is that the transformed ambidentate ligands also absorb photons which can cause an equilibrium between the two states.

In a photocrystallographic experiment, the LED ring is positioned over the open-flow crystal cooling device designed to fit a number of cryostats including Cryosteam Plus (Figure 4) and Cryojet HT. The LED ring does not obstruct the Cryostream flow rate and therefore no ice effects are observed. The LED ring is translated up and down on the cryostat nozzle so that the LEDs are pointing at the aligned crystal; the device can then be rotated so that X-rays can pass through the 5 mm gap to the crystal without obstruction, and then secured in place using a grub screw. Marking on the exact positioning of the LED ring can make future experiment set-up trivial.

As the LED ring is located on the cryostat, the footprint only restricts *kappa* (*ca.* ± 80), all other drives are able to move freely to their normal limits (*Phi*, *omega*, *theta* and detector distance). During data collection, the *theta* position has to be selected so

that the detector is in a position where the diffracted X-ray from the crystal is not shadowed by the LED ring casing. The LED ring was designed so that the detector is positioned with a *theta* angle similar to standard data collections, with the detector face able to collect from low to high resolution (resolution ≈ ∞ to 0.7 Å).

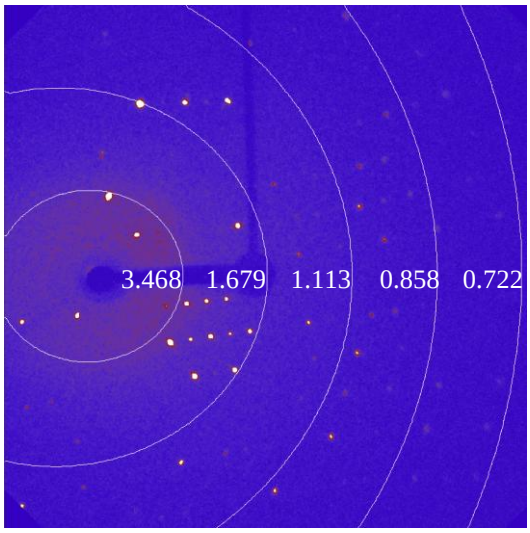

Figure 7: Oxford diffraction resolution limits for LED ring set-up.

Photocrystallographic experiments using the LED ring have been successfully performed on a number of different X-ray diffractometers. The experimental set-ups for a number of different diffractometers are shown, all other theta positions cause shading on the detector and the data can not be integrated without the use of masks:[8]

- Advanced Light Source, Lawrence Berkeley National Laboratory, Beamline 11.3.1. The ring is mounted on an Oxford Cryosystems 700 series cryostream, running on a fixed *chi* D8 diffractometer, with an Apex II detector (diameter 62 mm) and detector-sample distance of 55 mm. The *theta* position was restricted to between 10º to 40º (unshaded area), permitting a collection with a resolution greater than 0.7 Å (at wavelengths near the Zirconium edge) (Figure 8).
- In-house Nonius Kappa machine, with a CCD detector (95 mm diameter) at a distance of 50 mm, and a *theta* position is restricted to between 21º to 29º (unshaded area), permitting a collection with a resolution greater than 0.7 *Å* (using Mo-K_α radiation).
- In-house Oxford Diffraction Gemini, with an Atlas CCD (135 mm diameter) at a distance of 70 mm and a theta position of 25º, permitting a collection with a resolution up to 0.7 *Å* (using Mo-K_α radiation).

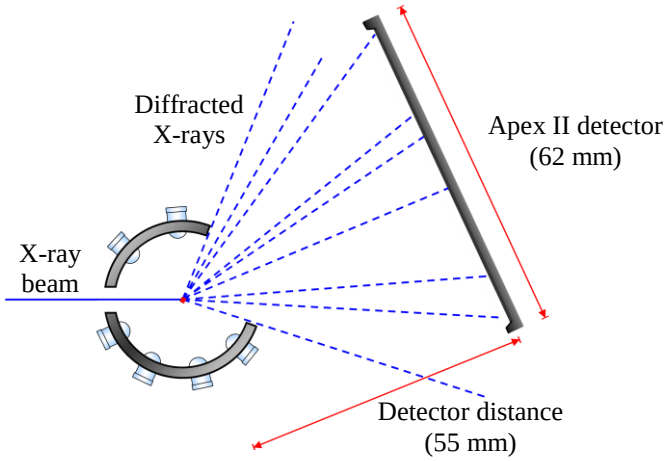

Figure 8: Schematic set-up for D8 diffractometer with an Apex II detector.

3.2.1. Single-Crystal Photocrystallographic Procedure

The crystals being studied in this report can be thermally trapped at low temperature so that the lifetime of the photoinduced state far exceeds the time scale of the crystallographic experiment and therefore can be investigated using steady state methods as previously described.

Ground State Data Collection

Firstly, the LED ring is positioned over the cryostat and the crystal is mounted and aligned. To obtain a clean ground state structure, and to ensure any metastable state is fully dispersed, the crystal is deprived of any light exposure prior to the data collection. For highly light sensitive complexes in which light used for aligning the crystal causes a transformation, the crystal can be mounted and aligned at ambient temperatures at which the metastable state has an insignificant lifetime, after which the crystal can be cooled to the desired temperature in the absence of light.

Once at the desired temperature, a high quality ground state is collected. The structure is inspected for any contamination of photoactivated species by looking for any residual electron density peaks in the structural model and the electron density map. The clean ground state structure can be used as a comparison for subsequent photoactivated data collections.

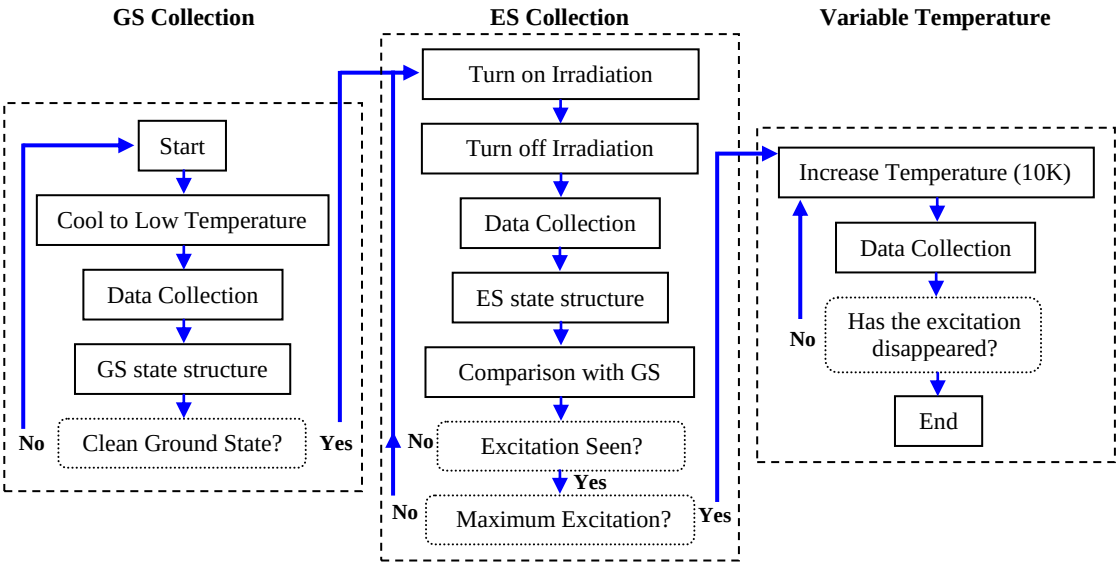

Figure 9: Experimental procedure of a steady state photocrystallographic study.

Excited-state Collection

Once the ground state structure is established, the crystal can be irradiated with the appropriate wavelength and time period depending on the system. The period of irradiation is also dependant on the crystal size. In general, smaller crystals require less irradiation and greater conversion percentages of the photoactivated species are typically observed. It is therefore beneficial to use synchrotron sources with extremely small crystals and quick data collection times. During irradiation, the crystal is continuously rotated to ensure a uniformity of radiation. It is useful to continuously collect frames which can give an indication that the photoreaction is occurring. To prevent extensive crystal decomposition during irradiation, inspecting data quality and any changes in peak shapes can give a good sign when to stop irradiation. Some smearing of peaks can be a good indication that the structure rearrangement is occurring, but extensive smearing will result in low quality data which may not give a structure solution able to reliably detect the photoactivated species. After a period of time, the irradiation is stopped to let the crystal equilibrate; a metastable data-set, is obtained which may contain a photoactivated species, obtained preferentially using the same strategy as for the ground state structure. In a number of cases, the X-ray exposure time is increased to regain resolution lost due to structural rearrangement. The loss of resolution in the photoactivated crystal can result from either a slight loss of crystallinity due to the movement within the structure (e.g. crystal shearing) or if the structure is partially excited, from an added amount of disorder reducing the uniformity in the lattice. The resulting crystal

structure is then inspected for a photoactivated species i.e. residual electron density in the structural model around the ambidentate ligand, or for changes in the electron density difference maps identifying regions where there is a reduction in electron density arising from the transformation. If the structure contains a new metastable species it is often only partially occupied and can be modelled as disorder within the structure. The occupancy of the metastable state can be used to determine the level of conversion, but it has to be noted that differences in the way that the disorder is modelled result in a variation in occupancy. A minimum of 5 % occupancy is required to be confident in the assignment of a new photo-activated species. The crystal can be further irradiated to achieve higher photo-activated conversions using the same strategy.

Variable temperature

Once the crystal has achieved the maximum conversion, either because of crystal degradation or because the crystal has reached a photostationary point, parametric variable temperature studies can shows the temperature range which the metastable state persists. This is simply done by slowly increasing the temperature in steps of 10 K, and collecting a data set at each point. Again, after each temperature increase, the crystal is allowed a period of time for the crystal to equilibrate. The resulting crystal structures are inspected after every temperature step and the parametric study is stopped when the metastable species has completely disappeared. To achieve a greater accuracy the parametric variable temperature studies can be repeated with smaller steps near the transition temperature.

3.2.2. Preliminary Experiments

Obtaining information about the crystal system prior to the photocrystallographic experiments helps increase the chances of success. Knowledge of the excitation wavelength associated with the linkage isomerism can be gained from UV/vis spectroscopy and whenever possible is coupled with TD-DFT calculations. From the knowledge obtained from the experiments, the choice of irradiation wavelength can either be at the peak maximum or at an absorption shoulder. When irradiating at the absorption maximum, in various systems, photons are absorbed by the surface molecules and therefore only low conversions are achieved. Alternatively,

irradiating at an absorption shoulder can increase penetration depth and consequently increase conversion. For work with lasers, calculating laser penetration depth for a specific wavelength of light is also to be recommended. The heat load may also need to be considered.

In UV/emission spectra (exciting with a wavelength previously gained from an UV/visible absorption experiment), a small Stokes Shift (difference between the absorption and emission peaks) suggests a loss of energy from vibrational relaxation, whereas a large Stokes Shift can be explained by a structural rearrangement, for example linkage isomerisation.

In this report, the photocrystallographic experiments on the generation of linkage isomer occur in the solid state at low temperature. Since, in the solid state there are additional intermolecular interactions, so the excitation wavelength obtained from solution and gas phase DFT calculations will be approximate and should only be used as a guide. Wherever possible the primary experiments should be carried out on the solid state material. Solid state Raman spectroscopy can be used to investigate whether a species changes under photoactivation and also gives information on the temperature dependence.

3.3. Powder Diffraction Setup

The D8 Bruker Advance with the flat plate TTK450 arm has low temperature capabilities making it possible to carry out metastable photocrystallographic experiments on powder samples. The TTK450 is modified with the inclusion of 4 LEDs (easily interchangeable) pointing towards the powder sample. A powder diffraction photocrystallographic experiment has distinct differences to its single-crystal equivalent. From single-crystal analysis, full structural information is usually obtained. From powder diffraction studies, structure solution is not trivial and in those rare cases where structure solution is possible the resulting structure will not be of sufficient quality to differentiate between conversions of disordered ambidentate coordination modes. Therefore, in the majority of cases the technique is only used as a fingerprint tool and as a comparison to simulated powder patterns

from single-crystal studies. As the photocrystallographic experiments are carried out using the TTK450 with the flat plate mode, preferred orientation is a common problem which affects the peak intensities and therefore deviations occur in comparison to predicted patterns.

The major advantage of powder diffraction photocrystallography is that crystal shearing from photoactivation does not affect the diffraction pattern, as it does in single crystal experiments. For systems where irradiation causes extensive crystal decomposition, powder photocrystallographic experiments can provide a helpful alternative.

The procedure for powder photocrystallographic experiments is comparable to single crystal routines. First, a high quality ground state is collected, this is used as a comparison tool to subsequent patterns. If a single-crystal structure of the material is available, a comparison to the predicted powder pattern can show the quality and reliability of the pattern. The powder is then irradiated, with the time and wavelength dependent on the system. During the irradiation period, powder patterns are continuously collected showing real time effects. Alternatively, a small theta range can be collected providing very quick scans. The selected theta range commonly contains peaks with significant intensity difference giving a good indication that a chemical process has occurred.

The irradiation is discontinued when the powder patterns stop altering, this is an indication that the transformation has ended or has reached a photostationary point. A second high quality metastable state powder pattern is then collected with the same strategy as for the ground state.

3.4. References

1	Maiman, T. H. *J. Opt. Soc. Am.* **1960**, *50*, 1134.
2	Geusic, J. E.; Marcos, H. M.; Vanuitert, L. G. *Appl. Phys. Lett.* **1964**, *4*, 182.
3	Bridges, W. B. *Appl. Phys. Lett.* **1964**, *4*, 128.
4	Protopapas, M.; Keitel, C. H.; Knight, P. L. *Rep. Prog. Phys.* **1997**, *60*, 389.
5	Round, H. J. *Electrical World* **1907**, *49*, 309.
6	Zheludev, N. *Nat. Phot.* **2007**, *1*, 189.
7	Denk, W.; Strickler, J.; Webb, W. *Science* **1990**, *248*, 73.
8	Brayshaw, S. K.; Knight, J. W.; Raithby, P. R.; Savarese, T. L.; Schiffers, S.; Teat, S. J.; Warren, J. E.; Warren, M. R. *J. Appl. Crystallogr.* **2010**, *43*, 337.

Chapter 4 – Search for Linkage Isomer Complexes with Nitrogen-based Auxiliary Ligands

Chapter 4 – Search for Linkage Isomer Complexes with Nitrogen-based Auxiliary Ligands

There are many complexes containing ambidentate ligands capable of undergoing linkage isomerism. Complexes of nitrite (NO_2^-), nitrosyl (NO^+) sulfur dioxide (SO_2^-), cyanide (CN^-), carbon dioxide (CO_2), thiocyanate (NCS^-) and some other more diverse ligands have been studied in the solution state. However, some potential industrial applications for these materials are in the solid state, and therefore to truly understand the mechanism of the isomerisation, and thereby improve the desirable properties of the material, the analysis must be performed in the same state. More recently photoinduced linkage isomerism has been studied using crystallography which gives an accurate model of the species in the solid state photoreaction.

In this chapter, the ambidentate *N*-bound nitro-(η^1-*N*O_2) and the *O*-bound nitrito-(η^1-*O*NO) ligands in their nickel complexes with nitrogen donor auxiliary ligands are investigated, with the aims of understanding the factors that favour the formation of either the nitro or nitrito ligands in the synthesis, and to find efficient ways of converting one isomer to the other to obtain high conversion in short time periods at temperatures approaching room temperature. Furthermore, for complexes which undergo the linkage isomerism, to examine the reasons behind the conversion percentage achieved with respect to the type of ligand, steric and electronic factors, and the crystal decomposition.

The starting point of the project was completing work on the systems $Ni(L)_2(NO_2)_2$ where L = 1-(2-aminoethyl)morpholine, 1-(2-aminoethyl)piperidine, 1-(2-aminoethyl)pyrolidine. These complexes have now been extensively reported by both Dr. T. Savarese[1] and Dr. S. Schiffers[2] and also outlined in the background literature Chapter 1 section 1.5.3.2.2. In this chapter, similar complexes following on from these successful studies are investigated. The role of the nitrogen-base auxiliary ligand in the formation of the linkage isomerism is assessed.

4.1. Search for Linkage Isomerism in Complexes with N-alkyl Substituted Ethylenediamine Auxiliary Ligands

4.1.1. *Trans*-*Bis*(ethylenediamine)di(η^1-*N*-nitro)nickel(II) - (1)

In the search for complexes which readily undergo linkage isomerism in the solid state, it is important to investigate some of the theories and explanations that have already been outlined in literature. One of the recurring ideas is that the steric properties of the auxiliary ligand play a major role in the isomerisation process.

The complex of $Ni(en)_2(\eta^1\text{-}NO_2)_2$ (en = ethylenediamine) is the smallest homolog of the series of N-alkyl substituted ethylenediamines.[3] Using the extreme situation of the smallest possible unit, comparison to successful systems can highlight the reasons and factors favouring linkage isomerism in the solid state. The findings from compound **1** can then be used as a comparison to subsequent *N*-alkyl substituted ethylenediamine ligands investigated in this chapter.

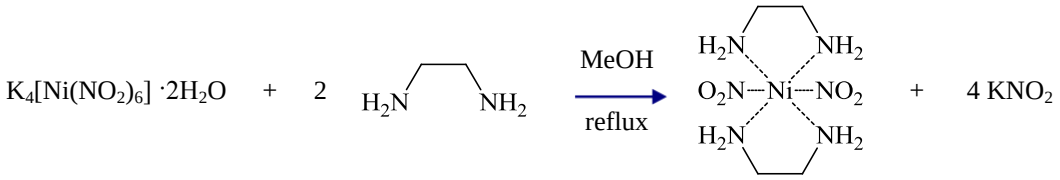

Scheme 1: Synthesis of compound **1**.

Compound **1** can be prepared using a modified procedure from the literature.[4] A freshly prepared sample of potassium hexanitritenickel(II)hydrate is treated with two equivalents of ethylenediamine (Scheme 1). Crystals of X-ray diffraction quality were grown from methanol using slow evaporation techniques. The *N*-bound nitro complex *trans*-$Ni(en)_2(\eta^1\text{-}NO_2)_2$, crystallizes in the monoclinic space group $P2_1/c$ (Figure 1). The nickel atom sits on an inversion centre and has *psudo* octahedral coordination geometry. The four nitrogen atoms of the ethylenediamine group (N2, N3) and their symmetry related atoms are situated around the equatorial plane. This complies with the trend outlined by Woike, that the nitrite group coordinates *N*-bound to the metal atom in the absence of sterically large auxiliary ligands due to intramolecular interaction.[5-7] Crystallographic data for compound **1** are presented in the experimental section

(Chapter 7). For compound **1** the nickel-nitro (Ni1-N1) bond length is 2.1152(11) Å, and the ethylenediamine Ni1-N2 and Ni1-N3 bond distances are 2.0951(12) Å and 2.1021(12) Å, respectively. Examination of the crystal structure reveals a comprehensive network of intermolecular interactions. Hydrogen bonding is observed between O1···N2 and O2···N3 with distances of 3.0053(16) and 3.165(2) respectively (Figure 3 blue dashed lines). There are also a number of close contacts O1···O2 and O2···C1 with intermolecular distance of 3.1638(20) Å and 3.1705(19) Å, respectively.

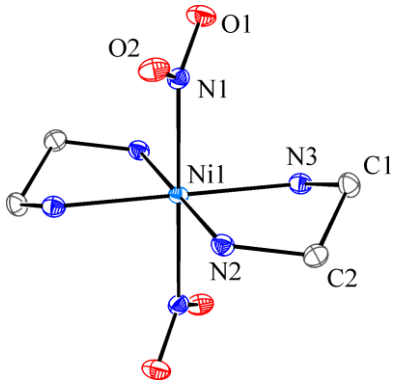

Figure 1: X-ray structure for compound **1** with 50 % ellipsoids with hydrogen atoms removed for clarity.

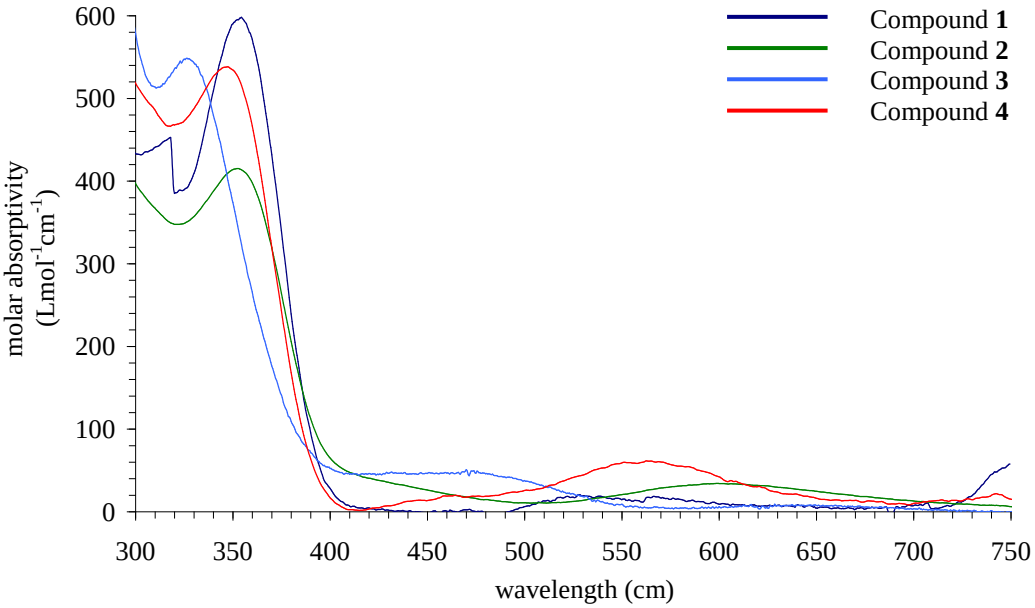

Figure 2: UV/visible absorption data for compounds **1** to **4.** UVvisible analysis was carried out in methanol with a concentration of $5x10^{-4}$ dm mol^{-1}.

The UV/visible absorption spectrum of compound **1** contains a strong absorption at 360 nm and a weaker broad absorption peaking at 550 nm (Figure 2). Single crystals of

compound **1** were investigated photocrystallographically at temperatures of 100 K and 150 K using irradiation wavelengths of UV 400 nm (UV) and 590 nm (yellow). Even after prolonged irradiation, no evidence of linkage isomerism was observed; there were no new peaks in the residual electron density in the structural model and the electron density map remained unchanged. It is likely that this result is due to the strong hydrogen bonding network present in the structure of compound **1**. For linkage isomerism to occur many hydrogen bonds would need to be broken, greatly increasing the energy requirement for the process. Additionally, there are a number of short contacts and little flexibility within the ligand, thus the movement of the nitro ambidentate ligand is restricted, again making the transformation unfavorable.

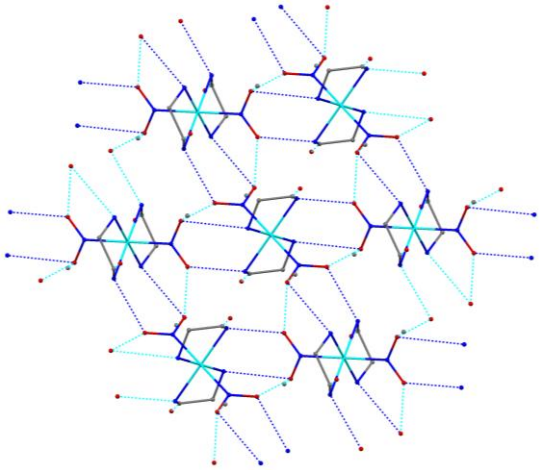

Figure 3: Hydrogen bonds (blue) and intermolecular close contracts (turquoise) for compound **1**. Hydrogen atoms have been removed for clarity.

4.1.2. *Trans-Bis*(N-isopropyl-1,2-ethylenediamine)di(η^1-*N*-nitro)nickel(II) – (2)

From the photocrystallographic investigation of compound **1,** it was suggested that incorporating a degree of flexibility into the auxiliary ligand could greatly improve the chances of a linkage isomerism transformation. Theoretically, the addition of the isopropyl group on the ethylenediamine ligand could increase flexibility and also block a potential hydrogen donating group. Additionally, for compound **2**, both nitro-(η^1-*N*O_2) and nitrito-(η^1-*O*NO) isomers are known from literature, having been prepared by

different synthetic routes,[8] this suggests that the energy difference between the two conformations may be small.

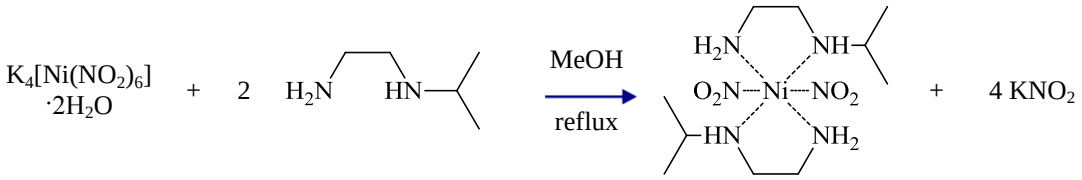

Scheme 2: Synthesis of compound **2**.

Compound **2** can be prepared using a modified literature method.[8] A solution of potassium hexanitritenickel(II)hydrate is treated with two equivalents of *iso*-propylethylenediamine (Scheme 2). Crystals of X-ray quality were grown from methanol using slow evaporation. Figure 4 shows the crystal structure of compound **2** which crystallizes in the monoclinic space group $P2_1/n$. The nickel centre has an octahedral coordination geometry, with the *iso*propylethylenediamine nitrogen atoms (N3-N6) occupying the equatorial plane. The two nitro groups assemble *trans* in the nitro-(η^1-NO_2) binding mode. The crystallographic information of compound **2** can be found in the experimental section (Chapter 7).

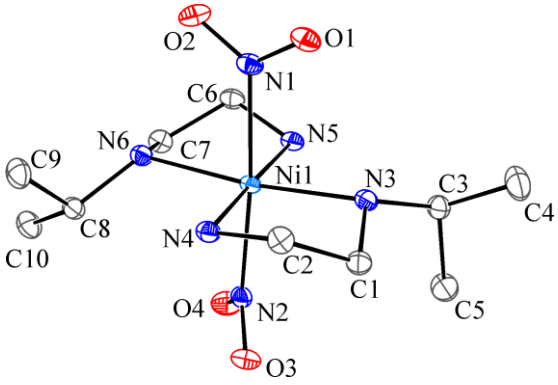

Figure 4: X-ray structure for compound **2** with 50 % ellipsoids with hydrogen atoms removed for clarity.

Compound **2** has nickel-nitrite (Ni1-N1 and Ni1-N2) bond lengths of 2.1752(11) Å and 2.1179(11) Å, respectively. The Ni1-N2 bond length is comparable to that in compound **1**, whereas Ni1-N1 two is distinctly longer. In the structure solution, if the nickel nitrite bonds are constrained to have similar values using the SADI command, the resulting structure has an increase in R_1 and new residual electron density peak arise in the electron density map, confirming the difference in bond lengths is real. The difference

in the nickel-nitro bond length is due to the packing constraints; the N2-O3-O4 nitro group has more short contacts to the neighbouring molecules compared to N1-O1-O2. The nickel to *iso*propylethylenediamine (Ni–N3, Ni-N4, Ni-N5 and Ni-N6) bond lengths are 2.1343(11), 2.1135(11), 2.0847(11) and 2.1482(11) Å, respectively. As expected the secondary amines have slightly longer metal-nitrogen bond lengths than the primary amine nitrogen atoms in the *iso*propylethylenediamine. Compound **2** contains an extensive hydrogen bonding network in the a-c plane between the nitro oxygen atoms and the unsubstituted nitrogen atom in the *iso*propylethylenediamine ligand. Hydrogen bonding occurs between O1···N4, O2···N5, O3···N5 and O4···N4 with intermolecular distances of 3.1286(15), 3.2009(15), 3.0011(15) and 2.9993(15) Å respectively (Figure 5).

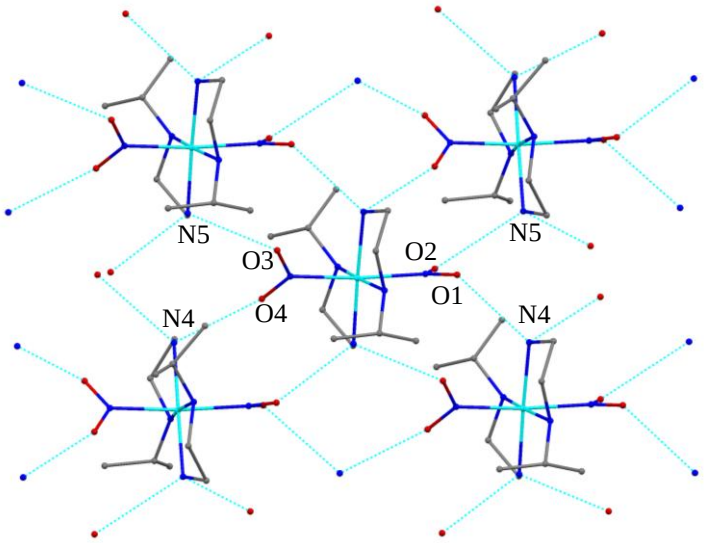

Figure 5: Hydrogen bond network for compound **2**. Hydrogen atoms have been removed for clarity.

The UV/visible absorption spectrum of compound **2** contains a strong absorption at 360 nm with a weaker shoulder peak around 420 nm. There is also a weaker broad absorption peaking at 600 nm. Therefore, in both compounds **1** and **2** the dominant peak is at 360 nm and there is also a weaker broad absorption, which for compound **2** is shifted approximately 100 nm to longer wavelength (Figure 2). Unfortunately, photocrystallographic experiments were not successful and no indication of the linkage isomerism process was apparent after prolonged irradiation periods using UV 400 nm or yellow 590 nm LEDs. The strong hydrogen bonding network could explain why the

linkage isomerism transformation did not occur. Presumably, the energy obtained by the absorption of a photon was insufficient to overcome the energy required to break hydrogen bonds.

4.1.3. (N,N,N',N'-Tetraethyldiethylenetriamine)(η^2-*O,O*-chelating nitrito)(η^1-*N*-nitro/η^1-*O*-nitrito)nickel(II) – (3)

In the search for compounds capable of high linkage isomerism conversion, altering the characteristics of auxiliary ligand can increase the chances of success. Firstly, protecting the potential hydrogen bonding amine groups, with alkyl groups can reduce the changes of strong intermolecular interactions. In small complexes, a large proportion of the overall structure changes if linkage isomerism occurs, leading to crystal decomposition. Therefore incorporation of bulky auxiliary ligands, reduces the proportion of the crystal which rearranges and maximizes the chances of retaining crystallinity. Finally, complexes which contain flexible spectator ligands can alter position to allow the rotation of the ambidentate ligand. Using these ideas, the ligand of N,N,N',N'-tetraethyldiethylenetriamine was selected as it possessed these characteristics.

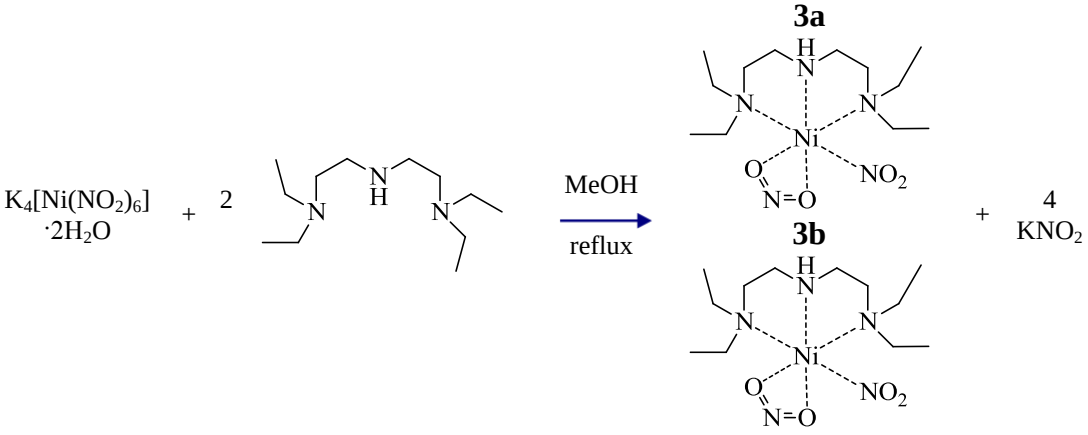

Scheme 3: Synthesis of compound **3**.

Compound **3a/b** can be prepared by treating potassium hexanitritenickel(II)hydrate with stoichiometric amounts of N,N,N',N'-tetraethyldiethylenetriamine, giving a crystalline product directly from the reaction mixture (Scheme 3). Compound **3a/b** crystallises in the orthorhombic space group $P2_12_12_1$. From a crystal which is flash cooled to 100 K, the nickel atom has a distorted octahedral geometry connected to three nitrogen atoms

of the N,N,N',N'-tetraethyldiethylenetriamine ligand, two oxygen atoms from a (O,O')-chelating nitrite group and a disordered nitrite ligand bound either in nitro-(η^1-*N*O_2) or nitrito-(η^1-*O*NO) coordination modes with occupancies of 87 % and 13 %, respectively. The difference in energy between nitro-(η^1-*N*O_2) and nitrito-(η^1-*O*NO) must be small as the structure contains both isomers. In compound **3** the nitrite group is *trans* to η^2-*O,O*-chelating nitrito group and has a metal-nitro (Ni1-N1) bond distance of 2.043(2) Å. The bond distance is shorter than observed in compounds **1** and **2**. The trialkyl-substituted nitrogen atoms in the N,N,N',N'-tetraethyldiethylenetriamine ligand have nickel-nitrogen (Ni1-N3 and Ni1-N5) bond lengths of 2.2959(12) and 2.2746(12) Å, the remaining dialkyl-substituted nitrogen has a metal-nitrogen (Ni1-N4) bond length of 2.0172(12) Å, the shorter bond-length is explained by the presence of the *trans* η^2-*O,O*-chelating nitrito group which has low *trans* influence.

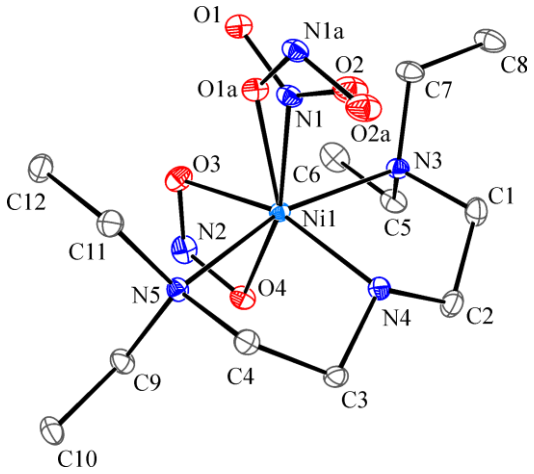

Figure 6: Ground state X-ray structure of compound **3a/b** with 30 % ellipsoids and hydrogen remove for clarity.

The only hydrogen bonding in this system is between tetraethyldiethylenetriamine N4 and the chelating nitrito group (O4) with a N4-O4 intermolecular distance of 3.080(3) Å. It is important to note that there is no hydrogen bonding between the nitro-(η^1-*N*O_2) and any other hydrogen bond acceptor atom restricting the occurrence of linkage isomers (Figure 7)

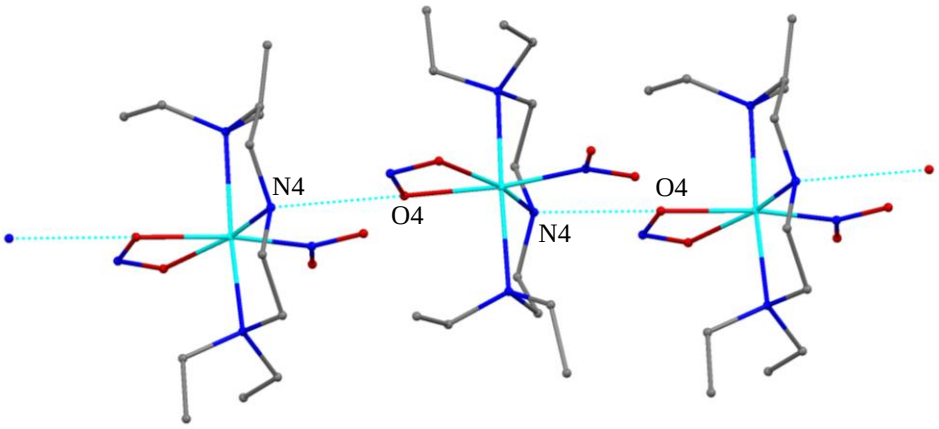

Figure 7: Hydrogen bonds network compound **3**. Hydrogen atoms have been removed for clarity.

Compound **3a/b** contains a tridentate N-alkyl substituted ethylenediamine-based auxiliary ligand and therefore has a significantly different UV-visible spectrum to complexes **1** and **2**. Compound **3a/b** has a major absorption at 330 nm shifted 30 nm compared to the complexes with bidentate nitrogen ligands. There is also a weaker broad absorption at 460 nm and a very weak broad absorption at 660 nm (Figure 2).

When a crystal of compound **3a/b** is irradiated at 100 K using six 400 nm LEDs for a period of 60 minutes (procedure outlined in chapter 3, section 2.1), a dramatic change in the nitro/nitrito ratio is observed. The nitrito-(η^1-*O*NO) occupancy increases from 13 % to 85 % in the irradiated structure. Figure 8 shows the metastable crystal structure with only the 85 % occupancy of the nitrito-(η^1-*O*NO) modelled and the nitro-(η^1-*N*O_2) isomer removed for clarity. Prolonged irradiation did not increase the nitrito-(η^1-*O*NO) occupancy, hence after 60 minutes illumination compound **3a/b** reached the photostationary point. Table 1 shows the crystallographic data of ground and metastable states.

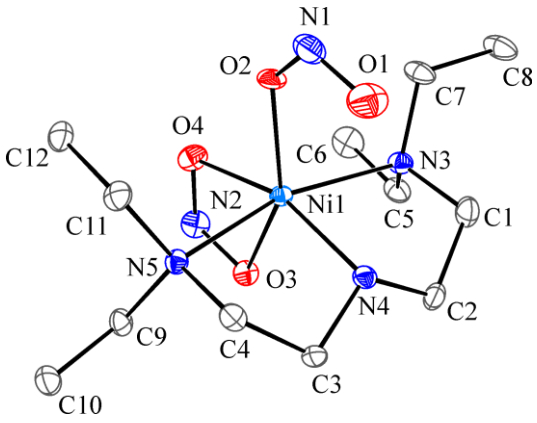

Figure 8: Metastable state X-ray structure of compound **3** with 30 % ellipsoids after irradiation at 100 K. The nitro-(η^1-NO_2) minor component and hydrogen atoms have been removed for clarity.

Table 1: Crystallographic data for ground-state and metastable-state compound **3**.

Identification code	Ground state - prr122	Metastable state - prr122a
η^1-*O*-nitrito occupancy	13 %	85 %
Empirical formula	C12 H29 N5 Ni O4	C12 H29 N5 Ni O4
Formula weight	366.11	366.11
Temperature	150(2) K	150(2) K
Wavelength	0.7107 Å	0.7107 Å
Crystal system	Orthorhombic	Orthorhombic
Space group	$P2_12_12_1$	$P2_12_12_1$
Unit cell dimensions	a = 11.340(5) Å	a = 11.4753(8) Å
	b = 11.612(5) Å	b = 11.6580(5) Å
	c = 12.835(5) Å	c = 12.8151(5) Å
Volume	1690.1(12) Å^3	1714.39(16) Å^3
Z	4	4
Crystal size	0.09 x 0.05 x 0.05 mm	0.05 x 0.05 x 0.09 mm
Theta range for data collection	2.97 to 30.64°	2.95 to 30.69°
Independent reflections	4333 [R(int) = 0.0206]	3837 [R(int) = 0.0269]
Completeness to theta	94.6 %	85.7 %
Data / restraints / parameters	4333 / 0 / 229	3837 / 4 / 220
Final R indices [I>2sigma(I)]	$R1$ = 0.0261, $wR2$ = 0.0431	$R1$ = 0.0349, $wR2$ = 0.0559
R indices (all data)	$R1$ = 0.0361, $wR2$ = 0.0441	$R1$ = 0.0546, $wR2$ = 0.0580

The unit cell remains fairly constant with the largest alteration of 1% increase in the *a*-axis, which is coincidental with the direction of nickel-nitrite bonds. Accompanying the dramatic transformation, there is slight decrease in the data quality from ground state to metastable datasets, observed in the increase in *R(int)* from 0.0206 to 0.0269.

The structural differences between the ground state and metastable state structures can clearly be observed in the electron density map (Figure 9). The map shows a decrease in electron density (red dotted lines) around the nitro-(η^1-NO_2) ground state conformation

and an increase in electron density (solid blue lines) around the new nitrito-(η^1-*O*NO) isomer.

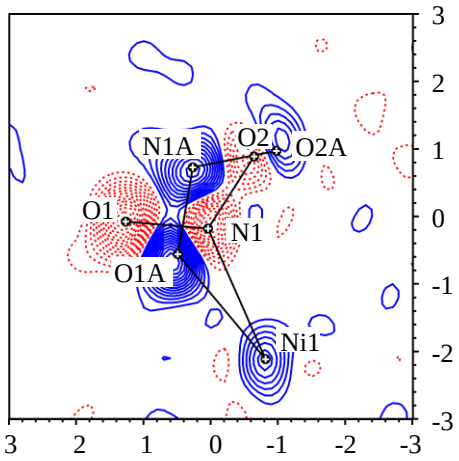

Figure 9: Slant plane Fourier map through the Ni1-N1-O1-O2 atoms, with red dotted line and blue solid line showing the decrease and increase in electron density.

The photocrystallographic results can be reliably repeated. In a second photocrystallographic investigation, after the crystal has been flash-cooled to 100 K, the ground state structure also contains both nitro-(η^1-*N*O_2) and nitrito-(η^1-*O*NO) coordination modes with occupancies of 71% and 29% respectively. The ratios between the nitrite conformations observed crystallographically after it has been flash-cooled to 100 K are dependent on the temperature during crystal picking and mounting. Irradiation of the single crystal at 100 K causes a dramatic linkage isomerism transformation. The nitrito-(η^1-*O*NO) occupancies change from 29% in the ground state structure to 82% in the irradiated metastable state structure.

Parametric variable temperature studies show that the metastable nitrito species still exist with high occupancies to 160 K. Raising the temperature to 180 K causes the nitrito-(η^1-*O*NO) species to convert back to the ground state nitro-(η^1-*N*O_2) species with an occupancy of 10 %. Interestingly, the ratio of nitro/nitrito is less than what was initially observed in the ground state structure. Raising the temperature above 180 K in expectation of completely dissipating the nitrito-(η^1-*O*NO) species produced a remarkable discovery, with the conversion to the nitrito -(η^1-*O*NO) conformation mode increasing to 23 % at 270 K, 37 % at 350 K and finally to 49 % at 370 K. This is the first complex to be crystallographically investigated showing both low temperature

light-induced and thermally-induced linkage isomerism. It is to be noted that at the elevated temperature there is an increase in displacement ellipsoids of all atoms and crystal degradation is clear, with the resolution decreasing. The crystal degradation is irreversible and does not regain crystallinity when the temperature is reduced. The high temperature analysis definitely shows an increase in the occupancy of the nitrito-(η^1-*O*NO) species, but due to high temperature effects, the precision of the structure determination is reduced. Table 3 shows the crystallographic data for photochemical and thermal studies.

Table 2: Crystallographic data for ground-state and metastable-state compound **3a/b**.

Experiment	Ground state	Metastable state after irradiation	Parametric temperature studies of metastable State after irradiation - 140 K	Parametric temperature studies of metastable State after irradiation – 160 K
η^1-*O*-nitrito occupancy	29 %	82 %	78 %	69 %
Identification code	db171	db172	db175	db176
Empirical formula	C12 H29 N5 Ni O4	C12 H29 N5 Ni O4	C12 H29 N5 Ni O4	C12 H29 N5 Ni O4
Formula weight	366.11	366.11	366.11	366.11
Temperature	100(2) K	100(2) K	140(2) K	160(2) K
Wavelength	0.68890 Å	0.68890 Å	0.68890 Å	0.68890 Å
Crystal system	Orthorhombic	Orthorhombic	Orthorhombic	Orthorhombic
Space group	$P\ 2_12_12_1$	$P\ 2_12_12_1$	$P\ 2_12_12_1$	$P\ 2_12_12_1$
Unit cell dimensions	a = 11.364(2) Å	a = 11.506(10) Å	a = 11.520(9) Å	a = 11.503(9) Å
	b = 11.628(2) Å	b = 11.686(10) Å	b = 11.702(9) Å	b = 11.702(10) Å
	c = 12.844(3) Å	c = 12.859(11) Å	c = 12.879(10) Å	c = 12.893(11) Å
Volume	1697.2(6) Å^3	1729(3) Å^3	1736(2) Å^3	1735(2) Å^3
Z	4	4	4	4
Crystal size	0.07 x 0.07 x 0.01 mm	0.07 x 0.07 x 0.01 mm	0.07 x 0.07 x 0.01 mm	0.07 x 0.07 x 0.01 mm
Theta range for data collection	2.32 to 31.66°.	2.30 to 31.52°.	2.37 to 32.80°.	2.37 to 32.83°.
Independent reflections	5841 [R(int) = 0.0697]	5913 [R(int) = 0.0766]	5815 [R(int) = 0.0715]	5988 [R(int) = 0.0832]
Completeness to theta	99.4 %	99.5 %	98.4 %	99.6 %
Data / restraints / parameters	5841 / 0 / 229	5913 / 0 / 229	5815 / 0 / 229	5988 / 0 / 229
Final R indices [I>2sigma(I)]	$R1$ = 0.0297, $wR2$ = 0.0674	$R1$ = 0.0354, $wR2$ = 0.0851	$R1$ = 0.0465, $wR2$ = 0.1144	$R1$ = 0.0416, $wR2$ = 0.1033
R indices (all data)	$R1$ = 0.0314, $wR2$ = 0.0696	$R1$ = 0.0387, $wR2$ = 0.0893	$R1$ = 0.0553, $wR2$ = 0.1263	$R1$ = 0.0477, $wR2$ = 0.1101

Table 3: Crystallographic data for ground-state and metastable-state compound **3a/b**.

Experiment	Parametric temperature studies of metastable State after irradiation – 180 K	Parametric temperature studies of metastable State after irradiation – 270 K	Parametric temperature studies of metastable State after irradiation – 350 K	Parametric temperature studies of metastable State after irradiation – 370 K
η^1-*O*-nitrito occupancy	10 %	23 %	37 %	49 %
Identification code	db179	db180	db181	db182
Empirical formula	C12 H29 N5 Ni O4	C12 H29 N5 Ni O4	C12 H29 N5 Ni O4	C12 H29 N5 Ni O4
Formula weight	366.11	366.11	366.11	366.11
Temperature	180(2) K	270(2) K	350(2) K	370(2) K
Wavelength	0.68890 Å	0.68890 Å	0.68890 Å	0.68890 Å
Crystal system	Orthorhombic	Orthorhombic	Orthorhombic	Orthorhombic
Space group	$P\ 2_12_12_1$	$P\ 2_12_12_1$	$P\ 2_12_12_1$	$P\ 2_12_12_1$
Unit cell dimensions	a = 11.353(4) Å	a = 11.421(6) Å	a = 11.466(6) Å	a = 11.455(5) Å
	b = 11.663(4) Å	b = 11.753(6) Å	b = 11.792(7) Å	b = 11.799(5) Å
	c = 12.912(5) Å	c = 12.997(7) Å	c = 13.051(7) Å	c = 13.058(5) Å
Volume	1709.8(11) Å^3	1744.7(16) Å^3	1764.6(17) Å^3	1764.8(12) Å^3
Z	4	4	4	4
Crystal size	0.07 x 0.07 x 0.01 mm	0.07 x 0.07 x 0.01 mm	0.07 x 0.07 x 0.01 mm	0.07 x 0.07 x 0.01 mm
Theta range for data collection	2.32 to 31.74°.	2.30 to 31.83°.	2.29 to 31.77°.	2.29 to 31.90°.
Independent reflections	5931 [R(int) = 0.0602]	6094 [R(int) = 0.0502]	6177 [R(int) = 0.0414]	6213 [R(int) = 0.0478]
Completeness to theta = 30.00°	99.7 %	95.4 %	99.6 %	99.8 %
Data / restraints / parameters	5931 / 4 / 220	6094 / 4 / 220	6177 / 4 / 229	6213 / 4 / 204
Final R indices [I>2sigma(I)]	$R1$ = 0.0324, $wR2$ = 0.0756	$R1$ = 0.0399, $wR2$ = 0.0982	$R1$ = 0.0427, $wR2$ = 0.1134	$R1$ = 0.0524, $wR2$ = 0.1290
R indices (all data)	$R1$ = 0.0353, $wR2$ = 0.0795	$R1$ = 0.0489, $wR2$ = 0.1071	$R1$ = 0.0536, $wR2$ = 0.1236	$R1$ = 0.0768, $wR2$ = 0.1440

To establish the equilibrium between the nitro-(η^1-*N*O_2) and nitrito-(η^1-*O*NO) conformation mode, a parametric temperature variation study can be carried out from room temperature (300 K) down to 100 K where the species can be thermally trapped. These studies were carried out in the dark without any illumination. After leaving the crystal to equilibrate for 1 h, the first data were collected at 300 K. The resulting crystal structure had a nitrito-(η^1-*O*NO) occupancy of 14%. The cryostat temperature was then reduced to 233 K and after a period of 1 h for the crystal to equilibrate, a subsequent dataset was obtained. Using the same model as the previous temperature, the nitrito-(η^1-*O*NO) occupancy had reduced to 8 %. When the crystal was reduced to 166 K, and then to 100 K, both crystal structures were absent of the nitrito-(η^1-*O*NO) species. The cryostat was increased in temperature to a starting point of 300 K and allowed to equilibrate once again; the resulting structural solution has the same occupancy of 14 % previously obtained at this temperature.

The relative energies of the nitro-(η^1-*N*O_2) and nitrito-(η^1-*O*NO) species are dependent on the temperature. At lower temperatures (100 K), the nitro-(η^1-*N*O_2) becomes the favorable species. At these temperatures, both species can be thermally trapped, and interchanging between states is not possible. If the crystal is flash-cooled to a temperature of 100 K, the crystal will contain the same equilibrium of nitro-(η^1-*N*O_2) and nitrito-(η^1-*O*NO) as at room temperature. Therefore to obtain a clean ground state absent of any nitrito-(η^1-*O*NO) species, the crystal has to be slowly decreased in temperature to allow the crystal to equilibrate. At higher temperatures, the difference in energy between the two states is relatively small and thermal energy can induce a transformation causing an equilibrium between the two species. The higher the temperature, the more stable the nitrito-(η^1-*O*NO) becomes relative to the nitro-(η^1-*N*O_2), therefore increasing the occupancy.

One possible explanation is that nitrito-(η^1-*O*NO) has more flexibility and therefore perhaps a greater entropy value compared to a complex which contains the nitro-(η^1-*N*O_2) species. At high temperatures, the entropy becomes more important and therefore at higher temperature the equilibrium will shift towards the nitrito-(η^1-*O*NO) species (Equation 1).

Equation 1: Gibbs free energy (ΔG), where ΔH is change in enthalpy, T is temperature and ΔS is the change in entropy.

$$\Delta G = \Delta H - T\Delta S$$

The equilibrium between the nitro and nitrito conformation changes with temperature. Therefore, by assessing the equilibrium at different temperatures it is possible to calculate the Gibbs free energy between the two states (Equation 2). An extensive parametric variable temperature study was carried out to obtain the Gibbs free energy between the two states.

First, a suitable crystal with adequate diffraction was glued to the fibre and mounted on the diffractometer. Before each data collection was carried out at a given temperature, a 15 minutes period is allocated for the nitro/nitrito ratio to equilibrate within the crystal. The time period for the crystal to equilibrate will vary depending on the temperature; as the temperature reduces the crystal will take longer to equilibrate. Thus at a given temperature, the data set was repeated to confirm that the occupancy of the nitro-*N*O_2 in the structural model remains constant. A parametric temperature variation study was set up from 300 K to 150 K, with a step size 30 K. Each data set was refined against the same starting structural model, with the nitro and nitrito constrained to ensure that the change in occupancy was not due to a shift in the atom positions. As predicted, the ratio of the nitro/nitrito is dependent on temperature and follows a general trend. At 300 K, the nitrito-*O*NO coordination mode has an occupancy of approximately 19 %. As the temperature reduces, the equilibrium shifts further towards the nitro species until a temperature of 150 K where a structural model with 100 % occupancy of the nitro-*N*O_2 is observed. A similar effect is observed when the temperature is increased. At 150 K, the structural model is absent of the nitrito-*O*NO species. As the temperature is raised, the occupancy of the nitrito-*O*NO species increases. The final structure was obtained at 360 K with the nitrito occupancy at approximately 27 %. Data sets at higher temperatures were of inadequate quality due to crystal decomposition. The crystallographic data of the parametric variable temperature studies can be found in Table 4.

From this collected data, it is possible to work out the Gibbs free energy between the two states (Table 4). The Gibbs free energy can be obtained from the gradient of the plot of l*n*K against -1/RT (Equation 4).

Equation 2: Gibbs free energy (ΔG), where R is the gas constant, K is the equilibrium constant enthalpy and T is temperature.

$$\Delta G = -RT\ln K$$

Equation 3: Equilibrium constant

$$K_{eq} = \text{nitrito/nitro}$$

Equation 4: Rearranged Equation 2 for plot to calculate Gibbs free energy.

$$\ln K_{eq} = (\Delta G)(-1/RT)$$

Table 4: Parametric temperature variation study for the calculation of Gibbs free energy of compound **3a/b**.

Structure	Temperature (K)	-1/RT	Nitro Occupancy	K_{eq}	$\ln(K_{eq})$
bath1202	300	-0.000401	0.814	0.229	-1.474
bath1203a	270	-0.000445	0.853	0.173	-1.755
bath1203b	270	-0.000445	0.858	0.166	-1.797
bath1204	240	-0.000501	0.891	0.122	-2.102
bath1205	240	-0.000501	0.893	0.120	-2.119
bath1206	240	-0.000501	0.893	0.120	-2.120
bath1207	210	-0.000573	0.925	0.081	-2.508
bath1208	210	-0.000573	0.926	0.079	-2.533
bath1209	180	-0.000668	0.959	0.042	-3.159
bath1210	180	-0.000668	0.959	0.043	-3.146
bath1211	150	-0.000802	0.997	0.003	-5.806
bath1212	210	-0.000573	0.919	0.088	-2.434
bath1213	270	-0.000445	0.838	0.193	-1.646
bath1214	300	-0.000401	0.789	0.267	-1.319
bath1215	330	-0.000364	0.757	0.320	-1.139
bath1216	360	-0.000334	0.735	0.360	-1.022

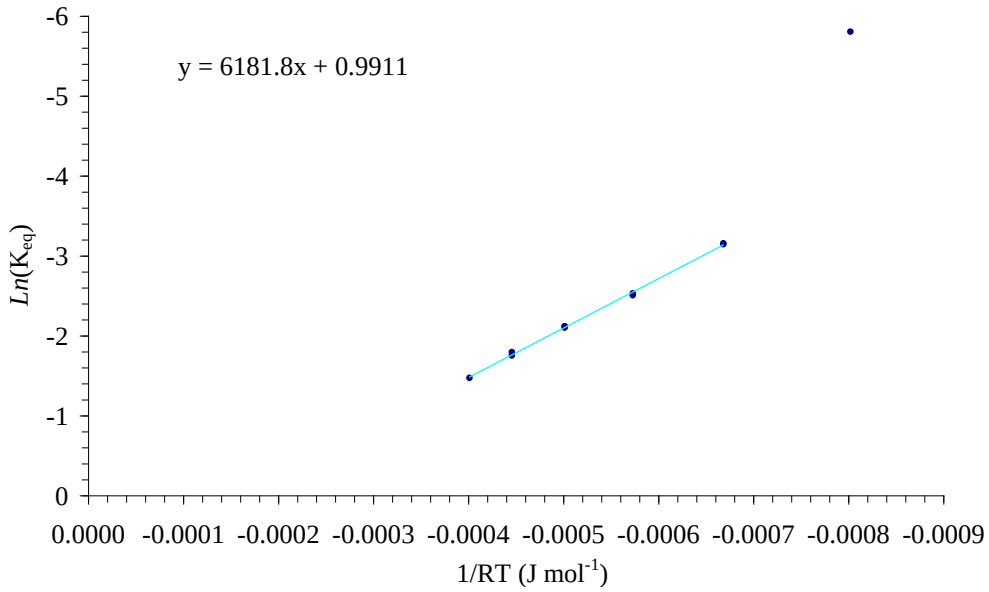

Figure 10: Graph of Gibbs free energy of parametric temperature study decreasing from 300 K to 150 K. Data point at 150 K (-1/RT = -0.000802) not included in line of best fit.

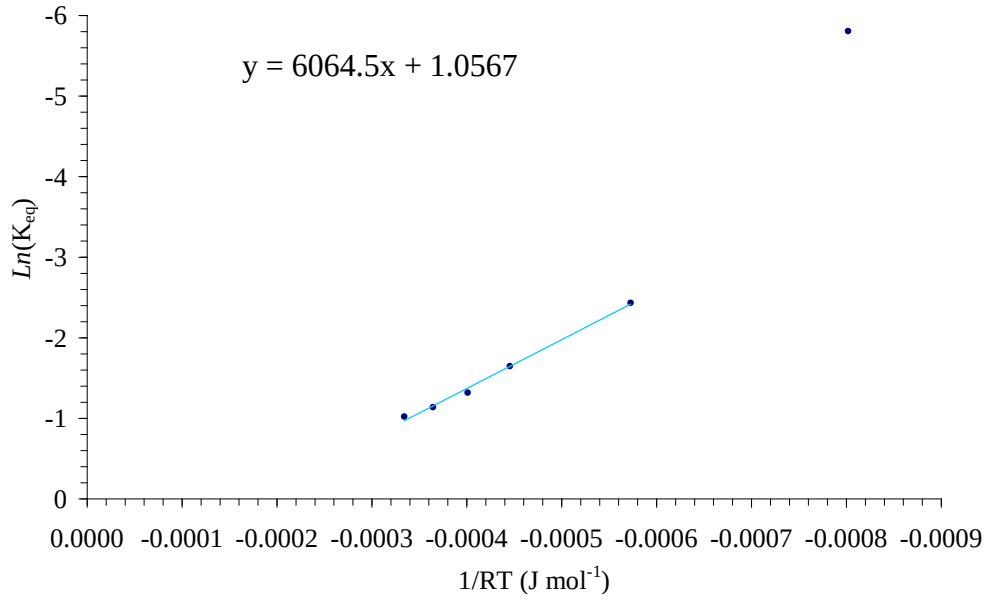

Figure 11: Graph of Gibbs free energy of parametric temperature study increasing from 150 K to 360 K. Data point at 150 K (-1/RT = -0.000802) not included in line of best fit.

The data point for a temperature at 150 K (-1/RT = -0.000802) is an anomaly from both the increase and decrease graphs and thus is not included in working out the line of best fit. The reason for this anomaly could be an error in the occupancy of the nitro in the structural model. Using the equation obtained from the line of best fit (y = 6181.8x + 0.9911) (Figure 10), the occupancy of the nitro conformation at 150 K should be 0.981

(98.1 %). The nitrito species at the low occupancy of 0.019 as this would indistinguishable at this level. Therefore, a clean ground state absent of the nitrito conformation can be obtained at approximately 100 K. The slope obtained from the graph of the forward and backward conversions is slightly different (Figure 10 and Figure 11). This could be a result of experimental error with the time taken for the crystal to fully equilibrate, or there could be a slight hysteresis in the forward and backward conversion.

From the parametric variable temperature studies, the Gibbs free energy corisponding to the activation energy between the structure of containing the nitro and nitrito states is approximately 6 KJ. The Gibbs free energy obtained is typical in value to the difference in coordination modes.

Table 5: Crystallographic data of compound **3** in parametric temperature variation study from 300 K to 100 K of compound **3**.

Identification code	bath1202 – 300 K	1203a – 270 K	bath1203b – 270 K	bath1204 – 240 K	bath1205 – 240 K
Nitro occupancy (%)	81.4 %	85.3 %	85.8 %	89.1 %	89.3 %
Empirical formula	C12 H29 N5 Ni O4	C12 H29 N5 Ni O4	C12 H29 N5 Ni O4	C12 H29 N5 Ni O4	C12 H29 N5 Ni O4
Formula weight	366.11	366.11	366.11	366.11	366.11
Temperature	300(2) K	270(2) K	270(2) K	240(2) K	240(2) K
Wavelength	0.77490 Å	0.77490 Å	0.77490 Å	0.77490 Å	0.77490 Å
Crystal system	Orthorhombic	Orthorhombic	Orthorhombic	Orthorhombic	Orthorhombic
Space group	$P\ 2_1\ 2_1\ 2_1$	$P\ 2_1\ 2_1\ 2_1$	$P\ 2_1\ 2_1\ 2_1$	$P\ 2_1\ 2_1\ 2_1$	$P\ 2_1\ 2_1\ 2_1$
Unit cell dimensions	a = 11.4362(8) Å	a = 11.4127(5) Å	a = 11.399(7) Å	a = 11.3921(7) Å	a = 11.3926(7) Å
	b = 11.7602(9) Å	b = 11.7352(5) Å	b = 11.717(7) Å	b = 11.7104(7) Å	b = 11.7109(7) Å
	c = 12.9787(9) Å	c = 12.9546(6) Å	c = 12.942(8) Å	c = 12.9326(8) Å	c = 12.9330(8) Å
Volume	1745.5(2) $Å^3$	1735.01(13) $Å^3$	1728.6(18) $Å^3$	1725.29(18) $Å^3$	1725.49(18) $Å^3$
Z	4	4	4	4	4
Crystal size	0.09 x 0.08 x 0.08 mm	0.09 x 0.08 x 0.08 mm	0.09 x 0.08 x 0.08 mm	0.09 x 0.08 x 0.08 mm	0.09 x 0.08 x 0.08 mm
Theta range for data collection	3.20 to 33.75°	3.21 to 33.58°	3.21 to 33.64°	3.22 to 33.64°	3.22 to 33.66°
Independent reflections	5351 [R(int) = 0.0916]	5268 [R(int) = 0.0901]	5274 [R(int) = 0.0937]	5263 [R(int) = 0.0884]	5270 [R(int) = 0.0904]
Completeness to theta	99.6 %	99.6 %	99.7 %	99.6 %	99.6 %
Data / restraints / parameters	5351 / 12 / 193	5268 / 12 / 193	5274 / 12 / 193	5263 / 12 / 193	5270 / 12 / 193
Final R indices [I>2sigma(I)]	R1 = 0.0543, wR2 = 0.1220	R1 = 0.0545, wR2 = 0.1275	R1 = 0.0563, wR2 = 0.1325	R1 = 0.0531, wR2 = 0.1217	R1 = 0.0535, wR2 = 0.1245
R indices (all data)	R1 = 0.0882, wR2 = 0.1401	R1 = 0.0775, wR2 = 0.1412	R1 = 0.0808, wR2 = 0.1468	R1 = 0.0727, wR2 = 0.1331	R1 = 0.0722, wR2 = 0.1359

Table 6: Crystallographic data of compound **3** in parametric temperature variation study from 300 K to 100 K of compound **3**.

Identification code	bath1206 – 240 K	bath1207 – 210 K	bath1208 – 210 K	bath1210 – 180 K	bath1211 – 150 K
Nitro occupancy	89.3 %	92.5 %	92.6 %	95.9 %	100.0 %
Empirical formula	C12 H29 N5 Ni O4	C12 H29 N5 Ni O4	C12 H29 N5 Ni O4	C12 H29 N5 Ni O4	C12 H29 N5 Ni O4
Formula weight	366.11	366.11	366.11	366.11	366.11
Temperature	240(2) K	210(2) K	210(2) K	180(2) K	180(2) K
Wavelength	0.77490 Å	0.77490 Å	0.77490 Å	0.77490 Å	0.77490 Å
Crystal system	Orthorhombic	Orthorhombic	Orthorhombic	Orthorhombic	Orthorhombic
Space group	$P\ 2_1\ 2_1\ 2_1$	$P\ 2_1\ 2_1\ 2_1$	$P\ 2_1\ 2_1\ 2_1$	$P\ 2_1\ 2_1\ 2_1$	$P\ 2_1\ 2_1\ 2_1$
Unit cell dimensions	a = 11.3941(7) Å	a = 11.3760(8) Å	a = 11.3771(8) Å	a = 11.3617(14) Å	a = 11.3522(9) Å
	b = 11.7126(7) Å	b = 11.6888(8) Å	b = 11.6905(8) Å	b = 11.6691(14) Å	b = 11.6544(9) Å
	c = 12.9355(8) Å	c = 12.9145(9) Å	c = 12.9166(9) Å	c = 12.8990(15) Å	c = 12.8827(10) Å
Volume	1726.30(18) $Å^3$	1717.3(2) $Å^3$	1718.0(2) $Å^3$	1710.2(4) $Å^3$	1704.4(2) $Å^3$
Z	4	4	4	4	4
Crystal size	0.09 x 0.08 x 0.08 mm	0.09 x 0.08 x 0.08 mm	0.09 x 0.08 x 0.08 mm	0.09 x 0.08 x 0.08 mm	0.09 x 0.08 x 0.08 mm
Theta range for data collection	3.22 to 33.63°	3.22 to 33.63°	3.22 to 33.65°	3.23 to 33.67°	3.23 to 33.67°
Independent reflections	5266 [R(int) = 0.0878]	5235 [R(int) = 0.0873]	5249 [R(int) = 0.0872]	5229 [R(int) = 0.0864]	5209 [R(int) = 0.0605]
Completeness to theta	99.6 %	99.5 %	99.6 %	99.5 %	99.4 %
Data / restraints / parameters	5266 / 12 / 193	5235 / 12 / 193	5249 / 12 / 193	5229 / 12 / 193	5209 / 0 / 199
Final R indices [I>2sigma(I)]	$R1$ = 0.0543, $wR2$ = 0.1285	$R1$ = 0.0508, $wR2$ = 0.1205	$R1$ = 0.0510, $wR2$ = 0.1210	$R1$ = 0.0510, $wR2$ = 0.1183	$R1$ = 0.0357, $wR2$ = 0.0820
R indices (all data)	$R1$ = 0.0734, $wR2$ = 0.1403	$R1$ = 0.0668, $wR2$ = 0.1302	$R1$ = 0.0667, $wR2$ = 0.1306	$R1$ = 0.0639, $wR2$ = 0.1258	$R1$ = 0.0424, $wR2$ = 0.0850

Table 7: Crystallographic data of compound **3** in parametric temperature variation study from 300 K to 100 K of compound **3**.

Identification code	bath1212	bath1213	bath1214	bath1215	bath1216
Nitro occupancy	91.9 %	83.8 %	78.9 %	75.7 %	73.5 %
Empirical formula	C12 H29 N5 Ni O4	C12 H29 N5 Ni O4	C12 H29 N5 Ni O4	C12 H29 N5 Ni O4	C12 H29 N5 Ni O4
Formula weight	366.11	366.11	366.11	366.11	366.11
Temperature	210(2) K	270(2) K	300(2) K	300(2) K	300(2) K
Wavelength	0.77490 Å	0.77490 Å	0.77490 Å	0.77490 Å	0.77490 Å
Crystal system	Orthorhombic	Orthorhombic	Orthorhombic	Orthorhombic	Orthorhombic
Space group	$P\ 2_1\ 2_1\ 2_1$	$P\ 2_1\ 2_1\ 2_1$	$P\ 2_1\ 2_1\ 2_1$	$P\ 2_1\ 2_1\ 2_1$	$P\ 2_1\ 2_1\ 2_1$
Unit cell dimensions	a = 11.3835(8) Å	a = 11.4304(7) Å	a = 11.4646(5) Å	a = 11.4910(6) Å	a = 11.529(5) Å
	b = 11.7007(8) Å	b = 11.7555(7) Å	b = 11.7918(6) Å	b = 11.8285(6) Å	b = 11.870(5) Å
	c = 12.9275(9) Å	c = 12.9808(8) Å	c = 13.0227(6) Å	c = 13.0814(7) Å	c = 13.112(5) Å
Volume	1721.9(2) $Å^3$	1744.23(18) $Å^3$	1760.52(14) $Å^3$	1778.04(16) $Å^3$	1794.3(12) $Å^3$
Z	4	4	4	4	4
Crystal size	0.09 x 0.08 x 0.08 mm	0.09 x 0.08 x 0.08 mm	0.09 x 0.08 x 0.08 mm	0.09 x 0.08 x 0.08 mm	0.09 x 0.08 x 0.08 mm
Theta range for data collection	3.22 to 33.62°	3.21 to 33.69°	3.41 to 33.94°	3.19 to 33.70°	3.18 to 33.56°
Independent reflections	5249 [R(int) = 0.0925]	5333 [R(int) = 0.0912]	5457 [R(int) = 0.0649]	5433 [R(int) = 0.0680]	5430 [R(int) = 0.0814]
Completeness to theta	99.6 %	99.6 %	99.4 %	99.7 %	99.6 %
Data / restraints / parameters	5249 / 12 / 193	5333 / 12 / 193	5457 / 12 / 193	5433 / 12 / 193	5430 / 12 / 193
Final R indices [I>2sigma(I)]	R1 = 0.0540, wR2 = 0.1279	R1 = 0.0546, wR2 = 0.1241	R1 = 0.0482, wR2 = 0.1081	R1 = 0.0494, wR2 = 0.1009	R1 = 0.0509, wR2 = 0.1062
R indices (all data)	R1 = 0.0721, wR2 = 0.1389	R1 = 0.0829, wR2 = 0.1408	R1 = 0.0842, wR2 = 0.1247	R1 = 0.1078, wR2 = 0.1212	R1 = 0.1475, wR2 = 0.1370

4.1.4. *Trans*-*Bis*((+/-)-1,2-Diaminocyclohexane)di(η^1-*N*-nitro)nickel(II) – (4)

To prepare a related system with different steric properties to the previous complexes, the auxiliary ligand of (+/-)-trans-1,2-Diaminocyclohexane was incorporated, as the steric bulk of the ligand is situated away from the centre of the complex. Compound **4** can be prepared by treating potassium hexanitritenickel(II)hydrate with two equivalents of diaminocyclohexane (Scheme 4). Small crystals of X-ray quality were grown from acetonitrile using slow evaporation techniques.

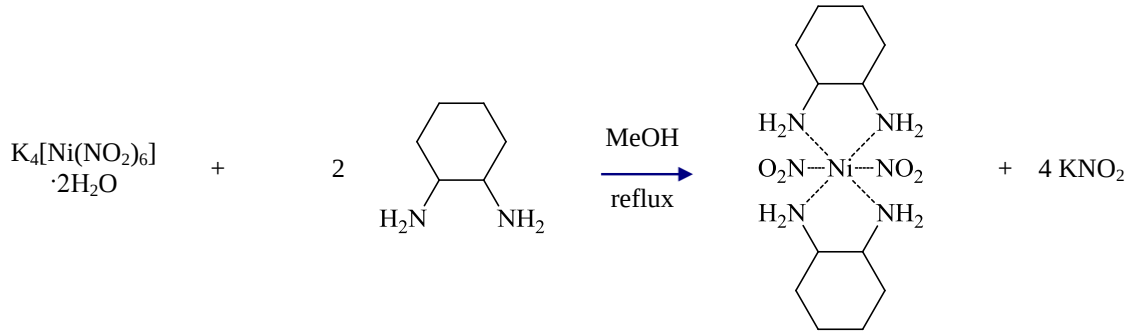

Scheme 4: Synthesis of compound **4**.

trans-Bis((+/-)-*trans*-1,2-diaminocyclohexane)bis(η^1-*N*-nitro)nickel(II) crystallises in the monoclinic space group $P2_1/c$. The nickel atom sits on an inversion centre and has an octahedral geometry. The equatorial plane is occupied by two diaminocyclohexane groups (N2, N3) and their centrosymmetrically related atoms, while the two nitro-(η^1-*N*O_2) groups assemble in the axial positions. The nickel-nitrite (Ni1-N1) bond distance is 2.1323(16) Å, and the metal-diaminocyclohexane (Ni1-N2 and Ni1-N3) bond lengths are 2.0845(17) and 2.0853(18) Å, respectively (Figure 13a).

Inspection of the of the crystal packing reveals that there is a hydrogen bonding network involving the nitro groups with N2···O2 and N3···O1 having interatomic distances of 2.967(2) and 3.159(2) Å, respectively (Figure 12).

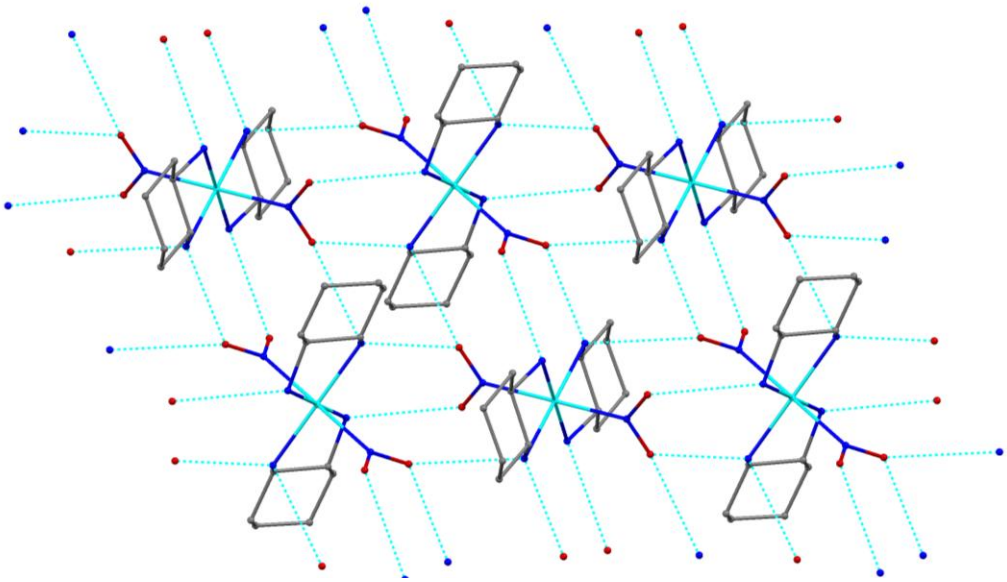

Figure 12: Hydrogen bonds network for compound **4**. Hydrogen atoms have been removed for clarity.

The UV/visible absorption spectrum of compound **4** contains a strong absorption at 360 nm (comparable to compounds **1** and **2**), and a weak broad absorption at approximately 560 nm (Figure 2). Despite the hydrogen bonding network, photocrystallographic studies were undertaken. After a high quality ground state data set was collected, the crystal was irradiated at 100 K for a period of 40 minutes using four 400 nm LEDs (irradiation procedure outlined in chapter 3, section 2.1) and the irradiation was discontinued before a second data set was collected. The resulting crystal structure had new residual electron density peaks in the Fourier map, which could be modelled as the nitrito-(η^1-*O*NO) coordination mode (Figure 13b). The single-crystal to single-crystal transformation did not proceed to completion and the new nitrito-(η^1-*O*NO) species had an occupancy of 8%, with 92% of the ground state still remaining (Figure 13b).

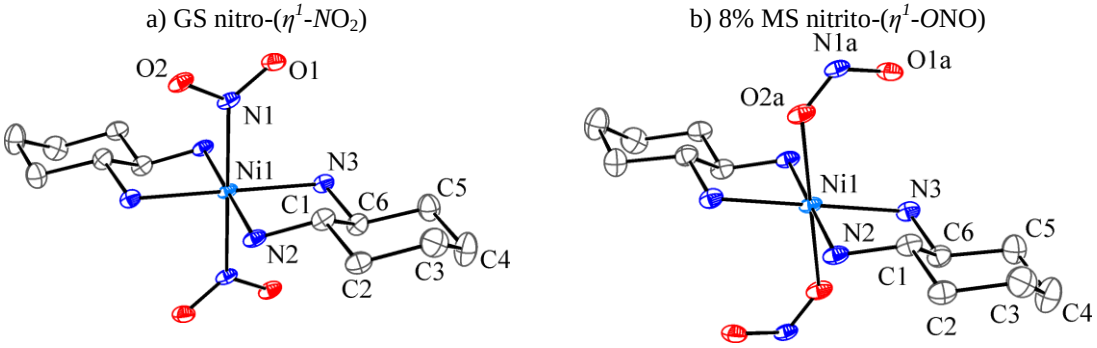

Figure 13: X-ray structure of compound **4** a) ground state structure and b) 8 % of metastable isomer. Remaining 92 % ground state is removed for clarity. 50 % ellipsoids and hydrogen's removed for clarity.

Table 8: Crystallographic data for compound **4**.

	Ground State	Metastable State
Empirical formula	C12 H28 N6 Ni O4	C12 H28 N6 Ni O4
Formula weight	379.11	379.11
Temperature	100(2) K	100(2) K
Wavelength	0.68960 Å	0.68960 Å
Crystal system	Monoclinic	Monoclinic
Space group	$P2_1/c$	$P2_1/c$
Unit cell dimensions	a = 12.1116(11) Å	a = 12.0539(11) Å
	b = 7.0730(6) Å	b = 7.1129(6) Å
	c = 10.7699(9) Å	c = 10.7487(9) Å
	β= 112.4250(10)°	β = 111.8960(10)°
Volume	852.84(13) Å^3	855.09(13) Å^3
Z	2	2
Crystal size	0.06 x 0.04 x 0.01 mm	0.06 x 0.04 x 0.01 mm
Theta range for data collection	3.55 to 29.26°	4.24 to 29.76°.
Independent reflections	2456 [R(int) = 0.0298]	2561 [R(int) = 0.0292]
Completeness to theta	98.6 %	98.0 %
Data / restraints / parameters	2456 / 0 / 106	2561 / 0 / 116
Final R indices [I>2sigma(I)]	$R1$ = 0.0416, $wR2$ = 0.1064	$R1$ = 0.0432, $wR2$ = 0.1464
R indices (all data)	$R1$ = 0.0479, $wR2$ = 0.1102	$R1$ = 0.0500, $wR2$ = 0.1523

The changes in the unit cell are insignificant (< 1%); the alteration might be more noticeable if higher linkage isomerism conversion was achieved. The electron density map of the difference between the ground state and metastable state structures clearly shows the decrease in electron density (red dotted lines) around the nitro-(η^1-NO_2) ground state conformation and an increase in electron density (solid blue lines) around the new nitrito-(η^1-ONO) isomer.

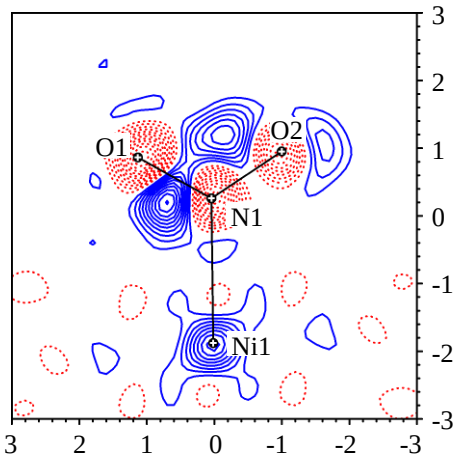

Figure 14: Slant plane Fourier map through the Ni1-N1-O1-O2 atoms in compound **4**, with red dotted line and blue solid line showing the decrease and increase in electron density.

The occupancy of the newly formed nitrito-(η^1-*O*NO) conformation did not alter with prolonged irradiation and the photostationary point was achieved after the initial 40 minutes. Repeating the experiment with different crystals gave virtually identical results. Parametric variable temperature studies (procedure outlined in chapter 3, section 2.1) revealed that the nitrito-(η^1-*O*NO) species converted back to the ground state at temperatures above 120 K.

Compound **4** illustrates that species can still undergo a linkage isomerism process even with an extensive hydrogen bonding network. This result implies that whether or not a complex undergoes linkage isomerism in the crystalline state is not limited to whether hydrogen-bonding is present or whether other intermolecular interactions have been disrupted. A plausible reason why the species does not achieve higher conversion is that the nitro and nitrito absorptions are overlapping, and irradiation at 400 nm causes both the forward process to nitrito and the reverse process to the nitro species.[9]

4.2. Search for Linkage Isomer Complexes with N-alkyl Substituted Pyridine Auxiliary Ligands

4.2.1. *Trans-Bis*(aminomethylpyridine)di(η^1-*O*-nitrito)nickel(II) – (5)

The type of auxiliary ligand can be altered to change the absorption peaks for the complex. Ideally, the absorption for the nitro and the nitrito would not overlap, possibly enabling higher conversions in photocrystallographic experiments. Pyridine-based auxiliary ligands form similar complexes to the species already investigated in this chapter, but have high absorption characteristics. Due to the insolubility of complexes containing N-alkyl substituted pyridine auxiliary ligands (compounds **5-8**), it was not possible to carry out solution-based analysis. Compound **5** was prepared using a modified procedure previously reported in literature.[10] Nickel (II) chloride hexahydrate was treated with two equivalents of aminomethylpyridine followed by an excess of potassium nitrite (Scheme 5). Single crystals of compound **5** were produced directly from the reaction mixture.

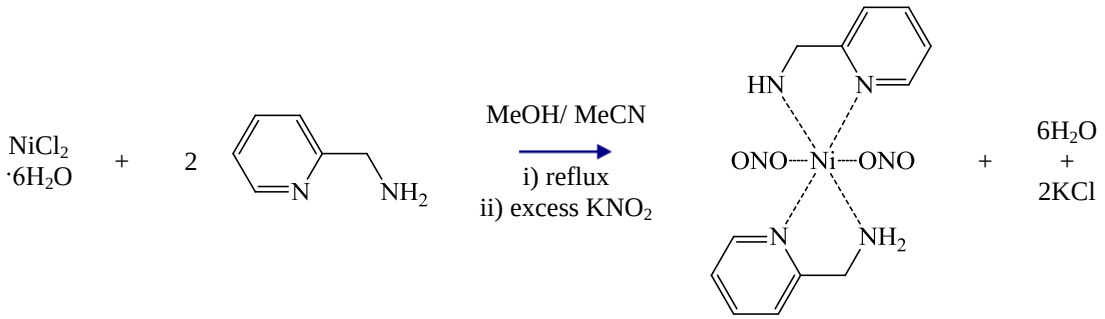

Scheme 5: Synthesis of compound **5**.

*trans-B*is(aminomethylpyridine)bis(η^1-*O*-nitrito)nickel(II) crystallizes in the monoclinic space group $P2_1/c$. The nickel centre sits on an inversion centre and has octahedral coordination geometry. Four nitrogen atoms of the aminomethylpyridine group (N2, N3) and their centrosymetric equivalent atoms occupy the equatorial plane around the metal centre. The two nitrite groups assemble *trans* in the axial position and are *O*-bound to the metal centre (Figure 15).

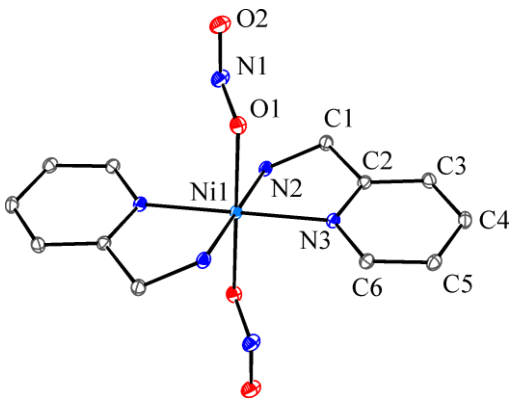

Figure 15: Ground state X-ray structure of compound **5** with 50 % ellipsoids and hydrogen atoms removed for clarity.

The structure contains the nitrito-(η^1-*O*NO) which is thought of as the energetically unfavorable species in the absence of inter- or intra-molecular interactions. From literature accounts, the nitrito-(η^1-*O*NO) species in the solid state is common for all compounds which contain bulky auxiliary ligands and exists due to the unfavorable steric interactions present in the nitro isomer.[5-7] The aminomethylpyridine is essentially a planar ligand and does not restrict the nitro-(η^1-*N*O_2) conformation, meaning that formation of a nitrito-(η^1-*O*NO) is not entirely due to these effects. Whether a complex crystallizes with either nitro-(η^1-*N*O_2) or nitrito-(η^1-*O*NO) coordination is determined by the overall energy of the system in the solid state. If the energy difference between nitro-(η^1-*N*O_2) and nitrito-(η^1-*O*NO) coordination modes is smaller than the difference between the crystal packing energies for the two isomers, the nitrito conformation will be adopted as this has the lowest overall energy.

In compound **5,** the nitrito group is *trans* to the symmetry equivalent partner with a nickel-oxygen (Ni1-O1) bond length of 2.1062(9) Å. The aminomethylpyridine ligand has nickel-nitrogen (Ni1-N2 and Ni1-N3) bond lengths of 2.0796(10) and 2.0898(10) Å, respectively. These distances are comparable to those observed in the *N*-alkyl substituent ethylenediamine auxiliary ligands.

In attempts to transform from nitrito-(η^1-*O*NO) to nitro-(η^1-*N*O_2) conformations, crystals of **5** were cooled to 100 K and irradiated for prolonged periods using six 400 nm or 460 nm LEDs. This experiment was not successful and no indication of the linkage isomerism process was evident. Examining the crystal packing reveals that the

nitro-(η^1-*N*O_2) coordination mode is not possible without having unfavorable interactions with neighbouring molecules, and for a linkage isomerism process to occur major structural reorganization would be necessary.

4.2.2. (2,2'-biquinoline)(methanol)(η^2-*O,O*-chelating-nitrito)(η^1-*O*-nitrito)nickel(II) – (6)

To prepare an analog with different steric properties to the previous complex, in the hope of altering the intermolecular interactions and therefore producing a complex containing a nitro-(η^1-*N*O_2) conformation capable of linkage isomerism, the auxiliary ligand 2,2'-biquinoline was incorporated. Compound **6** was synthesised by treating nickel (II) chloride hexahydrate with stoichiometric amounts of 2,2'-biquinoline followed by an excess of potassium nitrite (Scheme 6). Single crystals of compound **6** were produced directly from the reaction mixture and were insoluble in all common solvents, and as a result solution-based analysis could not be carried out.

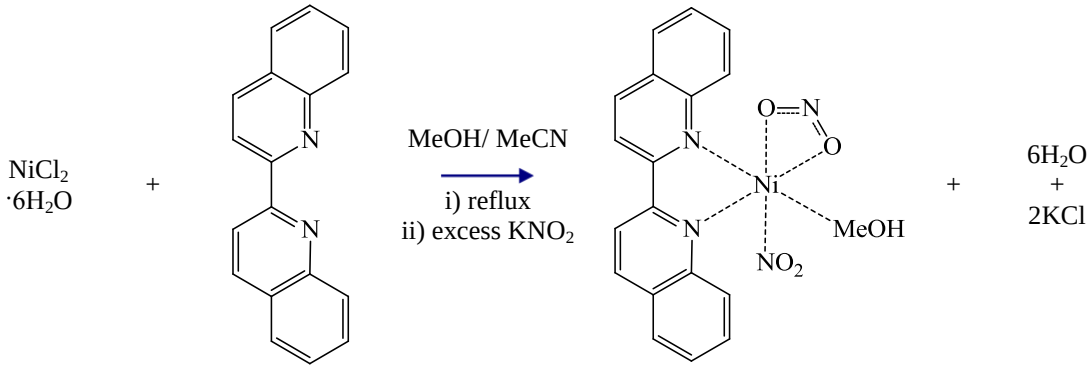

Scheme 6: Synthesis of compound **6**.

The structure of the (2,2'-biquinoline)(methanol)(η^2-*O,O*-nitrito)(η^1-*O*-nitrito)nickel(II) also contains the nitrito-(η^1-*O*NO) bound isomer, again with an essentially planar auxiliary ligand. The structure crystallizes in the monoclinic space group $P2_1/c$. The nickel metal centre has an octahedral geometry with the 2,2'-biquinoline (N3, N4) and chelating nitrito (O3, O4) occupying the equatorial plane. A η^1-*O*-nitrito (O1) and a methanol (O5) situated *trans* in the axial positions (Figure 16). Crystallographic data can be found in the experimental section, Chapter 7.

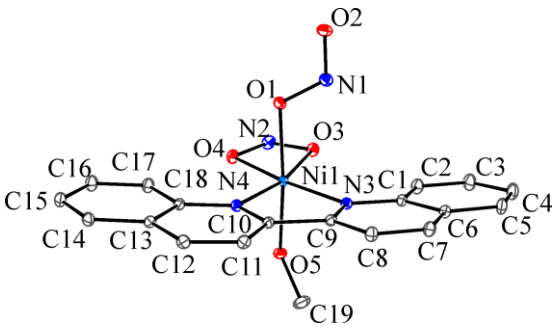

Figure 16: X-ray structure of compound **6** with 50 % ellipsoids and hydrogen atoms removed for clarity.

The nitrito-(η^1-*O*NO) is *trans* to a methanol ligand with a nickel-oxygen (Ni1-O1) bond length of 2.0315(14) Å. The metal-2,2'-biquinoline (Ni-N3 and Ni-N4) bond lengths are 2.0546(12) and 2.0743(15) Å, respectively. Inspecting the crystal packing reveals an intermolecular interaction between O1-H12 with a distance of 2.537 which restricts the nitro-(η^1-*N*O_2) conformation (Figure 17). The photocrystallographic studies were not successful. Upon irradiation at 100 K using six 400 nm or 460 nm LEDs, the crystal structure remained unchanged. In general, if the complex contains the nitrito-(η^1-*O*NO) bound isomer, then the nitro-(η^1-*N*O_2) conformation must be sterically restricted either from intramolecular of intermolecular interaction, consequently irradiation of the complex cannot convert to another nitrite isomer.

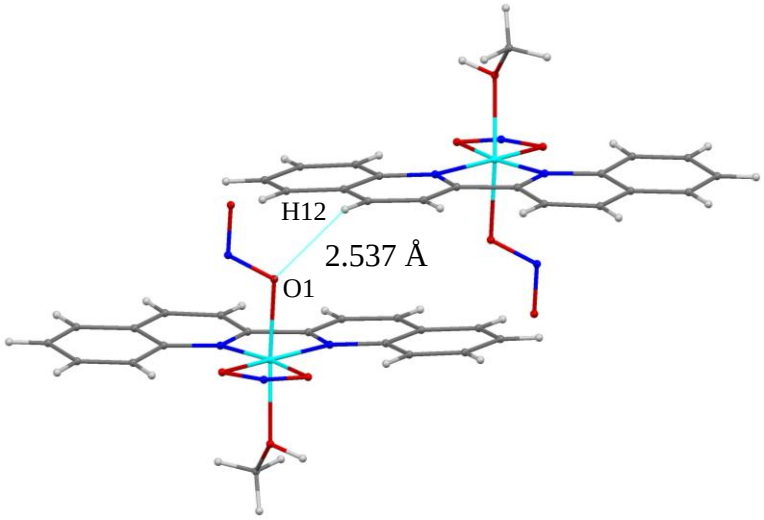

Figure 17: Intermolecular interaction restricting the formation of the nitro-(η^1-*N*O_2) coordination mode in compound **6**.

4.2.3. *Bis*(1,10-Phenanthroline)di(η^1-*N*-nitro)nickel(II) – (7)

The phenanthroline spectator ligand was used for its high absorption characteristics in the hope of increasing LMCT which could possibly enhance the linkage isomerism process.

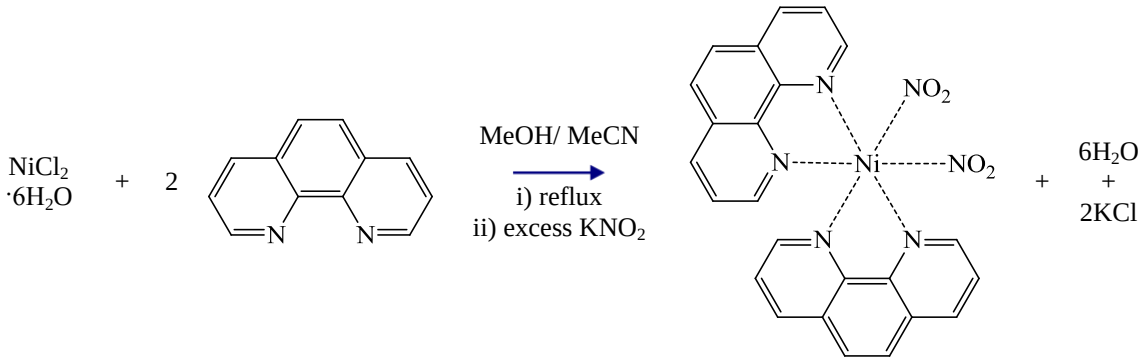

Scheme 7: Synthesis of compound **7**.

Compound **7** was prepared by treating nickel (II) chloride hexahydrate with two equivalents of 1,10-phenanthroline followed by an excess of potassium nitrite (Scheme 7). Single crystals of compound **7** were produced directly from the reaction mixture and were insoluble in all common solvents; as a result solution-based analysis could not be carried out. The crystal structure of compound **7** assembles in the *cis* arrangement and crystallizes in the triclinic space group *P*-1, with two independent *bis*(1,10-Phenanthroline)di(η^1-*N*-nitro)nickel(II) complexes in the asymmetric unit. Both nickel centres have an octahedral geometry and are surrounded by two bidentate phenanthroline ligands and two nitrite groups (Figure 18). The photocrystallographic studies were not successful. Upon irradiation at 100 K using six 400 nm or 460 nm LEDs, the crystal structure remained unchanged.

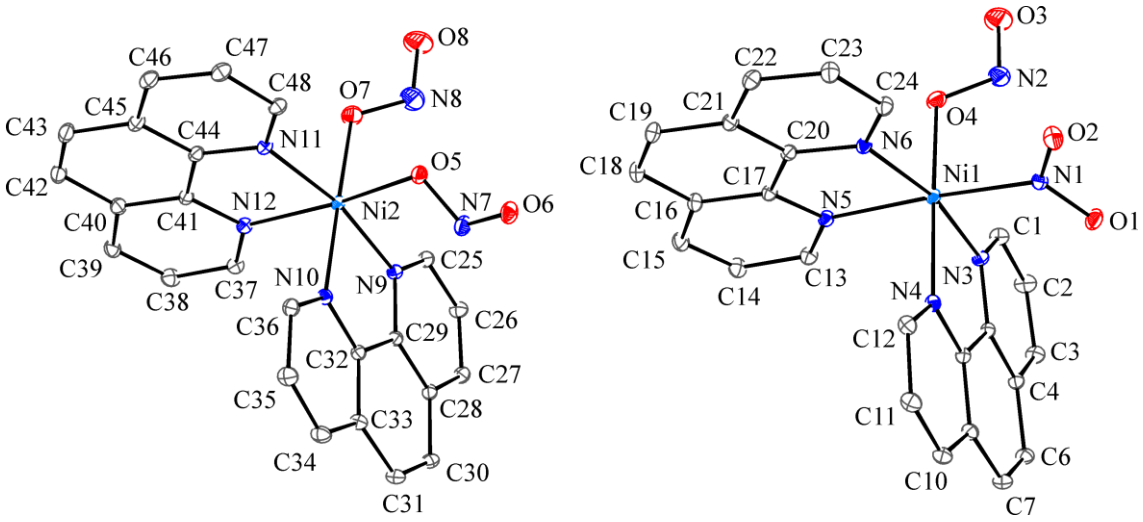

Figure 18: X-ray structure of compound **7** with 50 % ellipsoids and hydrogen atoms removed for clarity.

Interestingly, compound **7** contains both nitro-(η^1-NO_2) and nitrito-(η^1-ONO) conformations in the same cell, therefore the coordination mode of the ambidentate ligand must be determined by packing and intermolecular interactions. In this packing arrangement there is not enough void space to allow a nitro-(η^1-NO_2) coordination mode. Inspecting the nitrito-(η^1-ONO) ligands within the crystal structure, it is clear that O4-N2-O3 and O7-N8-O8 have very close contacts to hydrogen atoms in the neighbouring molecule with intermolecular distances of 2.43 and 2.62 Å, respectively.

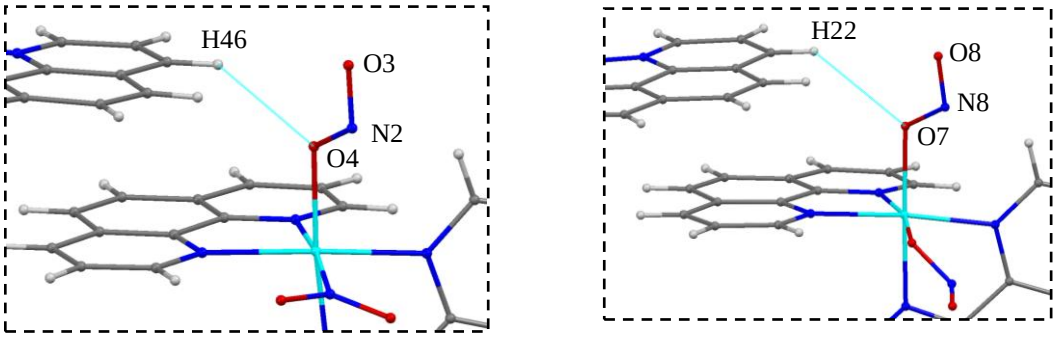

Figure 19: Close contact diagram for O4-N2-O3 and O7-N8-O8 nitrito species in compound **7**.

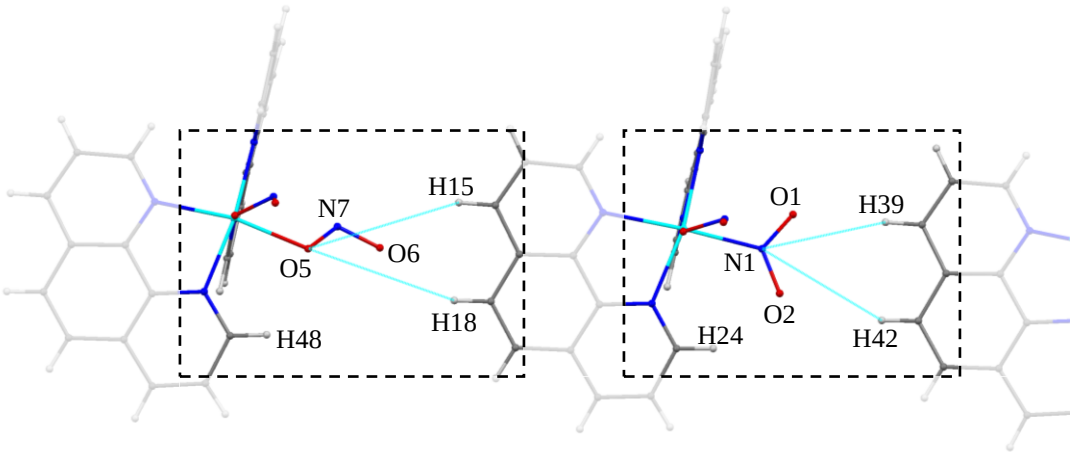

Figure 20: Close contact diagram for nitrito O5-N7-O6 and nitro N1-O1-O2 in compound **7**.

Because of the way that molecules are organized in the structure of compound **7,** the nitrito group O5-N7-O6 has no close-contacts to neighbouring molecules and there is not enough void space to contain the nitro-(η^1-*N*O_2) coordination mode without an unfavourable intramolecular interaction between O5-H48. The nitro N1-O1-O2 is in a very similar intramolecular environment to O5-N7-O6, and possesses the equivalent unfavourable intramolecular interaction (O2-H24), but still adopts the nitro-(η^1-*N*O_2) coordination mode. The intermolecular close contacts to neighbouring molecules sterically prohibits the nitrito conformation and therefore N1-O1-O2 adopts the nitro-(η^1-*N*O_2) coordination mode. The bond lengths for the nitrite ligands of the nitro-(η^1-*N*O_2) (Ni1-N1) and nitrito-(η^1-*O*NO) (Ni1-O4, Ni2-O5 and Ni2-O7) are 2.1177(15), 2.0285(14), 2.0709(13) and 2.0337(14) Å, respectively. The nickel-nitrogen bond lengths of the 1,10-phenanthroline vary depending on the group *trans* to the nitrogen. The bond length of the nitrogen atom *trans* to the nitrito-(η^1-*O*NO) (Ni1-N4) 2.0882(15) Å are shorter than the nitrogen atom *trans* to the nitro-(η^1-*N*O_2) (Ni1-N5) 2.1264(15) Å. The other two phenanthroline nitrogen atoms are *trans* each other with bond lengths (Ni1-N3 and Ni1-N6) of 2.0903(15) and 2.1134(15) Å, respectively. In the second molecule in the asymmetric unit, the nickel-nitrogen atoms in the phenanthroline ligand *trans* to a nitrito ligands have bond lengths (Ni2-N10 and Ni2-N12) of 2.0949(15) Å and 2.1117(15) Å, respectively. These distances are longer than the nickel-nitrogen

atoms in the mutually *trans* phenanthroline nitrogen atoms with bond lengths (Ni2-N9 and Ni2-N11) of 2.0781(15) Å and 2.0748(15) Å, respectively.

4.2.4. (2,2':6',2"-Terpyridine)*bis*(η^1-*N*-nitro)nickel(II)hydrate – (8)

From previous experiments described in this chapter, for photocrystallographic studies to be successful the complex must contain the nitro-(η^1-*N*O_2) isomer in the ground state crystal. In an attempt to obtain a crystal structure with a nitro-(η^1-*N*O_2) coordination mode in the same complex as N-alkyl substituted pyridine auxiliary ligands, the terpyridine ligand was incorporated.

Compound **8** was synthesised by treating nickel (II) chloride hexahydrate with stoichiometric amounts of 2,2'-biquinoline followed by an excess of potassium nitrite (Scheme 8). Crystals of compound **8** were produced directly from the reaction mixture and were insoluble in all common solvents; as a result solution-based analysis could not be carried out.

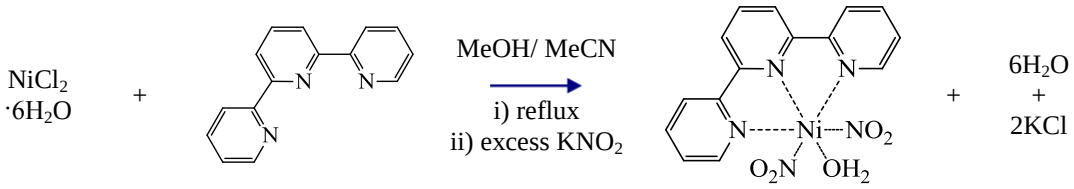

Scheme 8: Synthesis of compound **8**.

Compound **8** crystallizes in the monoclinic space group *C*2/*c*. The complex sits on a 2-fold axis bisecting the nickel centre, terpyridine and the water ligands. The nickel has an octahedral geometry, with terpyridine (N2, N3, N2') and water (O3) ligands occupying the equatorial plane, and two nitro-(η^1-*N*O_2) (N1, N1') in the axial positions (Figure 21). The crystallographic information for compound **8** can be found in the experimental chapter.

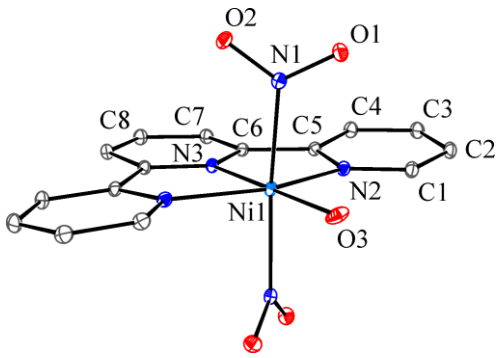

Figure 21: X-ray structure of compound **8** with 50 % ellipsoids and hydrogen atoms removed for clarity.

The nickel-nitrite (Ni1-N1) has a bond length of 2.0969(13) Å. The nickel-nitrogen *trans* to its symmetric equivalent partner in terpyridine has a bond length of 2.0043(15) Å. The nitrogen in the terpyridine *trans* to the water has a nickel-nitrogen bond length of 2.1202(13) Å. The complexes are connected through conjugated hydrogen bonding chains between nitro O2 atoms and the water O3-H3A (2.8870(14) Å) in the *a/c* axis direction (Figure 22). Photocrystallographic experiments on compound **8** were carried out at 100 K and 150 K, with a range of LEDs using the LED-ring (experimental procedure outlined in chapter 3) with wavelengths of UV 400 nm, blue 470 nm and red 660 nm. The photocrystallographic experiments were not successful and no indication of the linkage isomerism process was evident. In the structural model, there was no evidence of new residual electron density peaks and no changes to the electron density map.

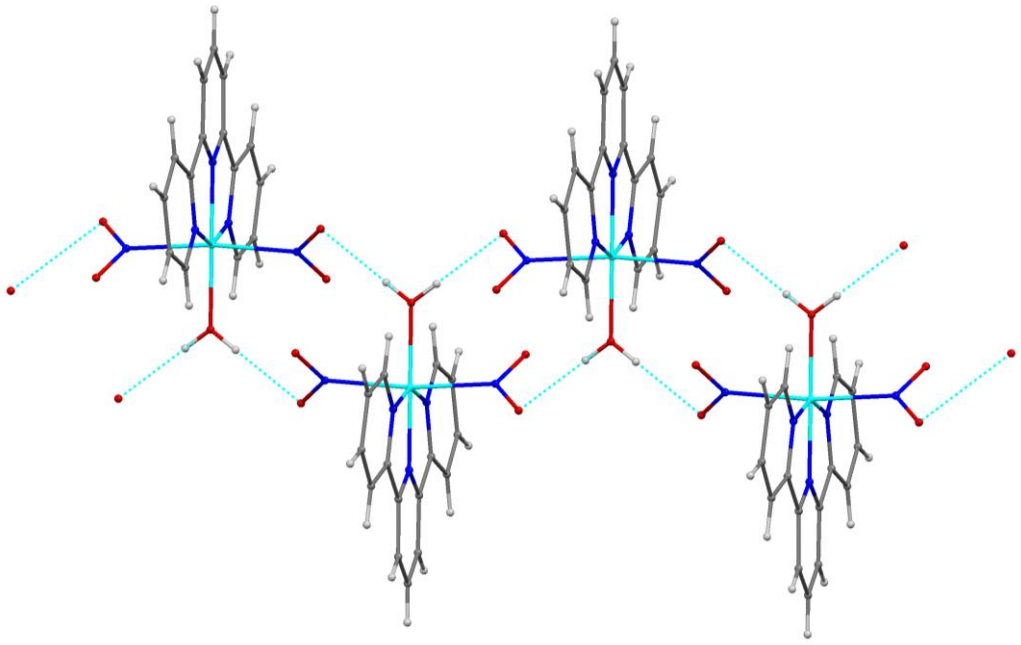

Figure 22: Hydrogen-bonding network shown by dashed lines in compound **8**.

4.3. Conclusions

Nickel complexes containing a nitrite group, with either the nitro-(η^1-*N*O_2) or nitrito-(η^1-*O*NO) coordination mode, can be synthesised, with the coordination mode being dependent upon the auxiliary ligands. Although the nitro-(η^1-*N*O_2) is the energetically favored orientation in the absence of intra/inter-molecular interactions, it appears that there is little energy difference between the two isomers. If an interaction occurs in the crystal, involving the nitrite ligand that has a more favourable energy than the difference between the preferred coordination modes, then the conformation will switch. This occurs if there is an unfavourable intramolecular interaction between the nitro-(η^1-*N*O_2) and the auxiliary ligand, commonly observed with bulky ligands. Another scenario occurs if the energy difference between nitro-(η^1-*N*O_2) and nitrito-(η^1-*O*NO) coordination modes is smaller than the difference between the crystal packing energies for the two isomers; the nitrito conformation will be adopted as this has the lowest overall energy. In a number of complexes which contain the nitro conformation, irradiation of the complexes does not cause a linkage isomerism transformation. The reason for this can not be easily attributed to one specific factor. One explanation is that

there is not enough void space for the nitro-(η^1-*N*O_2) group to swivel about its position to form the nitrito-(η^1-*O*NO) species. Strong intermolecular interactions with neighbouring molecules can prevent linkage isomerism and additional energy would be required to overcome the interaction.

The presence of hydrogen-bonding does not always prevent the isomerisation process in the solid state as observed in compound **4**.

In the crystal structure of compound **3**, there is an equilibrium between the nitro-(η^1-*N*O_2) and nitrito-(η^1-*O*NO) species. At low temperature, the nitro-(η^1-*N*O_2) form is the dominant species, but increasing the temperature causes the nitrito-(η^1-*O*NO) form to become more favorable. One explanation is that nitrito-(η^1-*O*NO) form has more degrees of freedom and therefore greater entropy compared to a complex which contains the nitro-(η^1-*N*O_2) species.

There is no evidence for a correlation between the nickel-nitrite bond lengths and linkage isomerism capabilities of the complex. Complexes with shorter nickel-nitrite bond lengths suggest greater bond strengths, but these can still readily undergo linkage isomerism.

For complexes which undergo a linkage isomerism process, it is extremely rare for the photoreaction to reach completion, and in the majority of cases less than 50 % is observed. In some experiments, the crystal decomposes due to the linkage isomerism transformation and the data reduces in quality so that a crystal structure can no longer be achieved. In all other cases, the crystal reaches a photostationary point, in which further irradiation does not change the conversion amount. The photostationary point is thought to be achieved if the irradiation wavelength converts both nitro-(η^1-*N*O_2) to nitrito-(η^1-*O*NO) and the reverse. The results obtained in this chapter are consistent with Woike's explanation that the equilibrium point is determined by the ratio of the overlapping of the two absorption bands at the specified wavelength corresponding to the metal-nitro and –nitrito antibonding orbitals.[9]

4.4. References

1	Savarese, T. L. *Photocrystallography*; University of Bath, 2010, PhD Thesis.
2	Schiffers, S. *Time Resolved Crystallographic Studies*; University of Bath, 2010, PhD Thesis.
3	Brayshaw, S. K.; Easun, T. L.; George, M. W.; Griffin, A. M. E.; Johnson, A. L.; Raithby, P. R.; Savarese, T. L.; Schiffers, S.; Warren, J. E.; Warren, M. R.; Teat, S. J. *Dalton Trans.* **2010 (accepted)**.
4	Takeuchi, A.; Sato, K.; Sone, K.; Yamada, S.; Yamasaki, K. *Inorg. Chim. Acta* **1967**, *1*, 399.
5	Goodgame, D. M.; Hitchman, M. A. *Inorg. Chem.* **1964**, *3*, 1389.
6	Elsayed, L.; Ragsdale, R. O. *Inorg. Chem.* **1967**, *6*, 1640.
7	Goodgame, D. M.; Hitchman, M. A. *Inorg. Chem.* **1965**, *4*, 721.
8	Chattopadhyay, T.; Ghosh, M.; Banerjee, A.; Banu, K. S.; Das, D.; Nethaji, M. *Transition Met. Chem.* **2007**, *32*, 531.
9	Cormary, B.; Malfant, I.; Valade, L.; Cointe, M. B. L.; Toupet, L.; Todorova, T.; Delley, B.; Schaniel, D.; Mockus, N.; Woike, T.; Fejfarova, K.; Petricek, V.; Dusek, M. *Acta Crystallogr. Sect. B: Struct. Sci.* **2009**, *65*, 787.
10	El-Sayed, L.; Ragsdale, R. O. *Inorg. Chem.* **1967**, *6*, 1640.

Chapter 5 – Linkage Isomer in Nitrate Complexes with Phosphorus-based Auxiliary Ligands

5.1. Introduction

The majority of linkage isomerism studies carried out to date have been performed on metal complexes bearing nitrogen-based auxiliary ligands. Changing to other types of auxiliary ligands may alter a number of properties, possibly giving systems which can achieve higher levels of isomerisation. Ideally, these transformations would be highly reversible without decomposition and the coordination isomers would have good thermal stability.

As well as changing the structural properties, changing the donor atom type in the auxiliary ligand can completely change the orbital configuration. Therefore the system is likely to possess different absorption characteristics and electronic transitions. From literature accounts, one of the underlying ideas as to why some systems do not undergo complete linkage isomerism transformations upon irradiation, is that there is an overlap between the absorption bands corresponding to the two forms of the linkage isomer, and so the two forms are in equilibrium.[1] Incorporation of different auxiliary ligands or using different metal centres can separate these absorption bands, hopefully producing a system capable of higher conversion. Also, using different auxiliary ligands or metal centres can alter the energies of the coordination isomers, thus changing the activation energy between the two states, and which can alter the thermal stability of the metastable species.

In the investigation into nitro and nitrito linkage isomers, a convenient way of modifying the structural and electronic environment is to alter the auxiliary ligand. In metal complexes, increasing the size of the ligand can reduce the percentage of atoms within the molecule, which move during linkage isomerism and therefore decreases crystal decomposition. Also, altering the auxiliary ligand can completely change the packing arrangement, and so the intermolecular interactions, often involving the ambidentite ligand, also change, which can affect the linkage isomerism process.

A range of phosphorus-based spectator ligands are incorporated to distinguish the important factors in the linkage isomerism process and to alter the properties of the system as discussed above.

5.2. *Cis*- Orientated Nitrate Ligands in Nickel Complexes

5.2.1. (1,2-*Bis*(diphenylphosphino)ethane)(η^1-*N*-nitro)nickel(II)chloride – 9

With the aim of developing systems which afford reversible, high percentage isomerisation between the nitro and nitrito forms, and which have good thermal stability, the 1,2-*bis*(diphenylphosphino)ethane auxiliary ligand was incorporated. (1,2-b*is*(diphenylphosphino)ethane)(η^1-*N*-nitro)nickel(II)chloride (**9**) was synthesised by treating nickel chloride with stoichiometric amounts of 1,2-*bis*(diphenylphosphino)ethane (*dppe*) and reacting the resulting compound with one equivalent of potassium nitrite (Scheme 1).

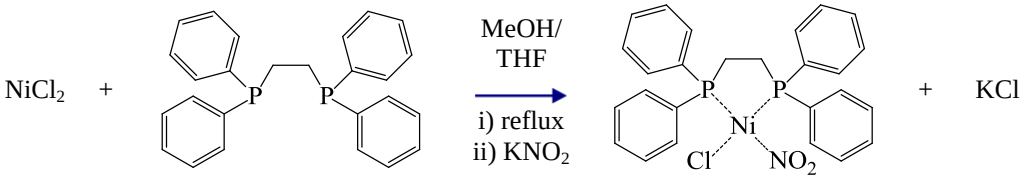

Scheme 1: Synthesis of compound **9**.

Crystals suitable for X-ray diffraction were obtained and a high quality data set was collected in the absence of light at 100 K. The resulting ground state structure crystallizes in the monoclinic space group *Cc*. The nickel centre has a square planar geometry and is bound to the bidentate *dppe* (P1 and P2) and a nitro-(η^1-*N*O_2) (N1) and chlorine (Cl1) ligand *trans* to the *dppe* ligand, with bond lengths of 2.1697(15), 2.1815(14), 1.947(4) and 2.1983(15) Å, respectively (Figure 1a).

In compound **9**, there are a number of short contacts between nitro-(η^1-*N*O_2) and the adjacent molecules. The interactions occur between O1-H22, O1-H2B, O1-H6, O2-H24 and O2-H12 which have interatomic distances of 2.4914(4), 2.6020(4), 2.6779(4), 2.4690(5) and 2.6533(5) Å, respectively. The crystal was irradiated at 100 K, using six 400 nm UV LEDs mounted 1 cm from the crystal using the LED ring.[2] After a period of approximately 70 min, the irradiation was terminated and a second metastable dataset was obtained. The resulting crystal structure had a 100 % conversion from the nitro-(η^1-*N*O_2) to nitrito-(η^1-ONO) isomer (Figure 1b). The crystal structure remains in the same space group and the unit cell dimension deviates slightly upon linkage isomerism, with the largest alteration being a 2.7 % decrease in the *a*-axis. Overlaying the crystal structure of the ground state (blue) and metastable state (turquoise) reveals there is only slight deviation, with a root mean

square (RMS) difference for non-hydrogen atoms excluding the nitrite group of 0.1 Å (Figure 2). The nickel-phosphorus distances have an approximately 1% decrease upon photoactivation with Ni1-P1, changing from 2.1697(15) to 2.145(3) Å, and Ni1-P2 changing from 2.1815(14) to 2.165(3) Å. While the crystal was irradiated, frames were continuously collected. It is evident from these X-ray images that the data quality reduced with the drop-off of resolution and slight smearing of peaks. From a combination of the reduction in crystal quality and movement within the lattice during the linkage isomerism process, the thermal ellipsoids have noticeably increased (Figure 1a-b). However, when the temperature is raised above the threshold where the nitrito isomer exist and the ground state is reverted, the displacement ellipsoids return their pre-irradation values.

a)

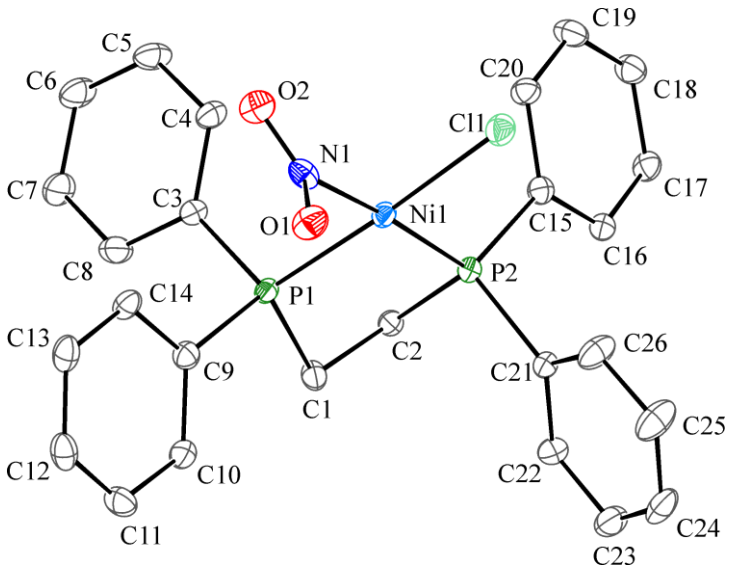

b)

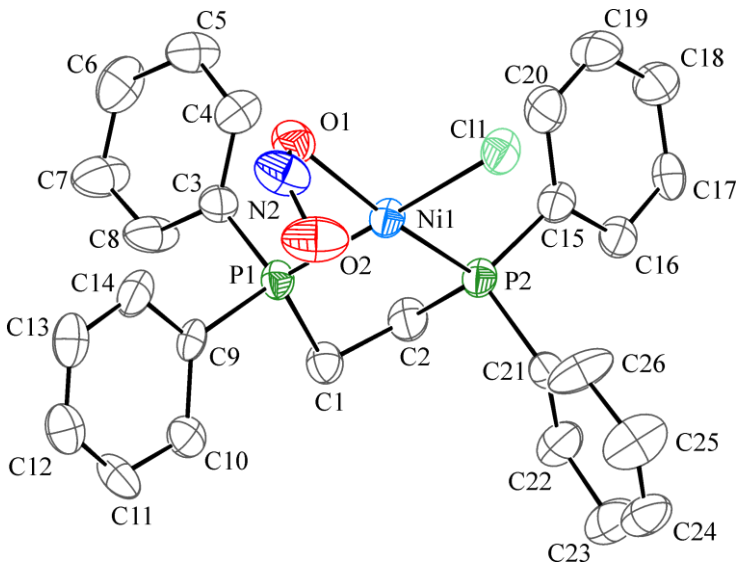

Figure 1: X-ray structure of compound **9** a) ground-state compound and b) metastable-state with thermal ellipsoids set at 30% probability and hydrogen atoms removed for clarity.

Table 1: Crystallographic data of compound **9**.

	Ground-state	Metastable-state
η^1-*O*-nitrito occupancy	0%	100%
Empirical formula	C26 H24 Cl N Ni O2 P2	C26 H24 Cl N Ni O2 P2
Formula weight	538.56	538.56
Temperature	100(2) K	100(2) K
Wavelength	0.69400 Å	0.69400 Å
Crystal system	Monoclinic	Monoclinic
Space group	*Cc*	*Cc*
Unit cell dimensions	a = 13.424(3) Å	a = 13.803(5) Å
	b = 11.430(2) Å	b = 11.283(4) Å
	c = 17.040(5) Å	c = 17.008(6) Å
	β = 110.526(2)°	β = 111.264(4)°.
Volume	2448.6(10) Å^3	2468.5(14) Å^3
Z	4	4
Crystal size	0.09 x 0.04 x 0.03 mm	0.09 x 0.04 x 0.03 mm
Theta range for data collection	2.35 to 29.76°	2.34 to 23.86°
Independent reflections	7052 [R(*int*) = 0.0630]	4012 [R(*int*) = 0.0726]
Completeness	99.2 %	99.5 %
Data / restraints / parameters	7052 / 2 / 298	4012 / 2 / 298
Final R indices [I>2sigma(I)]	R1 = 0.0562, wR2 = 0.1172	R1 = 0.0722, wR2 = 0.1555
R indices (all data)	R1 = 0.0945, wR2 = 0.1335	R1 = 0.1355, wR2 = 0.1854

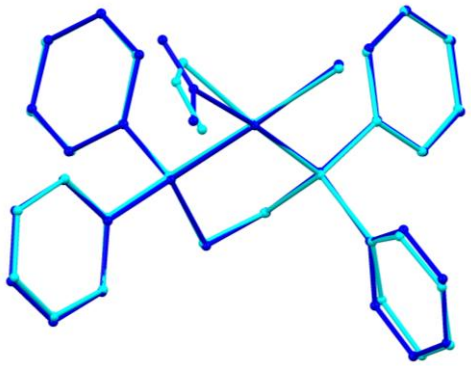

Figure 2: Compound **9** structural overlay of ground state (blue) and metastable sate (turquoise) with an RMS of 0.1 Å.

Comparing the structures before and after irradiation, the slant plane Fourier maps clearly show a reduction in electron density (red dotted lines) around the ground state nitro-(η^1-*N*O_2) and an increase in electron density (blue solid lines) for the new positions of the nitrito-(η^1-*O*NO) species (**Figure 3**). The metastable structure has increased thermal ellipsoids, and as a result, in the Slant plane Fourier map, the nitrito-(η^1-*O*NO) is not well-defined. There are also numerous other alterations in the electron density map implying that there is movement within other parts of the structure model or this could be an effect of thermal ellipsoids changes compared to the ground state structure.

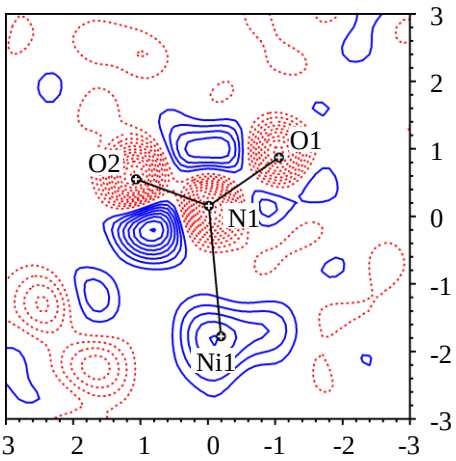

Figure 3: Compound **9** Slant plane Fourier maps of the ground state vs. the metastable state. The contour lines indicate a 0.5 increase (solid blue lines) or decrease (dotted red lines) in electron density. The zero contours are omitted for clarity.

Structural determination of the irradiated crystal as a function of temperature showed that when the temperature of the crystal was slowly heated up in 10 K steps, with data collection at each interval, the metastable species was stable between temperatures of 100 K to 160 K, and converted completely back to the ground state at 180 K. After the metastable species was fully dissipated, the temperature was reduced to 100 K and a data set was obtained revealing a crystal structure with a similar atomic position, thermal ellipsoids and data quality to that of the initial ground state. The photocrystallographic experiment can be cycled numerous times without major crystal degradation.

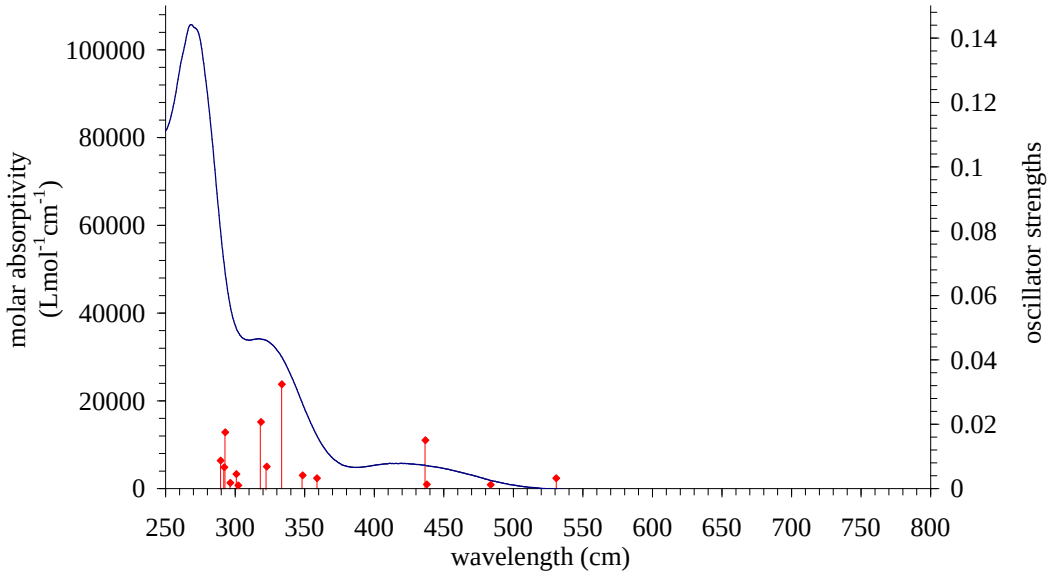

Figure 4: UV-visible spectra of and DFT calculated oscillator strengths for compound **9**.

The UV-visible spectra of compound **9** consist of a major peak at 270 nm (104895 $Lmol^{-1}cm^{-1}$), a broad absorption at approximately 315 nm (34108 $Lmol^{-1}cm^{-1}$) and a broad absorption at 420 nm (5706 $Lmol^{-1}cm^{-1}$). Gas phase density functional theory (DFT) calculations were used to find electronic transitions responsible for the linkage isomerism. DFT calculations were carried out for the first 15 electronic transitions. For compound **9**, these 15 transitions range from 530 nm to 289 nm. Beyond 289 nm to lower wavelengths, the electronic transitions were not evaluated. Even though the simulated electronic transitions were complex, there were some general trends. All electronic transitions between 530 nm to 330 nm are associated with electrons being promoted into LUMO anti-bonding orbitals with respect to the nickel-nitro bond. Figure 5 shows one common electronic transition in this range, from the HOMO (-1) bonding with respect to the metal-nitro bonds into LUMO as described above. These electronic transitions weaken the nickel-nitrate bond and could explain the occurrence of the linkage-isomerism.

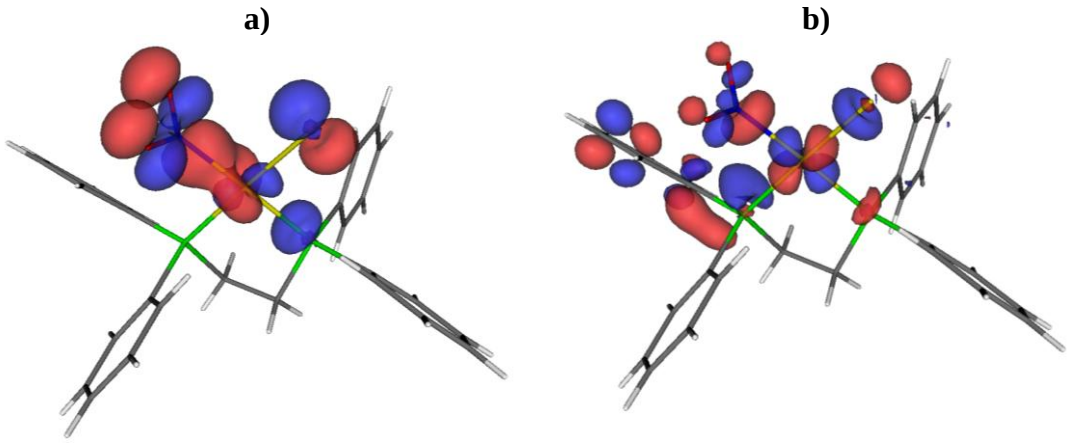

Figure 5: Molecular orbitals of compound **9** associated with the 306 nm transition from a) bonding nickel($d_{x^2-y^2}$)-NO_2 orbitals (HOMO -1) to b) antibonding nickel($d_{x^2-y^2}$)-NO_2 orbitals (LUMO).

Solid-state Raman spectroscopy was carried out in collaboration with Dr. Timothy Easun and Prof. Michael George at the University of Nottingham. A crystal of compound **9** was cooled to 115 K on the variable-temperature stage and a ground state spectrum was obtained (Figure 6). The spectra contains a $\delta(NO_2)$ band at 813 cm^{-1} and the υ(N-O) stretches at 1333 cm^{-1}, typical of the nitro conformation; other bands were too weak to characterize easily. The crystal was then irradiated using the visible light from the illuminator on the confocal Raman microscope for a period of 10 min, after which a metastable spectrum was obtained. The $\delta(NO_2)$ deformation shifts 14 cm^{-1} to 829 cm^{-1} and the υ(N-O) stretches shifts by 71 cm^{-1} to 1404 cm^{-1}.

These shifts to higher energies are a clear indication of the complete conversion to the nitrito conformation. On the photoactivated crystal, parametric variable temperature studies were carried out from 120 K to 300 K with Raman spectra being recorded every 10 K. As the temperature is raised, the $\delta(NO_2)$ band at 829 cm^{-1} from the nitrito conformation decreases, with the full retention of the 813 cm^{-1} band at 180 K (Figure 7). These results are consistent with single-crystal X-ray diffraction results. Slight discrepancies can be explained by the localized heating effects caused by the probing laser.[3-5]

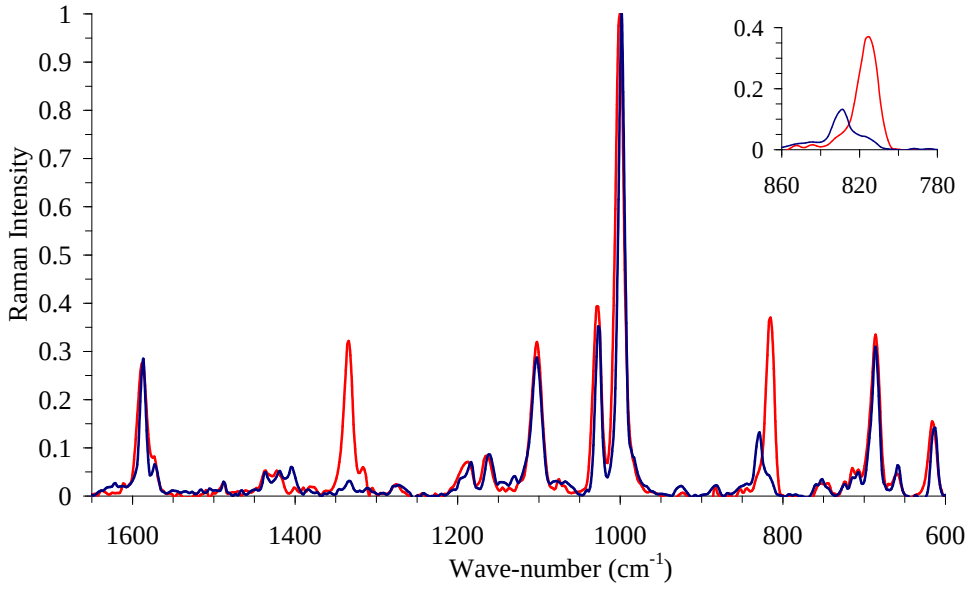

Figure 6: Solid-state Raman spectra at 115 K of before (blue) and after (red) photolysis of compound **9**. Inset expansion of the $\delta(NO_2)$ spectral region from 860 to 780 cm^{-1}.

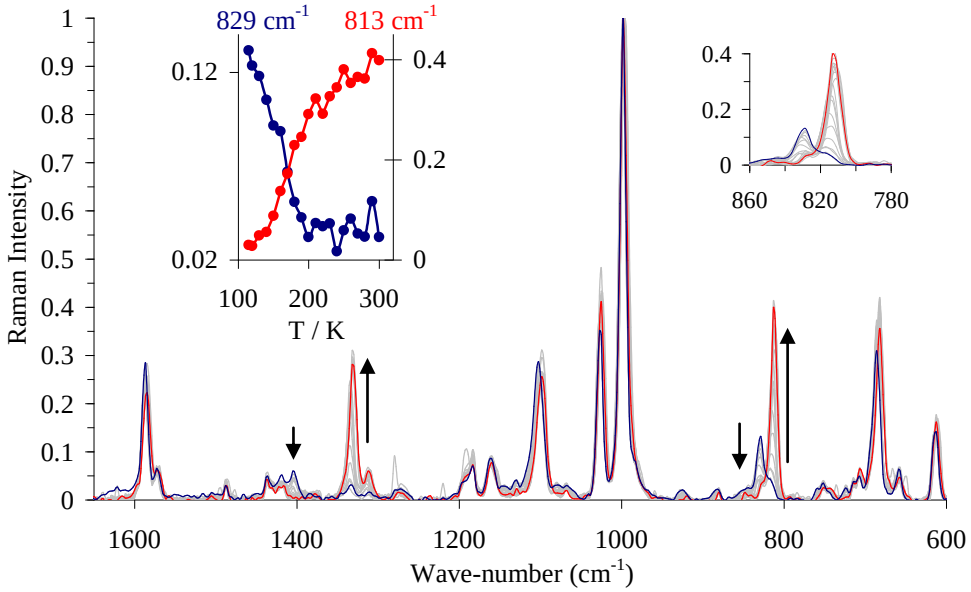

Figure 7: Solid-state Raman variable temperature study of compound **9** after photolysis recorded at 10 K intervals from 120 K to 300 K. Inset expansion of the $\delta(NO_2)$ spectral region (right) and temperature dependence of the $\delta(NO_2)$ bands of the nitro-(η^1-NO_2) isomer (813 cm^{-1}, left y axis) and the nitrito-(η^1-ONO) isomer (829 cm^{-1}, right y axis)

5.2.2. (1,2-*Bis*(diphenylphosphino)ethane)di(η^1-*N*-nitro)nickel(II) hydrate – 10

Compound **9** undergoes a remarkable 100 % reversible conversion from nitro-(η^1-*N*O_2) to nitrito-(η^1-*O*NO) upon irradiation. To see if the transformation is possible with similar analogues, compound **10** was prepared with the identical nickel and *dppe* auxiliary ligand, but the chlorine ligand was replaced with another nitro ligand to produce a complex with two nitro-(η^1-*N*O_2) ligands in the hope of a double linkage isomerism (Scheme 2).

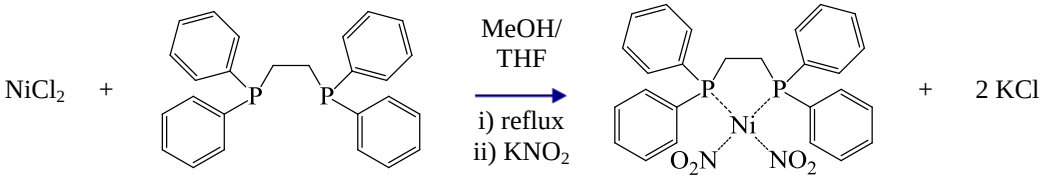

Scheme 2: Synthesis of compound **10**.

Compound **10** was synthesised using a modified procedure from literature,[6] and red/orange crystals suitable for X-ray structure determination were obtained by slow evaporation from acetone/water. A high quality X-ray data set was collected in the absence of light at 100 K to produce a ground state structure (Figure 8a). Compound **10** crystallises with one molecule of water in the asymmetric unit in the orthorhombic space group $P2_12_12_1$. The square planar nickel is bound to a bidentate *dppe* ligand and two nitro-(η^1-*N*O_2) groups *trans* to the phosphorus atoms. This structure showed no significant residual electron density and could be used as a comparison against subsequent metastable structures. Compound **10** has nickel-nitrite (Ni1-N1 and Ni1-N2) distances of 1.902(2) and 1.970(2) Å, respectively and nickel-phosphorus bond lengths of 2.1686(7) and 2.1837(7) Å, respectively.

The crystal was irradiated for 120 min using six 400 nm UV light-emitting diodes (LEDs) 1 cm from the crystal. The irradiation was stopped, and after a period for the crystal to equilibrate a metastable data set was obtained. The resulting crystal structure showed a remarkable double transformation from *N*-bound nitro-(η^1-*N*O_2) to the metastable *O*-bound nitrito-(η^1-*O*NO) with 100% conversion (Figure 8b). Overlaying the ground and metastable states crystal structures and comparing all non-hydrogen atoms positions, excluding the nitro/nitrito groups, revealed there was no major rearrangement of the structures during irradiation and only small structural

changes amounting to a RMS of 0.109 Å was observed. On closer inspection there are some subtle changes, with the Ni1-P1 and Ni1-P2 distances shortening from 2.1686(7) to 2.1541(15) Å and from 2.1837(7) to 2.1563(13) Å, respectively, and with an approximate 1% increase unit cell volume (Table 2). These changes are similar to those observed for compound 9.

Variable temperature parametric studies were carried out to establish the temperature range at which the photoactivated metastable species converts back to the ground state. After formation of a clean metastable species, the temperature was slowly increased starting at 100K with 10 K steps, and data sets were collected at regular intervals. At each step, the crystal was given a period of time for the crystal to equilibrate. The metastable species exists between temperatures of 100 K – 170 K and converts back to the ground state at 180 K.

a)

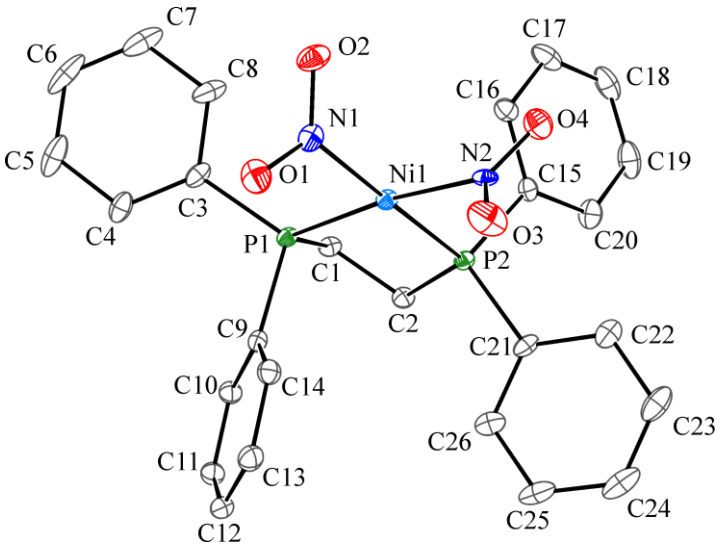

b)

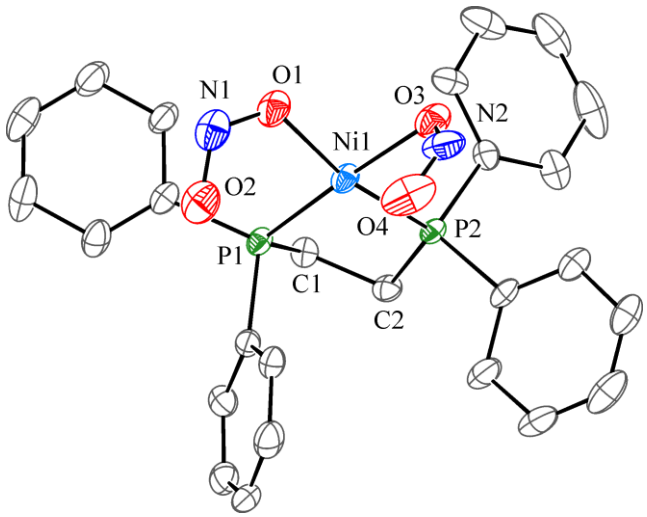

Figure 8: X-ray structure of a) ground-state and b) metastable-state of compound **10** with thermal ellipsoids set at 30% probability and hydrogen atoms removed for clarity.

Table 2: Compound **10** crystallographic data of the ground and metastable states.

	Ground-state	Metastable-state
η^1-*O*-nitrito occupancy	0%	100%
Empirical formula	C26 H24 N2 Ni O5 P2	C26 H24 N2 Ni O5 P2
Formula weight	565.12	565.12
Temperature	100(2) K	100(2) K
Wavelength	0.68960 Å	0.68960 Å
Crystal system	Orthorhombic	Orthorhombic
Space group	$P2_12_12_1$	$P2_12_12_1$
Unit cell dimensions	a = 8.1137(2) Å	a = 7.9997(5) Å
	b = 13.7208(4) Å	b = 13.9307(8) Å
	c = 22.6701(7) Å	c = 22.8956(14) Å
Volume	2523.78(12) Å^3	2551.5(3) Å^3
Z	4	4
Crystal size	0.08 x 0.08 x 0.04 mm	0.08 x 0.08 x 0.04 mm
Theta range for data collection	1.70 to 29.73°	2.64 to 29.84°
Independent reflections	7512 [R(int) = 0.0517]	7527 [R(int) = 0.0463]
Completeness to theta	98.7 %	97.4 %
Data / restraints / parameters	7512 / 0 / 325	7527 / 0 / 325
Final R indices [I>2sigma(I)]	$R1$ = 0.0427, $wR2$ = 0.1106	$R1$ = 0.0742, $wR2$ = 0.1959
R indices (all data)	$R1$ = 0.0472, $wR2$ = 0.1141	$R1$ = 0.1076, $wR2$ = 0.2198

The Slant plane Fourier maps of the comparison between the ground state structure and the metastable structure of compound **10** clearly show the reduction in electron density (dotted lines) around the nitro-(η^1-NO_2), with the increase in electron density (solid lines) accountable to the new position of the nitrito-(η^1-*ONO*) metastable species (Figure 9).

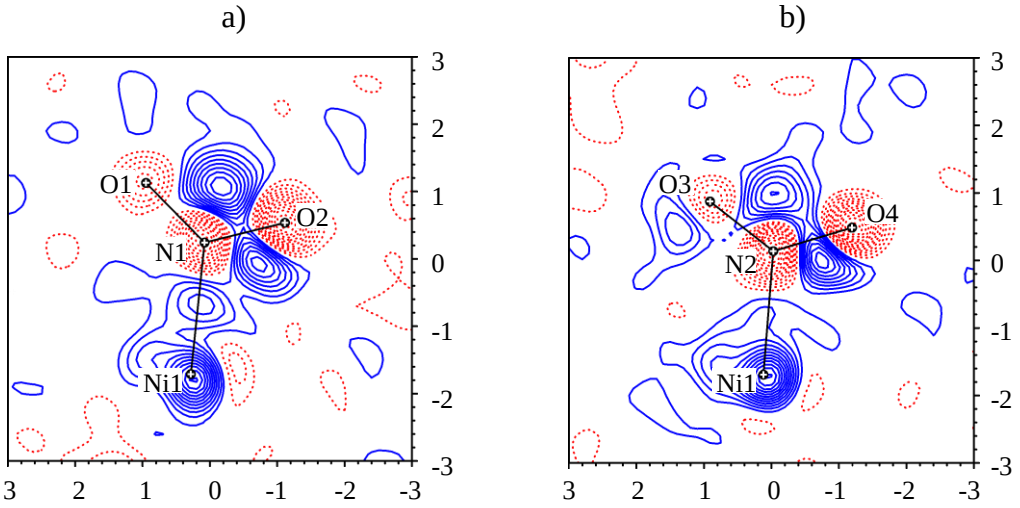

Figure 9: Slant plane Fourier maps from the difference of the ground state vs. the metastable state of the plane through the nickel nitro groups. The contour lines indicate a 0.5 (a) and 0.38 (b) increase (solid blue lines) or decrease (dotted red lines) in electron density. The zero contours are omitted for clarity. a) Plane through Ni1-N1-O1-O2; b) Plane through Ni1-N2-O3-O4.

The ground state structure of compound **10** has a number of short intermolecular interactions, the shortest of which are between O2 and H1A with an interatomic distance of 2.3437(21) Å. Upon photoactivation, the nitro-(η^1-NO_2) transforms to the nitrito-(η^1-ONO) isomer in the direction of the greatest void space. Figure 10 shows the interatomic distance and that in the metastable structure the short intermolecular interactions are no longer present.

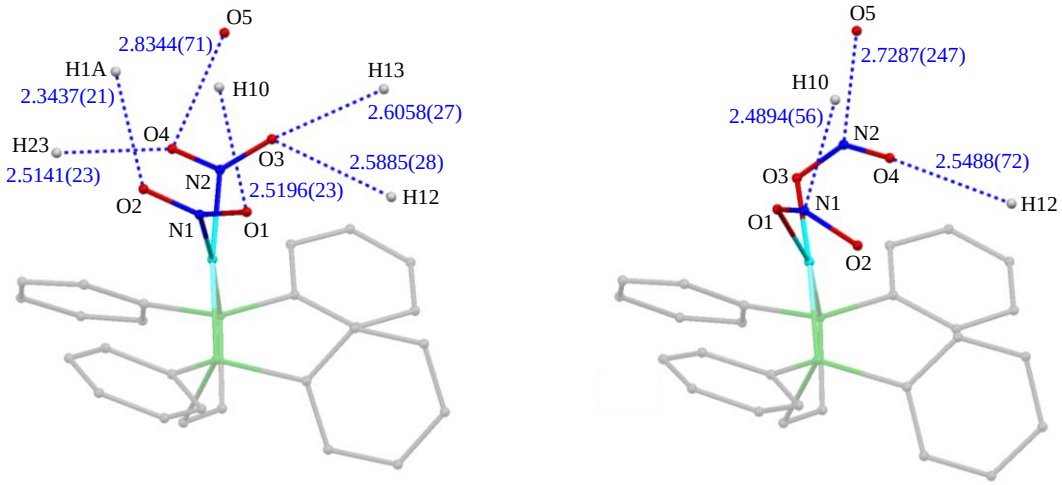

Figure 10: Close contacts for the nitrite ligand in the ground and metastable states structures.

The major absorption peaks in the UV-visible spectra are at 252 nm (66253 $Lmol^{-1}cm^{-1}$), 295 nm (14446 $Lmol^{-1}cm^{-1}$) and 313 nm (12626 $Lmol^{-1}cm^{-1}$). DFT calculations were used to find electronic transitions responsible for the linkage isomerism. There is good agreement between experimental UV-visible spectra and theoretical DFT electronic transition calculations. DFT calculations were carried out for the first 15 electronic transitions. For compound **10**, these 15 transitions range from 559 nm to 287 nm. Beyond 287 nm to lower wavelengths, the electronic transitions were not evaluated (Figure 11). Even though the simulated electronic transitions were complex, there were some general trends. The most intense absorptions were dominated by transitions into LUMO antibonding, with respect to the nickel-nitro bonds. Electronic transitions at 306 nm are associated with electrons being promoted from bonding HOMO (-1) with reference to the nickel-nitro bond, into antibonding orbitals with reference for both nickel-nitrite and nickel-phosphorus bonds (Figure 12). In photocrystallographic experiments, the crystal was irradiating at 400 nm to cause the linkage isomerism. Inspecting the UV spectra and DFT predicted electronic transitions, the irradiation wavelength of 400 nm can be can be associated with absorptions from either a shoulder of an intense broad peak (309

nm), or at a more specific wavelength (373 nm). Both absorptions cause transitions from non-bonding nickel orbitals into antibonding orbitals with reference to the nickel-nitro bond (Figure 12). These transitions result in a weakening of the nickel-nitro(η^1-NO_2) bond and could explain the occurrence of the linkage-isomerism.

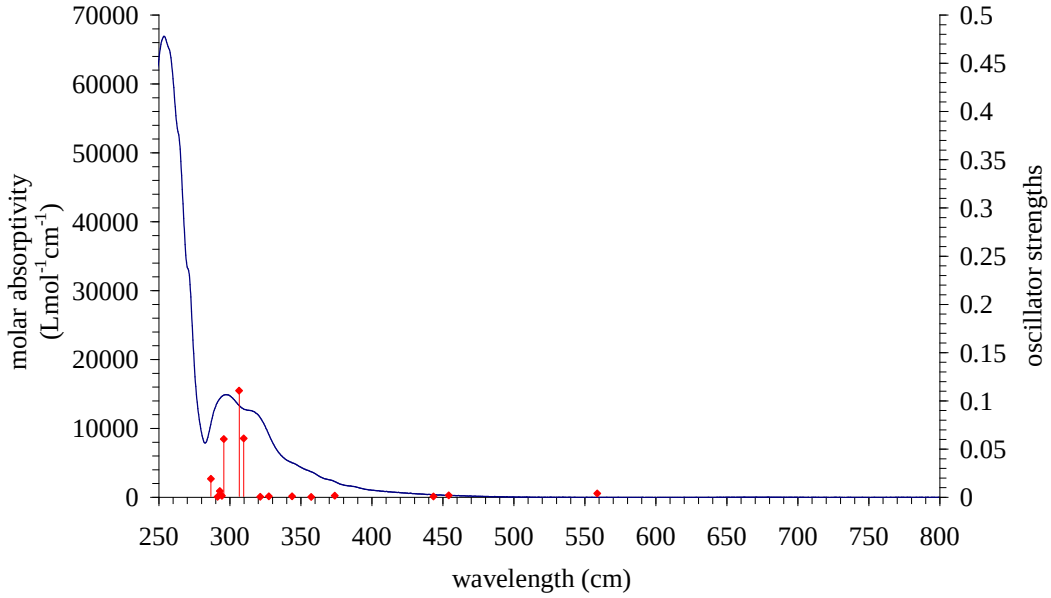

Figure 11: UV-visible spectra of and DFT calculated oscillator strengths for compound **10**.

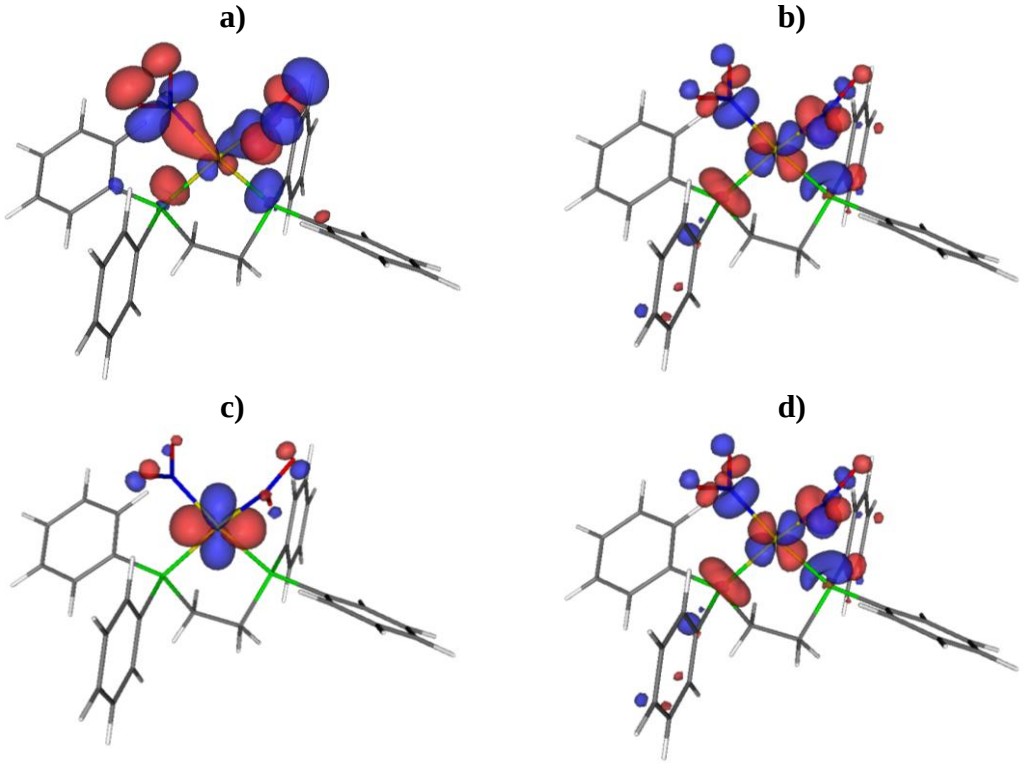

Figure 12: Compound **10** molecular orbitals from strongest transition 306 nm from a) bonding nickel($d_{x^2-y^2}$)-NO_2 orbitals (HOMO -1) to b) antibonding nickel($d_{x^2-y^2}$)-NO_2 orbitals (LUMO) and 373 nm transition from c) non-bonding nickel(d_{xy}) orbitals (HOMO -17) to d) antibonding nickel($d_{x^2-y^2}$)-NO_2 orbitals (LUMO).

A crystal of compound **10** was cooled to 115 K on the variable-temperature stage and a ground state spectrum was obtained (Figure 13). The spectrum contains a $\delta(NO_2)$ band at 812, 831 and 836 cm^{-1}, typical of the nitro conformation; other bands were too weak and overlapped, and were not easily characterized. The crystal was then irradiated using the visible light from the illuminator on the confocal Raman microscope for a period of 80 min, after which a metastable spectrum was obtained. The $\delta(NO_2)$ shifts to form new bands at 811 and 816 cm^{-1}. These shifts are a clear indication of the complete conversion to the nitrito conformation (Figure 13).

On the photoactivated crystal, parametric variable temperature studies were carried out from 120 K to 300 K with Raman spectra being recorded every 10 K. The metastable state fully converted back to the ground state spectra at 170 K.[3-4]

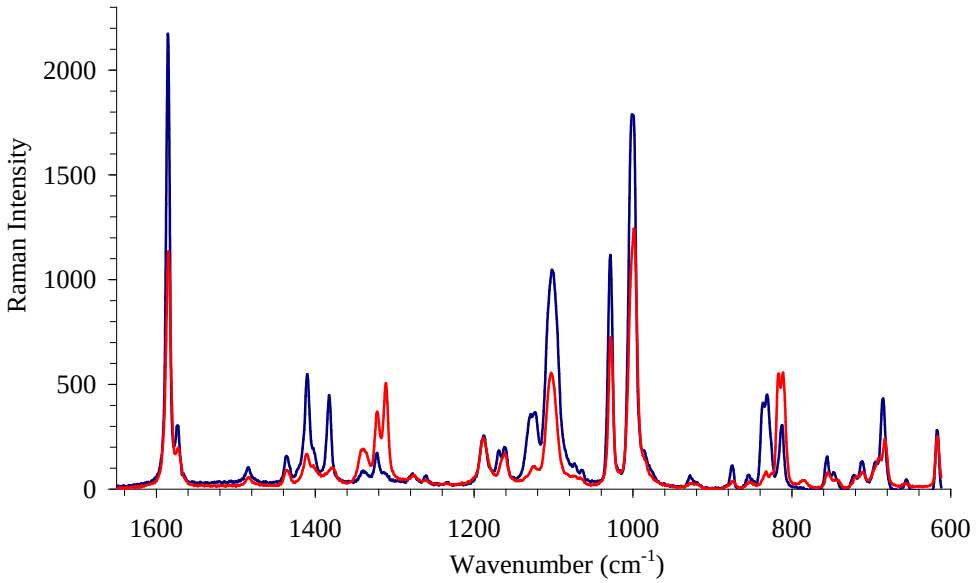

Figure 13: Solid-state Raman spectra at 115 K of before (blue) and after (red) photolysis of compound **10**.

5.2.3. (1,2-*Bis*(dicyclohexylphosphino)ethane)di(η^1-*N*-nitro)nickel(II) – 11

Compound **9** and **10** both undergo an outstanding 100 % conversion from nitro-(η^1-*N*O_2) to nitrito-(η^1-*O*NO) upon irradiation. To investigate the factors that govern the unprecedented interconversion between linkage isomers for compounds **9** and **10,** the variables of nickel-nitro bond lengths, intramolecular interactions, void space around the ambidentate ligand, packing arrangement and the type of auxiliary ligands have to be investigated. The auxiliary ligand 1,2-*bis*(dicyclohexylphosphino)ethane is incorporated to investigate these factors. Compound **11** was synthesised according to literature[7] and was crystallised from DCM/toluene using slow evaporation (Scheme 3).

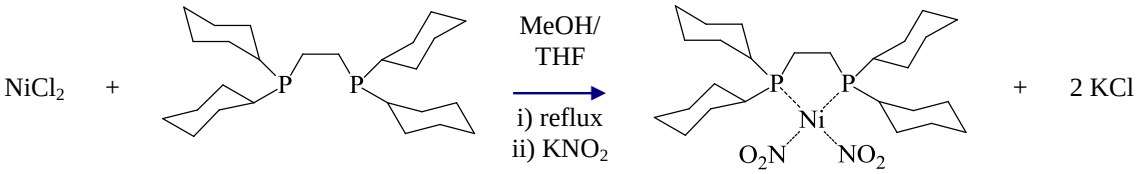

Scheme 3: Synthesis of compound **11**.

If a crystal of compound **11** is cooled to 100 K, any exposure to light during the mounting, aligning or data collection, results in mixture of the nitro and nitrito conformations. To avoid this problem, the crystal was mounted and aligned at room temperature and then cooled down to the desired temperature in the absence of light. A high quality dataset was collected in the absence of light at 100 K to produce a ground state structure (Figure 14a). The complex crystallised in the monoclinic space group $P2_1/c$ with one equivalent of toluene in the asymmetric unit. The square planar nickel centre is bound to a bidentate *dcpe* ligand and two nitro-(η^1-*N*O_2) groups *trans* to the phosphorus atoms. Compound **11** contains nickel-nitrite (Ni1-N1 and Ni1-N2) bond lengths of 1.9060(16) and 1.9114(15) Å, and nickel-phosphorus (Ni1-P1 and Ni1-P2) bond lengths of 2.1931(4) and 2.1843(4) Å, respectively; these bond lengths are comparable to compounds **9** and **10**.

The crystal was irradiated for a period of 60 min, using six 400 nm UV LEDs 1 cm from the crystal. The irradiation was stopped and a data set was collected. A 100% single-crystal to single-crystal transformation of both nitro-(η^1-*N*O_2) groups to the nitrito-(η^1-*O*NO) metastable species was obtained (Figure 14b). The O1-N1-O2

group adopts only one special orientation, whereas the second nitrito group is disordered over two positions. The nitrito groups *O3-N2-O4* and *O3A-N2A-O4A* have an occupancy of 60% and 40% respectively.

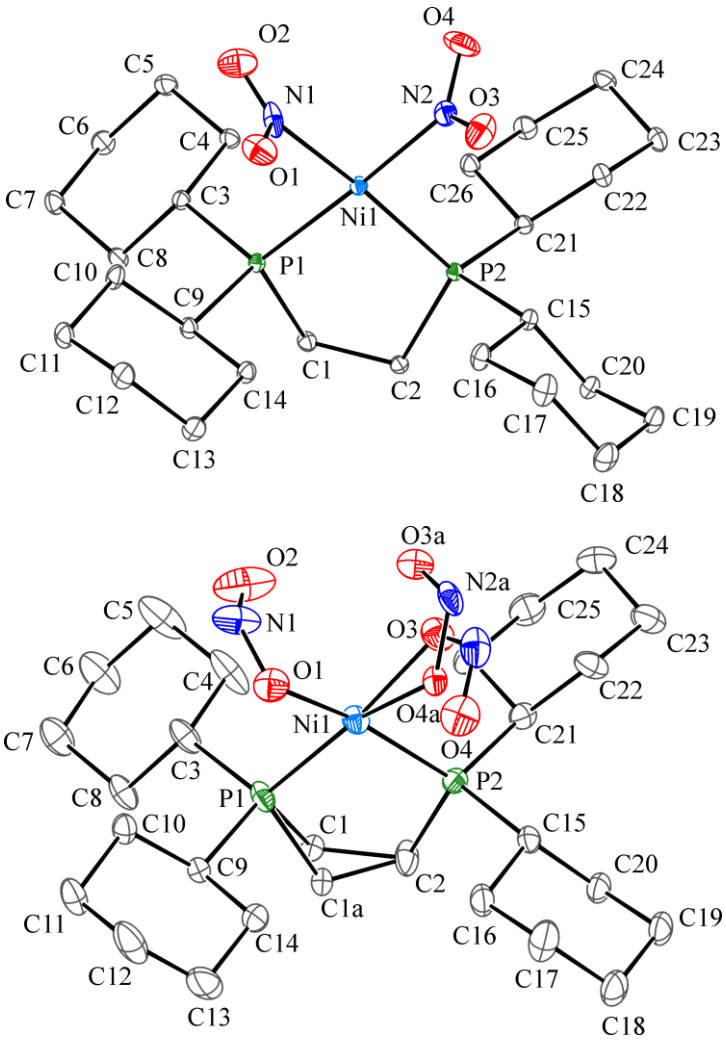

Figure 14: X-ray structure a) ground state and b) metastable state of compound **11** with thermal ellipsoids set at 30% probability and hydrogen atoms removed for clarity.

Table 3: Crystallographic data for compounds **11.**

	Ground State	Metastable State
η^1-*O*-nitrito occupancy	0%	100%
Empirical formula	C33 H56 N2 Ni O4 P2	C33 H56 N2 Ni O4 P2
Formula weight	665.45	665.45
Temperature	100(2) K	100(2) K
Wavelength	0.68960 Å	0.68960 Å
Crystal system	Monoclinic	Monoclinic
Space group	*P*2(1)/*c*	*P*2(1)/*c*
Unit cell dimensions	*a* = 12.2125(5) Å	*a* = 12.199(10) Å
	b = 18.7052(8) Å	*b* = 19.146(8) Å
	c = 15.1718(6) Å	*c* = 15.093(10) Å
	β =97.2610(10)°	β = 101.00(5)°
Volume	3438.0(2) Å^3	3461(4) Å^3
Z	4	4
Crystal size	0.10 x 0.05 x 0.02 mm	0.10 x 0.05 x 0.02 mm

Theta range for data collection	1.70 to 29.70°	2.19 to 29.73°
Independent reflections	10185 [*R*(int) = 0.0474]	10272 [*R*(int) = 0.0437]
Completeness to theta	97.4 %	97.3 %
Data / restraints / parameters	10185 / 0 / 380	10272 / 0 / 460
Final R indices [I>2sigma(I)]	*R*1 = 0.0394, *wR*2 = 0.0933	*R*1 = 0.0946, *wR*2 = 0.2501
R indices (all data)	*R*1 = 0.0497, *wR*2 = 0.0992	*R*1 = 0.1177, *wR*2 = 0.2704

Close contacts and Hirshfeld surfaces (Figure 15a) of the ground state structure were analysed to work out why the O1-N1-O2 only goes in one direction and showing that the O1 atom has a close contact between O1-H26A and O1-H1B with intermolecular distances of 2.4071(15) and 2.1694(15) Å, respectively. In contrast, the shortest contact to the O2 is 2.6758(18) Å. Thus when the nitro N1-O1,O2 is photoactivated, the orientation of the nitrito species favours the direction of least steric hindrance (Figure 15b). The close contacts of the N2-O3-O4 nitro group were also established. The nearest intermolecular distances for O3 and O4 were 2.651 and 2.821 Å, respectively. These distances are large enough not to greatly affect the direction of the photoactivated species, allowing the transformation of the nitro species to the nitrito species the freedom to adopt two orientations, but with a preference towards O4 (Figure 15c).

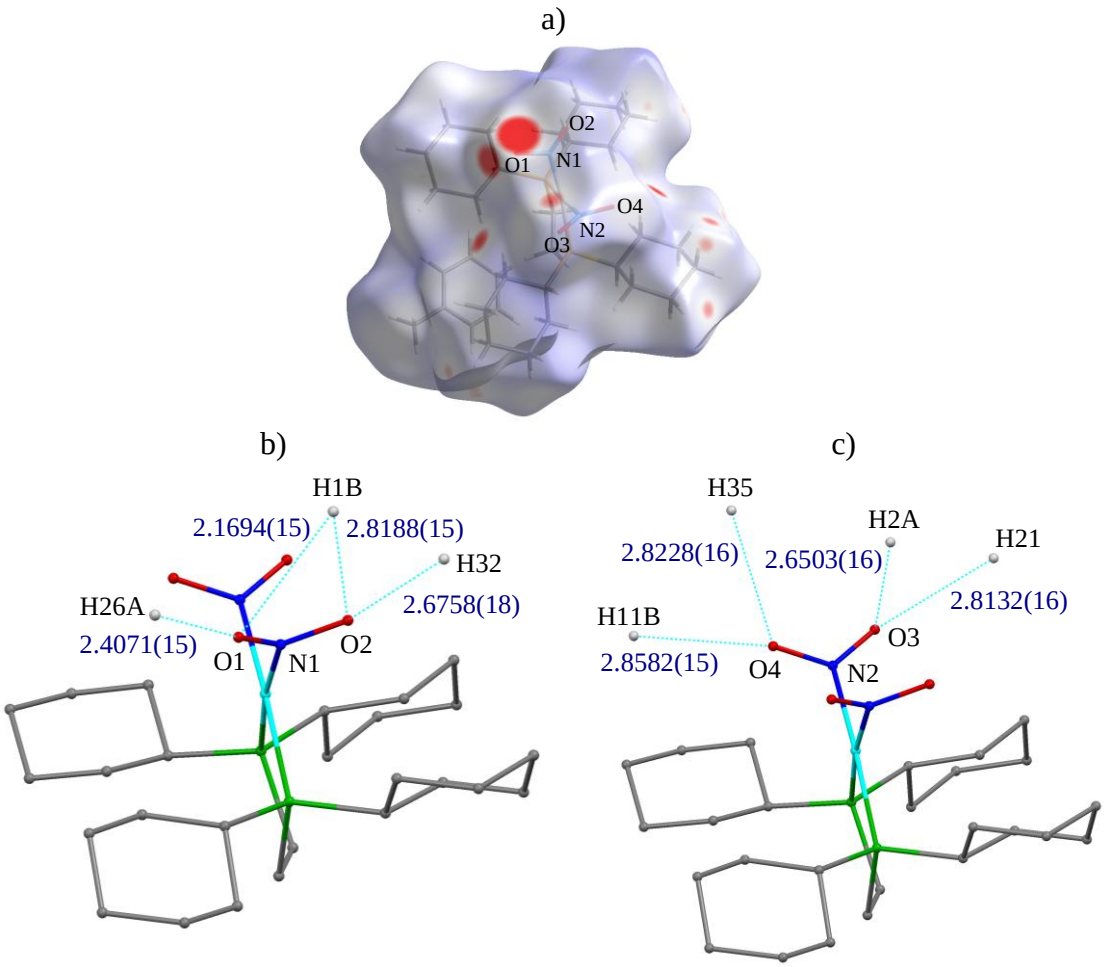

Figure 15: Close contact information for Compound **11** a) Hirshfeld surfaces (red is close contact) interactions, b) distances for N1-O1-O2 and c) distances for N2-O3-O4.

Overlaying the crystal structures of the ground state (blue) and metastable state (turquoise), reveals some changes in the crystal structure (Figure 16). Upon linkage isomerism, the toluene guest solvent molecule has the most profound movement compared to the ground state structure, and in the metastable state structure is disordered over two positions. The toluene group has close contacts with the nitro/nitrito groups, and the disorder might be correlated to the linkage isomerism. Also, accompanying the conformational changes are the bond shortening of the Ni1-P1 and Ni1-P2 distances from 2.1841(4) to 2.1638(19) and 2.1934(4) to 2.1767(19) Å, respectively. The unit cell dimensions remain approximately constant with less than a 1 % change after irradiation.

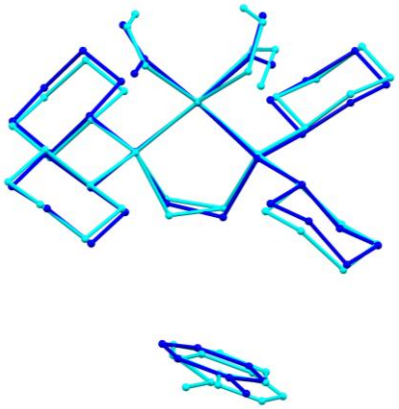

Figure 16: Structure overlay of ground state (blue) and metastable state (turquoise), RMS of 0.221

The Slant plane Fourier maps of the comparison between the ground state structure and the excited state structure of Ni(dcpe)$(NO_2)_2$ show the reduction of electron density (dotted lines) around the positions of the nitro-(η^1-*N*O_2), and with an increase in electron density (solid lines) accountable for the nitrito-(η^1-*ONO*) metastable species (Figure 17). The electron density map for the N2-O1,O2 (Figure 17b) does not clearly show the second nitrito species (N2A-O2A-O3A) as the photoactive species has more diffused electron density and an occupancy of 40%.

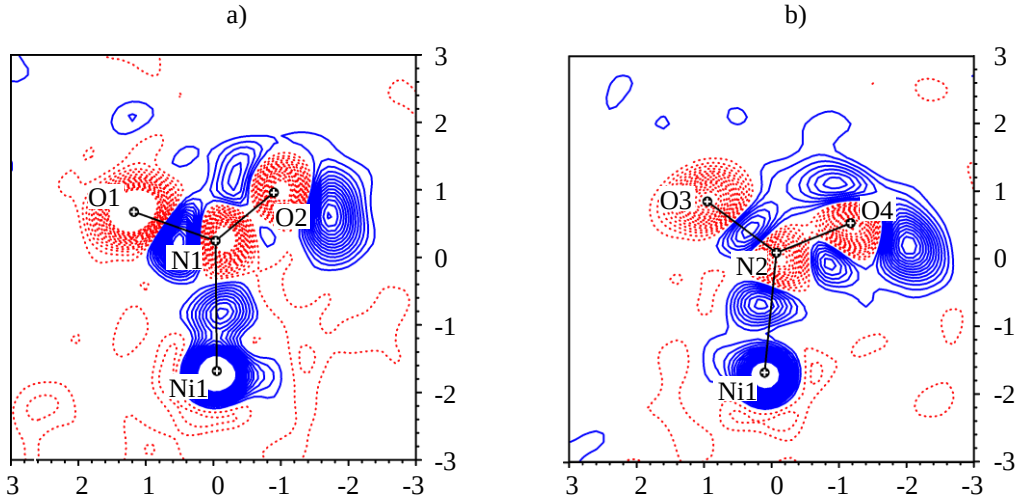

Figure 17: Slant plane Fourier maps of the ground state vs. the metastable state. The contour lines indicate a 0.45 (a) and 0.5 (b) increase (solid blue lines) or decrease (dotted red lines) in electron density. The zero contours are omitted for clarity. a) Plane through *Ni1-N1-O1-O2*; b) Plane through *Ni1-N2-O3-O4*.

Variable temperature parametric studies were carried out to establish the temperature range at which the photoactivated metastable species converts back to the ground state. The temperature was slowly increased from 100 K and data sets were collected at regular intervals. The metastable species exists between temperatures of 100 K – 170 K and converts back to the ground state at 180 K.

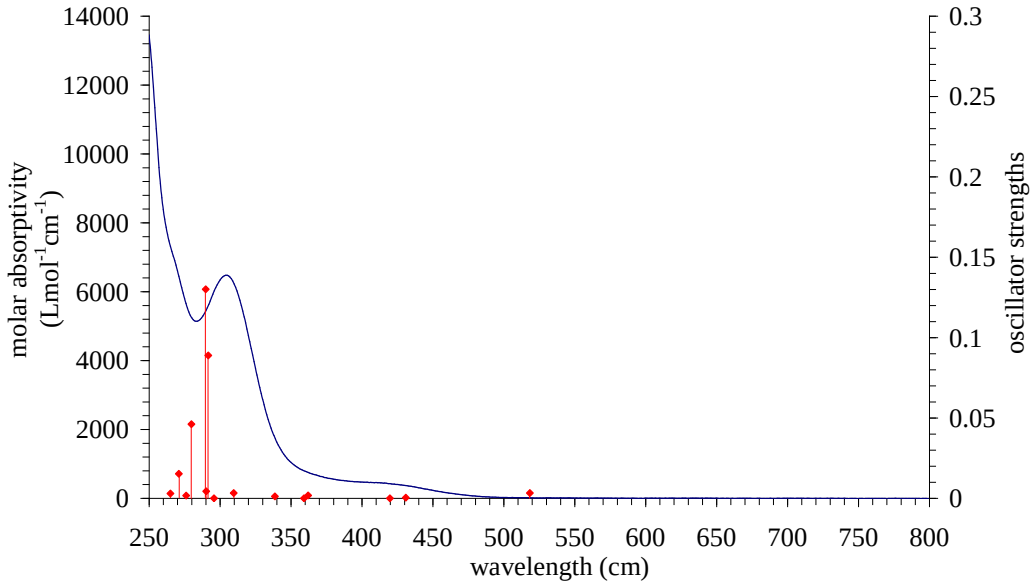

Figure 18: UV-visible spectra of and DFT calculated oscillator strengths for compound **11**.

The UV-visible spectrum shows an absorption at 250 nm and 300 nm, and a broad absorption at in the region of 400 nm. Gas phase DFT calculations were used to find electronic transitions responsible for the linkage isomerism. There is a good agreement between the predicted theoretical and experimental absorption spectra of compound **11**. Even though the simulated electronic transitions were complex, there were some general trends. The entire electronic transitions were comprised of a mixture of transitions from non-bonding orbitals into antibonding nickel-nitro orbitals or from bonding nickel-nitro orbitals into antibonding nickel-nitro orbitals. Figure 19 shows one of possible electronic transitions from non-bonding orbital (HOMO -4) to an antibonding orbitals with respects to the nickel-nitro bond (LUMO).

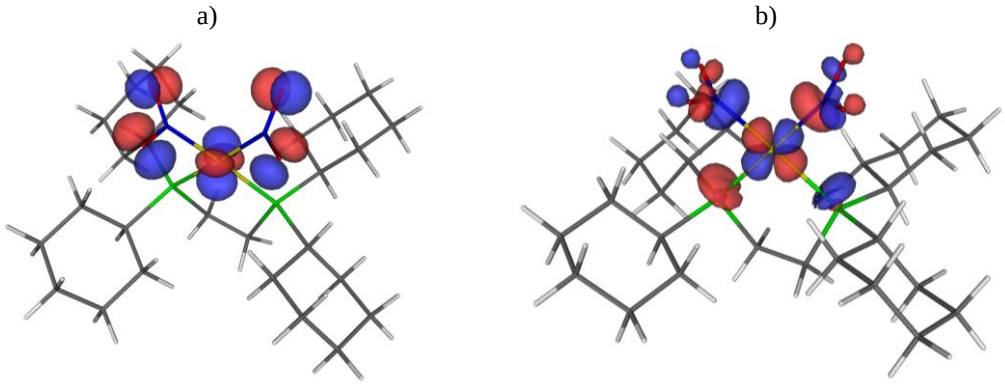

Figure 19: Compound **11** molecular orbitals for the transition at 419 nm from a) non-bonding nickel(d_{xz}) and non-bonding NO_2 orbitals to antibonding orbital with respects to the nickel-nitro and nickel-phosphorus.

A crystal of compound **11** was cooled to 115 K on the variable-temperature stage and a ground state spectrum was obtained (Figure 20). The spectra contains a $\delta(NO_2)$ band at 828 cm^{-1}, typical of the nitro conformation; other bands were too weak and overlapped and were not easily characterized. The crystal was then irradiated using the visible light from the illuminator on the confocal Raman microscope for 60 s, after which a metastable spectrum was obtained. The $\delta(NO_2)$ shifts to form new bands at 813 and 817 cm^{-1}. These shifts are a clear indication of the complete conversion to the nitrito conformation (Figure 20). On the photoactivated crystal, parametric variable temperature studies were carried out from 120 K to 300 K with Raman spectra being recorded every 10 K. The metastable state fully converted back to the ground state spectra with a sharp change at 180 K.

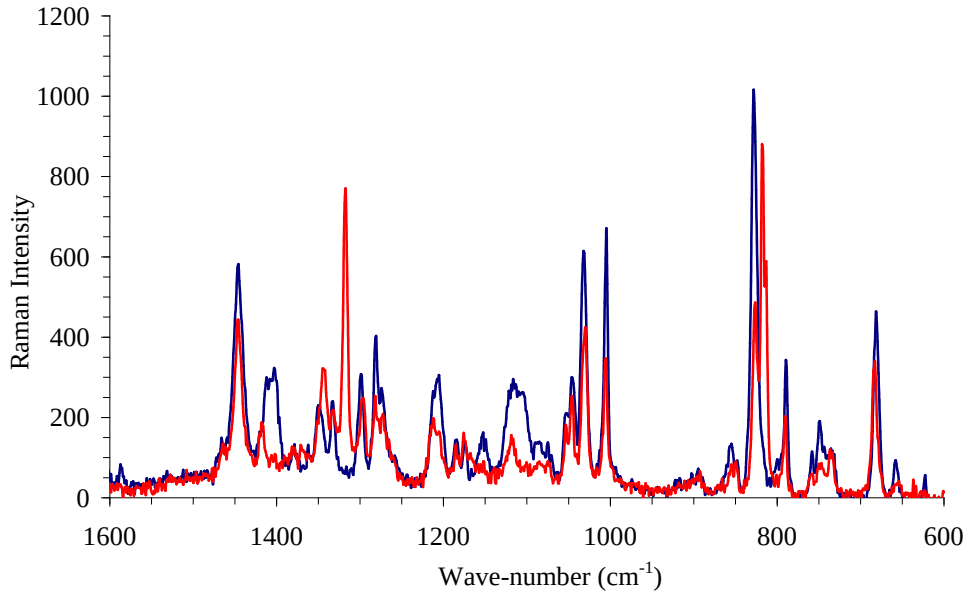

Figure 20: Solid-state Raman spectra at 115 K of before (blue) and after (red) photolysis of compound **11**.

5.2.4. (*Bis*(2-diphenylphosphinoethyl)phenylphosphine)(η^1-*N*-nitro)nickel(II) tetraphenylborate – 12

During photoactivation in compounds **9-11**, there is a slight reduction in data quality, and combined with movement within the structure from the linkage isomerism, there is an increase in the thermal ellipsoids. Increasing the steric bulk of the auxiliary ligand and/or using large counter ions reduce the proportion of lattice which undergoes transformation.[8] In the search for compounds capable of high linkage isomerism conversion without decomposition, the auxiliary ligand *bis*(2-diphenylphosphinoethyl)phenylphosphine was incorporated. The novel compound **11** was prepared by treating a freshly-prepared sample of anhydrous potassium hexanitritenickel(II) with stoichiometric amounts of the *bis*(2-diphenylphosphinoethyl)phenylphosphine, and the subsequent addition of sodium tetraphenylborate (Scheme 4).

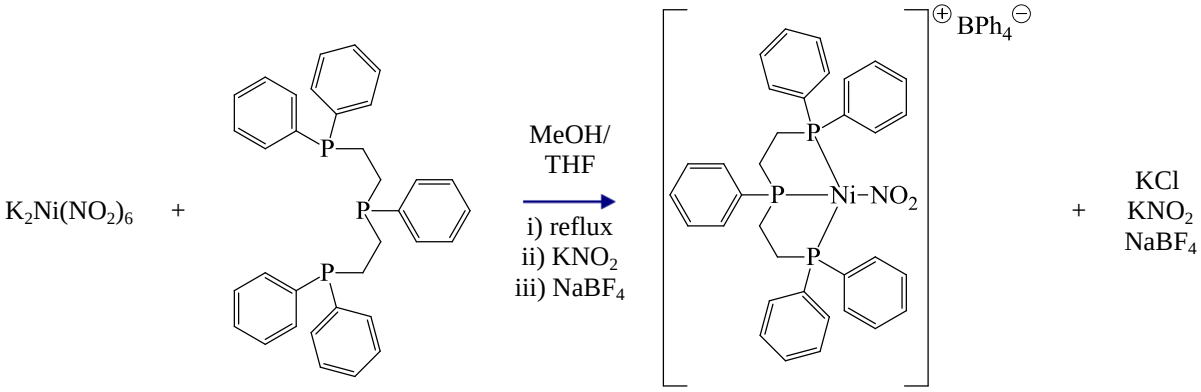

Scheme 4: Synthesis of compound **12**.

A crystal of compound **12** was mounted and aligned at room temperature with minimal light exposure and cooled to 100 K in the absence of light. The resulting structure crystallizes in the triclinic space group *P*-1. The nickel centre has a square planar geometry bound to three phosphorus atoms and either an *N*- or *O*-bound nitrite. The ground state structure contains nitro-(η^1-*N*O_2) and nitrito-(η^1-*O*NO) coordination modes with occupancies of 88 % and 12 %, respectively. Compound **12** has nickel-phosphorus (Ni1-P1, Ni1-P2 and Ni1-P3) bond lengths of 2.1987(7), 2.1302(8) and 2.2079(7) Å, respectively. The nickel-nitrite (Ni1-N1 and Ni1-O1A) bond lengths are 1.9135(18) and 2.050(9) Å, respectively (Figure 21a). The nitrito-

(η^1-*O*NO) could not be modelled sensibly at the low occupancy and constraints were implemented using parameters generated from data from a search on the CSD.

The crystal was irradiated for a period of 20 min using six 400 nm LEDs 1 cm from the crystal. The resulting crystal structure had a major increase in the occupancy of the nitrito-(η^1-*O*NO) isomers, increasing from 12 % in the ground state to 80 % in second metastable dataset. Additional irradiation of 10 min increased the occupancy of the nitrito-(η^1-*O*NO) isomers again to 85 %. Figure 21a shows the crystal structure with the minor nitro-(η^1-*N*O_2) removed for clarity. The nitro-(η^1-*N*O_2) could not be modelled without a number of crystallographic constraints which were obtained from the ground state structure. Subsequent irradiation of the crystal did not increase the linkage isomerism of the complex to the nitrito-(η^1-*O*NO) isomer. The conversion to 85% is the photostationary point and can be repeated to obtain comparable results.

a)

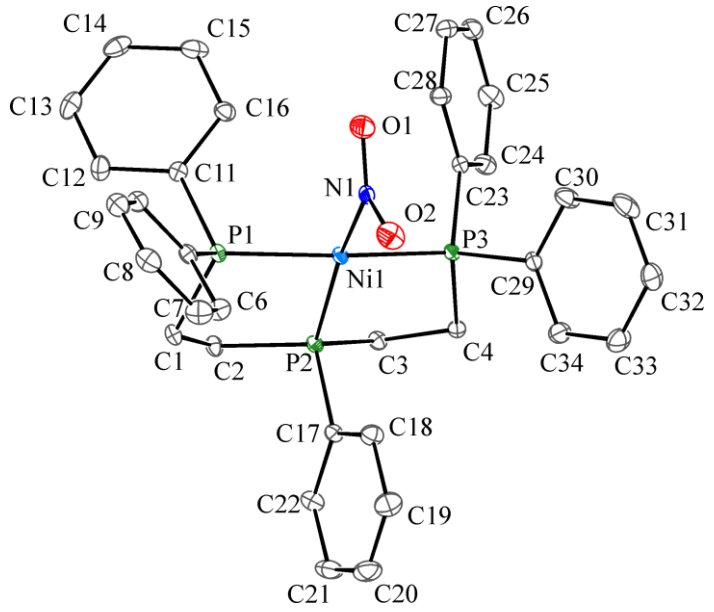

b)

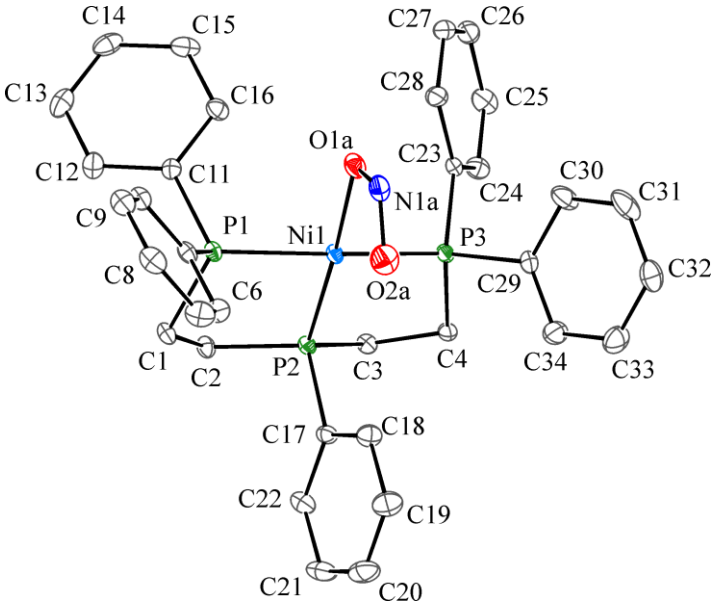

Figure 21: X-ray structures of compound **12** a) ground-state with minor nitrito component and tetraphenylborate removed and b) metastable-state with minor nitro component and tetraphenylborate removed. Thermal ellipsoids set at 30% probability and hydrogen atoms removed for clarity.

Table 4: Crystallographic data for compounds **12**.

	Ground State	Metastable State
η^1-*O*-nitrito occupancy	12%	85 %
Empirical formula	C58 H53 B N Ni O2 P3	C58 H53 B N Ni O2 P3
Formula weight	958.44	958.44
Temperature	100(2) K	100(2) K
Wavelength	0.68960 Å	0.68960 Å
Crystal system	Triclinic	Triclinic
Space group	*P*-1	*P*-1
Unit cell dimensions	*a* = 11.439(5) Å	*a* = 11.4586(5) Å
	b = 14.386(5) Å	*b* = 14.3876(6) Å
	c = 17.108(5) Å	*c* = 17.0954(8) Å
	α = 96.407(5)°	α = 95.7470(10)°

	β = 105.182(5)°	β = 105.5350(10)°
	γ = 112.927(5)°	γ = 112.5510(10)°
Volume	2429.1(15) Å^3	2441.75(19) Å^3
Z	2	2
Crystal size	0.08 x 0.06 x 0.04 mm	0.08 x 0.06 x 0.04 mm
Theta range for data collection	1.27 to 30.53°	1.24 to 29.72°
Independent reflections	13970 [*R*(*int*) = 0.0286]	14049 [*R*(*int*) = 0.0313]
Completeness to theta	96.6 %	97.7 %
Data / restraints / parameters	13970 / 10 / 609	14049 / 5 / 605
Final R indices [I>2sigma(I)]	*R*1 = 0.0398, *wR*2 = 0.1191	*R*1 = 0.0472, *wR*2 = 0.1077
R indices (all data)	*R*1 = 0.0493, *wR*2 = 0.1297	*R*1 = 0.0599, *wR*2 = 0.1147

The Slant plane Fourier maps of the comparison between the ground state structure and the metastable state structure of compound **12** show the reduction of election density (dotted lines) around the positions of the nitro-(η^1-*N*O$_2$) and with increase in electron density (solid lines) accountable for the nitrito-(η^1-*ONO*) metastable species (Figure 22).

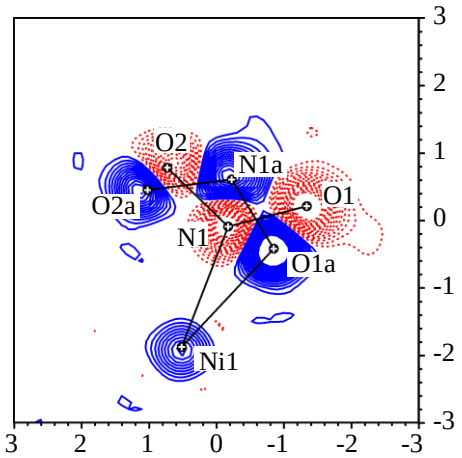

Figure 22: Slant plane Fourier maps of the ground state vs. the metastable state. The contour lines indicate a 0.5 increase (solid blue lines) or decrease (dotted red lines) in electron density. The zero contours are omitted for clarity.

Variable temperature parametric studies were carried out to establish the temperature range over which the photoactivated nitrito species remains. The temperature was slowly increased from 100K and data sets were collected at regular intervals. The metastable species exists with high occupancies between temperatures of 100 K – 180 K. Raising the temperature to 200 K, the nitrito-(η^1-*O*NO) occupancy reduces to the initial ground state occupancy.

Crystal structures of compound **12** contain both isomers as a ratio between nitro-(η^1-*N*O$_2$) and nitrito-(η^1-*ONO*), which gives an indication that in this packing arrangement both isomers are similar in energy. The nitro-(η^1-*N*O$_2$) isomer in

compound **12** has a distorted geometry which is likely to destabilise the nitro-(η^1-NO_2) energy relative to the nitrito-(η^1-*ONO*) species, and explains why an equilibrium between the two states is present. The nitro group which is normally symmetric in shape has Ni-N1-O1 and Ni-N1-O2 angles of 101.48(15)º and 122.87(18)º, respectively. Compound **12** has close contacts in the direction of the nitro group O1···H19 and O1···H20, with intermolecular interaction of 2.5124(16) Å and 2.6126(21) Å, respectively (Figure 23). The nitro group distorts to prevent unfavourable interaction between the atoms in the neighbouring molecule.

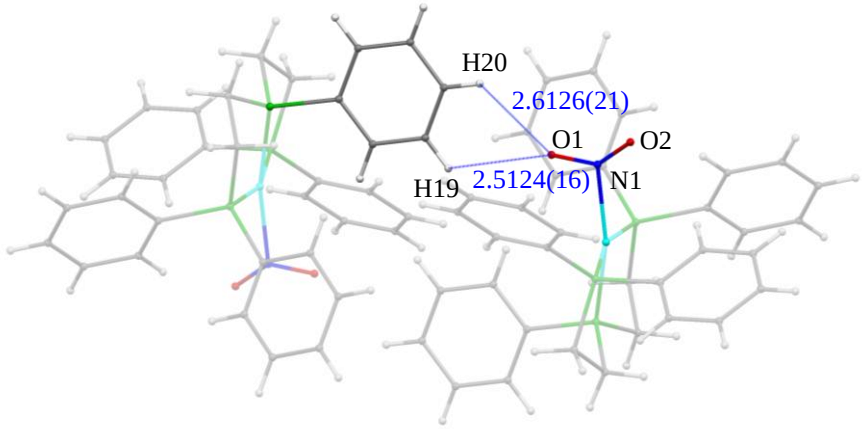

Figure 23: Close contacts of the nitro group in compound **12**.

The UV-visible spectrum of compound **12** contains a strong absorption at 286 nm, a shoulder peak at 314 nm, and a broad absorption peak at 400 nm. Gas phase DFT calculations of the electronic transitions and experimental UV-visible solution-based spectra have good correlation, and the small deviation could be related to the absence of tetraphenylborate anion in the theoretical calculations. From DFT analysis, the electronic transition of wavelengths longer than 320 nm is mainly associated with transitions from bonding orbitals into antibonding orbitals with respects to the nickel-nitro bond. There are also electronic transition contributions from non-bonding orbitals and auxiliary ligand orbital into the antibonding LUMO with respects to the nickel-nitro bond. In photocrystallographic investigation the crystal was irradiated with an LED of 400 nm wavelength. More specifically, irradiation at 400 nm can be associated with electronic transitions from bonding (LUMO -7) to anti-bonding orbitals (HOMO) with respects to the nickel-nitro bond (Figure 25).

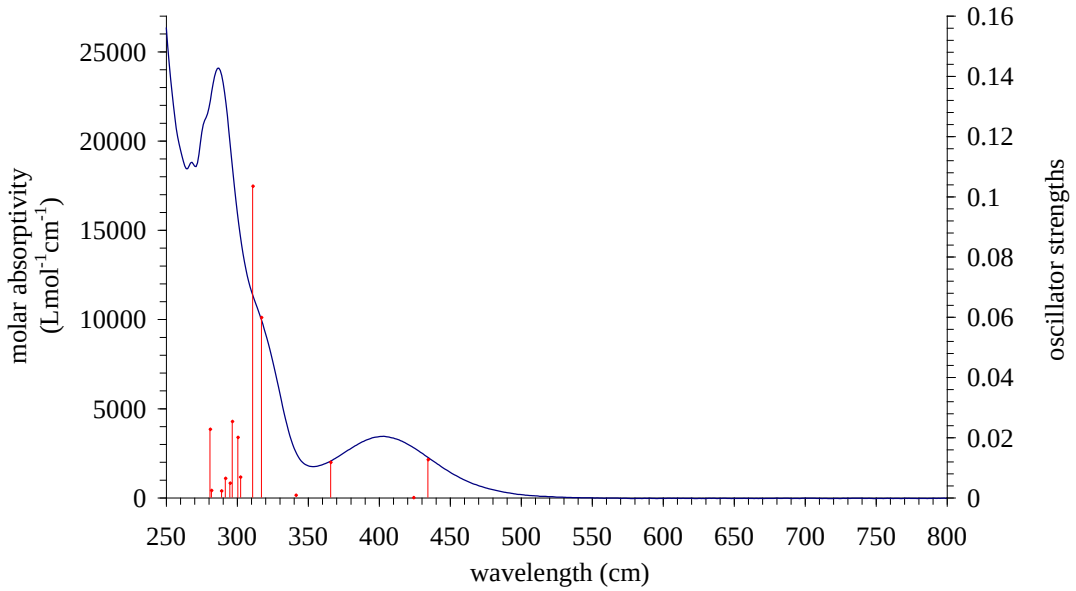

Figure 24: UV-visible spectra of and DFT calculated oscillator strengths for compound **12**.

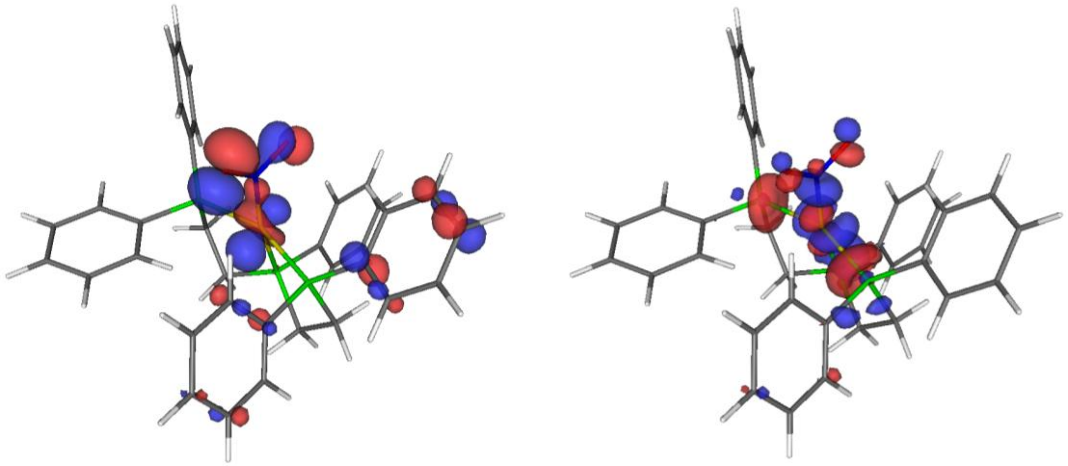

Figure 25: Compound **12** molecular orbitals for the electronic transition at 424 nm from a) non-bonding nickel (d_{xy}) and non-bonding NO_2 orbitals to antibonding orbital with respects to the nickel-nitro and nickel-phosphorus.

A crystal of compound **12** was cooled to 115 K on the variable-temperature stage and a ground state spectrum was obtained (Figure 26). The spectra contains $\delta(NO_2)$ bending modes at 816 and 817 cm^{-1}, typical of the nitro conformation; other bands were too weak and overlapped, and were not easily characterized. The crystal was then irradiated using the visible light from the illuminator on the confocal Raman microscope for 100 min, after which a metastable spectrum was obtained. The $\delta(NO_2)$ shifts formed new bands at 831 cm^{-1}. These shifts are a clear indication of the complete conversion to the nitrito conformation (Figure 26). This result differs from the crystallographic investigations which do not show a complete conversion to the nitrito conformation. One plausible explanation would be that the Raman

spectroscopy only characterizes the surface layers of the crystal and therefore light penetration into the crystal does not present as a problem.

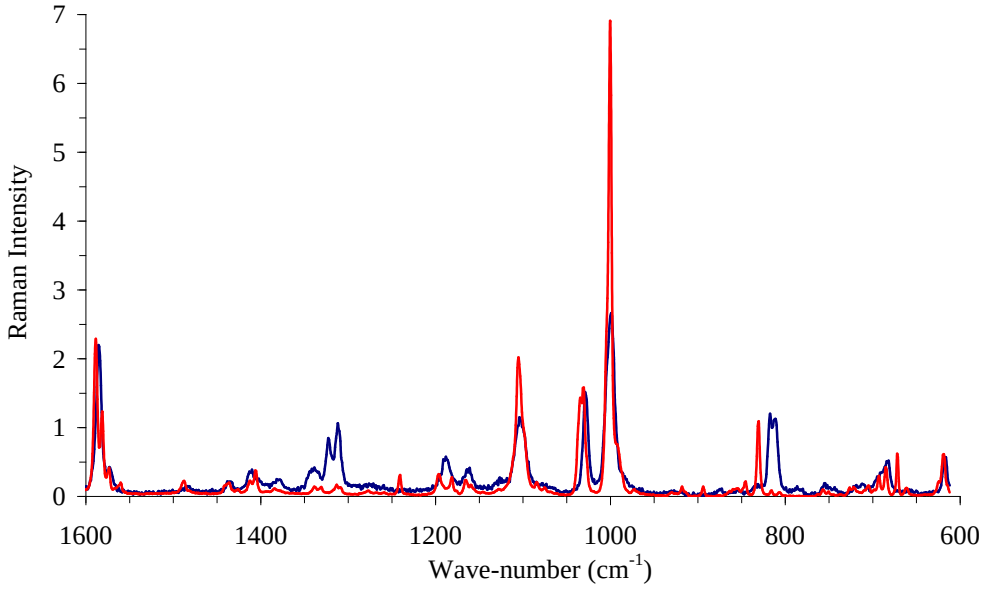

Figure 26: Solid-state Raman spectra at 115 K of before (blue) and after (red) photolysis of compound **12**.

In the previous photocrystallographic studies, the ground state structure contained a small occupancy of the nitrito (η^1-*O*NO) species. Different synthetic routes were investigated in an attempt to produce a crystalline material free of the nitrito η^1-*O*NO species. From these studies aimed at preventing contamination of the ground state structure with the nitrito-(η^1-*O*NO) species, the synthesis was carried out in the dark with the temperature of reaction not raised above 320 K, and recrystallization carried out at a reduced temperature (278 K). A crystal was mounted at room temperature on the diffractometer and the temperature was slowly reduced to 100 K before the data collection. The resulting crystal structure contained a fully occupied nitro-(η^1-*N*O_2) species absent of the nitrito-(η^1-*O*NO) species (Figure 27). The clean ground state obtained from crystallization at reduced temperature, and slow cooling to 100 K before crystallographic experiments, suggest that the nitrite ambidentate ligand exists in equilibrium, and that at reduced temperatures the nitro is the favoured conformation. This mimics the results observed in compound **12** ((N,N,N',N'-Tetraethyldiethylenetriamine)(η^2-*O*,*O*-chelating nitrito)(η^1-*N*-nitro/η^1-*O*-nitrito)nickel) for which the nitrito/nitro equilibrium shifts depending on the temperature. Crystallographic parametric temperature studies could be used to

determine the nitro/nitrito occupancies at different temperatures and calculate the equilibrium constant and the relative energies between the conformations.

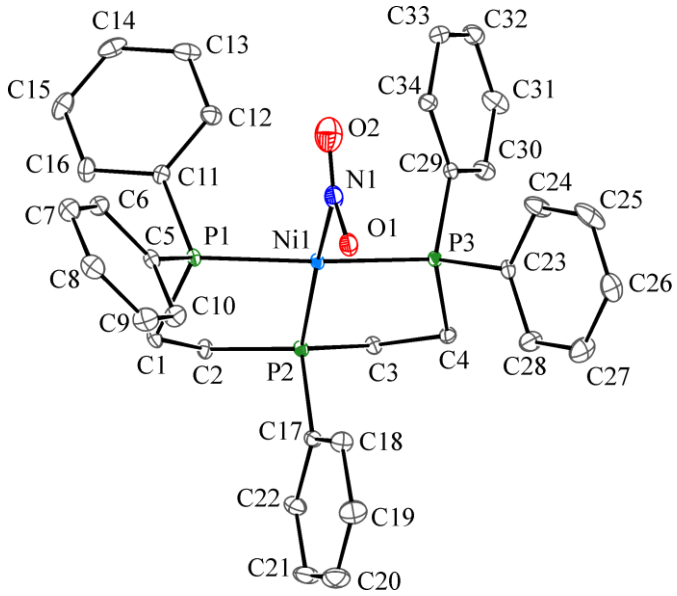

Figure 27: Crystallographic structure of the cationic component of compound **12**. The tetraphenylborate anion and minor component nitrito-(η^1-*ONO*) state have been removed for clarity.

High linkage isomerism conversions were achieved in compounds **9** to **11** in which the phenylphosphine based auxiliary ligand is situated *trans* to the nitrite ambidentate ligand. To test whether high conversions were possible in a system with the nitrite ligand situated *cis*, the synthesis of *bis*(triphenylphosphine)di(η^1-*N*-nitro)nickel was attempted. Unfortunately, the nickel derivative could not be successfully prepared and the phosphine ligands underwent oxidation with the addition of potassium nitrate. A plausible mechanism can be found in literature.[9]

5.3. *Trans* Orientated Nitrate Ligands in Nickel Complexes

5.3.1. *Bis*(triethylphosphine)di(η^1-*N*-nitro)nickel (II) - 13

Compounds **9-12** contain nitrite groups, which are situated *trans* with respect to a phosphorus ligand which could play an important role in the occurrence of the complete transformation. To evaluate whether the phosphine *trans* to the nitro ligand is crucial to the complete linkage isomerism, monodentate triethylphosphine or tricyclohexylphosphine auxiliary ligands were incorporated with the aim of producing a complex in which the nitrite group is situated *cis* to the phosphorus ligand. Compound **13** was synthesised using a procedure from literature,[10] and orange crystals suitable for X-ray diffraction experiments were obtained *via* slow evaporation from DCM/toluene (Scheme 5).

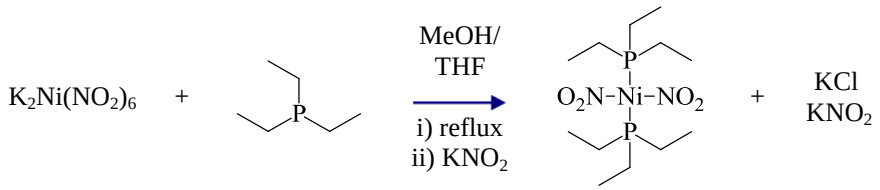

Scheme 5: Synthesis of compound **13**.

Compound **13** crystallizes in the monoclinic space group $P2_1/c$. The square planar nickel atom sits on an inversion centre and is bound to phosphorus (P1) and a nitro (N1) and their symmetry equivalents, with bond lengths of 2.2324(10) and 1.8725(19) Å, respectively. The only short intermolecular interaction involving the nitrite group is between O1 and H6A with an interatomic distance of 2.5200(20) Å. This structure was of good quality and could be used as a comparison against subsequent metastable data sets.

The crystal was irradiated with six 400 nm LED for a period of 10 min, after which the irradiation was stopped and a metastable data set was obtained. The resulting crystal structure had a total conversion from nitro-(η^1-NO_2) to nitrito-(η^1-*O*NO) of 26%, with 74% of the ground state component still remaining (Figure 28). Subsequent irradiation in an attempt to achieve higher conversion caused the crystal to completely decompose and a data set was not able to be obtained.

The 25% conversion of the nitrito-(η^1-*O*NO) species was disordered over two positions. The nitrito species is split into two parts with an *endo*-nitrito-(η^1-*O*NO) (Figure 29b) and an *exo*-nitrito-(η^1-*O*NO) (Figure 29c) with occupancies of 16% and 9% respectively. There was evidence of a third *endo*-nitrito-(η^1-*O*NO) component with very low conversion in the reverse direction from the existing nitrito group O1A-N1A-O2A, but this could not be modelled satisfactorily.

Variable temperature parametric studies were carried out to establish the temperature range at which the photoactivated metastable species converts back to the ground state. The temperature was slowly increased from 100K and data sets were collected at regular intervals. The metastable species exists with high occupancies between temperatures of 100 K – 220 K and completely reverts back to the ground state at 250 K.

a)

b)

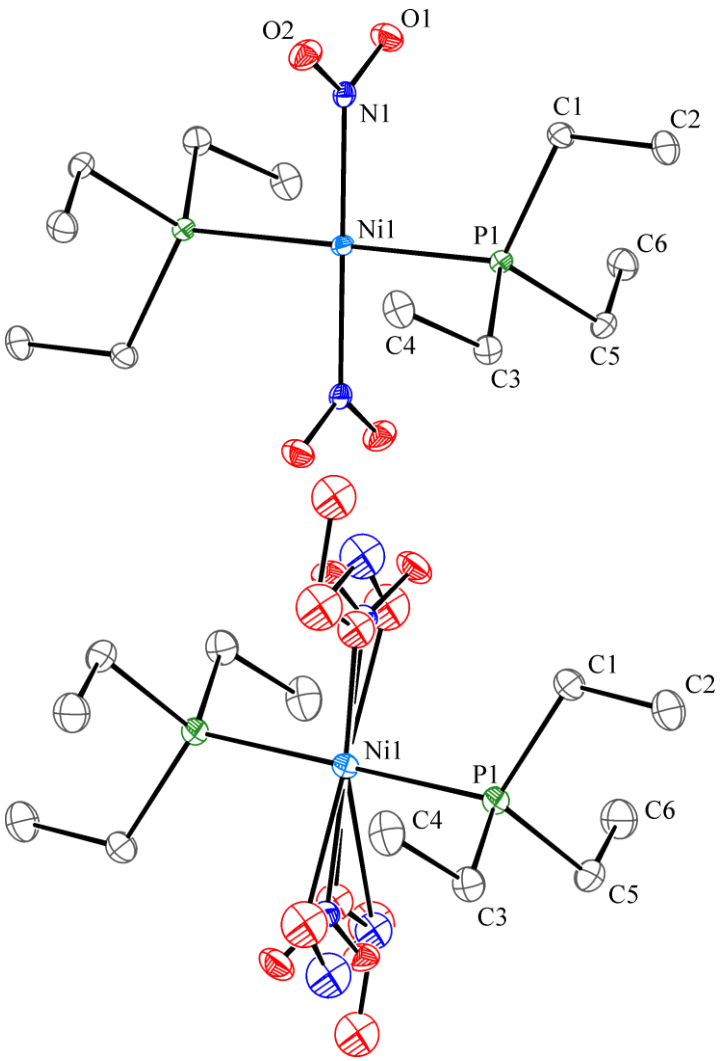

Figure 28: Compound **13** a) Ground state X-ray structure and b) metastable state after irradiation X-ray structures of with thermal ellipsoids set at 30% probability and hydrogen atoms removed for clarity.

Table 5: Crystallographic data for compounds **13.**

	Ground State	Metastable State
η^1-*O*-nitrito occupancy	0%	26%
Empirical formula	C12 H30 N2 Ni O4 P2	C12 H30 N2 Ni O4 P2
Formula weight	387.03	387.03
Temperature	100(2) K	100(2) K
Wavelength	0.68960 Å	0.68960 Å
Crystal system	Monoclinic	Monoclinic
Space group	*P*2(1)/*c*	*P*2(1)/*c*
Unit cell dimensions	*a* = 7.839(4) Å	*a* = 7.890(4) Å
	b = 7.814(4) Å	*b* = 7.787(3) Å
	c = 15.152(11) Å	*c* = 15.251(6) Å
	β = 95.15(4)°	β = 94.82(2)°
Volume	924.4(9) Å^3	933.6(7) Å^3
Z	2	2
Crystal size	0.05 x 0.05 x 0.03 mm	0.05 x 0.05 x 0.03 mm
Theta range for data collection	3.60 to 29.77°	3.60 to 29.77°
Independent reflections	2731 [*R*(*int*) = 0.0523]	2743 [*R*(*int*) = 0.0271]
Completeness to theta	99.2 %	98.6 %
Data / restraints / parameters	2731 / 0 / 100	2743 / 13 / 125
Final R indices [I>2sigma(I)]	*R*1 = 0.0443, *wR*2 = 0.0930	*R*1 = 0.0287, *wR*2 = 0.0717
R indices (all data)	R1 = 0.0494, wR2 = 0.0947	R1 = 0.0327, wR2 = 0.0735

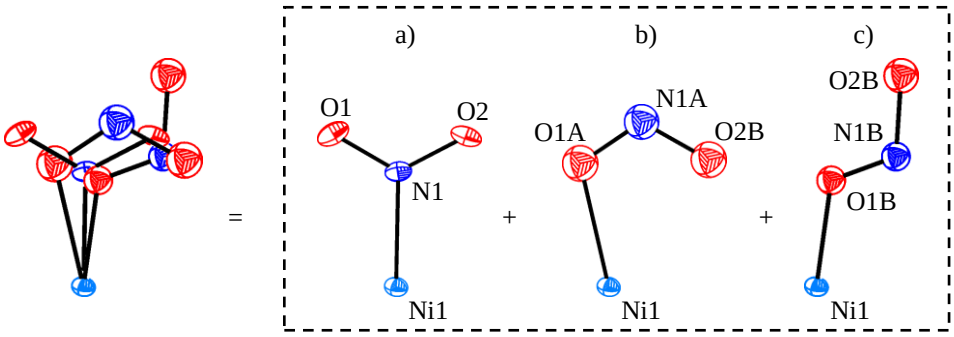

Figure 29: Constituent compounds of the nitro/nitrito transformation in compound **13**, a) ground state species nitro-(η^1-*N*O_2), b) metastable species *endo*-nitrito-(η^1-*O*NO); c) metastable *exo*-nitrito-(η^1-*O*NO) thermal ellipsoids set at 30% probability.

Figure 30 shows the Slant plane Fourier maps of the comparison between the ground and metastable state structures of compound **13**, with the reduction of election density (dotted red lines) around the positions of the nitro-(η^1-*N*O_2) (N1-O1-O2), and with an increase in the electron density (solid blue lines) accountable for the *endo*-nitrito-(η^1-*O*NO) (N1A-O1A-O2A) metastable species and *exo*-nitrito-(η^1-*O*NO) (N1B-O1B-O2B) metastable species (Figure 30).

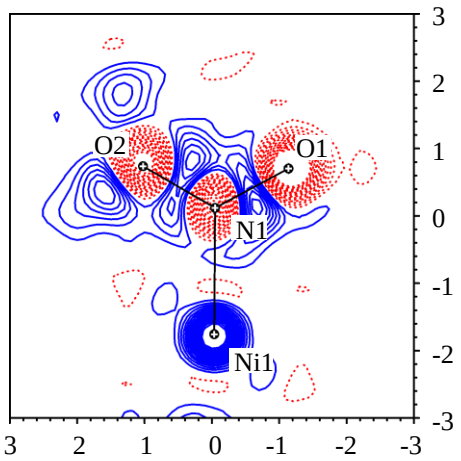

Figure 30: Compound **13** Slant plane fourier maps of the ground state vs. the metastable state of the *Ni1-N1-O1-O2* plane. The contour lines indicate a 0.3 increase (solid blue lines) or decrease (dotted red lines) in electron density. The zero contours are omitted for clarity.

The triethylphosphine ligand is a relatively small auxiliary ligand and this fact could explain why crystal decomposition occurs in compound **13**, whereas in compounds with large auxiliary ligands, for example compound **12,** little crystal decomposition is observed. Using a basic model[3] to predict the average volume of an atom type (similar to 18 Å rule) it is possible to obtain the approximate percentage of atoms in a molecule which move during isomerisation. In compound **13,** the nitro group makes up approximately 15 % of the total molecular volume. This proportion is much larger than for compound **12**, where the nitro group makes up only *ca.* 2.8 % of the total molecular volume.

The UV-visible spectra of compound **13** consist of a major peak at 280 nm, and at about 6% intensity there is a broad absorption at approximately 380 nm (Figure 30). Gas phase DFT calculations were used to find electronic transitions responsible for the linkage isomerism. Even though the DFT calculations were complex, there were some general trends. The strongest absorptions were dominated by transitions from bonding nitro orbitals into antibonding orbitals with respect to the nickel-nitro and nickel-phosphorus bonds. The all electronic transitions from 423 nm to 357 nm are predominantly from non-bonding to antibonding orbitals, with respect to the nickel-nitro and nickel-phosphorus bonds (Figure 31). Figure 32 shows an example of electronic transitions associated with illumination at 410 nm, which involves transitions from non-bonding metal d_{xz}-orbitals and non-bonding nitro *p*-orbitals (HOMO -9) into antibonding orbitals with respects to the nickel($d_{x^2-y^2}$)-nitro and nickel($d_{x^2-y^2}$)-phosphorus (LUMO) (Figure 32). Irradiating at 400 nm can be

associated with either the shoulder of these intense absorptions or at a more specific wavelength from non-bonding nickel orbitals into antibonding nickel-nitro orbitals (Figure 33). Both these transitions would suggest a weakening of the nickel-nitrite bond and could explain the occurrence of the linkage isomerism.

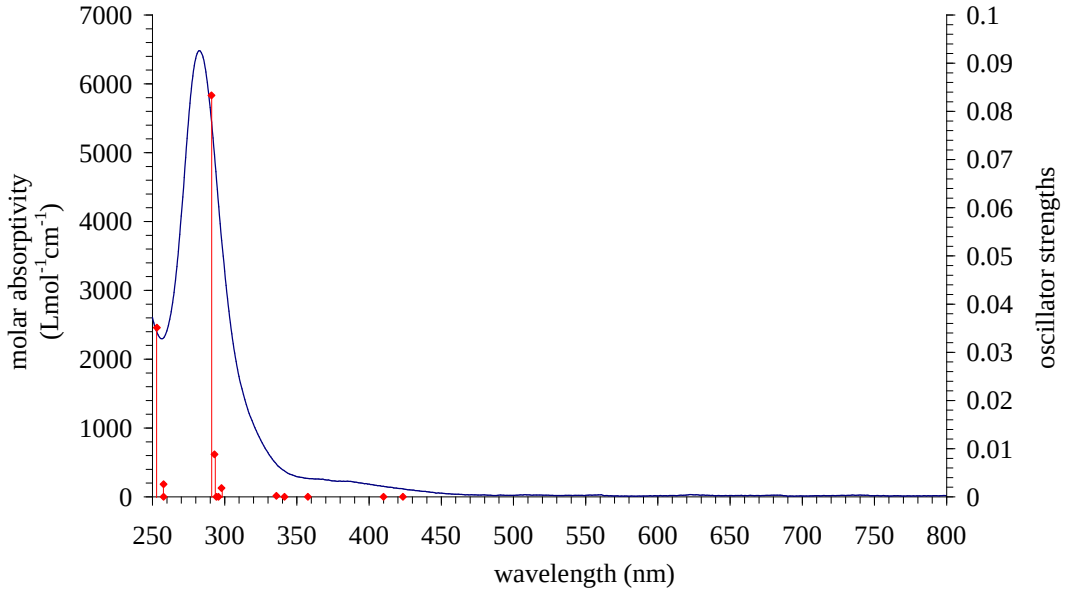

Figure 31: UV-visible spectra and DFT calculated oscillator strengths for compound **13**.

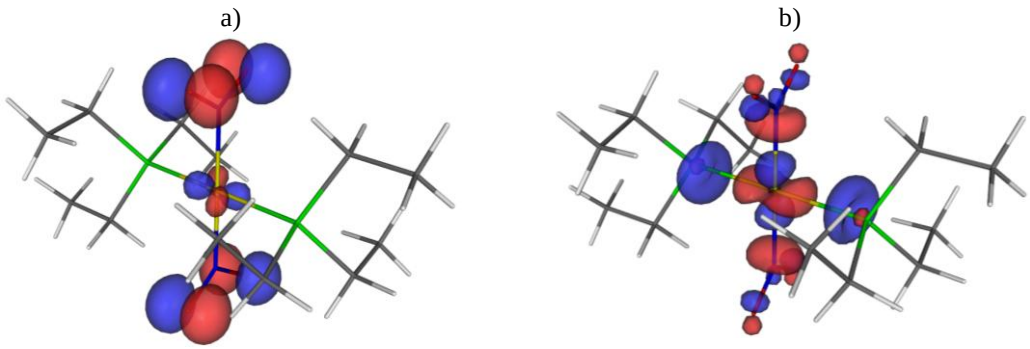

Figure 32: Compound **13** molecular orbitals for the transition at 410 nm from a) non-bonding nickel(d_{xz}) and non-bonding NO_2 orbitals into b) antibonding orbital with respects to the nickel-nitro and nickel-phosphorus.

5.3.2. *Bis*(tricyclohexylphosphine)di(η^1-*N*-nitro)nickel(II) - 14

The ligand tricyclohexylphosphine was used to investigate another system which contains a nitro-(η^1-*N*O_2) group *cis* to the phosphorus auxiliary ligand with increased ligand size, so that nitro group is a smaller proportion to the entire complex, in the hope of reducing crystal decomposition upon irradiation. Compound **14** can be directly compared to compound **10** which contains the bidentate equivalent (1,2-*bis*(dicyclohexylphosphino)ethane). Compound **14** was synthesised using a modified literature preparation.[6] Anhydrous nickel chloride was treated with two equivalents of tricyclohexylphosphine; the product was then filtered and the recrystallized product was reacted with potassium nitrite. Orange crystals suitable for X-ray diffraction experiments were produced from the DCM/THF solution (Scheme 6).

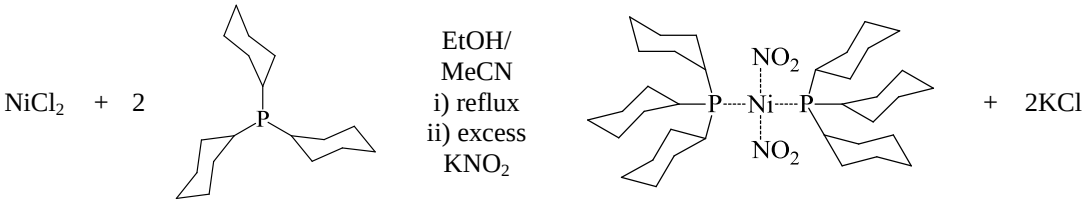

Scheme 6: Synthesis of compound **14**.

The ground state structure crystallizes in the triclinic space group *P*-1. The square planar nickel centre (Ni1) sits on an inversion centre and is bound to phosphorus (P1), and nitrogen (N1) and their symmetry related atoms, with bond lengths of 1.899(2) Å and 2.2881(7) Å, respectively. The nitro-(η^1-*N*O_2) group is situated *cis* to the phosphorus ligands and is *trans* to its symmetry related partner. The structure shows no significant residual electron density and could be used as a comparison against metastable structures (Figure 33a).

The crystal was irradiated using six 400 nm LEDs for a period of 11 min, after which the light source was removed and a data set was obtained. The resulting crystal structure (Figure 33a) had three different components consisting of the nitro-(η^1-*N*O_2) ground state species, a *endo*-nitrito(η^1-*O*NO) and an *exo*-nitrito(η^1-*O*NO) species, having occupancies of 17%, 63% and 20% respectively (Figure 34). The *endo*-nitrito(η^1-*O*NO) (O1A-N1A-O2A) species could easily be modelled; the other two components with low occupancies could clearly be observed in the residual electron density peaks, but needed a number of restraints for the species to refine

sensibly. The data quality in the irradiated crystal is reduced with the smearing of peaks and a loss of resolution; consequently the exposure time was double to counteract the degradation. The reduction in data quality was observed as soon as the crystal was subject to irradiation. The highest conversion of 82 % was obtained before the dataset was of inadequate quality and not publishable.

a)

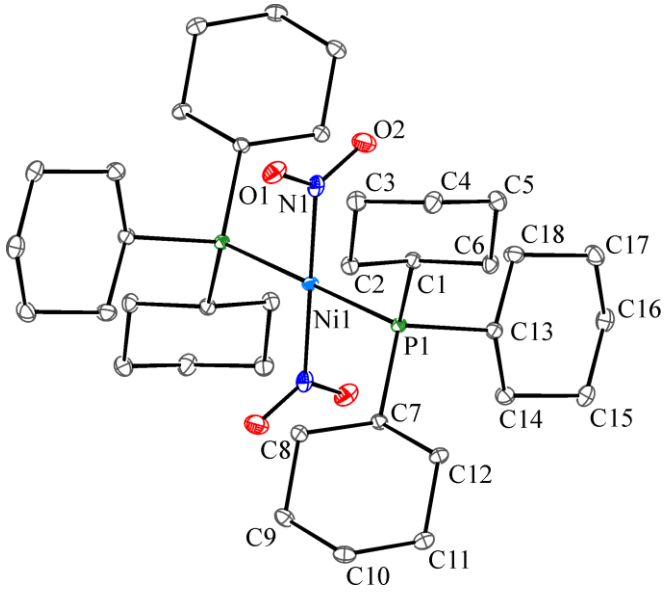

b)

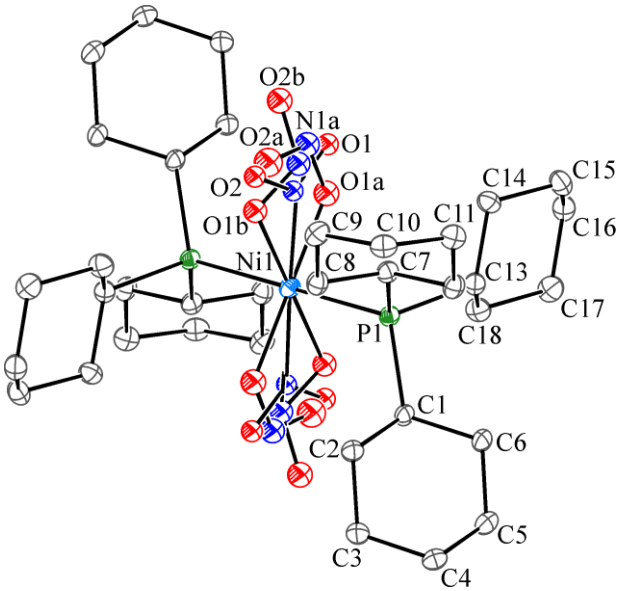

Figure 33: Solid state structure of compound **14** a) ground-state, b) metastable-state after irradiation. Thermal ellipsoids set at 30% probability and hydrogen atoms removed for clarity.

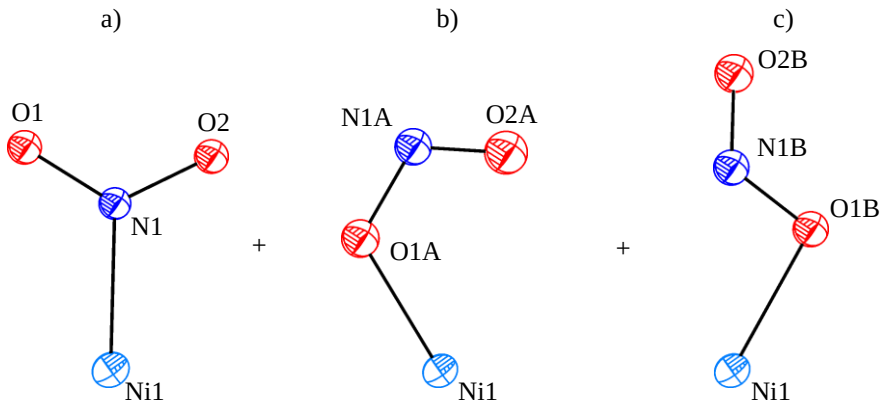

Figure 34: Constituent components of the nitro/nitrito transformation a) ground state species nitro-(η^1-NO_2); b) metastable species *endo*-nitrito-(η^1-*O*NO) thermal ellipsoids set at 30% probability; c) metastable *exo*-nitrito-(η^1-*O*NO).

Table 6: Crystallographic data for compound **14**.

	Ground state	Metastable state
η^1-*O*-nitrito occupancy	0%	83%
Empirical formula	C36 H66 N2 Ni O4 P2	C36 H66 N2 Ni O4 P2
Formula weight	711.56	711.56
Temperature	100(2) K	100(2) K
Wavelength	0.77490 Å	0.77490 Å
Crystal system	Triclinic	Triclinic
Space group	*P*-1	*P*-1
Unit cell dimensions	a = 10.084(2) Å	a = 10.005(4) Å
	b = 10.369(2) Å	b = 10.344(4) Å
	c = 10.464(2) Å	c = 10.713(4) Å
	α = 111.269(3)°	α = 112.515(6)°
	β = 110.575(3)°	β = 110.465(6)°
	γ = 94.503(3)°	γ = 93.518(6)°
Volume	927.5(3) Å^3	934.9(7) Å^3
Z	1	1
Crystal size	0.04 x 0.03 x 0.03 mm	0.04 x 0.03 x 0.03 mm
Theta range for data collection	2.96 to 33.69°	3.00 to 33.81°
Independent reflections	5575 [*R*(*int*) = 0.0926]	5619 [*R*(*int*) = 0.0531]
Completeness to theta	99.3 %	99.2 %
Data / restraints / parameters	5575 / 0 / 206	5619 / 13 / 217
Final R indices [I>2sigma(I)]	*R*1 = 0.0778, *wR*2 = 0.2008	*R*1 = 0.0596, *wR*2 = 0.1524
R indices (all data)	*R*1 = 0.0888, *wR*2 = 0.2118	*R*1 = 0.0988, *wR*2 = 0.1726

Overlaying the crystal structures of the ground state and metastable state of compound **14** shows there is very little change in the conformation, with a mean squares positional change (RMS) of non-hydrogen atoms excluding the nitro/nitrito groups to be 0.0304 Å. The unit cell volume changes by 1% from 927.53(3) to 934.89(7) Å. The *Ni-P1* distance changes from Ni1 P1 2.2881(7) Å in the ground state to Ni1 P1 2.2942(10) Å in the excited state (Table 6).

The Slant Fourier maps of the comparison between the ground state structure and the excited state structure of compound **14** show the reduction of election density

(dotted red lines) around the positions of the nitro-(η^1-NO_2) (N1-O1,O2) and an increase in electron density (solid blue lines) accountable for the *endo*-nitrito-(η^1-*O*NO) (N1A-O1A-O2A) metastable species (Figure 35). The electron density map does not clearly show the *exo*-nitrito-(η^1-*O*NO) (N1B-O1B-O2B) metastable species as it is not in the plane. Variable temperature parametric studies were carried out to establish the temperature range at which the photoactivated metastable species converts back to the ground state. The temperature was slowly increased from 100 K and data sets were collected at regular intervals. The metastable species exist between temperatures of 100 K – 130 K and converts back to the ground state at 140 K.

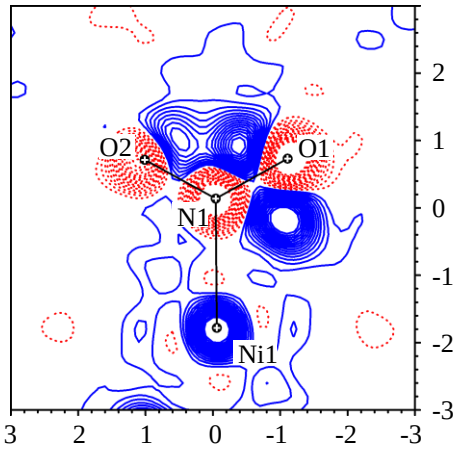

Figure 35: Slant plane fourier maps of the ground state vs. the metastable state of the Ni1-N1-O1-O2 plane. The contour lines indicate a 0.5 increase (solid blue lines) or decrease (dotted red lines) in electron density. The zero contours are omitted for clarity.

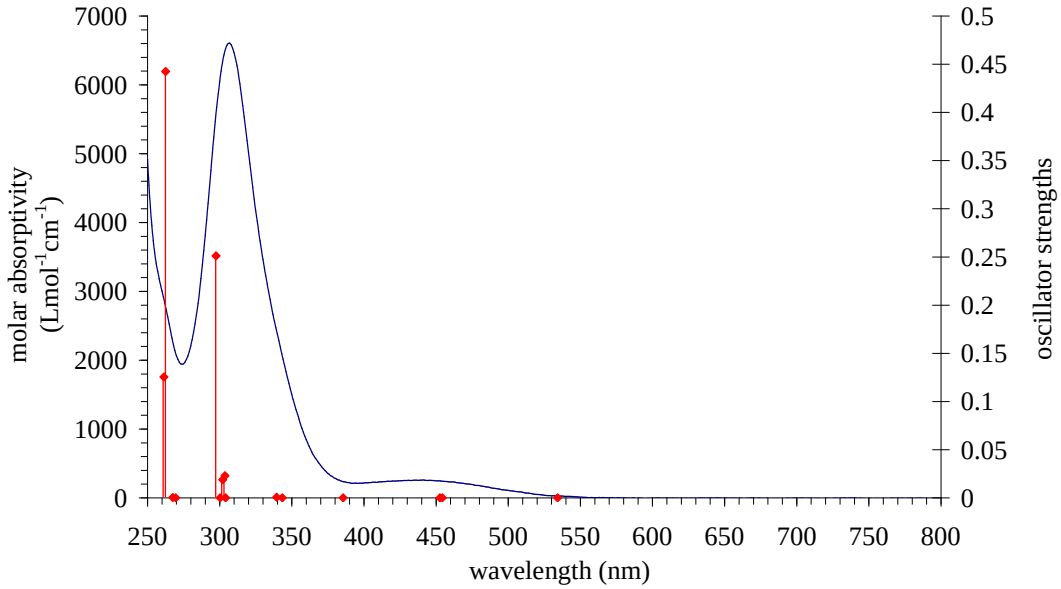

Figure 36: UV-visible spectra of and DFT calculated oscillator strengths for compound **14**.

The UV-visible spectra has a major absorption peak at 305 nm and a weaker broad absorption at 440 nm. Gas phase DFT calculations were used to find electronic transitions responsible for the linkage isomerism.

The predicted electronic transitions from DFT calculations have the correct energy gaps corresponding to the wavelength, but a reduction in absorption intensity in the ultravilot and visible wavelengths range, compared with the experimental UV-visible spectra. All calculated electronic transitions from 534 nm to 261 nm are dominated by transitions from non-bonding orbitals into anti-bonding metal-nitro orbitals. An example of one possible transition (Figure 37) is from the nitro non-bonding (HOMO -15) into the antibonding (LUMO) which is associated with nickel-nitro and nickel-phosphorus bonds. These transitions could result in the weakening of the metal-nitro bond and might explain the occurrence of the linkage isomerism.

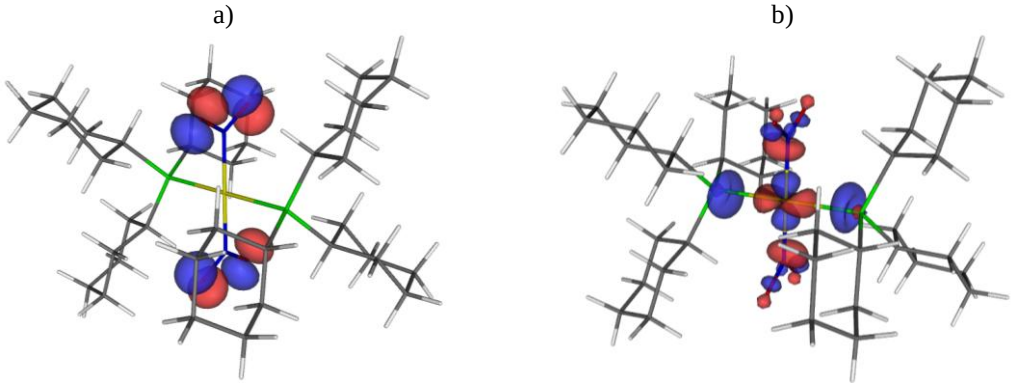

Figure 37: Compound **14** molecular orbitals for the 385 nm transition from a) non-bonding nickel(d_{xy}) orbitals (HOMO -15) to b) antibonding nickel($d_{x^2-y^2}$)-NO_2 orbitals 'b' (LUMO).

A crystal of compound **14** was cooled to 115 K on the variable-temperature stage and a ground state spectrum was obtained (Figure 38). The spectra contains a $\delta(NO_2)$ band at 826 and 829 cm^{-1}, typical of the nitro conformation. The crystal was then irradiated using the 400 nm UV LEDs for a period of 10 min, after which a metastable spectrum was obtained. The $\delta(NO_2)$ intensity changes for the bands at 826, 829 and 856 cm^{-1}. The conversion amount is unclear from the changes in intensity, but suggests that only part excitation is achieved (approximately 20 %) (Figure 38).

On the photoactivated crystal, parametric variable temperature studies were carried out from 120 K to 300 K with Raman spectra being recorded every 10 K. The metastable state fully converted back to the ground state spectra at 140 K.[3-4]

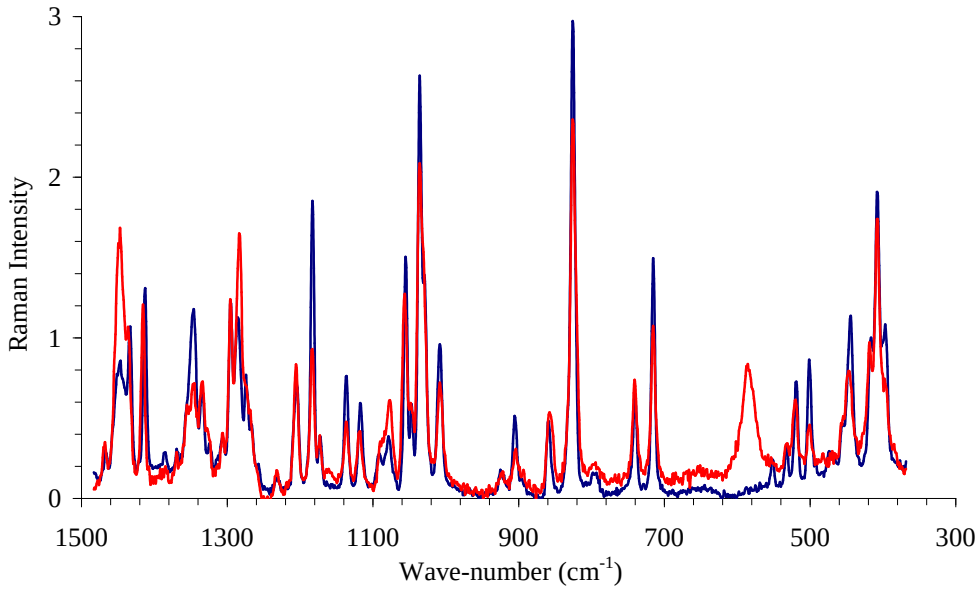

Figure 38: Solid-state Raman spectra at 115 K of before (blue) and after (red) photolysis of compound **14**.

Compounds **13** and **14** contain nitro groups and are mutually *trans* and situated *cis* to the phosphine auxiliary ligand. The photoactivation of these systems produces metastable states with both *endo*- and *exo*- nitrito conformation. Inspecting the void space around the nitro group shows there are no spatial restrictions and either conformation is possible. The *exo*-nitrito-(η^1-*O*NO) in compounds **13** and **14** may be more stable than the systems which contain the bidentate phosphines. The metastable state of *exo*-nitrito-(η-*O*NO) has been observed in other nitrite systems within literature in which the nitro groups are mutually *trans*.[11]

Compound **11** contains a *bis*(dicyclohexylphosphino)ethane ligand; the bidentate ligand produces a system in which the nitrite groups are *trans* to the phosphorus atoms. Compound **14** contains the monodentate of the auxiliary ligand; with the incorporation of the tricyclohexylphosphine ligand, the nitrite ligand is situated *cis* to the phosphorus atom and *trans* to another nitrite ligand. These structures have similar ligand properties and can be used as a direct comparison between *cis* and *trans* conformations. The UV spectra of compounds **11** and **14** are comparable with the major absorption peak around 300 nm and a weaker broad absorption at 440 nm.

There are distinct differences in the photoactivation of these systems. In photocrystallographic experiments, compound **11** reaches a 100 % conversion from nitro-(η^1-NO_2) to nitrito-(η^1-*ONO*) after 20 minutes of irradiation; whereas compound **14** decomposes upon irradiation and a maximum of 82 % conversion is observed after 11 min. Further irradiation causes the data quality to significantly deteriorate and a structure solution is no longer possible. Inspecting the packing of the structure could help with the understanding of why compound **14** undergoes greater decomposition upon irradiation compared to compound **11**. Compound **11** contains 18 close contacts (sum of van der Waal radii) of which 10 are involved with the nitrite group (56 %), compared to compound **14,** in which there are 20 close contacts, and of those 16 are involved with the nitrite group (80 %). This increase in proportion of close contacts with the nitrite group could explain the increase in decomposition upon irradiation. A basic model[3] is used to compare the proportion of the crystal which changes upon irradiation between compounds **11** and **14.** The nitrate group in compound **11** occupies approximately 7.7 % of the total molecular volume which moves during the linkage isomerism process. This is a comparable proportion to compound **14** in which 7 % of the crystal moves during linkage isomerism. Therefore the proportion of the crystal is not the underlying reason for crystal degradation.

Likewise, the changes in unit cell dimension in compounds **13** and **14** are very comparable, with the greatest difference in one axis of 2.3 % for both systems. Therefore, unit cell distortions are not a determining factor for reduction in data set quality upon irradiation.

One possible explanation of the data quality degradation which has not been explored during this comparison is the overlap of absorption peaks of the ground state and metastable states at 400 nm. If there is an overlap in the absorption, irradiating at this wavelength would cause both the forward and backward conversion and would result in an equilibrium between the two states. Also, the continuous flipping between the nitro and nitrito species could cause a greater movement within the lattice contributing toward crystal decomposition.

5.4. Nitrate Ligands in Palladium Complexes

5.4.1. *Bis*(tricyclohexylphosphine)di(η^1-*N*-nitro)palladium(II) - 15

To further investigate the occurrence of the complete linkage isomerism transformation in compounds **9** and **11**, nickel was substituted with a palladium metal centre. Palladium is also a group 10 element and produces comparable metal (II) complexes, but with different orbital configurations. The change in electronic configuration could alter the linkage isomerism capabilities.

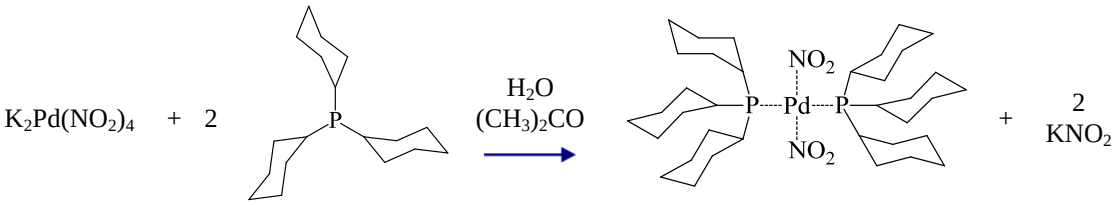

Scheme 7: Synthesis of compound **15**.

Compound **15** was synthesized according to literature methods[12] and colourless crystals suitable for X-ray structure experiments were obtained *via* slow evaporation from the DCM/Acetone solution (Scheme 7). Compound **15** crystallizes in the triclinic space group *P*-1 (Figure 39a). The packing configuration and unit cell dimensions are comparable to the nickel analogue (compound **14**) and therefore direct comparisons can be made between the two systems**.** The square planar palladium centre (Pd1) sits on an inversion centre and is bound to phosphorus (P1) and nitrogen (N1) and their symmetry related atoms with bond lengths of 2.022(3) Å and 2.3789(11) Å, respectively. The nitro-(η^1-*N*O_2) group is situated *cis* to the phosphorus ligands and is *trans* to its symmetry-related partner. The structure showed no significant residual electron density around the nitro ligand and could be used as a comparison against metastable structures.

The crystal was irradiated at 100 K using five 400 nm LEDs for a period of 338 min, after which the irradiation was stopped and a metastable dataset was obtained. The resulting crystal structure had a conversion of 44% from nitro-(η^1-*N*O_2) to nitrito-(η^1-*O*NO) (Figure 39a). Even with prolonged irradiation, higher conversions were not possible and the reaction had thus reached the photostationary point. The 44%

conversion of the nitrito species was disordered over two positions with 23% and 21% *endo*-nitrito-(η^1-*O*NO) (Figure 40).

a)

b)

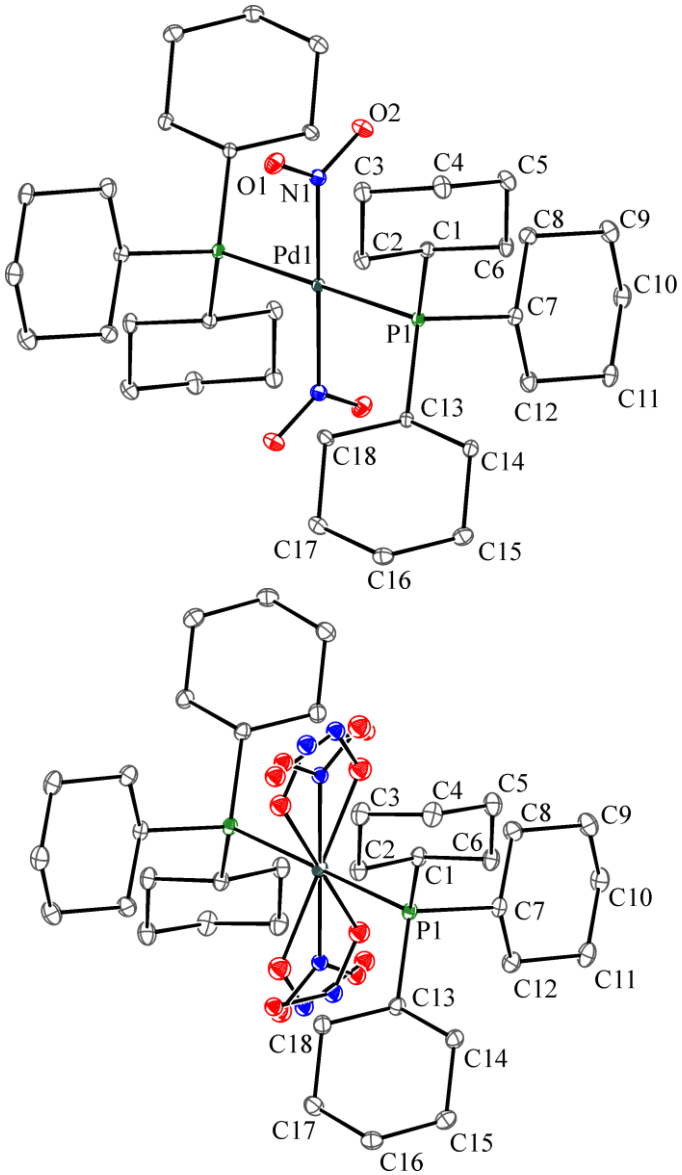

Figure 39: a) Ground-state X-ray structure of compound **15**; b) irradiated metastable-state X-ray structure of $Pd(PPh_3)_2(\eta^1$-*N*O2)$_2$ with thermal ellipsoids set at 30% probability and hydrogen atoms removed for clarity.

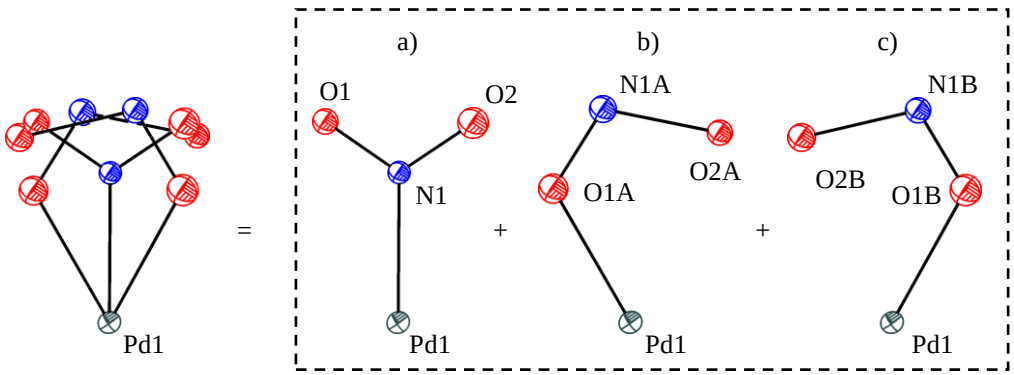

Figure 40: Constituent components of the nitro/nitrito transformation, a) ground state species nitro-(η^1-NO_2); b) and c) metastable species nitrito-(η^1-*O*NO). Thermal ellipsoids set at 30% probability.

Table 7: Crystallographic data of compound **15** before and after irradiation.

	Ground State	Metastable State
η^1-*O*-nitrito occupancy	0%	44%
Empirical formula	C36 H66 N2 O4 P2 Pd	C36 H66 N2 O4 P2 Pd
Formula weight	759.25	759.25
Temperature	100(2) K	100(2) K
Wavelength	0.77490 Å	0.77490 Å
Crystal system	Triclinic	Triclinic
Space group	*P*-1	*P*-1
Unit cell dimensions	a = 10.103(5) Å	a = 10.0521(7) Å
	b = 10.412(5) Å	b = 10.4185(7) Å
	c = 10.582(5) Å	c = 10.6814(7) Å
	α = 111.425(5)°	α = 112.0220(10)°
	β = 110.355(5)°	β = 110.3450(10)°
	γ = 94.508(5)°	γ = 94.0300(10)°
Volume	944.2(8) Å^3	946.07(11) Å^3
Z	1	1
Crystal size	0.08 x 0.08 x 0.07 mm	0.08 x 0.08 x 0.07 mm
Theta range for data collection	2.96 to 30.50°.	2.97 to 34.78°.
Independent reflections	5002 [R(*int*) = 0.0545]	5889 [R(*int*) = 0.0587]
Completeness to theta	87.5 %	99.2 %
Data / restraints / parameters	5002 / 0 / 205	5889 / 13 / 217
Final R indices [I>2sigma(I)]	R1 = 0.0559, wR2 = 0.1620	R1 = 0.0399, wR2 = 0.1033
R indices (all data)	R1 = 0.0591, wR2 = 0.1655	R1 = 0.0425, wR2 = 0.1054

The Slant Fourier maps of the comparison between the ground state structure and the excited state structure of compound **15** shows the reduction of election density (dotted lines) around the positions of the nitro-(η^1-*N*O_2) (N1-O1,O2), and with an increase in electron density (solid lines) representing the nitrito-(η^1-*O*NO) (N1A-O1A-O2A) (Figure 41) and nitrito-(η^1-*O*NO) (N1B-O1B-O2B) metastable species.

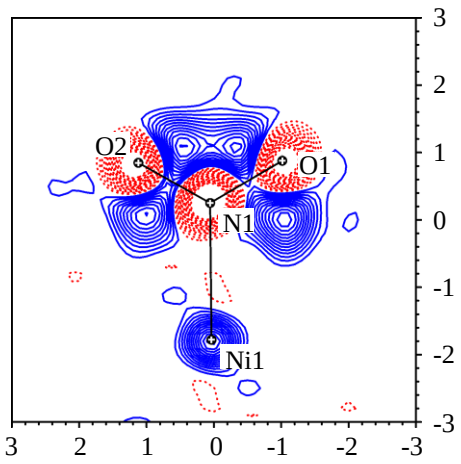

Figure 41: The compound **15** Slant plane fourier maps of the ground state vs. the metastable state of the *Ni1-N1-O1-O2* plane. The contour lines indicate a 0.3 increase (solid blue lines) or decrease (dotted red lines) in electron density. The zero contours are omitted for clarity.

Variable temperature parametric studies were carried out to establish the temperature range at which the photoactivated metastable species converts back to the ground state. The temperature was slowly increased from 100 K and data sets were collected at regular intervals. The metastable species exist with the same occupancy between temperatures of 100 – 170 K. At the temperature of 180 K, the occupancy of the metastable state reduces from 44% to 33% and reduces again to 20% for temperatures of 190, 200 and 230 K. The occupancy of 20 % remains in the crystal structure even at room temperature.

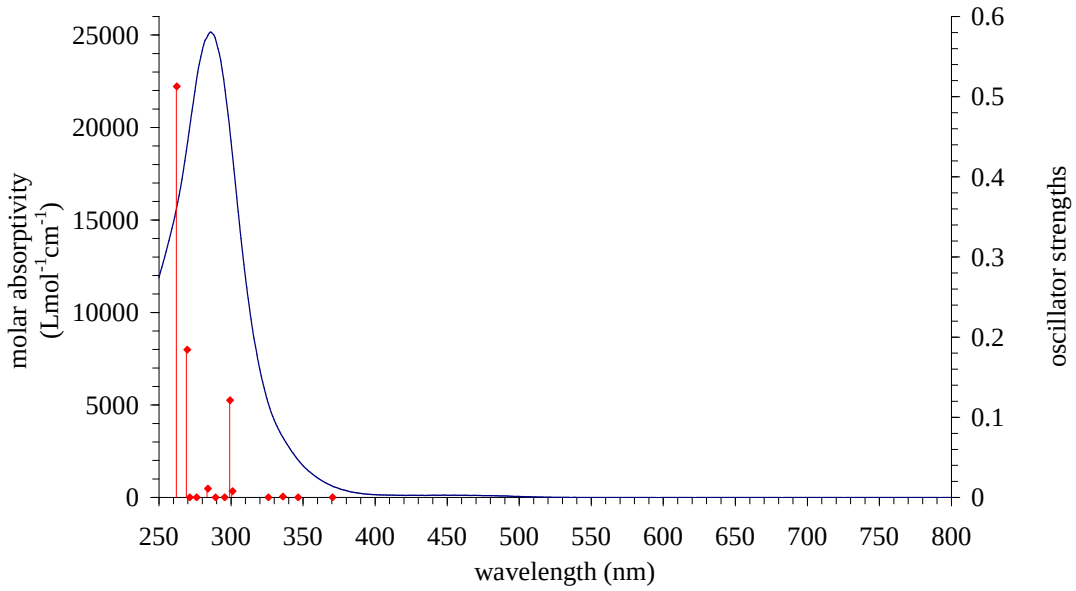

Figure 42: UV-visible spectra of and DFT calculated oscillator strengths for compound **15**.

The UV-visible spectra is dominated by an intense absorption at 285 nm; from the DFT calculation, the large absorption at 285 nm is predominantly associated with an electronic transition from non-bonding tricyclohexylphosphine-based orbitals (HOMO) into antibonding orbitals with respects to palladium-nitro and palladium-phosphorous (LUMO). From DFT analysis, the bulk of the electron transitions are from non-bonding orbital into antibonding orbitals with reference to palladium-nitro and palladium-phosphorous (LUMO). Figure 43 shows an electric transition from bonding *p*-orbitals of the nitro group (Figure 43a) into metal($d_{x^2-y^2}$)-nitro antibonding orbitals. These transitions could be accountable from the weakening of the metal-nitro bond and might explain the occurrence of the linkage isomerism. In photocrystallographic experiments, the crystal was irradiated at 400 nm to give a 44% conversion from nitro-(η^1-NO_2) to nitrito-(η^1-*ONO*). This wavelength is

positioned on the far shoulder of the main absorption peak in the solution-based UV-visible spectrum. Using a 365 nm wavelength LED, which from the UV-visible spectrum and DFT calculation would be a more suitable wavelength, produced comparable results in photocrystallographic experiments.

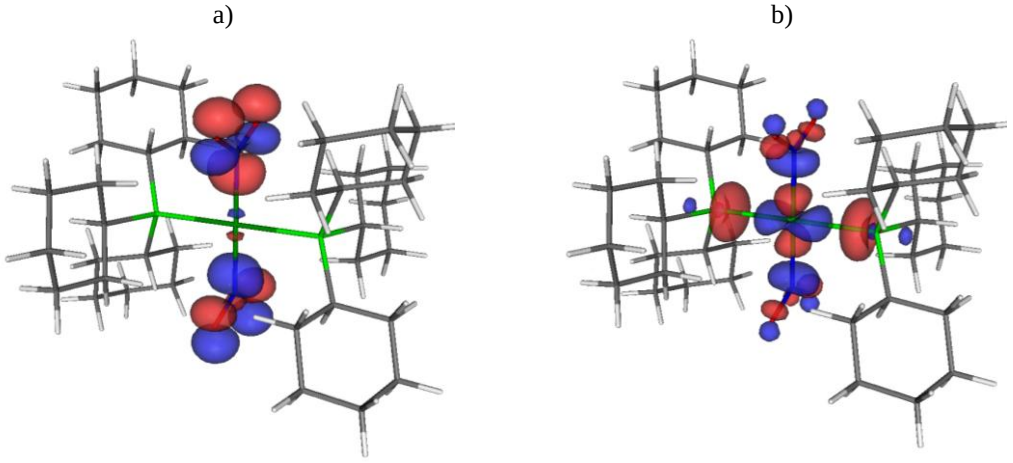

Figure 43: Compound **15** molecular orbitals for a typical transition from a) non-bonding nitro orbitals to b) antibonding palladium($d_{x^2-y^2}$)-NO_2 and palladium ($d_{x^2-y^2}$)-phosphorous orbitals.

A crystal of compound **15** was cooled to 115 K on the variable-temperature stage and a ground state spectrum was obtained (Figure 44). The spectra contained a $\delta(NO_2)$ band at 828 cm^{-1}, typical of the nitro conformation. The crystal was then irradiated using the 400 nm UV LEDs for a period of 100 min, after which a metastable spectrum was obtained. The $\delta(NO_2)$ bending mode corresponding to a peak at 828 cm^{-1}, changes intensity with conversion from nitro to nitrito. The conversion amount is unclear from the changes in intensity, but suggests that only low conversion to the metastable nitrito conformation is achieved, (approximately 12 %) (Figure 44). On the photoactivated crystal, parametric variable temperature studies were carried out from 120 K to 300 K with Raman spectra being recorded every 10 K. The metastable state fully converted back to the ground state spectra at 220 K.[3-4]

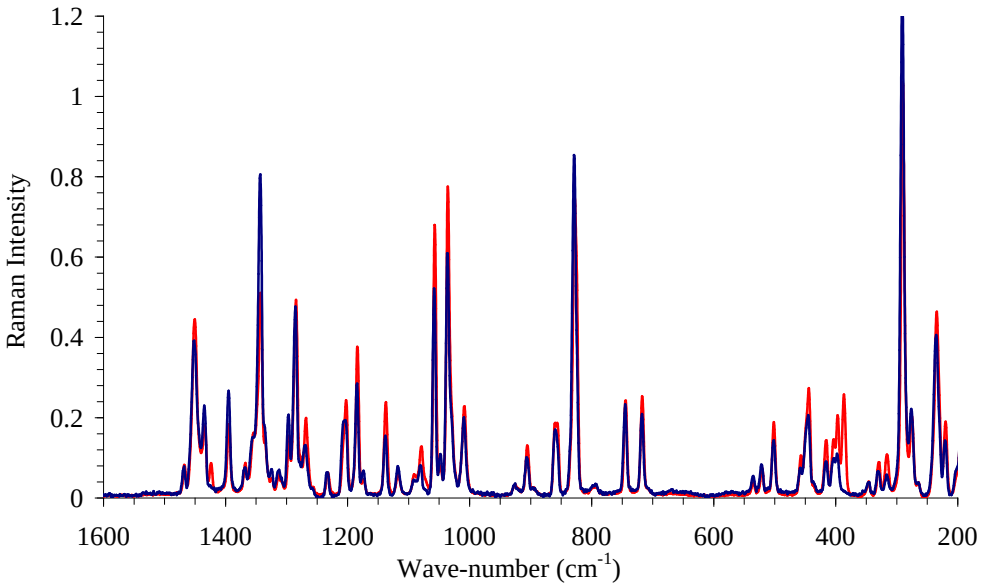

Figure 44: Solid-state Raman spectra at 115 K of before (blue) and after (red) photolysis of compound **15**.

5.4.2. *Bis*(triphenylphosphine)di(η^1-*N*-nitro)palladium (II) - 16

Triphenylphosphine was used as an alternative auxiliary ligand, with a palladium metal centre so that the linkage isomerism process can be compared to compound **11** with the bidentate equivalent 1,2-*bis*(diphenylphosphino)ethane. Compound **16** was synthesised according to literature accounts (Scheme 8).[4]

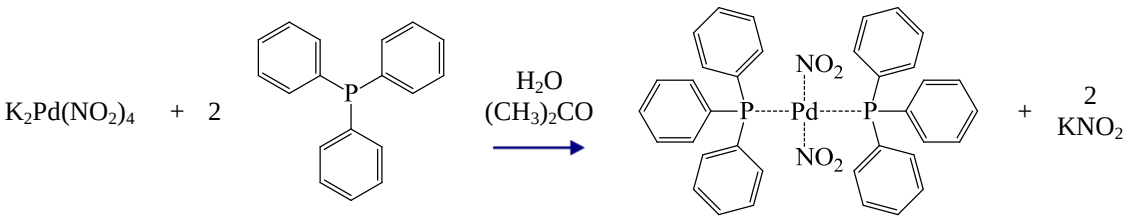

Scheme 8: Synthesis of compound **16**.

Crystals suitable for X-ray experiment were obtained from an acetone/dichloromethane solution. A high quality data set was collected at 100 K to produce a clean ground state absent of the nitrito species (Figure 45a). Compound **16** crystallises in the orthorhombic space group *Pbca*. The square planar palladium is positioned on an inversion centre and is bound to a triphenylphosphine ligand (P1) and nitro-(η^1-NO_2) group (N1) and their symmetry related partners with bond distances of 2.3798(13) and 2.031(2) Å, respectively.

A crystal of compound **16** was irradiated for a period of 288 min using six 362 nm LEDs 1 cm from the crystal. The irradiation was stopped, and after a period for the crystal to equilibrate, using the same strategy as the ground state collection, a high quality data set was obtained. The resulting crystal structure showed a 46 % conversion from the nitro-(η^1-NO_2) to the nitrito-(η^1-*ONO*) isomer upon irradiation (Figure 45b). Further irradiation showed little increase in occupancy of the nitrito-(η^1-*ONO*) species suggesting that the reaction had reached a photostationary point. Repeating the photocrystallographic experiment using 400 nm LEDs gives almost identical results. Interestingly, the crystal shows little sign of decomposition compared to the nickel complexes and could be attributable to little differences in the unit cell dimensions with less than 0.25% alterations (Table 8). There is also insignificant changes in the nickel-phosphorus bond lengths changing from 2.3798(13) to 2.3519(8) upon irradiation.

a)

b)

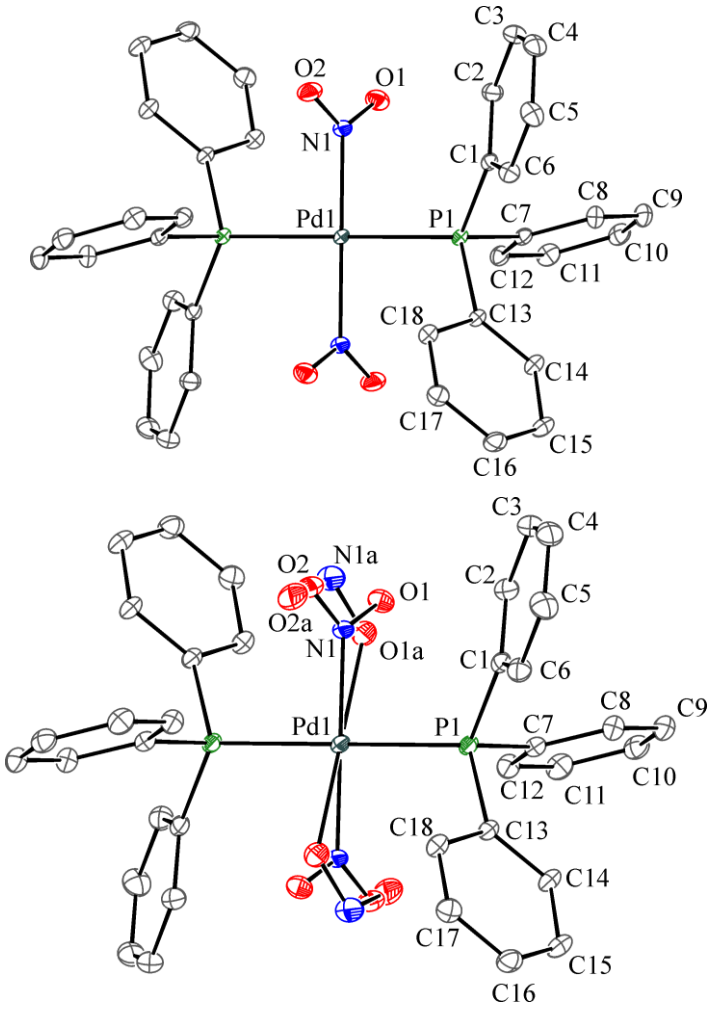

Figure 45: Compound **16** a) Ground-state X-ray structure and b) irradiated metastable state X-ray structure of with thermal ellipsoids set at 30% probability and hydrogen atoms removed for clarity.

Table 8: Crystallographic data for compound **16**.

	Ground state	Metastable state
Empirical formula	C38 H34 Cl4 N2 O4 P2 Pd	C38 H34 Cl4 N2 O4 P2 Pd
Formula weight	892.81	892.81
Temperature	100(2) K	100(2) K
Wavelength	0.77490 Å	0.77490 Å
Crystal system	Orthorhombic	Orthorhombic
Space group	*Pbca*	*Pbca*
Unit cell dimensions	a = 20.690(18) Å	a = 20.629(10) Å
	b = 8.069(7) Å	b = 7.985(4) Å
	c = 23.51(2) Å	c = 23.339(12) Å
Volume	3925(6) Å^3	3845(3) Å^3
Z	4	4
Crystal size	0.03 x 0.03 x 0.01 mm	0.03 x 0.03 x 0.01 mm
Theta range for data collection	3.49 to 33.36°	3.52 to 33.79°
Independent reflections	5807 [R(*int*) = 0.0941]	5879 [R(*int*) = 0.0742]
Completeness to theta	98.8 %	98.7 %
Data / restraints / parameters	5807 / 0 / 232	5879 / 0 / 260
Final R indices [I>2sigma(I)]	R1 = 0.0560, wR2 = 0.1512	R1 = 0.0392, wR2 = 0.1029
R indices (all data)	R1 = 0.0644, wR2 = 0.1624	R1 = 0.0483, wR2 = 0.1108

Parametric variable temperature studies showed that the nitrito-(η^1-*O*NO) metastable state was present with 46% conversion at 180 K, and remained with high occupancies until 230 K. Increasing the temperature of the crystal above 230 K, the metastable state dropped in occupancy and was fully dispersed at 260 K.

Slant plane Fourier maps of the comparison between ground state and metastable state structure of compound **16** clearly shows the reduction in electron density around the nitro-(η^1-*N*O_2) isomer (red dotted lines) and an increase in electron density accountable to the new positions of the nitrito-(η^1-*O*NO) metastable species (blue solid lines). It is to be noted that there is insignificant changes to other regions in the Slant plane Fourier maps which is consistent with thermal ellipsoids and unit cell dimensions remaining essentially unchanged (Figure 46).

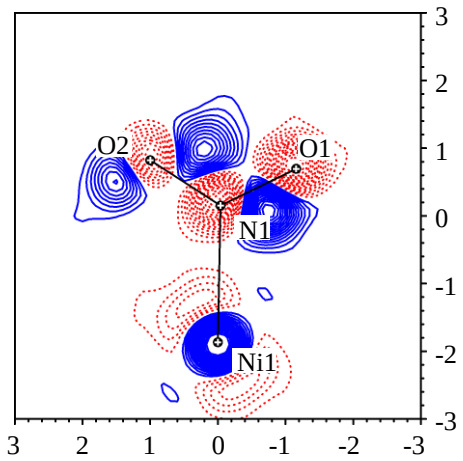

Figure 46: Compound **16** Slant plane fourier maps of the ground state vs. the metastable state of the *Ni1-N1-O1-O2* plane. The contour lines indicate a 0.4 increase (solid blue lines) or decrease (dotted red lines) in electron density. The zero contours are omitted for clarity.

The UV-visible spectra of compound **16** is dominated by an intense absorption at 311 nm. Gas phase DFT calculations were used to find the electronic transition responsible for the linkage isomerism when the complex is irradiated at 362 nm and 400 nm. The experimental spectrum is in perfect agreement with DFT calculation, with the strongest electron transition at 313 nm (Figure 47). Irradiating the crystal at 362 nm is likely to be associated with an electron transition from the shoulder of the most intense peak at 313 nm in which electronic transition occurs between triphenylphosphine-ligand based orbitals (HOMO -2) into LUMO antibonding with respects to both the platinum-nitro and platinum-phosphorus bonds. Irradiating at 400 nm or 362 nm causes linkage isomerism in photocrystallographic experiments. Comparing these results to the possible theoretical electronic transitions, these irradiation wavelengths could be associated with either absorptions from a shoulder of the most intense absorption at 313 nm, or that of a more comparable wavelength (394 nm). These signals are associated with electronic transitions from non-bonding orbitals (HOMO -1), based on the platinum and nitro orbitals, into orbitals (LUMO) antibonding with respect to the platinum-nitro and platinum-phosphorus bonds (Figure 48).

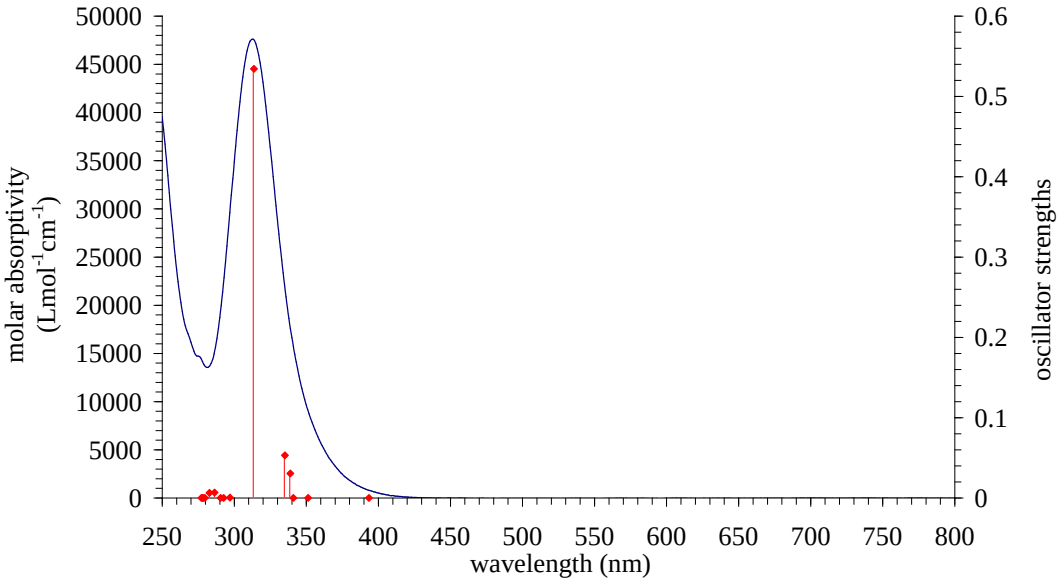

Figure 47: UV-visible spectra of and DFT calculated oscillator strengths for compound **16**.

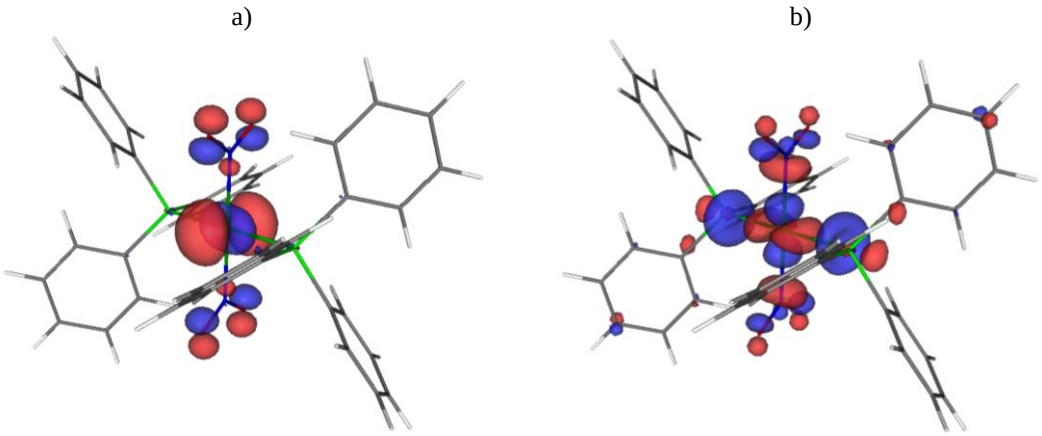

Figure 48: Compound **16** molecular orbitals for the electronic transition at 394 nm from a) non-bonding orbitals (HOMO -1) based on the platinum and nitro orbitals into b) antibonding orbitals (LUMO) with respects to the platinum-nitro and platinum-phosphorus bonds.

5.4.3. *Bis*(triphenylarsine)di(η^1-*N*-nitro)palladium (II) - 17

To investigate the role of the phosphine ligand in the linkage isomerism transformation, triphenylarsine was incorporated to produce a system analogous to compound **16**.

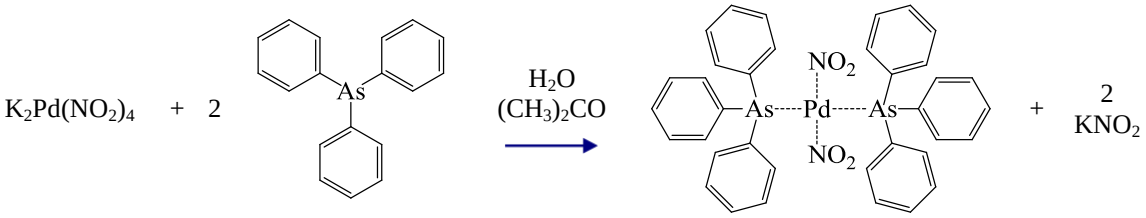

Scheme 9: Synthesis of compound **17**.

Compound **17** was synthesised according to literature accounts (Scheme 9).[4] Crystals suitable for X-ray experiment were obtained from dichloromethane solution. A high quality data set was collected at 100 K to produce a ground state structure in which the nitrito species was absent (Figure 49a). Compound **17** crystallizes in the triclinic space group *P*-1. The square planar palladium is positioned on an inversion centre and is bound to a triphenylarsine ligand (As1) and nitro-(η^1-*N*O$_2$) group (N1) and their symmetry related partners with bond distances of 2.4364(3) and 2.029(3) Å, respectively. There is no residual electron density around the nitro-(η^1-*N*O$_2$) group and this structure can be used as a comparison to subsequent metastable data sets.

a)

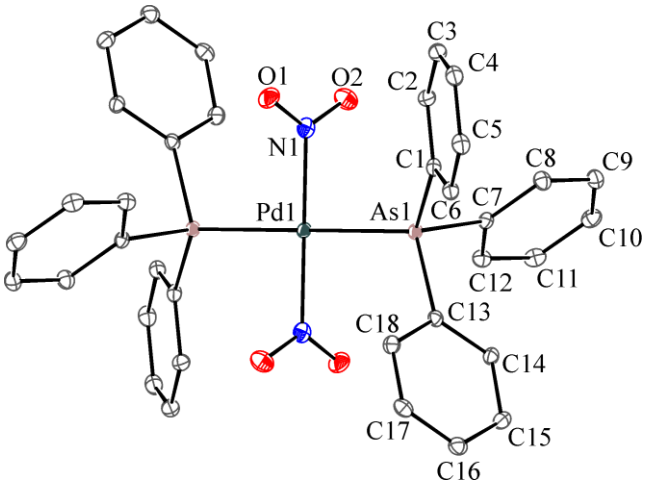

b)

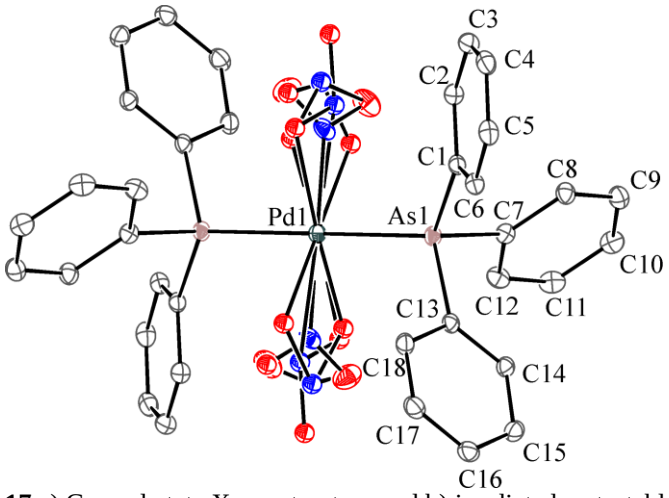

Figure 49: Compound **17** a) Ground-state X-ray structure and b) irradiated metastable-state X-ray structure of with thermal ellipsoids set at 30% probability and hydrogen atoms removed for clarity.

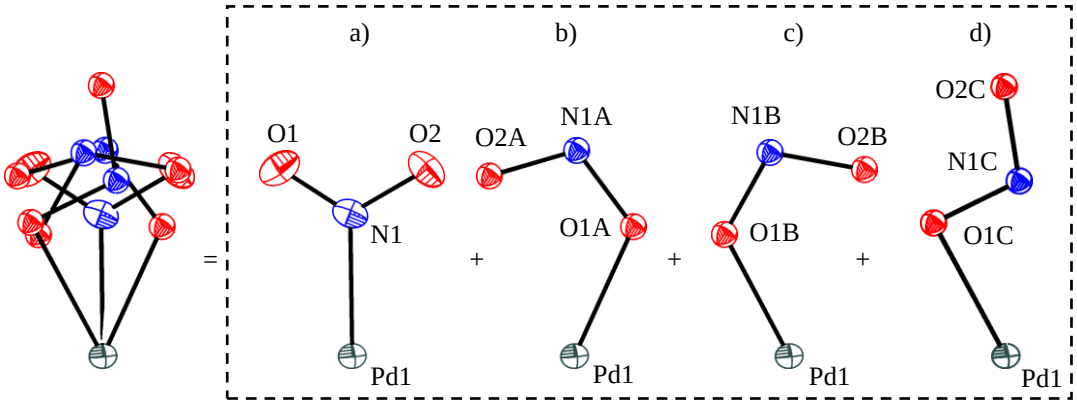

Figure 50: Constituent components of the nitro/nitrito transformation, a) ground state species nitro-(η^1-NO_2); b) and c) metastable species nitrito-(η^1-*O*NO). Thermal ellipsoids set at 30% probability.

Table 9: Crystallographic data of compound **17** before and after irradiation.

	Ground State	Metastable State
η^1-*O*-nitrito occupancy	0%	41%
Empirical formula	C36 H30 As2 N2 O4 Pd	C36 H30 As2 N2 O4 Pd
Formula weight	810.86	810.86
Temperature	100(2) K	100(2) K
Wavelength	0.77490 Å	0.77490 Å
Crystal system	Triclinic	Triclinic
Space group	*P*-1	*P*-1
Unit cell dimensions	a = 9.5940(7) Å	a = 9.5967(9) Å
	b = 9.9987(7) Å	b = 9.9479(9) Å
	c = 10.1274(7) Å	c = 10.1121(9) Å
	α =111.4900(10)°	α = 111.2620(10)°
	β = 90.4730(10)°	β = 90.9310(10)°
	γ =115.2090(10)°	γ = 114.4540(10)°
Volume	802.14(10) Å^3	803.05(13) Å^3
Z	1	1
Crystal size	0.05 x 0.02 x 0.01 mm	0.05 x 0.02 x 0.01 mm
Theta range for data collection	4.02 to 33.59°	4.03 to 33.65°
Independent reflections	4729 [*R*(*int*) = 0.0536]	4795 [*R*(*int*) = 0.0470]
Completeness to theta	97.7 %	98.6 %

Data / restraints / parameters	4729 / 0 / 205	4795 / 13 / 237
Final R indices [I>2sigma(I)]	*R*1 = 0.0525, *wR*2 = 0.1622	*R*1 = 0.0371, *wR*2 = 0.1170
R indices (all data)	*R*1 = 0.0546, *wR*2 = 0.1651	*R*1 = 0.0402, *wR*2 = 0.1213

The crystal was irradiated for a period 300 min using six 400 nm LEDs in a comparable photocrystallographic experiment to the investigation of compound **17**. The resulting crystal structure contains metastable species with total occupancies of 41%. There are three components of the metastable species, two of which are *endo*-nitrito-(η^1-*O*NO) with occupancies of 19 % and 13 %, and an *exo*-nitrito-(η^1-*O*NO) with an occupancy of 8 %. Slate plane Fourier maps of the comparison between the ground and metastable state show the clear reduction in electron density (red dotted lines) around the ground state nitro-(η^1-*N*O_2) isomer and an increase in electron density (blue solid lines) accountable for the new metastable state positions (Figure 51).

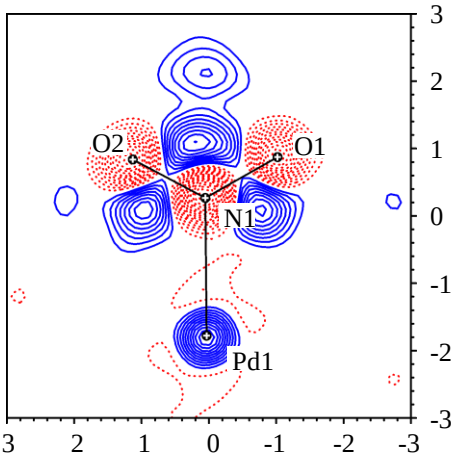

Figure 51: Compound **17** Slant plane fourier maps of the ground state vs. the metastable state of the *Pd1-N1-O1-O2* plane. The contour lines indicate a 0.39 increase (solid blue lines) or decrease (dotted red lines) in electron density. The zero contours are omitted for clarity.

Variable temperature parametric studies were carried out on compound **17** to establish the temperature range over which the metastable states exist. The temperature was increased in 10 K steps with data set collected at each interval. All metastable species exist with equivalent occupancies between 100 K and 160 K. When the temperature is raised to 240 K, the resulting crystal has no evidence of the *exo*-nitrito-(η^1-*O*NO) isomer, and there is a slight decrease in the occupancies of both *endo*-nitrito-(η^1-*O*NO) species. At 250 K, the metastable species has significantly reduced and one *endo*-nitrito-(η^1-*O*NO) species remains with 6 % occupancy. Raising the temperature to 260 K, the *endo*-nitrito-(η^1-*O*NO) can no

longer be modelled and can only be observed in the residual electron density in the structural model. All metastable species have completely dissipated at 270 K.

5.5. Nitrate Ligands in Platinum Complexes

5.5.1. *Bis*(tricyclohexylphosphine)di(η^1-N-nitro)platinum (II) - 18

Nickel and palladium complexes with phosphine auxiliary ligands can switch between the nitro and nitrito isomers upon irradiation. Upon irradiation, the palladium complexes **15** – **17** give metastable states which exist to higher temperatures than similar nickel species. To further investigate the occurrence of the linkage isomerism in different metal centres and to see if the trend continues through group 10 metals, platinum was incorporated.

Compound **18** was prepared by treating a freshly prepared sample of potassium tetranitrateplatinate with two equivalents of tricyclohexylphosphine, and crystals suitable for X-ray experiment were grown from dichloromethane layered with acetone (Scheme 10).

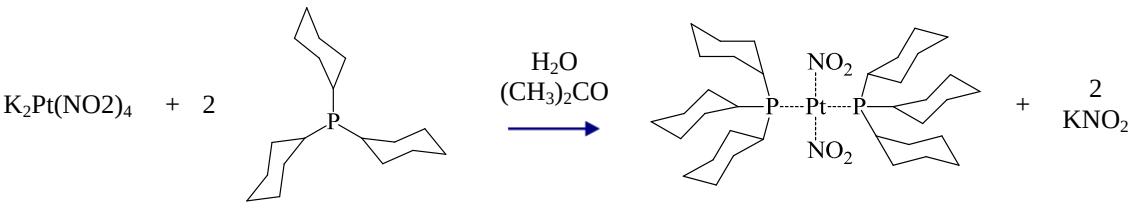

Scheme 10: Synthesis of compound **18**.

The ground state structure crystallized in the triclinic space group *P*-1. The crystallographic structure is comparable to the nickel and palladium analogues. The square planar palladium centre (Pt1) sits on an inversion centre and is bound to phosphorus (P1) and nitrogen (N1), and their symmetry related atoms, with bond lengths of 2.022(3) and 2.3789(11) Å, respectively. The nitro-(η^1-*N*O_2) group is situated *cis* to the phosphorus ligands and is *trans* to its symmetry-related partner. The structure showed no significant electron density around the nitro ligand and the structure could be used as a comparison against metastable structures (Figure 39a).

The crystal was then irradiated for a period of 240 min, after which the irradiation was stopped and a metastable dataset was collected. The resulting crystal structure

showed a linkage isomerism transformation from nitro-(η^1-NO_2) to nitrito-(η^1-ONO) of 20% (Figure 52b). Even with subsequent irradiation, higher conversion was not possible and the reaction had presumably reached a photostationary point.

a)

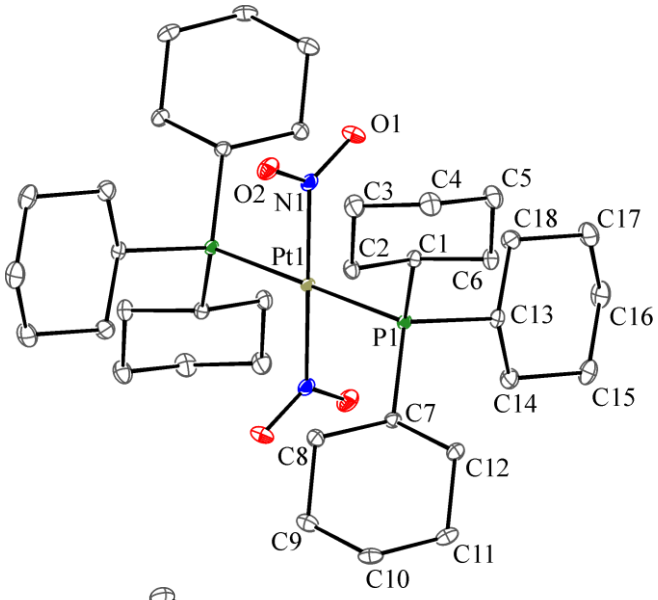

b)

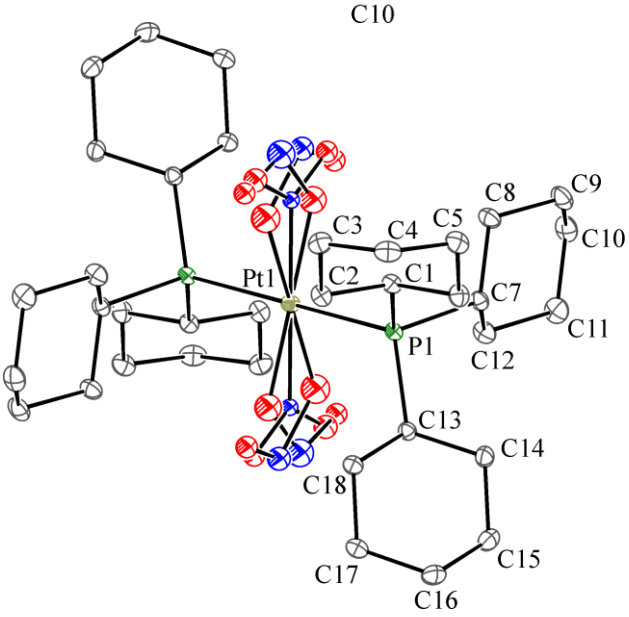

Figure 52: a) Ground-state X-ray structure of compound **18**; b) irradiated metastable-state X-ray structure of $Pt(PCy_3)_2(\eta^1$-$NO_2)_2$ with thermal ellipsoids set at 30% probability and hydrogen atoms removed for clarity.

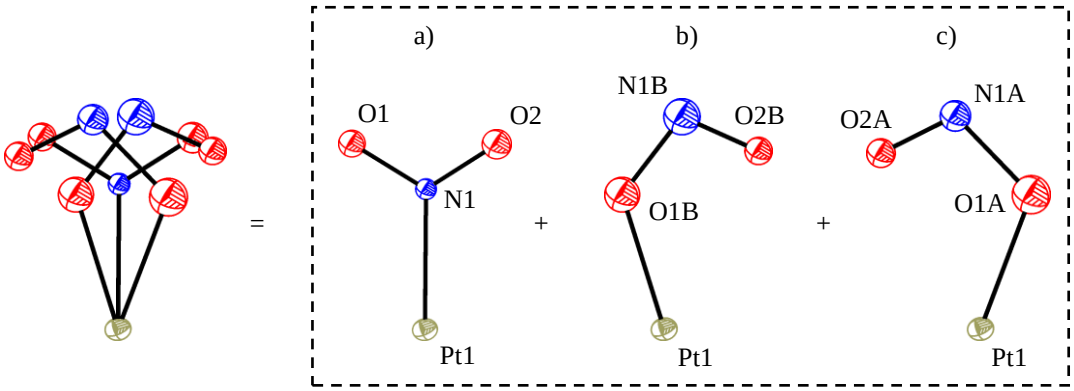

Figure 53: Constituent components of the nitro/nitrito transformation, a) ground state species nitro-(η^1-NO_2) thermal ellipsoids set at 30% probability; b) metastable species nitrito-(η^1-*O*NO).

Table 10: Crystallographic data of compound **18**.

	Ground-state	Metastable-state
η^1-*O*-nitrito occupancy	0%	20%
Empirical formula	C36 H66 N2 O4 P2 Pt	C36 H66 N2 O4 P2 Pt
Formula weight	847.94	847.94
Temperature	100(2) K	100(2) K
Wavelength	0.7107 Å	0.7107 Å
Crystal system	Triclinic	Triclinic
Space group	*P*-1	*P*-1
Unit cell dimensions	*a* = 10.122(5) Å	*a* = 10.107(5) Å
	b = 10.388(5) Å	*b* = 10.428(5) Å
	c = 10.617(5) Å	*c* = 10.676(5) Å
	α = 111.736(5)°	α = 112.184(5)°
	β = 110.638(5)°	β = 110.509(5)°
	γ = 94.229(5)°	γ = 93.825(5)°
Volume	943.3(8) Å^3	949.8(8) Å^3
Z	1	1
Crystal size	0.10 x 0.08 x 0.08 mm	0.10 x 0.08 x 0.08 mm
Theta range for data collection	2.95 to 32.58°	3.43 to 37.91°
Independent reflections	6334 [*R*(*int*) = 0.0287]	9014 [*R*(*int*) = 0.0430]
Completeness to theta	99.8 %	96.9 %
Data / restraints / parameters	6334 / 0 / 205	9014 / 7 / 218
Final R indices [I>2sigma(I)]	*R*1 = 0.0185, *wR*2 = 0.0352	*R*1 = 0.0340, *wR*2 = 0.0559
R indices (all data)	*R*1 = 0.0185, *wR*2 = 0.0352	*R*1 = 0.0402, *wR*2 = 0.0572

Slant plane Fourier maps of the comparison between ground state and metastable state structure of compound **18** clearly show the reduction in electron density around the nitro-(η^1-NO_2) isomer (red dotted lines), and an increase in electron density accountable to the new positions of the nitrito-(η^1-*ONO*) metastable species (blue solid lines). The final positions of the O2A and O2B atoms are not clearly observed on the Slant plane Fourier maps; this is because the positions are in the near proximity of the ground state O1 and O2 atoms (Figure 54).

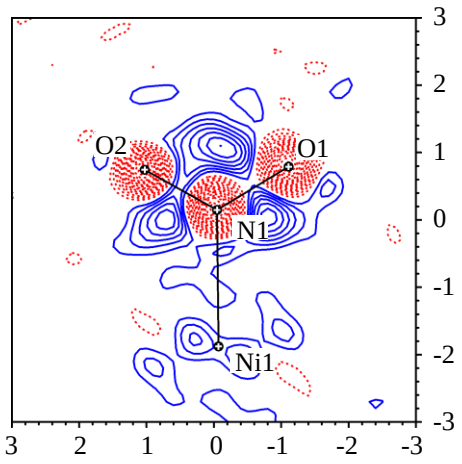

Figure 54: The compound **18** Slant plane Fourier maps of the ground state vs. the metastable state of the *Pt1-N1-O1-O2* plane. The contour lines indicate a 0.35 increase (solid blue lines) or decrease (dotted red lines) in electron density. The zero contours are omitted for clarity.

The UV-visible spectra has a shoulder of a peak arising at 250 nm and a small contribution at approximately 320 nm. Gas phase DFT calculation of the electronic transitions has good agreement with the experimental UV-visible spectra. Irradiation at 365 nm or 400 nm could cause an electronic transition which is either a shoulder of the most intense peak at 250 nm or from the peak at 330 nm. Both wavelengths are associated with electronic transitions from non-bonding orbitals into antibonding orbitals with reference to the platinum-nitro and platinum-phosphorus bonds. The electronic transition would be consistent with photocrystallographic experimental results with irradiation at 400 nm and 365 nm, a far shoulder to this absorption causing a nitro-(η^1-NO_2) to nitrito-(η^1-ONO) transformation.

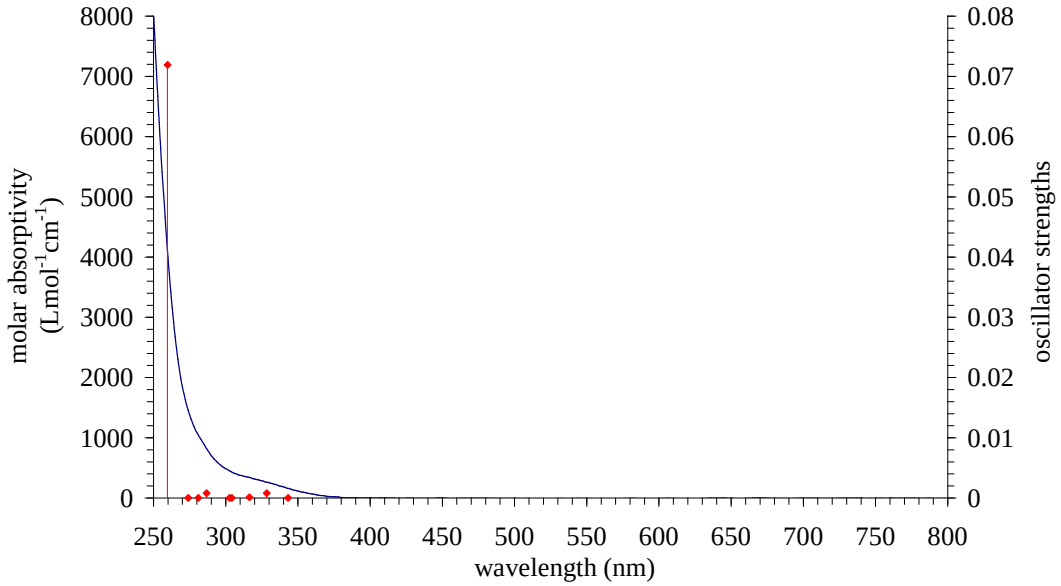

Figure 55: UV-visible spectra of and DFT calculated oscillator strengths for compound **18**.

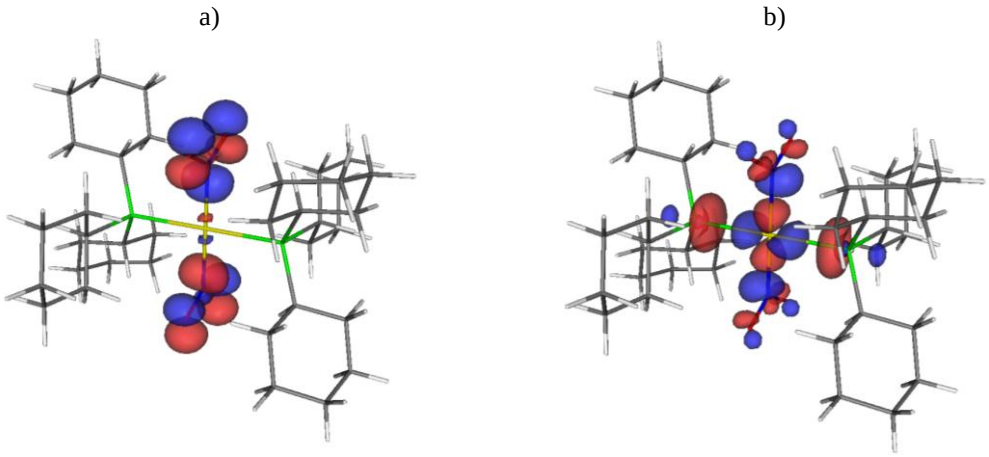

Figure 56: Compound **18** molecular orbitals for a typical transition from a) non-bonding nitro orbitals to b) antibonding with respects to platinum ($d_{x^2-y^2}$)-NO_2 and platinum ($d_{x^2-y^2}$)-phosphorous bonds.

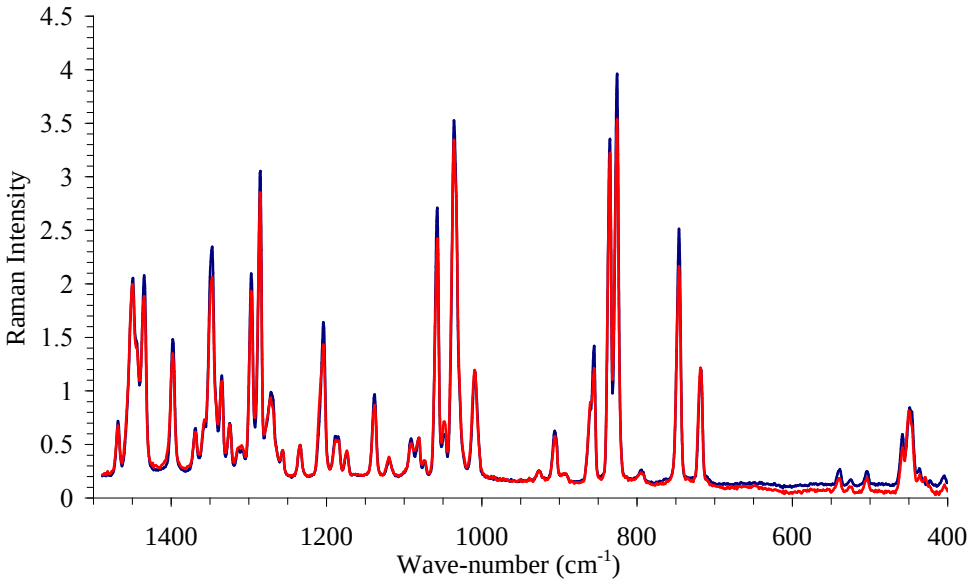

Figure 57: Solid-state Raman spectra at 115 K of before (blue) and after (red) photolysis of compound **18**.

A crystal of compound **18** was cooled to 115 K on the variable-temperature stage and a ground state spectrum was obtained (Figure 44). The spectra contains a $\delta(NO_2)$ band at 826, 835 cm^{-1}, typical of the nitro conformation. The crystal was then irradiated using the 400 nm UV LEDs for a period of 140 min, after which a metastable spectrum was obtained. The Raman spectra remained unchanged within experimental errors. This result is not consistent with crystallographic investigation where a 20 % conversion was achieved within the crystal structure.[3-4]

5.5.2. *Bis*(triphenylphosphine)di(η^1-N-nitro)platinum (II) - 19

Compound **19** was synthesised using a modified procedure from literature accounts.[13] Crystals suitable (Scheme 11) for photocrystallographic experiments were produced from acetonitrile. Compound **19** crystallizes in the orthorhombic space group *Pbca*. The square planar platinium is positioned on an inversion centre and is bound to a triphenylphosphine ligand (P1) and nitro-(η^1-NO_2) group (N1) and symmetry-related partners with bond distances of 2.3323(7) and 2.0132(16) Å, respectively. The structural packing and configuration are identical to compounds **16** and **17,** with the palladium systems with triphenylphosphine and triphenylarsine auxiliary ligands.

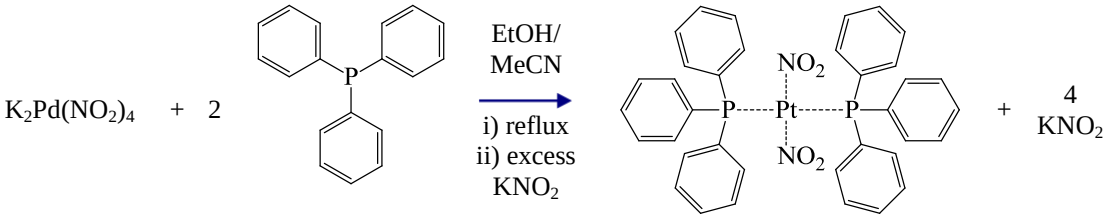

Scheme 11: Synthesis of compound **19**.

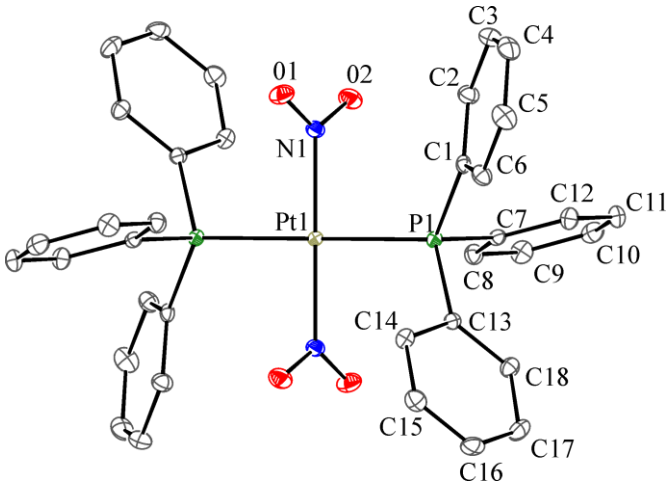

Figure 58: X-ray structure of compound **19** with thermal ellipsoids set at 50% probability and hydrogen atoms removed for clarity.

Photocrystallographic investigations were carried out at 100 K using either six 365 nm or six 400 nm LEDs. Even after prolonged irradiation, no evidence of linkage isomerism was observed; there were no new peaks in the residual electron density in the structural model and the electron density map remained unchanged.

The UV-visible spectra is dominated by an intense peak at 263 nm and the spectra fits well to the DFT calculation of the electronic transitions (Figure 59). The majority of electronic transitions are from non-bonding orbitals into triphenylphosphine-ligand based orbitals. There are no electronic transitions into orbitals antibonding with reference to the platinum-nitrate bond and this would explain why there was no evidence of photoreaction upon irradiation.

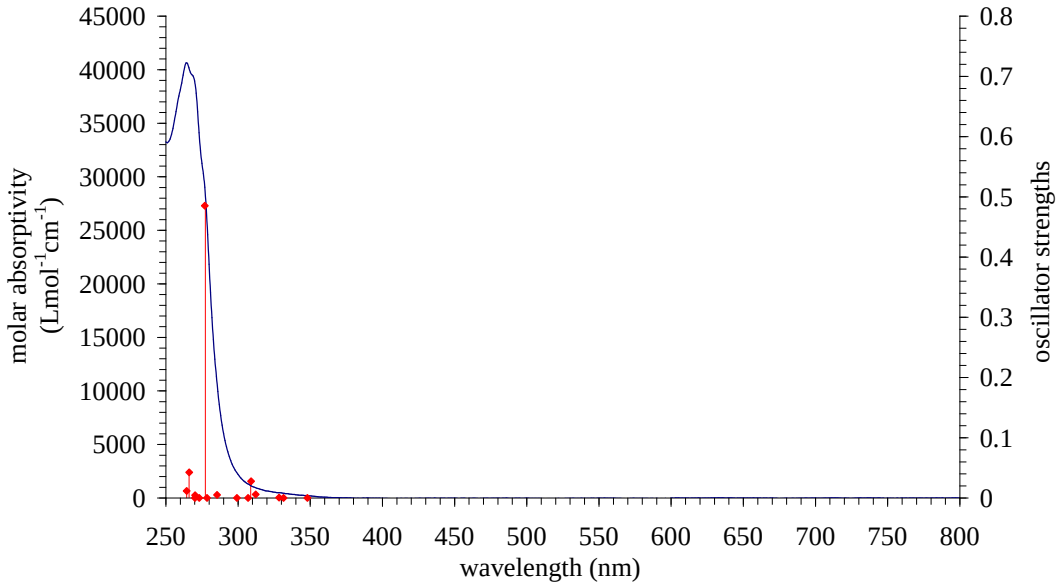

Figure 59: UV-visible spectra (blue) of and DFT calculated oscillator strengths (red) for compound **19**.

In chapter 5, systems containing a series of phosphorus auxiliary ligands were investigated for their nitro to nitrito linkage isomerism potential upon irradiation. There is a relationship between the bond lengths and the total conversion observed. It is evident that nickel-phosphorus bond lengths are shorter for systems in the *cis* configuration with the phosphorus ligand orientated *trans* to the nitro group (Table 12). The shortening of the bond lengths indicates backbonding from the metal to phosphorus. Backbonding between the phosphorus and nickel results in the weakening of the nickel-nitro bond situated *trans*, indicated by the longer Ni-N bond length for systems in the *cis* configuration (Table 11). The *cis* configuration systems, in which the phosphorus ligand is situated *trans* to the nitrite ambidentate group produce 100 % conversion from nitro-(η^1-*N*O_2) to nitrito-(η^1-*O*NO) upon irradiation (compounds **9** to **12**).

Table 11: Comparison of metal-nitrogen bond lengths for compounds 9 - 19.

Compound	Metal	Ligand	configuration	Conversion	M-N1	M-N2
9	Ni	dppe	*cis*		1.947(4)	
10		dppe		100%	1.924(4)	1.985(5)
11		dcpe		100%	1.9060(16)	1.9114(15)
12		triphos		85 %(ps)	1.9135(18)	1.843(8)
13		PEt_3	*trans*	26 %(d)	1.8725(19)	
14		PCy_3		83 %(d)	1.899(2)	
15	Pd	PCy_3	*trans*	44 %(ps)	2.022(3)	
16		PPh_3		46 %(ps)	2.031(2)	
17		$AsPh_3$		41 %(ps)	2.029(3)	
18	Pt	PCy_3	*trans*	20 %(ps)	2.0181(14)	
19		PPh_3		0%	2.0131(16)	

Table 12: Comparison of metal-phosphorus bond lengths for compounds 9 - 19.

Compound	Metal	Ligand	Orientation	Conversion	Ground-state			Excited-state			Bond length difference		
					M-P1 (Å)	M-P2 (Å)	M-P3 (Å)	M-P1 (Å)	M-P2 (Å)	M-P3 (Å)	M-P1 (Å)	M-P2 (Å)	M-P3 (Å)
9	Ni	dppe	*cis*	100 %	2.1697	2.1815		2.145	2.165		0.0247	0.0165	
10		dppe		100 %	2.1686	2.1837		2.1536	2.155		0.015	0.0287	
11		dcpe		100 %	2.1931	2.1843		2.1563	2.1774		0.0368	0.0069	
12		triphos		85 %(ps)	2.1987	2.1302	2.2079	2.1974	2.1211	2.2104	0.0013	0.0091	-0.0025
13		PEt_3	*trans*	26 %(d)	2.2324			2.2285			0.0039		
14		PCy_3		83 %(d)	2.2881			2.311			-0.0229		
15	Pd	PCy_3	*trans*	44 %(ps)	2.3789			2.3732			0.0057		
16		PPh_3		46 %(ps)	2.3798			2.3507			0.0291		
17		$AsPh_3$		41 %(ps)	2.4364			2.4336			0.0028		
18	Pt	PCy_3	*trans*	20 %(ps)	2.3561			2.3578			-0.0017		
19		PPh_3		0 %	2.3323								

5.6. Conclusions

From the results obtained in this chapter, it is evident that a number of systems which contain phosphorus-based auxiliary ligands are capable of high nitro/nitrite linkage isomer conversions, particularly nickel complexes with bi-dentate ligands, in which the phosphorus atom is situated *trans* to the nitrite ambidentate group producing 100 % conversion from nitro-(η^1-*N*O_2) to nitrito-(η^1-*O*NO) upon irradiation (compounds **9**, **10** and **11**). Nickel nitrite systems which contain monodentate phosphorus-based auxiliary ligands produce complex with the nitro ligand *cis* to the auxiliary ligand, and *trans* to another nitro ligand (compounds **13** and **14**), decomposing upon irradiation. The maximum conversion observed crystallographically is before the quality of the data degrades. As well as *endo*-nitrito-(η^1-*O*NO) species observed in pervious investigation, there is also evidence of an *exo*-nitrito-(η^1-*O*NO) isomer. This new isomer is less stable and in parametric temperature studies, the *exo*-nitrito-(η^1-*O*NO) isomer converted back to the ground state at lower temperature than the *endo*-nitrito-(η^1-*O*NO) species. Palladium analogues of the nickel systems with monodentate phosphorus-based auxiliary ligands *cis* to the nitrite group also produce metastable states. Upon irradiation, the conversions from nitro-(η^1-*N*O_2) to nitrito-(η^1-*O*NO) reaches a photostationary point. Although the palladium systems reached a photostationary point, the thermal stabilities of the metastable species exist to higher temperatures than the nickel equivalent species. These systems also retained crystallinity upon irradiation.

In general, the rate of photoreaction reduces from nickel and palladium through to platinum; this is consistent with kinetic reactivity of these compounds. The photocrystallographic rates need to be further investigated before any conclusive conclusions can be reached, as crystal size and absorption of particular wavelengths may vary between samples and crystals.

Systems with arsenic-based auxiliary ligands are also capable of linkage isomerism. Compound **18** with triphenylarsine ligands produces comparable photoactivation results to the phosphine analogues.

Importantly, DFT calculations on the platinum complex **19** did not involve electronic transitions into antibonding orbitals with respect to the platinum-nitro bond; this was consistent with photocrystallographic results, which showed no evidence of linkage isomerism.

5.7. References

1	Cormary, B.; Malfant, I.; Valade, L.; Cointe, M. B. L.; Toupet, L.; Todorova, T.; Delley, B.; Schaniel, D.; Mockus, N.; Woike, T.; Fejfarova, K.; Petricek, V.; Dusek, M. *Acta Crystallogr. Sect. B: Struct. Sci.* **2009**, *65*, 787.
2	Brayshaw, S. K.; Knight, J. W.; Raithby, P. R.; Savarese, T. L.; Schiffers, S.; Teat, S. J.; Warren, J. E.; Warren, M. R. *J. Appl. Crystallogr.* **2010**, *43*, 337.
3	Brooker, M. H.; Irish, D. E. *Inorg. Chem.* **1969**, *8*, 219.
4	Goodgame, D. M. L.; Hitchman, M. A. *Inorg. Chem.* **1966**, *5*, 1303.
5	Warren, M. R.; Brayshaw, S. K.; Johnson, A. L.; Schiffers, S.; Raithby, P. R.; Easun, T. L.; George, M. W.; Warren, J. E.; Teat, S. J. *Angew. Chem. Int. Ed.* **2009**, *48*, 5711.
6	Kriegesimondsen, J.; Feltham, R. D. *Inorg. Chim. Acta* **1983**, *71*, 185.
7	Angulo, I. M.; Bouwman, E.; van Gorkum, R.; Lok, S. M.; Lutz, M.; Spek, A. L. *J. Mol. Catal. A: Chem.* **2003**, *202*, 97.
8	Zheng, S.-L.; Messerschmidt, M.; Coppens, P. *Acta Crystallogr. Sect. B: Struct. Sci.* **2007**, *63*, 644.
9	Feltham, R. D. *Inorg. Chem.* **1964**, *3*, 116.
10	Doughty, D. T.; Gordon, G.; Stewart, R. P. *J. Am. Chem. Soc.* **1979**, *101*, 2645.
11	Brayshaw, S. K.; Easun, T. L.; George, M. W.; Griffin, A. M. E.; Johnson, A. L.; Raithby, P. R.; Savarese, T. L.; Schiffers, S.; Warren, J. E.; Warren, M. R.; Teat, S. J. *Dalton Trans.* **2010 (accepted)**.
12	Feltham, R. D.; Elbaze, G.; Ortega, R.; Eck, C.; Dubrawski, J. *Inorg. Chem.* **1985**, *24*, 1503.
13	Rigamonti, L.; Forni, A.; Manassero, M.; Manassero, C.; Pasini, A. *Inorg. Chem.* **2010**, *49*, 123.

Chapter 6 – Following the Progress of a Solid State Photoactivation via X-ray Diffraction

6.1. In-Situ Powder Diffraction Experiments

Conventionally, X-ray powder diffraction (XRPD) has been used as a fingerprint tool to identify solid state materials. XRPD can now be routinely used to monitor solid state transformations and many in-situ experiments have been reported.[1] An advantage of using powders is that crystal shearing and decomposition upon the transformations that may occur in single-crystal to single-crystal experiments does not majorly affect the powder pattern. The data collection time for an entire powder pattern can be routinely achieved in the order of minutes, and if more specialised equipment is used, it is now possible to collect powder patterns in the order of seconds. Once the peaks of interest which alter during the transformation are identified, the two theta range can be restricted to observe only the selected reflection and this greatly reduces the run time per observation.

6.1.1. Following the Photoactivation Process of Compound 11 Using Powder Diffraction

XRPD is used to investigate the progress of the solid state process for compound **11** as the linkage isomerism transformation occurs. In the single-crystal photocrystallographic experiments, the linkage isomerism transformation goes to completion. During photoactivation there are slight changes in the unit cell dimensions which cause the peak position to shift and also due to the transformation there is an alteration in peak intensities, both of which are detectable using XRPD.

In order to establish the reaction progress as it occurs, the ground state and photoactivated powder patterns have to be significantly different. Figure 1 shows the comparison between the predicted powder patterns from the single-crystal which undergoes conversion from one linkage isomer to the other. As the unit cell dimensions alter during photoactivation, a number of peaks positions shift and there are deviations in the peak intensities due to the change in electron density through specific planes. There is a good correlation between the predicted powder patterns from the single-crystal and the experimental (Figure 2). The experimental powder

pattern shows an increase half peak width and results in a loss of the finite peak shape and an increase peak overlap.

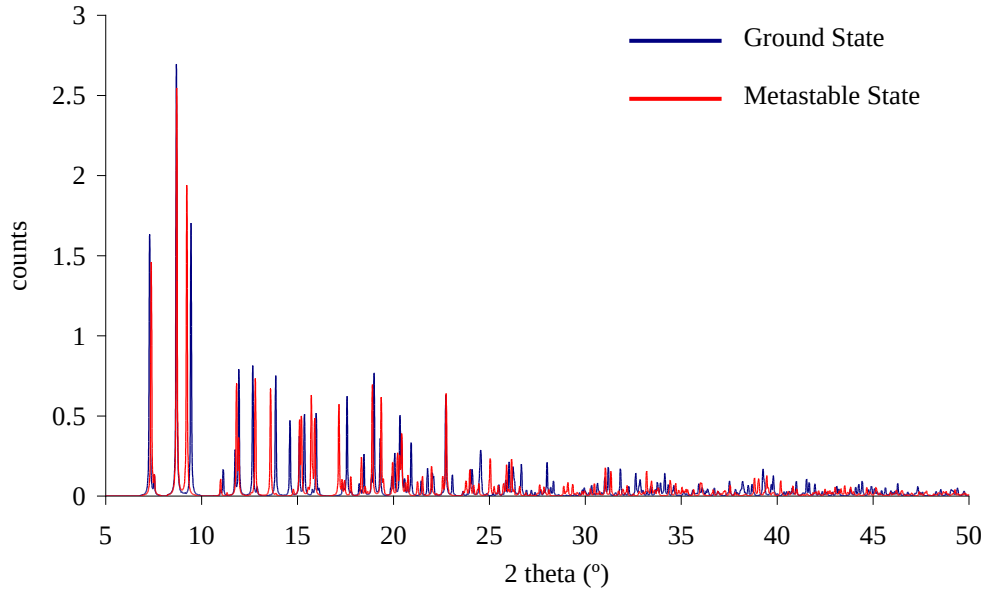

Figure 1: Predicted single-crystal powder patterns of compound **11**.

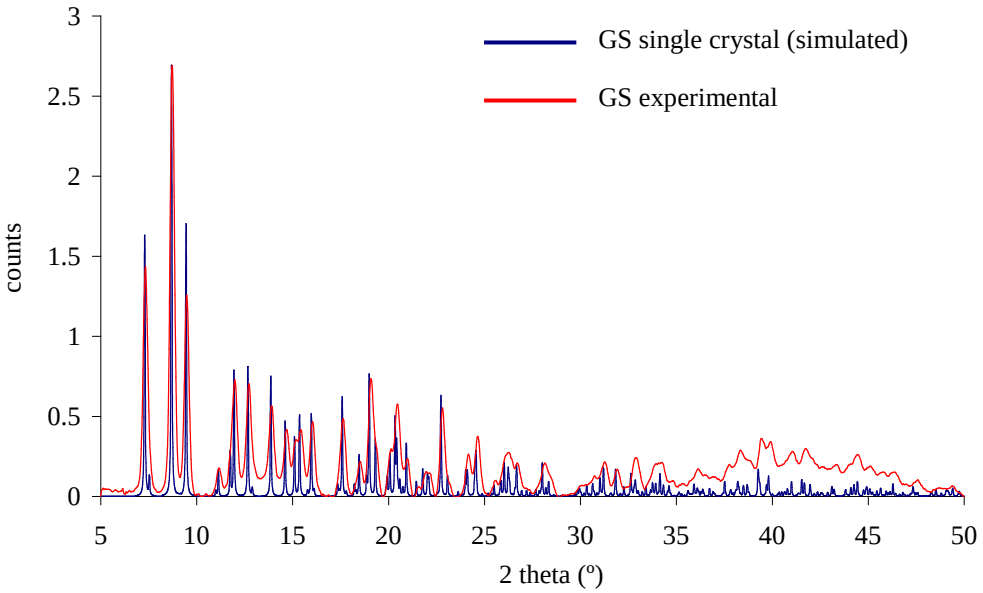

Figure 2: Predicted single-crystal (blue) and experimental powder pattern (red) powder patterns of compound **11**.

The initial photoactivation experiments were carried out using six LEDs, but as the experimental time for an entire powder pattern was longer than the time taken for complete photoactivation, it was not possible to follow the progress of the reaction. Therefore for subsequent investigations only one LED was used to photoactivate the powder. The powder was cooled to 100 K and a ground state pattern was obtained. The powder was then irradiated for 4 h using one 400 nm LED, 1 cm from the

powder. During irradiation, powder patterns (5-50º 2-theta) were continuously collected and specific peaks increased or decreased in intensity or shifted position (Figure 2).

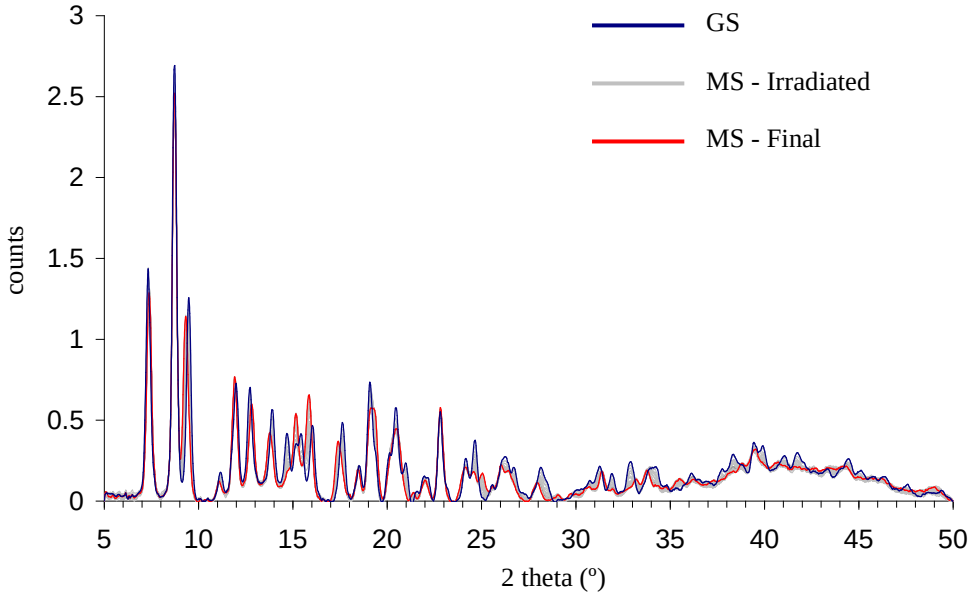

Figure 3: Compound **11**, ground state powder pattern (blue), patterns of irradiated powder (grey), and final powder pattern after irradiation (red).

A comparison of the predicted single-crystal powder pattern of the ground state versus the metastable state shows clear differences in the positions and intensity of a number of reflections. In the experimental powder patterns, due to the increase in peak width and overlapping peaks, the intensity changes and the shifts in peak positions are less obvious. The areas with large deviations from ground state to metastable state are between 2-theta values 14º and 16º and also between 17º and 18º. As the powder patterns were continuously collected during irradiation, the peak height could be measured as a function of time to obtain information about the progress of the reaction in real time. Figure 4a shows the continuous change of four peak positions and intensities. The intensities of the peak at 2-theta value of 14.722º and 15.162º are plotted against the time in sec. Figure 4a shows the progress of reaction reduces during photoactivation. There are a number of plausible reasons why this occurs, one possibility is that initially the molecules on the surface of the microcrystalline powder become photoactivated, after which the illumination needed to reach the centre of the microcrystalline powder which could result in a decreases the photo yield. The same drop-off in the peak changes can be observed in a number of peaks throughout the powder pattern. Figure 5 shows the change in intensity at

two theta values of 17.405 º and 17.625 º. The change in the peak intensity change is consistent with the peaks at 14.722º and 15.162º.

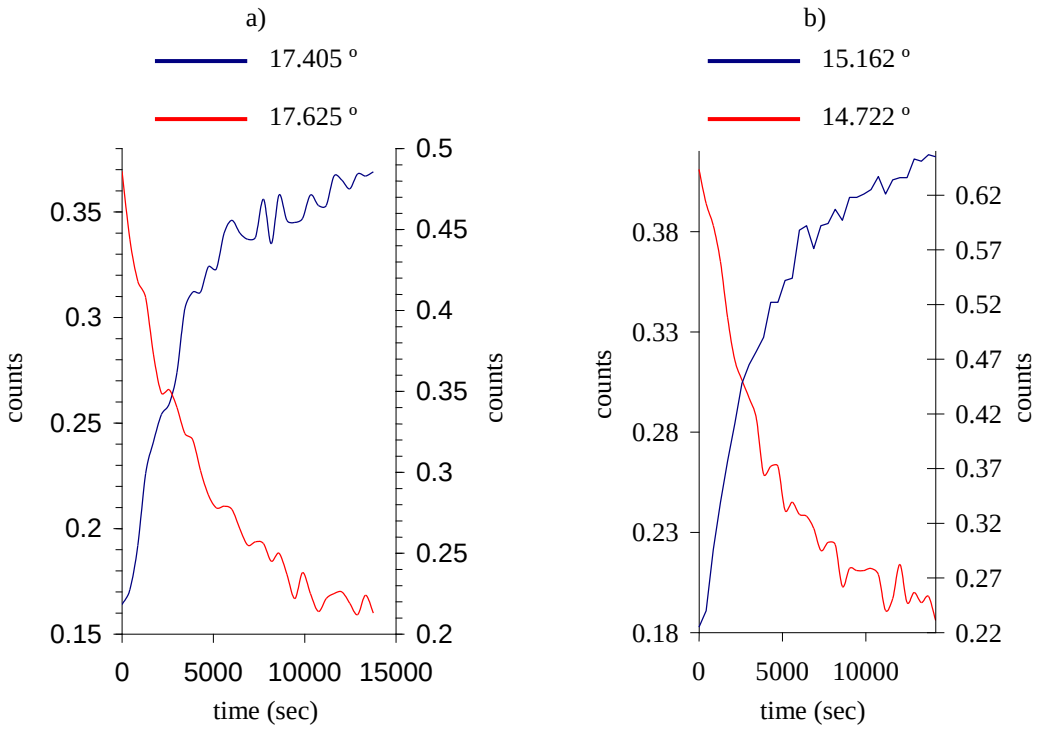

Figure 4: Compound **11**, a) series powder patterns between 14º and 16º during irradiation. b) Change in intensity of peaks at 14.722 and 15.162 during irradiation.

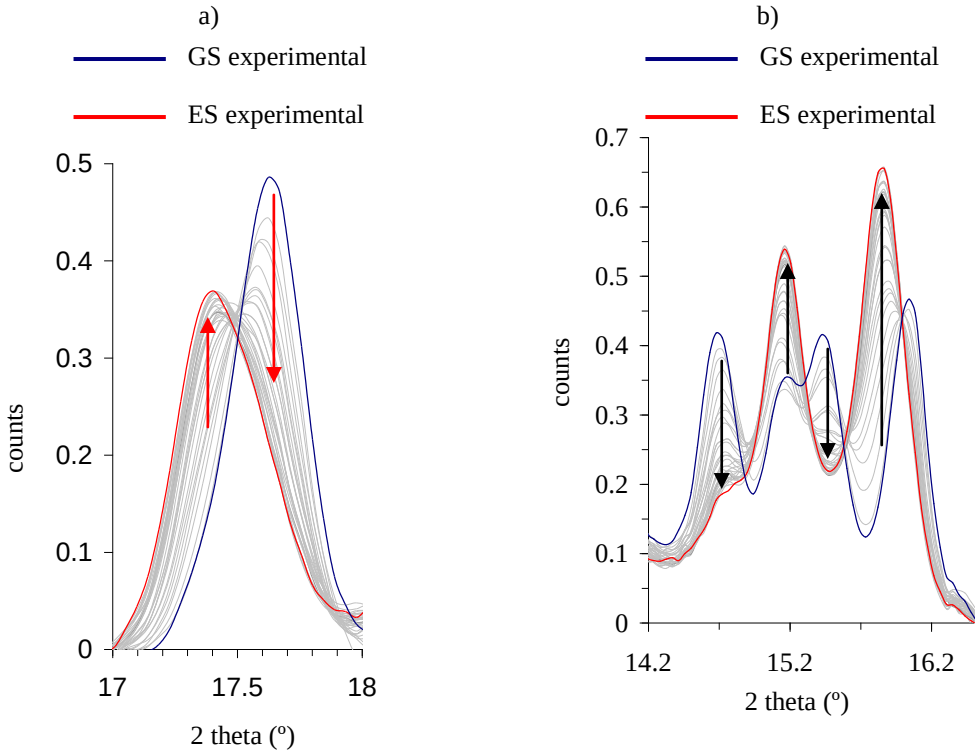

Figure 5: Compound **11**, a) series powder patterns between 17º and 18º during irradiation. b) Change in intensity of peaks at 17.405 º and 17.625 º during irradiation.

6.1.2. Following the Photoactivation Process of Compound 14 using powder diffraction

In single-crystal photocrystallographic experiments, compound **14** was irradiated for 11 min to achieve an 83 % transformation from nitro-(η^1-NO_2) to nitrito-(η^1-ONO). This conversion is relatively fast compared to other systems investigated in this thesis. To explore the reasons for the fast conversion, the progress of transformation was followed by powder diffraction. Inspecting the predicted powder patterns, calculated from the single-crystal structures of the initial and metastable state structures, show there are some peak alteration which can be monitored upon irradiation (Figure 6). The experimental powder pattern has good correlation to predicted powder pattern from the single-crystal structure. The experimental powder pattern displays broad peaks and much of the resolution of the individual peaks is lost because of the increased overlaps (Figure 7).

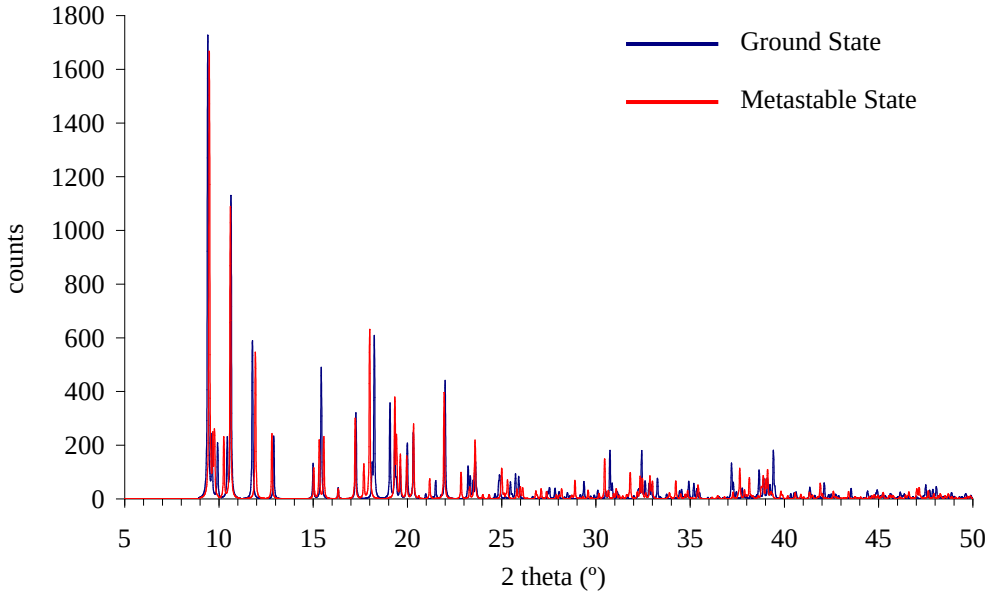

Figure 6: Predicted single-crystal powder patterns of compound **14**.

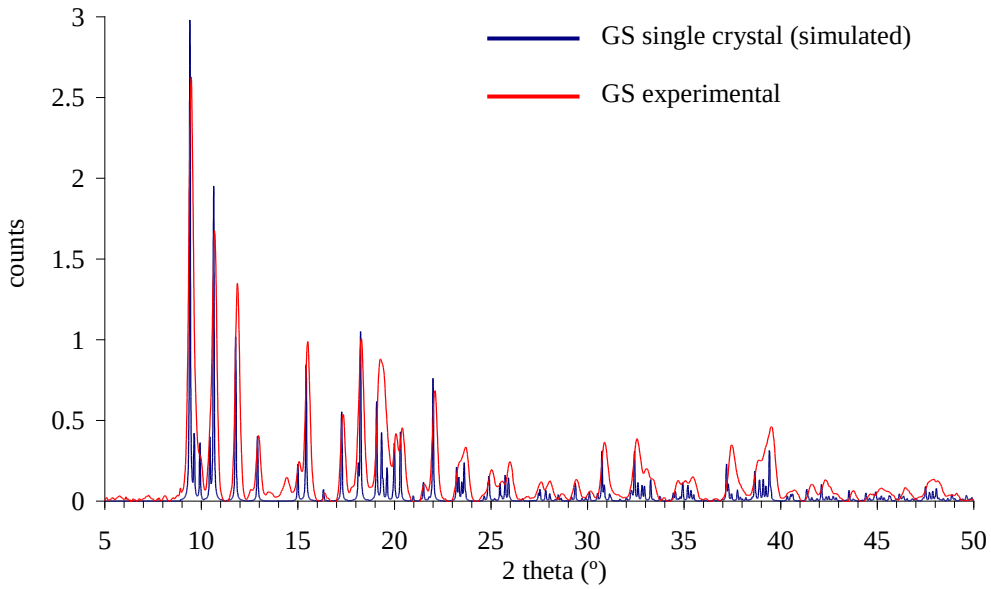

Figure 7: Predicted single-crystal (blue) and experimental powder pattern (red) powder patterns of compound **14**.

The powder of compound **14** was cooled 100 K and a ground state pattern was obtained. After which the irradiation and metastable data set was started simultaneously. The strategy for the metastable data set produced, involved the measuring of 32 powder patterns collected from 5º - 50º 2-theta. Each powder pattern takes approximately 420 sec, and the total irradiation time for the entire data set was 3¾ h. The powder was irradiated with one 400 nm LED, 1 cm from the powder.

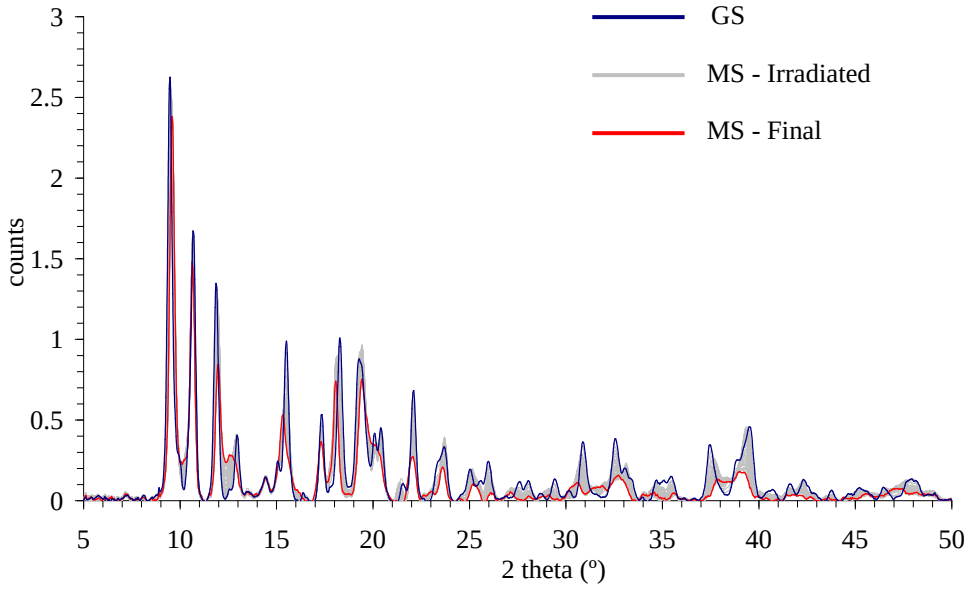

Figure 8: Compound **14**, Ground state powder pattern (blue), patterns of irradiated powder (grey) and final powder pattern after irradiation (red).

Upon irradiation, a number of peaks alter in peak position and intensity. The intensity of the peak at 22.112º is monitored with respect to time. The peak decreases from 0.682 to 0.258 in 224 min. The peak intensity changes is approximately linearly with time upon irradiation, and the rate of photoactivation does not decrease with time as seen in the previous study on compound **10**. The final irradiated powder pattern correlates well to the metastable single-crystal structure of 83 % conversion. As the intensity has not levelled off, it is likely that the reaction has not gone to completion. From these initial tests, the rate of reaction does not reduce as the reaction proceeds and could explain the fast conversion time observed in the single-crystal photocrystallographic experiments.

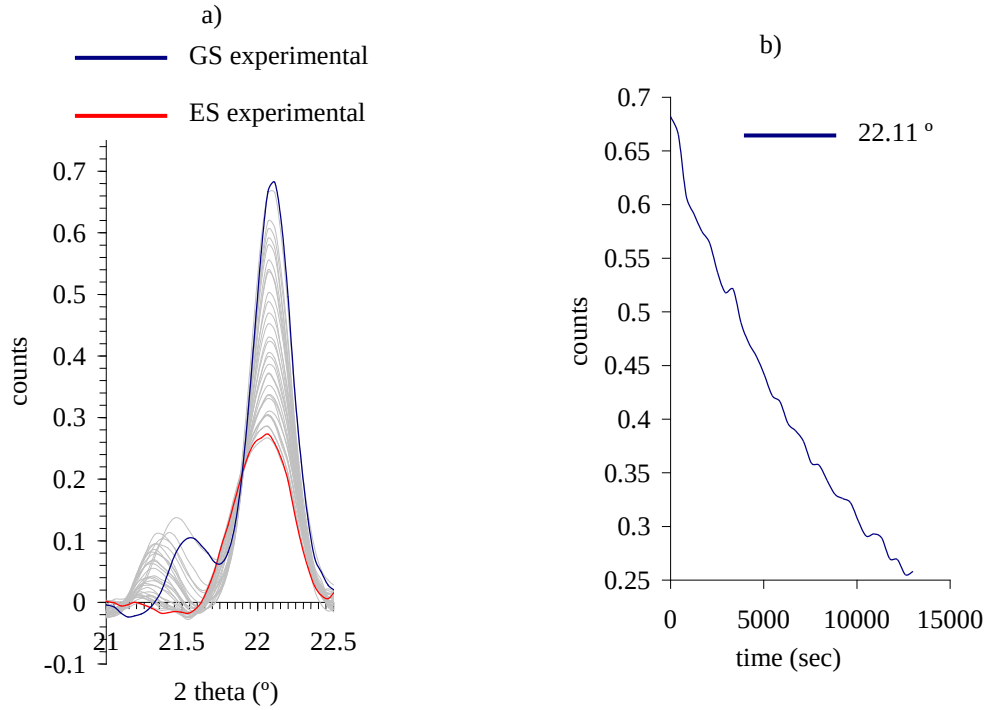

Figure 9: Compound **14**, a) series powder patterns between 21º and 22.5º during irradiation. b) Change in intensity of peaks at 22.112 º during irradiation.

It is also possible to follow the progress of a reaction using single-crystal diffraction by monitoring a single reflection or one frame from a ccd detector. To obtain a powder diffraction pattern, data needs to be collected over a 2-*theta* range, in comparison a single-crystal image from a ccd detector can be collected in a much shorter period, thus reducing the time between each observation. Another advantage of using single-crystal diffraction over powder diffraction is that the reflections are not overlapped which could cause ambiguity in the results.

6.2. Single-crystal Intensity Change

Kinetic studies using single-crystal experiments are normally conducted by repeatedly collecting a number of diffraction frames from which the unit cell dimensions can be obtained. The unit cell dimensions can then be plotted against the variable which is being changed to achieve the rates of reaction e.g. temperature, pressure or time of irradiation. These experiments are well-documented in literature and span a number of different types of transformations.[2-4]

For systems where unit cell dimensions remain fairly constant upon transformation, it is possible to monitor individual X-ray reflections to follow the progress of the reaction. One particular example of a [2+2]-cycloaddition reaction shows the intensities of 16 reflections were continuously measured as the crystal was irradiated. The intensities alterations were then plotted against a natural logarithm of time which produced a linear plot showing that the reaction follows a first order kinetics.[5] The next section of the report uses this same analogy of monitoring the intensity of certain reflections to follow the progress of the reaction as it occurs for the linkage isomerisation.

Following the real-time progress of a reaction can be achieved by continuously monitoring the intensity of a reflection as it changes with the isomerisation. Using single-crystal analysis to monitor the intensity of a single reflection by repeatedly collecting the same frame can be used to follow the transformation every 4 sec; this is relatively fast compared to collecting an entire powder pattern. One disadvantage of using single-crystal analysis is that crystal decomposition can dramatically affect the intensity of reflections. To overcome the decrease in intensity from minor crystal decomposition, reflections with low two theta values are selected as they are less affected.

In order to carry out the study, reflection lists from experimental ground state and metastable states were imported into a computer program to select suitable reflections to follow during irradiation. The computer program used to find reflections suitable for following the progress of a reaction was designed by Robert

Warren and the fundamentals are beyond the scope of this thesis. The computer program selected the reflection based on:

- Large intensity alteration
- Large percentage change of intensity
- Situated at a low resolution
- Intense reflection
- The peak was always present
- Low two theta values

For an experiment, where the intensity of peak is being monitored upon irradiation, it is preferential to use relatively large crystals so that the scan time is minimised and more intense spots can be observed. Firstly, an entire high-quality data set is collected to confirm a clean ground state structure absent of the nitrito species. The ground state data collection is inspected to find the orientation of the crystal and the frames which contain the certain reflection at low resolution. A strategy is then constructed using a wide omega scan to collect the selected reflection and allowing for two degrees clearance on either side. The four degree scan is important for collecting the entire reflection, and also to compensate for any slight changes to the unit cell and therefore the peak position. The data collection, which comprises a large number of the same scan, is started at the same time as the irradiation of the crystal. A second entire data set is collected to confirm the amount of photoactivation.

6.2.1. Monitoring X-ray Reflection Intensities upon Irradiation of compound 11

For compound **11,** the (0, 3, 2) reflection changes intensity as the linkage isomerism occurs. The intensity of the (-1, 2, 2) reflection is not affected by the linkage isomerism and remains fairly constant upon irradiation. Thus, as the crystal is being irradiated, the (0, 3, 2) reflection can be monitored for the reduction in intensity and the (-1, 2, 2) reflection can be used as a reference peak.

After a high quality data set for compound **11** was established, a strategy was constructed of 74 omega scans (four degree scan width) of the (0, 3, 2) and (-1, 2, 2) reflections. The total time for each frame is 16 sec with a total irradiation time

period of 1120 sec. Ideally, each peak would be integrated to obtain the entire volume of the peak. Unfortunately, at present this is not possible and the maximum height of the peak was used to monitor the progress of the reaction. The peak height of the (0, 3, 2) reflection changed from 16311 to 6207 counts upon irradiation which is 38 % of the original intensity. The (-1, 2, 2) reflection remained fairly constant upon irradiation (Figure 10). The graph shows that the rate of reaction is reducing with reaction progress and is consistent with powder studies.

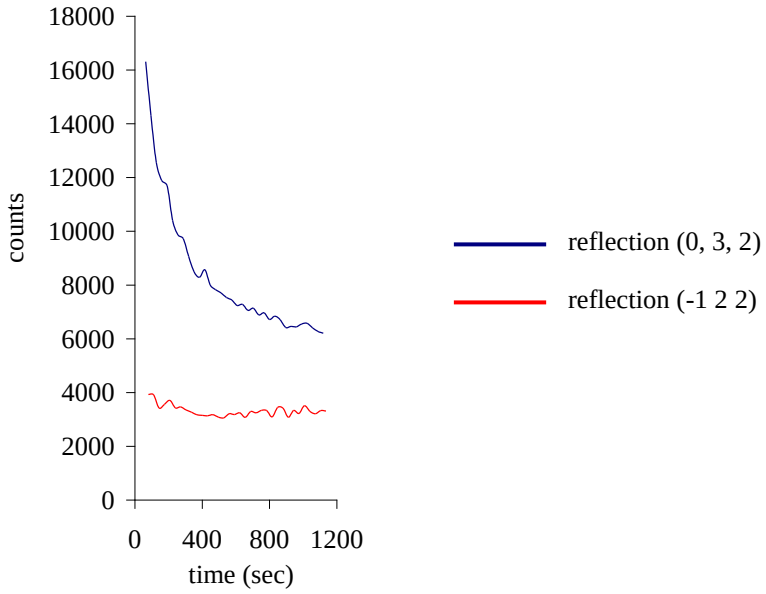

Figure 10: Change in intensity of reflections (0,3,2) and (-1,2,2) during irradiation.

6.2.2. Monitoring X-ray Reflection Intensities upon Irradiation of compound 10

Compound **10** was investigated to determine whether other systems show a decrease in the rate of reaction with reaction progress. The (0, 0, 8) reflection was selected to monitor the progress of reaction upon irradiation. Compound **10** crystallises in the orthorhombic space group $P2_12_12_1$ and therefore each reflection occurs eight times in the entire reciprocal space.

Before the crystal was irradiated, a high quality structure was obtained which confirmed the absence of the nitrito metastable species. Inspecting the reflections from the ground states structure, there were a number of symmetry equivalent (0, 0, 8) reflections, of which three were selected. During irradiation of the crystal all three symmetry equivalent reflections were collected to improve accuracy. The strategy comprised of a total of 99 four degree omega scans of the (0, 0, 8) reflection (33 scans for each crystal orientation). During the data collection, the crystal was irradiated for a total of 1700 sec (17.4 sec per frame. The irradiation and data collection were started simultaneously. All three reflections followed a consistent decrease in intensity (Figure 11).

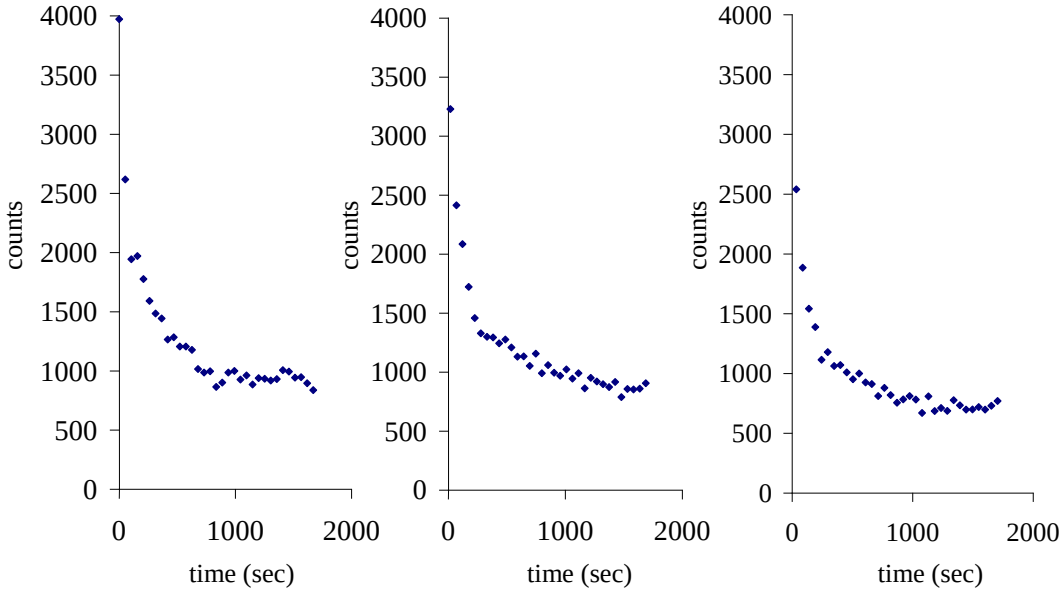

Figure 11: Intensity change for three symmetry equivalent (0,0,8) reflection upon irradiation of compound **10**.

From the combined data of all three reflections, the initial rate of reaction is approximately 15 counts/second (0.3 % linkage isomerism conversion per minute), this initial rate decrease to essential zero after 1700 sec of irradiation.

There are a number of reasons why the rate of reaction drops as the reactions proceed. A feasible reason is that the initial photoactivation is of surface molecules and this is relatively fast; as the reactions progress, the remaining molecules are in the centre of the molecule, and because the metastable molecules at the surface also absorb light and there is less illumination reaching the central molecules, hence the rate of reaction reduces. It is also possible that when a molecule is converted to the metastable form it prohibits the neighbouring molecules transformation. Thus, as the reaction proceeds more molecules are restricted by their neighbouring molecules.

Monitoring the intensity change of a reflection to assess the photoactivation in compounds **10** and **11** is in the experimental stages, but from the initial success there are number of interesting experiments to be carried out using this technique to help in the understanding of the process. To determine whether crystal size and penetration depth affect the rate of reaction, a series of different shapes and sizes of crystals of one compound can be investigated for the intensity change upon irradiation. Another possibility is to carry out the same experiment on one crystal and alter the number or power of the LEDs.

6.3. References

1	Evans, J. S. O.; Price, S. J.; Wong, H. V.; O'Hare, D. *J. Am. Chem. Soc.* **1998**, *120*, 10837.
2	Benedict, J. B.; Coppens, P. *J. Phys. Chem. A* **2009**, *113*, 3116.
3	Turowska-Tyrk, I.; Trzop, E.; Scheffer, J. R.; Chen, S. *Acta Crystallogr. Sect. B: Struct. Sci.* **2006**, *62*, 128.
4	Murali, C.; Shashidhar, M. S.; Gonnade, R. G.; Bhadbhade, M. M. *Chem. Eur. J.* **2009**, *15*, 261.
5	Honda, K.; Nakanishi, F.; Feeder, N. *J. Am. Chem. Soc.* **1999**, *121*, 8246.

Chapter 7 – Experimental

7.1. Instruments

7.1.1. Reagents, Materials and Solvents

All manipulations involving air sensitive reagents were performed using standard Schlenk techniques under an atmosphere of purified nitrogen. For reactions involving air sensitive species, all solvents were dried prior to use, using an automatic solvent purification system. All chemicals were purchased from commercial sources and used without further purification.

7.1.2. Elemental Analysis

Elemental analysis was obtained on dried samples by:

- Mr. Stephen Boyer (London Metropolitan University)
- Mr. Alan Carver using Exeter analytical CE-440 elemental analyzer (University of Bath)

7.1.3. Mass Spectroscopy

Mass Spectra were obtained on a Bruker micrOTOF electrospray ionization time-of-flight (ESI-TOF) machine using a confirm formula, positive 50 to 500 loop injection strategy.

7.1.4. Nuclear Magnetic Resonance

NMR spectra were obtained at room temperature on a Bruker Avance 300 MHz Ultrashield NMR spectrometer. All spectra were obtained in deuterated chloroform unless otherwise stated.

7.1.5. Ultra-Violet Spectroscopy

UV absorption spectra were collected on a Perkin Elmer, Lambda 650 UV/VIS spectrometer in glass cuvettes, the emission spectra were collected on a Perkin Elmer, LS 55 luminescence spectrometer.

7.1.6. Single crystal X-ray diffraction

Single crystal X-ray diffraction data were collected on either:

- Nonius Kappa CCD diffractometer (University of Bath)
- Oxford Diffraction Gemini A Ultra diffractometer (University of Bath)
- Bruker Apex2 CCD diffractometer on Station 9.8 (Daresbury Synchrotron)
- Bruker Apex2 CCD diffractometer on beamline 11.3.0. (Advanced Light Source, Berkely)
- Rigaku Saturn CCD diffractometer (Diamond Light Source, RAL, Didcot)

7.1.7. X-ray Powder Diffraction

X-ray powder diffraction patterns were obtained as follows:

- Routine powder diffraction data was collected using a Bruker AXS diffractometer with copper source (λ = 1.54) in capillary mode at room temperature with 2θ values of 5° to 60° (University of Bath).
- Low temperature metastable state diffraction data were collected using a Bruker AXS diffractometer using the TTK450 attachment (~100 K) with 2θ values of 5° to 50° or Oxford Diffraction Gemini A Ultra diffractometer in powder mode (University of Bath).

7.1.8. DFT Calculations

Gas phase density functional theory (DFT) calculations were performed using the B3LYP[1-2] hybrid density function under the Gaussian 03 package.[3] Geometry optimizations for all compounds were performed using a quasi-relativistic pseudopotential and associated basis set (SDD) for Nickel[4] and a 6-31G(d)[5-6] basic set for all other atoms. The generation of molecular orbitals was performed at the optimized geometries and the orbitals were visualized using Molekel.[7] The first 15 singlet and triplet electronic transitions (TD-DFT) and single point energies (‘tight convergence criteria) were calculated on the optimised geometries.

7.2. Preparation of Compounds

7.2.1. Preparation of potassium hexanitritenickel(II) dihydrate

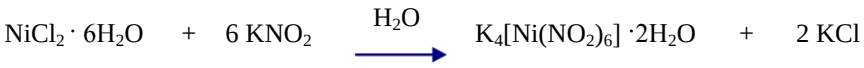

Scheme 1: Synthesis of of potassium hexanitritenickel(II)dihydrate.

The procedure is similar to that previously reported in literature.[8] Potassium nitrite (5 g, 58.7 mmol, 85.11 g/mol) was taken up in water (3 mL) and the solution was added with brisk stirring to a suspension of nickel(II) chloride hexahydrate (1.25 g, 2.38 mmol, 527.15 g/mol) in 2 mL of water (Scheme 1). The dark green solution was stirred for 2 h during which time orange crystals precipitated. The solution was cooled to *ca*. 2 °C, after which the crystalline material was filtered and washed with cold water and acetone. The compound was dried under vacuum before use. (70 % yield)

7.2.2. Preparation of potassium tetranitritepalladium(II)

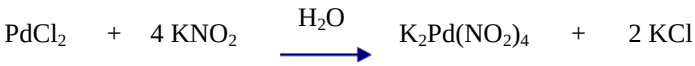

Scheme 2: Synthesis of potassium tetranitritepalladium(II).

Palladium chloride (0.264g, 1.5 mmol, 175.84 g/mol) was dissolved in a minimum amount of water (5mL) and the solution was added dropwise to a saturated solution of potassium nitrite (0.511g, 6 mmol, 85.11 g/mol) in water (1 mL) (Scheme 2). The brown mixture slowly became yellow. The resulting potassium tetranitritepalladium(II) was cooled to 0 ºC and crystalline precipitate was filtered.[9]

7.2.3. Preparation of potassium tetranitriteplatinum(II)

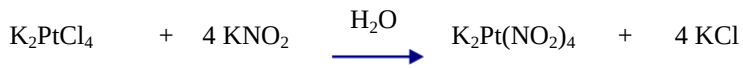

Scheme 3: Synthesis of potassium tetranitriteplatinum(II).

A suspension of potassium tetrachloroplatinum(II) (0.5 g, 1.083 mmol, 457.296 g/mol) was treated with a saturated solution of potassium nitrite (0.511g, 6 mmol, 85.11 g/mol) in water (5 mL). The mixture was heated until all material was dissolved and the

solution colour changed from the initial red to colourless. The remaining solution was cooled slowly to afford white crystals which were filtered and dried under vacuum (Scheme 3).

7.2.4. Preparation of trans-bis(ethylenediamine)bis(η^1-*N*-nitro)nickel(II) - 1

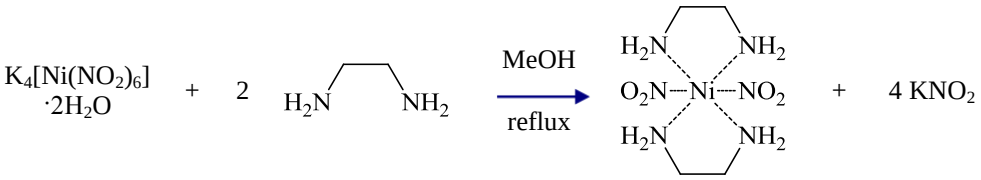

Scheme 4: Synthesis of compound **1**.

Compound **1** was prepared using a modification of a literature method.[10] A freshly prepared sample of potassium hexanitritenickel(II) hydrate (0.048 g, 0.0911 mmol, 527.15 g/mol) in methanol (5 mL) was treated with two equivalents of ethylenediamine (0.011 g, 0.182 mmol, 60.10 g/mol). The solution was refluxed for 2 h, after which the solvent was removed *in vacuo* and the solid residue was taken up in dichloromethane and filtered to give **1** as red crystals (Scheme 4).

Yield: 40 % (0.01 g, 0.0364 mmol)

ESI-MS: calc for $[C_4H_{17}N_6NiO_4]^+$ 272.066; obs 272.06.

Analysis: Calculated C 17.73 %, H 5.95 % N 31.02 % Found C 17.94 %, H 6.01 %, N 30.87 (impurities of potassium chloride).

UV spectrum could not be obtained as the ligand dissociated occurred in solution and decomposition products dominated absorptions.

Table 1: Crystallographic data for compound **1**.

Formula weight	270.94	
Temperature	100(2) K	
Wavelength	0.77490 Å	
Crystal system	Monoclinic	
Space group	*P*2(1)/*c*	
Unit cell dimensions	a = 7.4807(12) Å	α = 90°
	b = 6.6031(10) Å	β = 105.352(2)°
	c = 10.9134(17) Å	γ = 90°
Volume	519.84(14) Å^3	
Z	2	
Crystal size	0.04 x 0.03 x 0.02 mm	

Theta range for data collection	4.56 to 33.65°.
Independent reflections	1551 [*R*(int) = 0.0615]
Completeness to theta = 30.50°	96.9 %
Data / restraints / parameters	1551 / 0 / 71
Goodness-of-fit on F^2	1.085
Final R indices [I>2sigma(I)]	*R*1 = 0.0470, *wR*2 = 0.1303
R indices (all data)	*R*1 = 0.0479, *wR*2 = 0.1314

7.2.5. Preparation of trans-bis(isopropylethylenediamine)bis(η^1-*N*-nitro)nickel(II) – 2

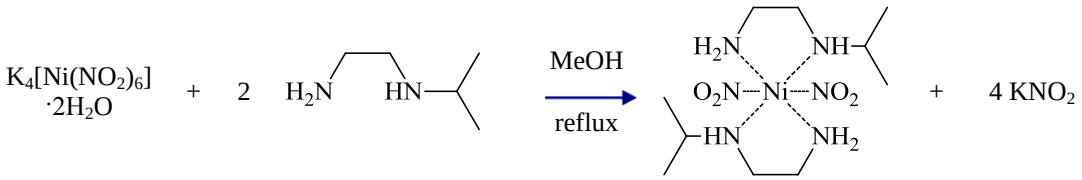

Scheme 5: Synthesis of compound **2**.

Compound **2** was prepared using a modification of a literature method.[11] A freshly prepared sample of potasiumhexanitritenickel(II)hydrate (0.1 g, 0.190 mmol, 527.15 g/mol) in methanol (8 mL) was treated with two equivalents of isopropylethylenediamine (0.0388 g, 0.38 mmol, 102.18 g/mol). The green solution of potassium hexanitronickelate (II) hydrate turned blue violet on addition of the ligand (Scheme 5). The solution was refluxed for 2 h, after which the solvent was removed *in vacuo*. The residue was dissolved in dichloromethane, filtered and the filtrated was evaporated to dryness. Purple crystals of X-ray quality were grown from methanol using slow evaporation techniques.

Yield: 70 % (0.047 g, 0.0364 mmol)

Analysis: Calculated C 33.83, H 7.95, N 23.67, Found C 12.85 %, H 3.23 %, N 17.90 % (impurities of potassium chloride and potassium nitrate).

UV spectrum could not be obtained as the ligand dissociated occurred in solution and decomposition products dominated absorptions.

Table 2: Crystallographic data compound **2**.

Temperature	100(2) K	
Wavelength	0.77490 Å	
Crystal system	Monoclinic	
Space group	*P*2(1)/*n*	
Unit cell dimensions	*a* = 6.5469(5) Å	α = 90°

	b = 19.4065(14) Å	β = 103.1480(10)°
	c = 13.1801(10) Å	γ = 90°
Volume	1630.7(2) Å^3	
Z	4	
Crystal size	0.11 x 0.09 x 0.03 mm	
Theta range for data collection	1.86 to 29.71°	
Independent reflections	4952 [R(int) = 0.0359]	
Completeness to theta = 29.71°	99.4 %	
Final R indices [I>2sigma(I)]	$R1$ = 0.0296, w$R2$ = 0.0731	
R indices (all data)	$R1$ = 0.0342, w$R2$ = 0.0757	

7.2.6. Preparation of (N,N,N',N'-tetraethyldiethylenetriamine)(η^2-*O,O*-chelating nitrito)(η^1-*N*-nitro/η^1-*O*-nitrito)nickel(II) – 3

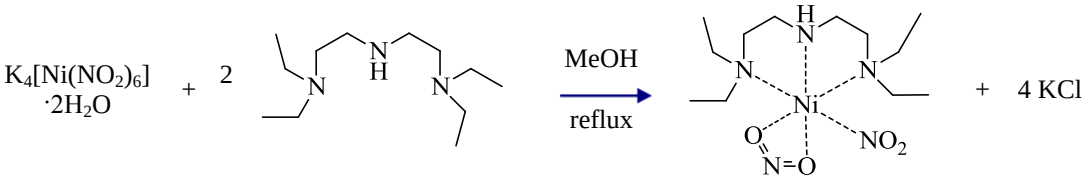

Scheme 6: Synthesis of compound **3**.

Compound **3** can be prepared by treating a suspension of potasiumhexanitritenickel(II)hydrate (0.880 g, 1.669 mmol, 527.15 g/mol) with stoichiometric amounts of N,N,N',N'-Tetraethyldiethylenetriamine (0.7189 g, 3.338 mmol, 215.38 g/mol) in methanol (25 mL) and vigorously stirred for 2 h. The initial orange suspension instantly dissolved to produce a dark green solution with a green precipitate. The mixture was concentrated in vacuo to ca. 5 mL and the green crystalline precipitate was isolated by filtration and recrystallised from methanol (Scheme 6).

Yield: 90 % (0.550 g, 1.5021 mmol)

Analysis: Calculated C 39.37, H 7.98, N 19.13, Found C 28.80 %, H 5.10 %, N 15.62 % (impurities of potassium chloride and potassium nitrate).

UV spectrum could not be obtained as the ligand dissociated occurred in solution and decomposition products dominated absorptions.

Table 3: Crystallographic data for compound **4**.

Temperature	150(2) K
Wavelength	0.7107 Å
Crystal system	Orthorhombic

Space group	$P\ 2_12_12_1$
Unit cell dimensions	a = 11.3454(2) Å
	b = 11.6419(2) Å
	c = 12.8959(2) Å
Volume	1703.32(5) Å^3
Z	4
Crystal size	0.07 x 0.07 x 0.01 mm
Theta range for data collection	2.96 to 29.21°
Independent reflections	4088 [R(int) = 0.0293]
Completeness to theta = 29.21°	92.8 %
Data / restraints / parameters	4088 / 0 / 207
Final R indices [I>2sigma(I)]	R1 = 0.0302, wR2 = 0.0555
R indices (all data)	R1 = 0.0436, wR2 = 0.0570

7.2.7. Preparation of trans-bis(2,2'aminocyclohexane)bis(η^1-*N*-nitro)nickel(II) – 4

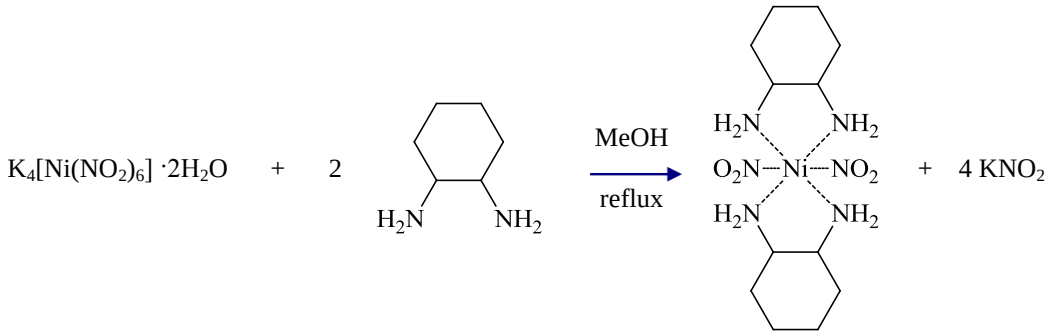

Scheme 7: Synthesis of compound **4**.

Compound **4** can be prepared by treating potassium hexanitritenickel(II)hydrate (0.0416 g, 0.079 mmol, 527.15 g/mol) with two equivalents of diaminocyclohexane (0.06 g, 0.158 mmol, 379.08 g/mol) (Scheme 7). The solution was refluxed for 4 h after which the solution was cooled. The pale pink crystalline precipitate was isolated by filtration and small crystals of X-ray quality were grown from acetonitrile using slow evaporation techniques.

Yield: 90 % (0.054 g, 0.142 mmol)

Analysis: Calculated C 38.02, H 7.44, N 22.17, Found C 38.14 %, H 7.36 %, N 22.06 %.

UV spectrum could not be obtained as the ligand dissociated occurred in solution and decomposition products dominated absorptions.

Table 4: Crystallographic data for compound **4**.

	Ground State	Metastable State
Empirical formula	C12 H28 N6 Ni O4	C12 H28 N6 Ni O4
Formula weight	379.11	379.11
Temperature	100(2) K	100(2) K
Wavelength	0.68960 Å	0.68960 Å
Crystal system	Monoclinic	Monoclinic
Space group	*P*2(1)/*c*	*P*2(1)/*c*
Unit cell dimensions	*a* = 12.1116(11) Å	*a* = 12.0539(11) Å
	b = 7.0730(6) Å	*b* = 7.1129(6) Å
	c = 10.7699(9) Å	*c* = 10.7487(9) Å
	β = 112.4250(10)°	*β* = 111.8960(10)°
Volume	852.84(13) Å^3	855.09(13) Å^3
Z	2	2
Crystal size	0.06 x 0.04 x 0.01 mm	0.06 x 0.04 x 0.01 mm
Theta range for data collection	3.55 to 29.26°	4.24 to 29.76°
Independent reflections	2456 [*R*(*int*) = 0.0298]	2561 [*R*(*int*) = 0.0292]
Completeness to theta = 29.26°	98.6 %	98.0 %
Data / restraints / parameters	2456 / 0 / 106	2561 / 0 / 116
Final R indices [I>2sigma(I)]	*R*1 = 0.0416, *wR*2 = 0.1064	*R*1 = 0.0432, *wR*2 = 0.1464
R indices (all data)	*R*1 = 0.0479, *wR*2 = 0.1102	*R*1 = 0.0500, *wR*2 = 0.1523

7.2.8. Preparation of trans-bis(aminomethylpyridine)bis(η^1-*O*-nitrito)nickel(II) – 5

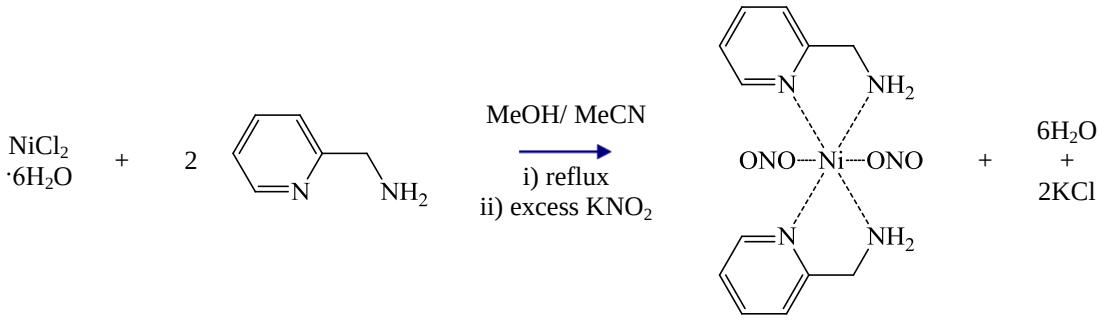

Scheme 8: Synthesis of compound **5**.

Compound **5** was prepared using a modification of a previously reported procedure.[12] A methanolic (5 mL) suspension of nickel (II) chloride hexahydrate (0.048 g, 0.2 mmol, 237.59 g/mol) was treated with two equivalents of aminomethylpyridine (0.0432 g, 0.4 mmol, 108.14 g/mol) in acetonitrile (10 mL) added dropwise, followed by the addition of a solution of potassium nitrite in methanol (10 mL) (Scheme 8). The solution was refluxed for 1 h, after which the resulting pink/purple crystalline material suitable for X-ray analysis was collected by filtration and dried under vacuum.

Yield: 98 % (0.0719 g, 0.196 mmol).

Analysis: Calculated C 39.27, H 4.39, N 22.90, Found C 39.4 %, H 4.31 %, N 22.79 %.

UV spectrum could not be obtained as the ligand dissociated occurred in solution and decomposition products dominated absorptions.

Table 5: Crystallographic data for compound **5**.

Empirical formula	C12 H16 N6 Ni O4	
Formula weight	367.02	
Temperature	150(2) K	
Wavelength	0.71073 Å	
Crystal system	Monoclinic	
Space group	$P2_1/c$	
Unit cell dimensions	a = 8.46310(10) Å	α = 90°
	b = 9.6250(2) Å	β = 99.708(2)°
	c = 8.9017(2) Å	γ = 90°
Volume	714.73(2) Å^3	
Z	2	
Crystal size	0.2591 x 0.2406 x 0.1970 mm	
Theta range for data collection	3.14 to 32.59°	
Independent reflections	2447 [R(int) = 0.0240]	
Completeness to theta = 30.00°	99.8 %	
Data / restraints / parameters	2447 / 0 / 106	
Final R indices [I>2sigma(I)]	$R1$ = 0.0269, $wR2$ = 0.0631	
R indices (all data)	$R1$ = 0.0397, $wR2$ = 0.0651	

7.2.9. Preparation of (2,2'-biquinoline)(methoxyl)(η^2-*O,O*-nitrito)(η^1-*O*-nitrito)nickel(II) – 6

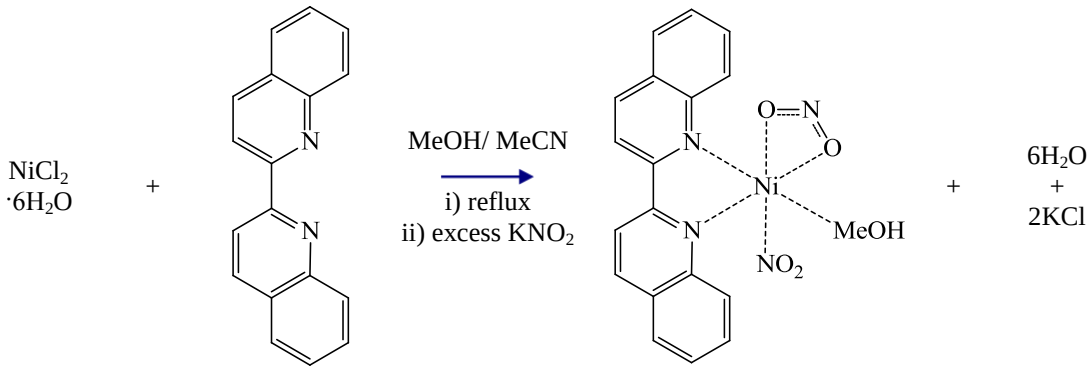

Scheme 9: Synthesis of compound **6**.

A methanolic solution (30 mL) of 2,2'-biquinoline (0.256 g, 1 mmol, 256.30 g/mol) was added dropwise with vigorous stirring to a methanolic (5 mL) suspension of nickel chloride (II) hexahydrate (0.24 g, 1 mmol, 237.59 g/mol). The solution was refluxed for 4 h after which a concentrated solution of potassium nitrite (0.34 g, 4 mmol, 85.11 g/mol) in methanol (10 mL) was added dropwise with vigorous stirring. The solution

was refluxed for a further 3 h after which the solvent was partially evaporated producing a green crystalline solid (Scheme 9). The compound was filtered, washed with water and dried in a $CaCl_2$ desiccator.

Yield: 83 % (0.036 g, 0.083 mmol).

Analysis: Calculated C 51.98 %, H 3.56 %, N 12.76 %, Found C 48.53 %, H 2.48 %, N 10.20 % (impurities of potassium chloride and potassium nitrate).

UV spectrum could not be obtained as the ligand dissociated occurred in solution and decomposition products dominated absorptions.

Table 6: Crystallographic data for compound **6**.

Empirical formula	C19 H16 N4 Ni O5	
Formula weight	439.07	
Temperature	100(2) K	
Wavelength	0.68960 Å	
Crystal system	Monoclinic	
Space group	$P2_1/c$	
Unit cell dimensions	a = 15.9560(14) Å	α = 90°
	b = 7.5503(6) Å	β = 99.8250(10)°
	c = 15.4703(13) Å	γ = 90°
Volume	1836.4(3) $Å^3$	
Z	4	
Crystal size	0.03 x 0.03 x 0.02 mm	
Theta range for data collection	2.59 to 29.55°	
Independent reflections	5568 [R(int) = 0.0396]	
Completeness to theta = 29.00°	99.0 %	
Data / restraints / parameters	5568 / 0 / 260	
Final R indices [I>2sigma(I)]	$R1$ = 0.0412, $wR2$ = 0.0999	
R indices (all data)	$R1$ = 0.0440, $wR2$ = 0.1016	

7.2.10. Preparation of (1,10-phenanthroline)bis(η^1-*N*-nitro)nickel(II) – 7

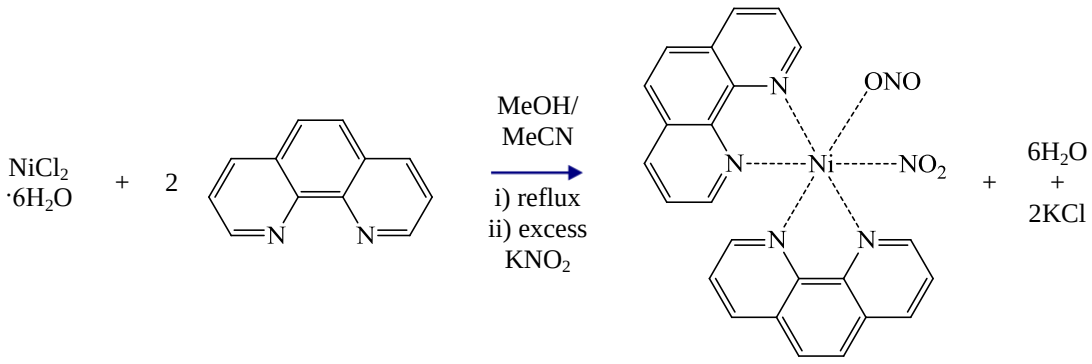

Scheme 10: Synthesis of compound **7**.

1,10-phenanthroline (0.0360 g, 0.2 mmol, 180.21 g/mol) in acetonitrile (10 mL) was added dropwise with vigorous stirring to a methanolic solution (15 mL) of nickel (II) chloride hexahydrate (0.0238 g, 0.1 mmol, 237.59 g/mol). The solution was refluxed for 4 h during which the solution turned a dark pink. The solution was cooled to room temperature and a saturated methanolic solution (5mL) of excess potassium nitrite (0.034 g, 0.4 mmol, 85.11 g/mol) was added (Scheme 10). The solution was refluxed for a further 2 h after which the solution was cooled slowly affording pink microcrystals suitable for X-ray diffraction experiments. The crystals were collected by filtration and washed with methanol. The crystalline material was insoluble in all common solvents, and as a result solution based analysis could not be carried out.

Yield: 75 % (0.038 g, 0.075 mmol).

Analysis: Calculated C 52.56 %, H 3.16 %, N 16.44 %, Found C 52.45 %, H 2.92 %, N 15.29 %.

UV spectrum could not be obtained as the ligand dissociated occurred in solution and decomposition products dominated absorptions.

Table 7: Crystallographic data for compound **7.**

Empirical formula	C48 H32 N12 Ni2 O8	
Formula weight	1022.28	
Temperature	100(2) K	
Wavelength	0.69400 *Å*	
Crystal system	Triclinic	
Space group	*P*-1	
Unit cell dimensions	*a* = 8.3964(4) *Å*	α = 77.4180(10)°
	b = 14.6698(8) *Å*	β = 77.4590(10)°
	c = 17.9542(9) *Å*	γ = 80.6970(10)°
Volume	2091.64(18) $Å^3$	
Z	2	
Crystal size	0.04 x 0.04 x 0.03 mm	
Theta range for data collection	1.16 to 30.70°	
Independent reflections	13382 [*R*(*int*) = 0.0812]	
Completeness to theta = 30.00°	98.8 %	
Data / restraints / parameters	13382 / 0 / 632	
Final R indices [I>2sigma(I)]	*R*1 = 0.0494, *wR*2 = 0.1191	
R indices (all data)	*R*1 = 0.0689, *wR*2 = 0.1275	

7.2.11. Preparation of (2,2':6',2"-terpyridine)bis(η^1-*N*-nitro)nickel(II)hydrate – 8

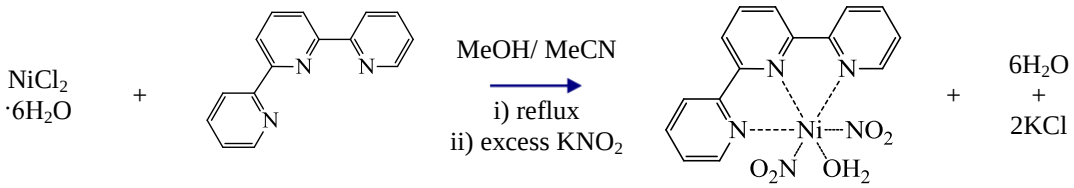

Scheme 11: Synthesis of compound **8**.

The preparation of compound **8** is reported in literature.[13] Using a modified procedure, compound **8** was synthesised by treating a methanolic solution (10 mL) of nickel (II) chloride hexahydrate (0.0238 g, 0.1 mmol, 237.59 g/mol) with stoichiometric amounts of acetonitrile solution (10 mL) of 2,2':6',2"-terpyridine (0.0233 g, 0.1 mmol, 233.27 g/mol). The solution was refluxed for 2 h after which the solvent was removed *in vacuo* and the resulting solid was purified by recrystallisation from methanol. The resulting solid was taken up in methanol and treated with a methanolic solution (5 mL) of potassium nitrite (0.034 g, 0.4 mmol, 85.11 g/mol) added dropwise, after which the solution was refluxed for 1 h (Scheme 11). The solvent was removed to afford a red/brown microcrystalline solid and white impurities of inorganic salts. The solid was (partially) dissolved in DCM and the mixture was filtered to remove the impurities. The filtrate was evaporated to dryness and the residue was recrystallized using slow evaporation in methanol, to give compound **8** as a red microcrystalline solid.

Yield: 80 % (0.032 g, 0.08 mmol).

Analysis: Calculated C 44.82 %, H 2.26 %, N 17.42 %, Found C 44.70 %, H 3.13 %, N 17.39 %.

UV spectrum could not be obtained as the ligand dissociated occurred in solution and decomposition products dominated absorptions.

X-ray powder patterns showed some impurities in the bulk sample.

Table 8: Crystallographic data for compound **8**.

Empirical formula	C15 H13 N5 Ni O5	
Formula weight	402.01	
Temperature	100(2) K	
Wavelength	0.77490 Å	
Crystal system	Monoclinic	
Space group	*C* 2/*c*	
Unit cell dimensions	*a* = 9.016(5) Å	α = 90°

	b = 18.791(5) Å	β = 112.785(5)°
	c = 9.842(5) Å	γ = 90°
Volume	1537.3(12) Å^3	
Z	4	
Crystal size	0.08 x 0.03 x 0.01 mm	
Theta range for data collection	4.43 to 33.70°	
Reflections collected	11050	
Independent reflections	2334 [R(int) = 0.0449]	
Completeness to theta = 30.00°	99.2 %	
Data / restraints / parameters	2334 / 0 / 124	
Final R indices [I>2sigma(I)]	$R1$ = 0.0265, $wR2$ = 0.0724	
R indices (all data)	$R1$ = 0.0277, $wR2$ = 0.0733	

7.2.12. Preparation of chloro(1,2-bis(diphenylphosphino)ethane)(η^1-*N*-nitro)nickel(II) – 9

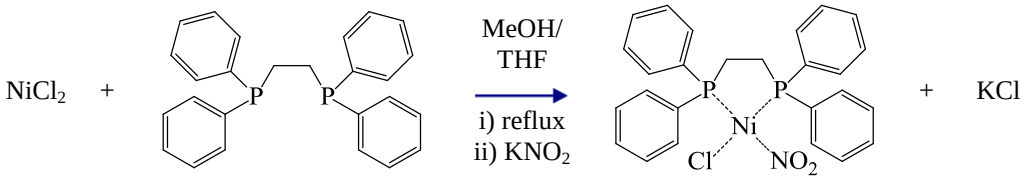

Scheme 12: Synthesis of compound **9**.

Bis-chloro(1,2-b*is*(diphenylphosphino)ethane)nickel(II) can be prepared using synthesis from literature.[14] The reaction was carried out under nitrogen in Schlenk glassware and solvents were dried by standard techniques. Nickel (II) chloride hexahydrate (0.238 g, 1 mmol, 237.59 g/mol) was heated under vacuum to produce anhydrous nickel chloride with a visible colour change from green to orange. The resulting solid was taken up in ethanol (5ml) and treated with stoichiometric amounts of 1,2-b*is*(diphenylphosphino)ethane (0.398 g, 1mol, 398.42 g/mol) in ethanol (10ml). The solution was refluxed for 3 h and after which the solvent was evaporated. The small red crystals were purified by recrystallisation in Acetone. The resulting *bis*-chloro(1,2-b*is*(diphenylphosphino)ethane)nickel(II) (0.421 g, 0.8 mmol, 526.02 g/mol) crystalline material was taken up in tetrahydrofuran (20 mL). and was treated with methanolic solution (15 ml) of potassium nitrite (0.068 g, 0.8 mmol, 85.11 g/mol) added over the period of 2 h with vigorous stirring. The solution was refluxed for 3 h after which the solvent was allowed to evaporate producing an orange solid and white impurities of

potassium chloride (Scheme 12). The solid was (partially) dissolved in DCM and the mixture was filtered removing the impurities. The filtrate was evaporated to dryness and the residue was crystallised from acetone using slow evaporation.

Yield: 60 % (0.323 g, 0.6 mmol).

Analysis: Calculated C 57.98 %, 4.49 %, N 2.60 %, Found C 57.33 %, H 4.41 %, N 2.74 %.

^{1}H NMR (300 MHz, CCl_3D): δ_H 2.17-2.12 (m, 4H, C$\underline{H_2}$C$\underline{H_2}$), 7.60-7.48 (m, 20H, C$_6\underline{H_5}$).

^{31}P NMR (300 MHz, CCl_3D): δ_P (58.38 (br s)).

ESI-MS: calc for $[C_{26}H_{27}Cl_1N_1Ni_1O_2P_2]^+$ 441.51; obs 441.

UVvis λ_{max}: 270 nm (104895 Lmol^{-1}cm^{-1}), 315 nm (34108 Lmol^{-1}cm^{-1}) and 420 nm (5706 Lmol^{-1}cm^{-1}).

Table 9: Crystallographic data of compound **9**.

	Ground-state	Metastable-state
η^1-*O*-nitrito occupancy	0%	100%
Empirical formula	C26 H24 Cl N Ni O2 P2	C26 H24 Cl N Ni O2 P2
Formula weight	538.56	538.56
Temperature	100(2) K	100(2) K
Wavelength	0.69400 Å	0.69400 Å
Crystal system	Monoclinic	Monoclinic
Space group	*Cc*	*Cc*
Unit cell dimensions	*a* = 13.424(3) Å	*a* = 13.803(5) Å
	b = 11.430(2) Å	*b* = 11.283(4) Å
	c = 17.040(5) Å	*c* = 17.008(6) Å
	β = 110.526(2)°	*β* = 111.264(4)°.
Volume	2448.6(10) Å^3	2468.5(14) Å^3
Z	4	4
Crystal size	0.09 x 0.04 x 0.03 mm	0.09 x 0.04 x 0.03 mm
Theta range for data collection	2.35 to 29.76°	2.34 to 23.86°
Independent reflections	7052 [*R*(*int*) = 0.0630]	4012 [*R*(*int*) = 0.0726]
Completeness to theta = 29.76°	99.2 %	99.5 %
Data / restraints / parameters	7052 / 2 / 298	4012 / 2 / 298
Final R indices [I>2sigma(I)]	*R*1 = 0.0562, *wR*2 = 0.1172	*R*1 = 0.0722, *wR*2 = 0.1555
R indices (all data)	*R*1 = 0.0945, *wR*2 = 0.1335	*R*1 = 0.1355, *wR*2 = 0.1854

7.2.13. Preparation of (1,2-bis(diphenylphosphino)ethane)bis(η^1-*N*-nitro)nickel(II) hydrate – 10

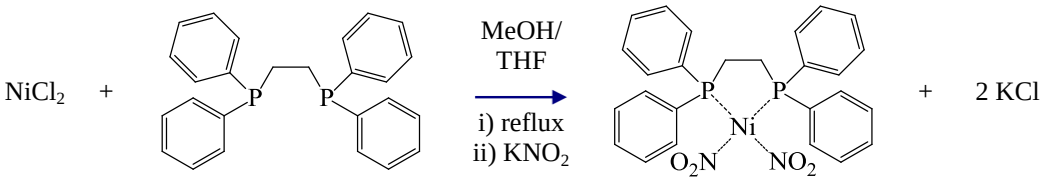

Scheme 13: Synthesis of compound **10**.

(1,2-*Bis*(diphenylphosphino)ethane)*bis*(η^1-*N*-nitro)nickel(II) (**10**) was synthesised using a modified procedure from the literature.[15] The reaction was carried out under nitrogen in Schlenk glassware and solvents were dried by standard techniques. *bis*-chloro (1,2-b*is*(diphenylphosphino)ethane)nickel(II) (0.263 g, 0.5 mmol, 526.02 g/mol) was taken up in tetrahydrofuran (15 mL) and the solution was treated with methanolic solution (15 mL) of excess potassium nitrite (0.255 g, 3 mmol, 85.11 g/mol) added over the period of 2 h with vigorous stirring. The resulting mixture was refluxed for 3 h after which the solvent was evaporated producing an orange solid and white impurities of potassium chloride and potassium nitrite. The solid was dissolved in DCM and filtered removing the inorganic salts. The filtrate was evaporated to dryness and the residue was redissolved in tetrahydrofuran (15 mL) and the resulting solution was treated again with potassium nitrite (0.085 g, 1 mmol, 85.11 g/mol) over a 30 minute period with vigorous stirring (Scheme 13). The solution was refluxed for 1 h after which the volatiles were removed and the resulting solid was taken up in DCM and the mixture was filtered removing the inorganic salts. Compound **10** was crystallised using slow evaporation in acetone.

Yield: 66 % (0.181 g, 0.33 mmol).

Analysis: Calculated C 56.87 %, 4.41 %, N 5.10 %, Found C 56.95 %, H 4.34 %, N 4.97 %.

^{1}H NMR (300 MHz, CCl_3D): δ_H 2.45 (br, 4H, C$\underline{H_2}$C$\underline{H_2}$), 7.76-7.29 (m, 20H, $C_6\underline{H_5}$).

^{31}P NMR (300 MHz, CCl_3D): δ_P 33.91

UVvis λ_{max}: 253 nm (66253 $Lmol^{-1}cm^{-1}$), 295 nm (14446 $Lmol^{-1}cm^{-1}$) and 313 nm (12626 $Lmol^{-1}cm^{-1}$).

Table 10: Compound **10** crystallographic data of the ground and metastable states.

	Ground-state	Metastable-state
η^1-*O*-nitrito occupancy	0%	100%
Empirical formula	C26 H24 N2 Ni O5 P2	C26 H24 N2 Ni O5 P2
Formula weight	565.12	565.12
Temperature	100(2) K	100(2) K
Wavelength	0.68960 Å	0.68960 Å
Crystal system	Orthorhombic	Orthorhombic
Space group	$P2_12_12_1$	$P2_12_12_1$
Unit cell dimensions	*a* = 8.1137(2) Å	*a* = 7.9997(5) Å
	b = 13.7208(4) Å	*b* = 13.9307(8) Å
	c = 22.6701(7) Å	*c* = 22.8956(14) Å
Volume	2523.78(12) Å^3	2551.5(3) Å^3
Z	4	4
Crystal size	0.08 x 0.08 x 0.04 mm^3	0.08 x 0.08 x 0.04 mm^3

Theta range for data collection	1.70 to 29.73°	2.64 to 29.84°
Independent reflections	7512 [*R*(int) = 0.0517]	7527 [*R*(int) = 0.0463]
Completeness to theta = 29.73°	98.7 %	97.4 %
Data / restraints / parameters	7512 / 0 / 325	7527 / 0 / 325
Final R indices [I>2sigma(I)]	*R*1 = 0.0427, *wR*2 = 0.1106	*R*1 = 0.0742, *wR*2 = 0.1959
R indices (all data)	*R*1 = 0.0472, *wR*2 = 0.1141	*R*1 = 0.1076, *wR*2 = 0.2198

7.2.14. Preparation of (1,2-bis(dicyclohexylphosphino)ethane)bis(η^1-*N*-nitro)nickel(II) – 11

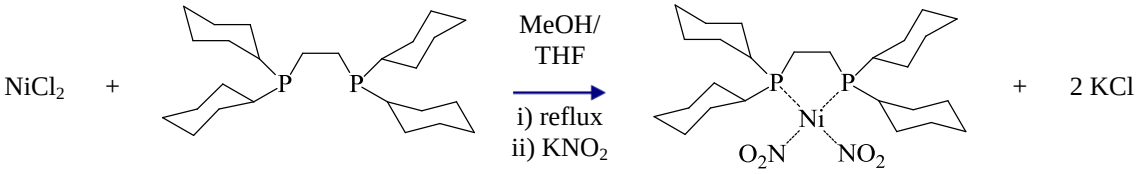

Scheme 14: Synthesis of compound **11**.

Compound **11** was synthesised using a modified procedure from the literature.[16] The reaction was carried out under nitrogen in Schlenk glassware and solvents were dried by standard techniques. Nickel (II) chloride hexahydrate (0.199 g, 0.5 mmol, 237.59 g/mol) was heated under vacuum to produce anhydrous nickel chloride as indicated by a visible colour change from green to orange. The resulting solid was taken up in ethanol (10 mL) and the solution was treated with stoichiometric amounts of 1,2-bis(dicyclohexylphosphino)ethane (0.211 g, 0.5 mmol, 422.61 g/mol) in ethanol (10mL). The solution was refluxed for 3 h after which the solvent was removed *in vacuo*. The small red crystals were purified by recrystallisation from dichloromethane. The resulting *bis*-chloro(1,2-bis(dicyclohexylphosphino)ethane)nickel(II) (0.221 g, 0.4 mmol, 552.21 g/mol) was taken up in tetrahydrofuran (20 mL) and was treated with a methanolic solution (15 mL) of potassium nitrite (0.085 g, 1 mmol, 85.11 g/mol) added over a 2 h period with vigorous stirring. The solution was refluxed for 3 h after which the solvent was evaporated, producing an orange solid and white impurities of inorganic salts. The resulting solid was (partially) dissolved in DCM, filtered removing the impurities and the filtrate was evaporated to dryness (Scheme 14). The addition of potassium nitrite and purification was repeated twice to ensure a complete substitution

of the chloro groups. Crystals suitable for single crystal diffraction experiments were obtained from slow evaporation from DCM/toluene solution.

Yield: 74 % (0.170 g, 0.30 mmol).

Analysis: Calculated C 59.56 %, 8.48 %, N 4.21 %, Found C 49.97 %, H 7.86 %, N 2.56 % (difference to due to toluene and DCM solvent).

^{1}H NMR (300 MHz, CCl_3D): δ_H 1.91-1.09 (m, 44H, C_6H_{11}) 2.46 (m, 4H, $C\underline{H_2}C\underline{H_2}$) (broad NMR with many overlapping peaks).

^{31}P NMR (300 MHz, CCl_3D): δ_P 74.81

UVvis λ_{max}: 250 nm (12516 $Lmol^{-1}cm^{-1}$), 300 nm (6434 $Lmol^{-1}cm^{-1}$) and 400 nm (459 $Lmol^{-1}cm^{-1}$).

ESI-MS: calc for $[C_{26}H_{48}Cl_1N_1Ni_1O_4P_2]^+$ 595.76; obs 596.

Table 11: Crystallographic data for compounds **11**.

	Ground State	Metastable State
η^1-*O*-nitrito occupancy	0%	100%
Empirical formula	C33 H56 N2 Ni O4 P2	C33 H56 N2 Ni O4 P2
Formula weight	665.45	665.45
Temperature	100(2) K	100(2) K
Wavelength	0.68960 Å	0.68960 Å
Crystal system	Monoclinic	Monoclinic
Space group	*P*2(1)/*c*	*P*2(1)/*c*
Unit cell dimensions	*a* = 12.2125(5) Å	*a* = 12.199(10) Å
	b = 18.7052(8) Å	*b* = 19.146(8) Å
	c = 15.1718(6) Å	*c* = 15.093(10) Å
	β =97.2610(10)°	β = 101.00(5)°
Volume	3438.0(2) Å^3	3461(4) Å^3
Z	4	4
Crystal size	0.10 x 0.05 x 0.02 mm^3	0.10 x 0.05 x 0.02 mm^3
Theta range for data collection	1.70 to 29.70°	2.19 to 29.73°
Independent reflections	10185 [*R*(int) = 0.0474]	10272 [*R*(int) = 0.0437]
Completeness to theta = 29.70°	97.4 %	97.3 %
Data / restraints / parameters	10185 / 0 / 380	10272 / 0 / 460
Final R indices [I>2sigma(I)]	*R*1 = 0.0394, *wR*2 = 0.0933	*R*1 = 0.0946, *wR*2 = 0.2501
R indices (all data)	*R*1 = 0.0497, *wR*2 = 0.0992	*R*1 = 0.1177, *wR*2 = 0.2704

7.2.15. Preparation of (bis(2-diphenylphosphinoethyl) phenylphosphine)(η^1-*N*-nitro)nickel(II) tetraphenylborate – 12

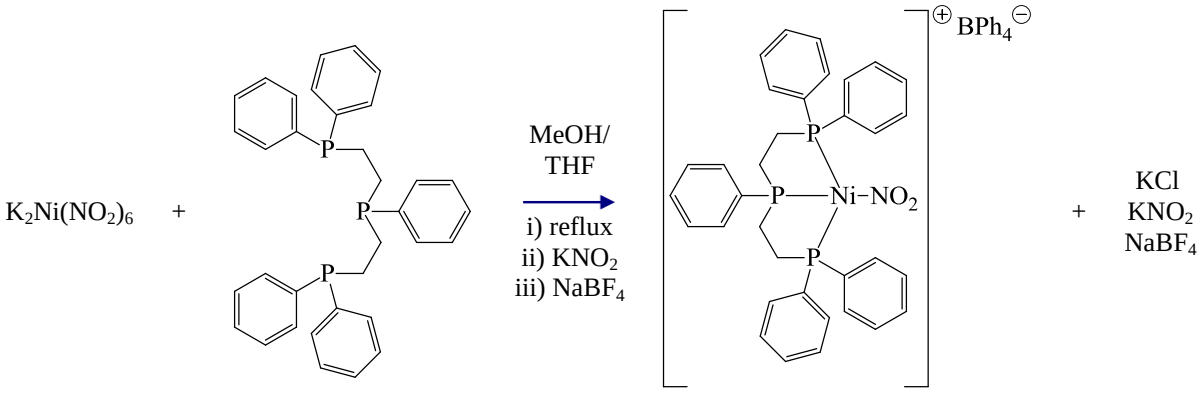

Scheme 15: Synthesis of compound **12**.

The reaction was carried out under nitrogen in Schlenk glassware and solvents were dried by standard techniques. A freshly prepared sample of potassium hexanitritenickel(II)hydrate (0.105 g, 0.2 mmol, 527.15 g/mol) in methanol (5 mL) is slowly treated with stoichiometric amounts of the Bis(2-diphenylphosphinoethyl)phenylphosphine (0.107 g, 0.2 mmol, 534.55 g/mol) with continuous stirring for 4 h, during which time the colour changed to red. The solution was treated with potassium nitrite (0.017 g, 0.2 mmol, 85.11 g/mol) stirred for a further 2 h. The solvent was removed and the resulting solid was taken up in dichloromethane and the mixture was filtered to remove any inorganic salts. The filtrate was evaporated to dryness and the residue was taken up in acetone and a yellow/orange precipitate formed on the addition of excess sodium tetraphenylborate (0.103 g, 0.3 mmol, 342.22 g/mol) in an water/acetone (30/1 ratio) (Scheme 15). Single crystals of compound **12** suitable for X-ray diffraction experiments were obtained by recrystallisation from acetonitrile.

Yield: 88 % (0.169 g, 0.176 mmol).

Analysis: Calculated C 72.68 %, 5.57 %, N 1.46 %, Found C 72.62 %, H 5.44 %, N 1.52 %.

^{1}H NMR (300 MHz, CCl_3D): δ_H 2.71-2.67 (m, 8H, $\underline{CH_2CH_2}$) 7.96-7.06 (m, ~25H, C_6H_5) (many overlapping peaks from toluene and tetraphenylborate).

^{31}P NMR (300 MHz, $(CH_3)_2CO$): δ_P 49.4-47.56 (br, m)

UVvis λ_{max}: 286 nm (25275 Lmol^{-1}cm^{-1}), 314 nm (23900 Lmol^{-1}cm^{-1}) and 400 nm (3445 Lmol^{-1}cm^{-1}).

Table 12: Crystallographic data for compounds **12**.

	Ground State	Metastable State
η^1-*O*-nitrito occupancy	0%	83 %
Empirical formula	C58 H53 B N Ni O2 P3	C58 H53 B N Ni O2 P3
Formula weight	958.44	958.44
Temperature	100(2) K	100(2) K
Wavelength	0.68960 Å	0.68960 Å
Crystal system	Triclinic	Triclinic
Space group	*P*-1	*P*-1
Unit cell dimensions	*a* = 11.439(5) Å	*a* = 11.4586(5) Å
	b = 14.386(5) Å	*b* = 14.3876(6) Å
	c = 17.108(5) Å	*c* = 17.0954(8) Å
	α = 96.407(5)°	α = 95.7470(10)°
	β = 105.182(5)°	β = 105.5350(10)°
	γ = 112.927(5)°	γ = 112.5510(10)°
Volume	2429.1(15) Å^3	2441.75(19) Å^3
Z	2	2
Crystal size	0.08 x 0.06 x 0.04 mm	0.08 x 0.06 x 0.05 mm
Theta range for data collection	1.27 to 30.53°	1.24 to 29.72°
Independent reflections	13970 [*R*(*int*) = 0.0286]	14049 [*R*(*int*) = 0.0313]
Completeness to theta = 30.00°	96.6 %	97.7 %
Data / restraints / parameters	13970 / 10 / 609	14049 / 5 / 605
Final R indices [I>2sigma(I)]	*R*1 = 0.0398, *wR*2 = 0.1191	*R*1 = 0.0472, *wR*2 = 0.1077
R indices (all data)	*R*1 = 0.0493, *wR*2 = 0.1297	*R*1 = 0.0599, *wR*2 = 0.1147

7.2.16. Preparation of bis(triethylphosphine)bis(η^1-*N*-nitro)nickel (II) - 13

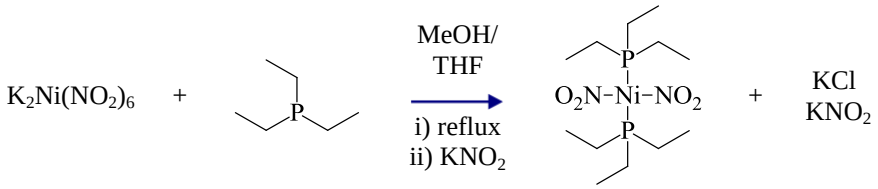

Scheme 16: Synthesis of compound **13**.

The compound **13** was synthesised using a procedure from the literature.[17] The reaction was carried out under nitrogen in Schlenk glassware and solvents were dried by standard techniques. An ethanolic solution (10 mL) of nickel (II) chloride hexahydrate (0.199 g, 0.5 mmol, 237.59 g/mol) was treated with two equivalents of triethylphosphine (1 cm^3 of 1.0 M triethylphosphine in THF, 1 mmol, 118.16 g/mol) in tetrahydrofuran (10mL) giving a colour change from pale green to purple. The solution was refluxed for 3 h after which the solvent was removed *in vacuo*. The small purple

crystals were purified by recrystallisation from acetone. The resulting *bis*-chloro(triethylphosphine)nickel(II) (0.146 g, 0.4 mmol, 365.91 g/mol) was taken up in tetrahydrofuran (20 mL) and the solution was treated with a methanolic solution (15 mL) of potassium nitrite (0.128 g, 1.5 mmol, 85.11 g/mol) added over a 2 h period with vigorous stirring. The solution was refluxed for 3 h after which the solvent was evaporated, producing an orange solid and white impurities of inorganic salts (Scheme 16). The solid was (partially) dissolved in DCM, the mixture was filtered, and the filtrate was evaporated to dryness to give **13** as an orange solid. Crystals suitable for single crystal diffraction experiments were obtained by slow evaporation from DCM/toluene solution.

Yield: 90 % (0.155 g, 0.36 mmol).

Analysis: Calculated C 37.24, H 7.81, N 7.24, Found C 37.12 %, H 7.22 %, N 7.27 %.

^{1}H NMR (300 MHz, CCl_3D): δ_H 1.10 (br, ~18H, $CH_2\underline{CH_3}$) 1.35 (br, 12H, $\underline{CH_2}CH_3$) (broad NMR with overlapping peaks).

^{31}P NMR (300 MHz, CCl_3D): δ_P 54.33

UVvis λ_{max}: 280 nm (6450 $Lmol^{-1}cm^{-1}$), 385 nm (408 $Lmol^{-1}cm^{-1}$).

Table 13: Crystallographic data for compounds **13**.

	Ground State	Metastable State
η^1-*O*-nitrito occupancy	0%	26%
Empirical formula	C12 H30 N2 Ni O4 P2	C12 H30 N2 Ni O4 P2
Formula weight	387.03	387.03
Temperature	100(2) K	100(2) K
Wavelength	0.68960 Å	0.68960 Å
Crystal system	Monoclinic	Monoclinic
Space group	*P*2(1)/*c*	*P*2(1)/*c*
Unit cell dimensions	*a* = 7.839(4) Å	*a* = 7.890(4) Å
	b = 7.814(4) Å	*b* = 7.787(3) Å
	c = 15.152(11) Å	*c* = 15.251(6) Å
	β = 95.15(4)°	β = 94.82(2)°
Volume	924.4(9) $Å^3$	933.6(7) $Å^3$
Z	2	2
Crystal size	0.05 x 0.05 x 0.03 mm^3	0.05 x 0.05 x 0.03 mm^3
Theta range for data collection	3.60 to 29.77°	3.60 to 29.77°
Independent reflections	2731 [*R*(*int*) = 0.0523]	2743 [*R*(*int*) = 0.0271]
Completeness to theta = 29.00°	99.2 %	98.6 %
Data / restraints / parameters	2731 / 0 / 100	2743 / 13 / 125
Final R indices [I>2sigma(I)]	*R*1 = 0.0443, *wR*2 = 0.0930	*R*1 = 0.0287, *wR*2 = 0.0717
R indices (all data)	R1 = 0.0494, wR2 = 0.0947	R1 = 0.0327, wR2 = 0.0735

7.2.17. Preparation of bis(tricyclohexylphosphine)bis(η^1-*N*-nitro)nickel(II) – 14

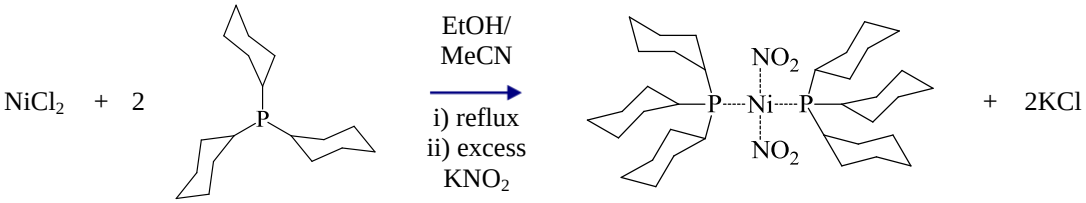

Scheme 17: Synthesis of compound **14**.

The compound **14** was synthesised using a procedure from the literature.[15] The reaction was carried out under nitrogen in Schlenk glassware and solvents were dried by standard techniques. An ethanolic solution (10 mL) of nickel (II) chloride hexahydrate (0.199 g, 0.5 mmol, 237.59 g/mol) was treated with tricyclohexylphosphine (0.208 g, 1 mmol, 208.43 g/mol) in tetrahydrofuran (10mL). The solution was refluxed for 3 h after which the solvent were evaporated. The small red crystals were purified by recrystallisation from acetone. The resulting *bis*-chlorobis(tricyclohexylphosphine)nickel(II) (0.276 g, 0.4 mmol, 690.46 g/mol) was taken up in tetrahydrofuran (20 mL) and the solution was treated with a methanolic solution (15 mL) of potassium nitrite (0.128 g, 1.5 mmol, 85.11 g/mol) added over a 2 h period with vigorous stirring. The solution was refluxed for 3 h after which the solvent was evaporated, producing an orange solid and white impurities of inorganic salts (Scheme 17). The resulting solid was (partially) dissolved in DCM, the mixture was filtered and the filtrate was evaporated to dryness. Crystals suitable for single crystal diffraction experiments were obtained by slow evaporation from DCM/THF solution.

Yield: 82 % (0.583 g, 0.33 mmol).

Analysis: Calculated C 60.77, H 9.35, N 3.94, Found C 59.85 %, H 9.25 %, N 3.98 %.

^{1}H NMR (300 MHz, CCl_3D): δ_H 1.08-1.9 (m, br) (broad NMR with overlapping peaks).

^{31}P NMR (300 MHz, CCl_3D): δ_P 51.41

UVvis λ_{max}: 280 nm (6450 $Lmol^{-1}cm^{-1}$), 385 nm (408 $Lmol^{-1}cm^{-1}$).

Table 14: Crystallographic data for compound **14.**

	Ground state	Metastable state
η^1-*O*-nitrito occupancy	0%	83%
Empirical formula	C36 H66 N2 Ni O4 P2	C36 H66 N2 Ni O4 P2
Formula weight	711.56	711.56
Temperature	100(2) K	100(2) K
Wavelength	0.77490 Å	0.77490 Å
Crystal system	Triclinic	Triclinic
Space group	*P*-1	*P*-1
Unit cell dimensions	*a* = 10.084(2) Å	*a* = 10.005(4) Å
	b = 10.369(2) Å	*b* = 10.344(4) Å
	c = 10.464(2) Å	*c* = 10.713(4) Å
	α = 111.269(3)°	α = 112.515(6)°
	β = 110.575(3)°	β = 110.465(6)°
	γ = 94.503(3)°	γ = 93.518(6)°
Volume	927.5(3) Å^3	934.9(7) Å^3
Z	1	1
Crystal size	0.04 x 0.03 x 0.03 mm^3	0.04 x 0.03 x 0.03 mm^3
Theta range for data collection	2.96 to 33.69°	3.00 to 33.81°
Independent reflections	5575 [*R*(*int*) = 0.0926]	5619 [*R*(*int*) = 0.0531]
Completeness to theta = 30.50°	99.3 %	99.2 %
Data / restraints / parameters	5575 / 0 / 206	5619 / 13 / 217
Final R indices [I>2sigma(I)]	*R*1 = 0.0778, *wR*2 = 0.2008	*R*1 = 0.0596, *wR*2 = 0.1524
R indices (all data)	*R*1 = 0.0888, *wR*2 = 0.2118	*R*1 = 0.0988, *wR*2 = 0.1726

7.2.18. Preparation of bis(tricyclohexylphosphine)bis(η^1-N-nitro)palladium(II) - 15

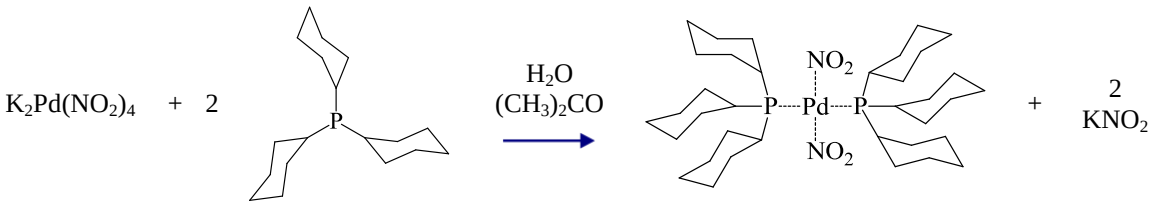

Scheme 18: Synthesis of compound **15**.

Compound **15** was synthesized according to literature procedures.[9] A potassium tetranitritepalladium(II) (0.1018 g, 0.276 mmol, 368.61 g/mol) in a water/acetone (30:5) solution (10mL) was treated with a solution of tricyclohexylphosphine (0.155 g, 0.552 mmol, 280.43 g/mol) in acetone (10 mL) and the mixture was stirred for 2 h. The initially homogeneous solution rapidly turned cloudy with the formation of the product (Scheme 18). The precipitate was collected by filtration, the residue was (partially) dissolved in dichloromethane and the mixture was filtered to remove potassium nitrite.

Colourless crystals of compound **15** suitable for X-ray structure experiments were obtained *via* slow evaporation from dichloromethane/acetone solution.

Yield: 65 % (0.136 g, 0.18 mmol).

Analysis: Calculated C 56.95, H 8.71, N 3.69, Found C 52.12 %, H 7.08 %, N 4.42 %.

^{1}H NMR (300 MHz, CCl_3D): δ_H 1.71-1.08 (m, 44H, $C_6H_{11(axial)}$) (broad NMR with overlapping peaks).

^{31}P NMR (300 MHz, CCl_3D): δ_P 25.09 (s)

UVvis λ_{max}: 285 nm (24818 $Lmol^{-1}cm^{-1}$).

Table 15: Crystallographic data of compound **15** before and after irradiation.

	Ground State	Metastable State
η^1-*O*-nitrito occupancy	0%	44%
Empirical formula	C36 H66 N2 O4 P2 Pd	C36 H66 N2 O4 P2 Pd
Formula weight	759.25	759.25
Temperature	100(2) K	100(2) K
Wavelength	0.77490 Å	0.77490 Å
Crystal system	Triclinic	Triclinic
Space group	*P*-1	*P*-1
Unit cell dimensions	*a* = 10.103(5) Å	*a* = 10.0521(7) Å
	b = 10.412(5) Å	*b* = 10.4185(7) Å
	c = 10.582(5) Å	*c* = 10.6814(7) Å
	α = 111.425(5)°	α = 112.0220(10)°
	β = 110.355(5)°	β = 110.3450(10)°
	γ = 94.508(5)°	γ = 94.0300(10)°
Volume	944.2(8) Å^3	946.07(11) Å^3
Z	1	1
Crystal size	0.08 x 0.08 x 0.07 mm	0.08 x 0.08 x 0.07 mm
Theta range for data collection	2.96 to 30.50°.	2.97 to 34.78°.
Independent reflections	5002 [*R*(*int*) = 0.0545]	5889 [*R*(*int*) = 0.0587]
Completeness to theta = 30.00°	87.5 %	99.2 %
Data / restraints / parameters	5002 / 0 / 205	5889 / 13 / 217
Final R indices [I>2sigma(I)]	*R*1 = 0.0559, *wR*2 = 0.1620	*R*1 = 0.0399, *wR*2 = 0.1033
R indices (all data)	*R*1 = 0.0591, *wR*2 = 0.1655	*R*1 = 0.0425, *wR*2 = 0.1054

7.2.19. Preparation of bis(triphenylphosphine)bis(η^1-*N*-nitro)palladium (II) – 16

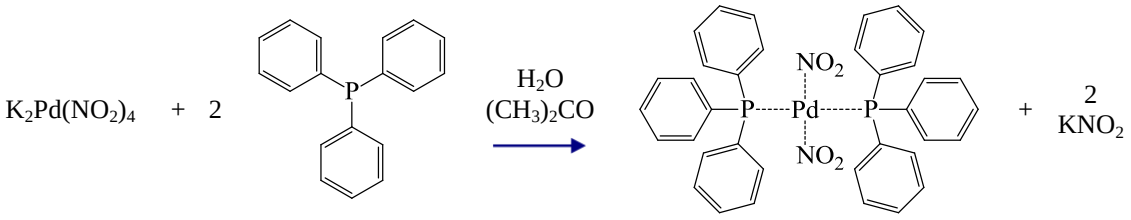

Scheme 19: Synthesis of compound **16**.

Compound **16** was synthesised according to literature accounts.[18] A potassium tetranitritepalladium(II) (0.1018 g, 0.276 mmol, 368.61 g/mol) in a water/acetone (30:5) solution (10mL) was treated with a solution of triphenylphosphine (0.145 g, 0.552 mmol, 262.29 g/mol) in acetone (10 mL) and the mixture was stirred for 2 h. The initially homogeneous solution rapidly turned cloudy with the formation of the product (Scheme 19). The precipitate was collected by filtration, the residue was (partially) dissolved in dichloromethane and the mixture was filtered to remove potassium nitrite. Colourless crystals of compound **16** suitable for X-ray structure experiments were obtained *via* slow evaporation from dichloromethane/acetone solution.

Yield: 69 % (0.138 g, 0.19 mmol).

^{1}H NMR (300 MHz, CCl_3D): δ_H 7.57-7.35 (m, 12H, o,p-ArH), 7.77-7.60 (m, 8H, m-ArH)

Analysis: Calculated C 59.8, H 4.18, N 3.87, Found C 58.68 %, H 2.56 %, N 3.19 %.

UVvis λ_{max}: 311 nm (47377 $Lmol^{-1}cm^{-1}$).

Table 16: Crystallographic data for compound **16**.

	Ground state	Metastable state
Empirical formula	C38 H34 Cl4 N2 O4 P2 Pd	C38 H34 Cl4 N2 O4 P2 Pd
Formula weight	892.81	892.81
Temperature	100(2) K	100(2) K
Wavelength	0.77490 Å	0.77490 Å
Crystal system	Orthorhombic	Orthorhombic
Space group	*Pbca*	*Pbca*
Unit cell dimensions	*a* = 20.690(18) Å	*a* = 20.629(10) Å
	b = 8.069(7) Å	*b* = 7.985(4) Å
	c = 23.51(2) Å	*c* = 23.339(12) Å
Volume	3925(6) Å^3	3845(3) Å^3
Z	4	4
Crystal size	0.03 x 0.03 x 0.01 mm	0.03 x 0.03 x 0.01 mm
Theta range for data collection	3.49 to 33.36°	3.52 to 33.79°
Independent reflections	5807 [*R*(*int*) = 0.0941]	5879 [*R*(*int*) = 0.0742]
Completeness to theta = 33.36°	98.8 %	98.7 %
Data / restraints / parameters	5807 / 0 / 232	5879 / 0 / 260
Final R indices [I>2sigma(I)]	*R*1 = 0.0560, *wR*2 = 0.1512	*R*1 = 0.0392, *wR*2 = 0.1029
R indices (all data)	*R*1 = 0.0644, *wR*2 = 0.1624	*R*1 = 0.0483, *wR*2 = 0.1108

7.2.20. Preparation of bis(triphenylarsine)bis(η^1-*N*-nitro)palladium (II) – 17

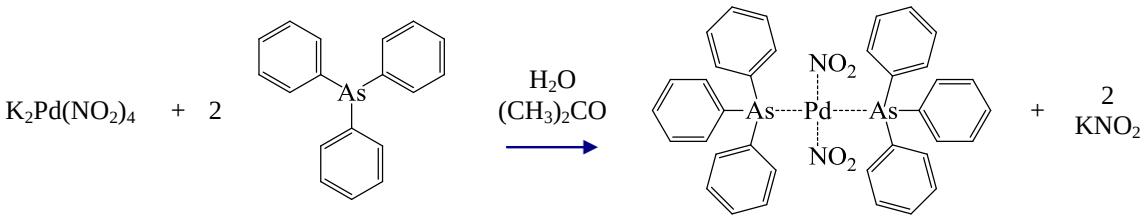

Scheme 20: Synthesis of compound **17**.

Compound **17** was synthesised according to literature accounts.[18] A potassium tetranitritepalladium(II) (0.1018 g, 0.276 mmol, 368.61 g/mol) in a water/acetone (30:5) solution (10mL) was treated with triphenylarsine (0.169 g, 0.552 mmol, 306.23 g/mol) in acetone solution (10 mL) and the mixture was stirred for 2 h. The initially homogeneous solution rapidly turned cloudy with the formation of the product (Scheme 20). The precipitate was collected by filtration, the solid was (partially) dissolved in dichloromethane and the mixture was filtered to remove potassium nitrite. Colourless crystals of compound **17** suitable for X-ray structure experiments were obtained *via* slow evaporation from dichloromethane solution.

Yield: 72 % (0.161 g, 0.20 mmol).

Analysis: Calculated C 53.32, H 3.73, N 3.45, Found C 53.89 %, H 3.34 %, N 3.11 %.

^{1}H NMR (300 MHz, CCl_3D): δ_H 7.28-7.44 (m, 12H, o,p-ArH), 7.9-7.53 (m, 8H, m-ArH)

Table 17: Crystallographic data of compound **17** before and after irradiation.

	Ground State	Metastable State
η^1-*O*-nitrito occupancy	0%	41%
Empirical formula	C36 H30 As2 N2 O4 Pd	C36 H30 As2 N2 O4 Pd
Formula weight	810.86	810.86
Temperature	100(2) K	100(2) K
Wavelength	0.77490 Å	0.77490 Å
Crystal system	Triclinic	Triclinic
Space group	*P*-1	*P*-1
Unit cell dimensions	a = 9.5940(7) Å	a = 9.5967(9) Å
	b = 9.9987(7) Å	b = 9.9479(9) Å
	c = 10.1274(7) Å	c = 10.1121(9) Å
	α =111.4900(10)°	α = 111.2620(10)°
	β = 90.4730(10)°	β = 90.9310(10)°
	γ =115.2090(10)°	γ = 114.4540(10)°

Volume	802.14(10) Å^3	803.05(13) Å^3
Z	1	1
Crystal size	0.05 x 0.02 x 0.01 mm	0.05 x 0.02 x 0.01 mm
Theta range for data collection	4.02 to 33.59°	4.03 to 33.65°
Independent reflections	4729 [*R*(*int*) = 0.0536]	4795 [*R*(*int*) = 0.0470]
Completeness to theta = 30.50°	97.7 %	98.6 %
Data / restraints / parameters	4729 / 0 / 205	4795 / 13 / 237
Final R indices [I>2sigma(I)]	*R*1 = 0.0525, *wR*2 = 0.1622	*R*1 = 0.0371, *wR*2 = 0.1170
R indices (all data)	*R*1 = 0.0546, *wR*2 = 0.1651	*R*1 = 0.0402, *wR*2 = 0.1213

7.2.21. Preparation of bis(tricyclohexylphosphine)bis(η^1-*N*-nitro)platinum (II) - 18

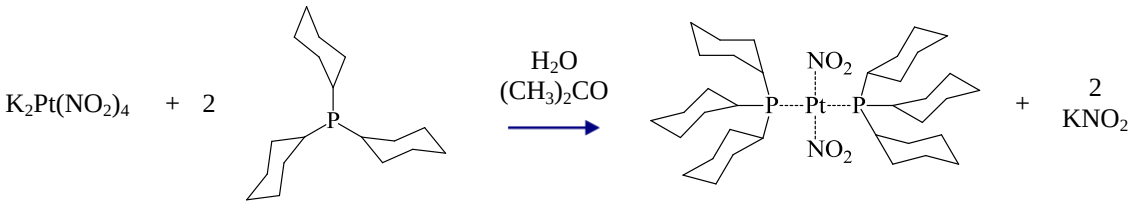

Scheme 21: Synthesis of compound **18**.

A freshly prepared sample of potassium tetranitroplatinate (0.1 g, 0.219 mmol MW = 457.3) was treated with a solution of tricyclohexylphosphine (0.123 g, 0.438 mmol, 280.43 g/mol) in acetone (10 mL) and the mixture was stirred for 24 h. The initial homogeneous solution rapidly turned cloudy with the formation of the product (Scheme 21). The precipitate was collected by filtration, the residue dissolved in dichloromethane and filtered to remove potassium nitrite. Crystals suitable for X-ray experiment were grown from dichloromethane layered with acetone.

Yield: 80 % (0.149 g, 0.18 mmol).

Analysis: Calculated C 50.99 %, H 7.85 %, N 3.30 %, Found C 50.54 %, H 7.33 %, N 3.10 %.

^{1}H NMR (300 MHz, CCl_3D): δ_H 2.87-1.07 (m, 44H, C_6H_{11}) (broad NMR with overlapping peaks).

^{31}P NMR (300 MHz, CCl_3D): δ_P 25.09

UVvis λ_{max}: 250 nm (7600 Lmol^{-1}cm^{-1}), 330 nm (253 Lmol^{-1}cm^{-1}).

Table 18: Crystallographic data of compound **18**.

	Ground-state	Metastable-state
η^1-*O*-nitrito occupancy	0%	20%
Empirical formula	C36 H66 N2 O4 P2 Pt	C36 H66 N2 O4 P2 Pt
Formula weight	847.94	847.94
Temperature	100(2) K	100(2) K
Wavelength	0.7107 Å	0.7107 Å

Crystal system	Triclinic	Triclinic
Space group	*P*-1	*P*-1
Unit cell dimensions	a = 10.122(5) Å	a = 10.107(5) Å
	b = 10.388(5) Å	b = 10.428(5) Å
	c = 10.617(5) Å	c = 10.676(5) Å
	α = 111.736(5)°	α = 112.184(5)°
	β = 110.638(5)°	β = 110.509(5)°
	γ = 94.229(5)°	γ = 93.825(5)°
Volume	943.3(8) Å^3	949.8(8) Å^3
Z	1	1
Crystal size	0.10 x 0.08 x 0.08 mm^3	0.10 x 0.08 x 0.08 mm^3
Theta range for data collection	2.95 to 32.58°	3.43 to 37.91°
Independent reflections	6334 [$R(int)$ = 0.0287]	9014 [$R(int)$ = 0.0430]
Completeness to theta = 30.50°	99.8 %	96.9 %
Data / restraints / parameters	6334 / 0 / 205	9014 / 7 / 218
Final R indices [I>2sigma(I)]	$R1$ = 0.0185, $wR2$ = 0.0352	$R1$ = 0.0340, $wR2$ = 0.0559
R indices (all data)	$R1$ = 0.0185, $wR2$ = 0.0352	$R1$ = 0.0402, $wR2$ = 0.0572

7.2.22. Preparation of bis(triphenylphosphine)bis(η^1-*N*-nitro)platinum (II) – 19

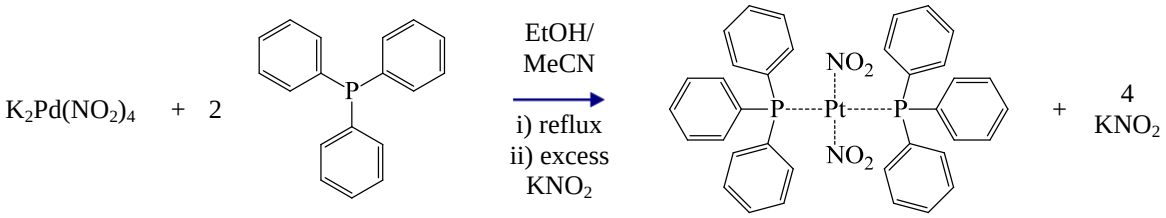

Scheme 22: Synthesis of compound **19**.

Compound **19** was synthesised using a modified procedure from literature accounts.[19] A freshly prepared sample of potassium tetranitroplatinate (0.1 g, 0.219 mmol MW = 457.3) was treated with two equivalents of triphenylphosphine (0.123 g, 0.438 mmol, 280.43 g/mol) in acetone (10 mL) and the mixture was stirred for 24 h. The initial homogeneous solution rapidly turned cloudy with the formation of the product (Scheme 22). The precipitate was collected by filtration, the solid was (partially) dissolved in dichloromethane and the mixture was filtered to remove potassium nitrite. Crystals suitable for X-ray experiment were grown from dichloromethane layered with acetonitrile.

Yield: 83 % (0.148 g, 0.18 mmol).

Analysis: Calculated C 53.27 %, H 3.73 %, N 3.45 %, Found C 55.16 %, H 3.59 %, N 3.17 %.

^{1}H NMR (300 MHz, CCl_3D): δ_H 7.78-7.35 (m, 20H, Ar).

UVvis λ_{max}: 263 nm (40199 $Lmol^{-1}cm^{-1}$).

Table 19: Crystallographic data of compound **19**.

Empirical formula	C38 H34 Cl4 N2 O4 P2 Pt
Formula weight	981.50
Temperature	150(2) K
Wavelength	0.7107 Å
Crystal system	Orthorhombic
Space group	*Pbca*
Unit cell dimensions	*a* = 20.471(5) Å
	b = 7.953(5) Å
	c = 23.261(5) Å
Volume	3787(3) $Å^3$
Z	4
Crystal size	0.10 x 0.08 x 0.08 mm^3
Theta range for data collection	2.65 to 32.92°
Independent reflections	6847 [*R*(*int*) = 0.0815]
Completeness to theta = 32.92°	96.6 %
Data / restraints / parameters	6847 / 0 / 232
Final R indices [I>2sigma(I)]	*R*1 = 0.0185, *wR*2 = 0.0306
R indices (all data)	*R*1 = 0.0727, *wR*2 = 0.0349

7.3. References

1	Lee, C. T.; Yang, W. T.; Parr, R. G. *Phys. Rev. B: Condens. Matter* **1988**, *37*, 785.
2	Becke, A. D. *J. Chem. Phys.* **1993**, *98*, 5648.
3	Frisch, M. J. *et al. Gaussian, Inc., Wallingford CT* **2004**.
4	Andrae, D.; Haussermann, U.; Dolg, M.; Stoll, H.; Preuss, H. *Theor. Chim. Acta* **1990**, *77*, 123.
5	Ditchfie.R; Hehre, W. J.; Pople, J. A. *J. Chem. Phys.* **1971**, *54*, 724.
6	Harihara.Pc; Pople, J. A. *Theor. Chim. Acta* **1973**, *28*, 213.
7	Varetto, U. *Swiss National Supercomputing Centre: Manno (Switzerland)*.
8	Green, R. W. B., Bernice *Aust. J. Chem.* **1973**, *26*, 1663.
9	Feltham, R. D.; Elbaze, G.; Ortega, R.; Eck, C.; Dubrawski, J. *Inorg. Chem.* **1985**, *24*, 1503.
10	Takeuchi, A.; Sato, K.; Sone, K.; Yamada, S.; Yamasaki, K. *Inorg. Chim. Acta* **1967**, *1*, 399.
11	Chattopadhyay, T.; Ghosh, M.; Banerjee, A.; Banu, K. S.; Das, D.; Nethaji, M. *Transition Met. Chem.* **2007**, *32*, 531.
12	El-Sayed, L.; Ragsdale, R. O. *Inorg. Chem.* **1967**, *6*, 1640.
13	Cortes, R.; Arriortua, M. I.; Mesa, J. L.; Rojo, T. *J. Appl. Crystallogr.* **1985**, *18*, 366.
14	Bomfim, J. A. S.; de Souza, F. P.; Filgueiras, C. A. L.; de Sousa, A. G.; Gambardella, M. T. P. *Polyhedron* **2003**, *22*, 1567.
15	Kriegesimondsen, J.; Feltham, R. D. *Inorg. Chim. Acta* **1983**, *71*, 185.
16	Angulo, I. M.; Bouwman, E.; van Gorkum, R.; Lok, S. M.; Lutz, M.; Spek, A. L. *J. Mol. Catal. A: Chem.* **2003**, *202*, 97.
17	Doughty, D. T.; Gordon, G.; Stewart, R. P. *J. Am. Chem. Soc.* **1979**, *101*, 2645.
18	Burmeister, J. L.; Timmer, R. C. *J. Inorg. Nucl. Chem.* **1966**, *28*, 1973.
19	Rigamonti, L.; Forni, A.; Manassero, M.; Manassero, C.; Pasini, A. *Inorg. Chem.* **2010**, *49*, 123.